MODELING OF ATMOSPHERIC PRESSURE PLASMA PROCESSING OF GASES AND SURFACES

BY

RAJESH DORAI

B.Tech., Indian Institute of Technology, Madras, 1998
M.S., University of Illinois at Urbana-Champaign, 2000

THESIS

Submitted in partial fulfillment of the requirements
for the degree of Doctor of Philosophy in Chemical and Biomolecular Engineering
in the Graduate College of the
University of Illinois at Urbana-Champaign, 2002

Urbana, Illinois

MODELING OF ATMOSPHERIC PRESSURE PLASMA PROCESSING
OF GASES AND SURFACES

Rajesh Dorai, Ph.D.
Department of Chemical and Biomolecular Engineering
University of Illinois at Urbana-Champaign, 2002
Mark J. Kushner, Adviser

Atmospheric pressure plasma based processes have become indispensable components of numerous industrial applications owing to their high efficiencies and low costs. In this work, we computationally investigate the applications of dielectric barrier discharges (DBDs), one of the commonly used atmospheric pressure plasma devices, to the remediation of nitrogen oxides (NO_x) from diesel exhausts and to the surface treatment of polypropylene (PP) for improved adhesion. We determine the kinetics of these processes in order to develop methods to optimize their energy efficiencies.

Unburned hydrocarbons (UHCs), inevitably present in diesel exhausts, significantly affect the plasma remediation of NO_x by oxidizing NO, the major form of NO_x in the exhaust, into NO_2. The efficiency of NO_x removal increases when a given amount of energy is deposited in a large number of shorter-duration pulses as opposed to in a single pulse.

Soot particles significantly affect the plasma remediation of NO_x by changing the composition of NO and NO_2 in the plasma. In general, NO_x removal improves in the presence of soot. Heterogeneous reactions on soot also result in the production of CO. At high number densities and large diameters, soot particles significantly affect the ionization kinetics in the gas phase. When using repetitively pulsed discharges in the presence of soot, both NO_x removal improves and soot oxidation increases.

Spatial dependencies can affect the energy efficiencies of remediation. Localized energy deposition in the streamer results in production of radicals in confined regions. Consumption of these radicals by UHCs limits their diffusion to outer radii thereby affecting the remediation.

Atmospheric pressure plasma processing of PP in humid air increases the surface densities of alcohol, peroxy, acid, and carbonyl groups. However, significant amounts of O_3 and N_xO_y are generated in the gas phase. Increasing the relative humidity results in decreased production of O_3 and increased concentrations of peroxy and acid groups on the surface. Increasing the gas temperature increases the surface concentration of peroxy radicals and decreases the concentrations of alcohol, carbonyl, and acid groups. For a given energy deposition, increasing the web speed results in decreased surface densities of peroxy, alcohol, carbonyl, and acid groups.

ACKNOWLEDGMENTS

I am thankful to my advisor, Professor Mark Kushner for his guidance, support and cooperation throughout the course of my education. This work is the result of his constant inspiration, encouragement and words of wisdom.

My sincere thanks to the members of my dissertation committee, Professor Edmund Seebauer, Professor Kevin Kim and Professor Paul Kenis for their thoughtful comments.

I am grateful to the Ford Motor Company, National Science Foundation and the 3M Company for their financial support. Further, I am thankful to Mr. John Hoard and Dr. Tim Wallington of the Ford Motor Company, and Dr. Mark Strobel of the 3M Company for their valuable suggestions and insights. Special thanks to Dr. Khaled Hassouni of CNRS (France) for an educational and fruitful collaboration.

I am also thankful to the past and present members of the Computational Optical and Discharge Physics group, Dr. Xudong "Peter" Xu, Dr. Ron Kinder, Dr. Trudy van der Straaten, Dr. Da Zhang, Dr. Junqing Lu, Dr. Trudy van der Straaten, Dr. Sang-Hoon Cho, Brian Lay, Kelly Collier, Dan Cronin, Pramod Subramonium, Arvind Sankaran, Kapil Rajaraman, Vivek Vyas, Richard Moss, and Ananth Bhoj.

I am most indebted to my parents, Sri. Dorai Krishnamurthy and Smt. Subhalakshmi Dorai, and my brother Mahesh Dorai, for their constant support, love, and encouragement. I also wish to express my thanks to my uncles and aunts for their constant motivation. I am grateful to my friend Dr. Kartik B. Ariyur for his valuable time and guidance. I am also thankful to my roommate Dr. Sarma L. Rani for his support. Finally, I wish to thank the Almighty and my ancestors for their love and blessings.

TABLE OF CONTENTS

1. INTRODUCTION

1.1 Introduction

Plasma-based processes have become an indispensable component for numerous industrial applications. Lower costs and higher efficiencies are some of the attractive features of plasma processing. In creating these plasmas, most of the electrical energy goes into the production of energetic electrons and excitation of feedstock gases rather than into gas heating. As a result, these plasmas contain "hot" electrons (few to tens of eV) and "cold" ions and neutral species (at or near the ambient temperature).

In recent years, a number of investigations have been performed to evaluate the potential of atmospheric pressure nonthermal plasmas for processing gases and surfaces. Some applications include remediation of toxic gases [1-5], processing of polymer surfaces [6-10], sterilization and decontamination of medical equipment and supplies [11,12], and production of ozone for disinfection of water supplies [13]. Advantages of atmospheric pressure processes compared to low pressure glow discharge processing include larger throughput and lower cost due to the lack of vacuum equipment and interfaces. In this work, we investigate two applications of atmospheric pressure plasmas, namely plasma remediation of NO_x and plasma surface modification of polymers. Commonly used atmospheric pressure plasma devices include electron-beam [14-20], corona discharges [21-31], and dielectric barrier discharges (DBDs) [1-5,9,32-37].

In the context of toxic gas remediation of combustion effluent, the electron-beam process is a dry-scrubbing process in which the gas is irradiated with high energy (hundreds of keV) electrons. These high-energy electrons ionize the background gases,

thereby creating a plasma. In addition to the charged particles, reactive free radicals are also produced. The applicability of this process to the remediation of SO_x (oxides of sulphur) and NO_x (oxides of nitrogen) has been investigated in detail for cleaning the effluent of coal fired power plants and as high as 80% NO_x remediation and 90% SO_x remediation have been achieved.[14,38,39] The radicals in the plasma react with the toxic components and convert them into harmless or less harmful species.

In corona discharges, the geometry confines the discharge to high-field ionization regions around the powered electrodes. Several configurations are used for these devices based on the polarity and geometry of the electrodes.[30] Corona discharge devices, which typically use an asymmetric electrode pair such as point-plane, are driven by fast-rising high voltage (10s of kV) discharge pulses which typically last a few to 10s of ns. The transient nature of the plasma is controlled by the applied voltage pulse.[40] The discharge develops in the high field region near the sharp electrode and spreads out towards the opposite electrode. It is a positive corona when the electrode with the strongest curvature is electrically positive and a negative corona otherwise. At relatively low voltages the discharge extinguishes due to the build up of space charge near the sharp electrode. This space charge then disappears due to diffusion and recombination and a new discharge pulse appears. This is a self-repetitive corona and occurs in the positive and in the negative case.

DBDs (also known as silent discharges), shown schematically in Fig. 1.1, consist of planar electrodes or concentric cylindrical tubes with either one or both of the electrodes being covered with dielectric layers, separating them from the gas. The electrode spacing is typically 2-5 mm. Voltages, typically a few to tens of kV, at

frequencies ranging from a few hundreds to several thousand Hz are applied across the electrodes to produce a number of filamentary microdischarges. Typically, these microdischarges last a few to 100 ns and are 10s to 100s of μm in diameter. The discharge channels are terminated when the charge accumulation on the surface of the dielectric reduces the voltage across the gap to a value below the sustaining level.

One of the important applications of atmospheric pressure plasmas is the remediation of toxic gases, and in particular NO_x. During the past decade, the removal of NO_x has become a central scientific concern because of its key role in many global environmental problems such as acid rain, photochemical smog formation, and the greenhouse effect. Approximately 50% of the NO_x emissions are from on road vehicles, particularly diesel engines.[41] Current measures for NO_x removal include catalytic reduction, plasma remediation, and direct decomposition using reductants such as ammonia and hydrocarbons. The use of catalysts for remediation has inherent problems of poisoning requiring periodic maintenance. Direct decomposition is impractical for mobile sources. Hence, plasma remediation is being investigated for the removal of NO_x (oxides of nitrogen). The critical issues in the practical implementation of atmospheric pressure plasmas for the remediation of toxic gases are twofold; electrical efficiency and generation of byproducts.

Although high levels of remediation have been achieved using e-beams, the large sizes of these devices make them impractical for mobile applications. Both corona and DBDs have been studied for remediation of toxic gases, but it still remains an open question as to which is more efficient for plasma chemical applications. For use in mobile sources such as on road vehicles, the plasma devices should ideally be

lightweight, use low voltage, and must be effective in removing the toxins without generating significant amounts of other unwanted compounds. In this regard, DBDs are known for their high-energy efficiency and reliability. They are in general compact, stable, can operate at high average power and with low voltages (a few to ten kV) compared to coronas or electron beams. Given these advantages of size, cost, and safety of the DBD over e-beam and coronas, the successful application of the DBDs will depend on the ability to arrive at optimal operating conditions for high efficiency of remediation and low byproduct formation. To this end, we have developed computer models for atmospheric pressure DBD processing of gases to study in detail the mechanisms responsible for the decomposition of the pollutant molecules in the plasma. An understanding of the plasma chemical kinetics serves as an important design tool in maximizing the energy efficiency and identifying the byproducts. By realistically modeling the exhaust gases and by understanding the process of their remediation, strategies for optimization can be proposed.

Several experimental and numerical investigations have been performed on the discharge dynamics [42,43] and the chemical kinetics [40,44,45] in DBD reactors used for diesel exhaust treatment. Typically, diesel exhausts contain N_2, O_2, H_2O, and CO_2 (mostly from the unreacted excess air and combustion products) with 100s of ppm of NO_x (primarily NO), CO, H_2, and unburned hydrocarbons (UHCs) due to the incomplete combustion of the fuel. Since the actual exhaust composition depends on the origin of the fuel, fuel-to-air ratio, and compression ratio, investigations are usually performed on model gases. For example, Niessen *et al.* [46] examined ethene (C_2H_4) as an additive to a NO_x-humid air mixture. Penetrante *et al*. [47] investigated the consequences of propene

(C_3H_6) in a NO_x-air feed. Both studies showed that UHCs significantly contribute to NO oxidation. Niessen *et al*. [46] found that adding 2000 ppm of C_2H_4 improved the NO removal efficiency from 60 eV to 5-10 eV with most of the remediated NO being converted to NO_2. With propene addition, Penetrante *et al.* [47] found that, at 300 ^oC, almost 100% of the initial NO (500 ppm) was converted to NO_2, whereas in the absence of propene, only 7% of NO was removed.

In this work, we have developed computer models to investigate the dynamics and kinetics of plasma remediation in DBDs. To address in detail the chemical processes during remediation, we have used a zero-dimensional (0-D) model called GLOBAL_KIN to capture the volumetric plasma kinetics. To investigate in further detail the dynamics and kinetics during the plasma remediation, one-dimensional (1-D) hydrodynamic models have been developed. The 1-D model is radially dependent and is applied to the study of a single microstreamer. The details of these models are discussed in Chapter 2.

In Chapter 3, GLOBAL_KIN is used to investigate the consequences of multiple pulse formats on the plasma remediation of NO_x in the presence of UHCs. The gas mixture used for this investigation contained N_2, O_2, H_2O, and CO_2 with ppm levels of NO_x (primarily NO), CO, H_2, C_3H_6 (propene), and C_3H_8 (propane). We found that it is more efficient with respect to remediation to deposit a given amount of energy in a large number of shorter duration pulses. With each pulse, radicals initiating the plasma chemistry are generated, and during the interpulse period, these radicals undergo reactions, thereby changing the composition of the plasma. The reaction chemistry for the follow-on pulses is different from that which would be obtained from an equivalent

energy deposition in a single or smaller number of pulses due to the accumulation of these interpulse products.

Another step towards more realistic modeling of plasma treatment of exhaust is accounting for carbonaceous particles in the exhaust. Soot particles in typical diesel exhausts have mass concentrations of 20-200 mg/m^3.[48] The average geometric diameter and particle density of the soot particles depend on the combustion regime. Typical values are around 100 nm [49] and 10^8 cm^{-3},[48,50] which are high enough to initiate heterogeneous chemistry. Soot influences the chemistry of NO_x plasma remediation dominantly through NO_2-soot interactions [51,52] and influences the ionization kinetics through electron attachment to and ion neutralizations with the particles. The resulting changes of electron density and temperature may then affect the rates of electron-impact processes.

To address the reactions on soot surfaces, a heterogeneous reaction chemistry model was developed and incorporated into GLOBAL_KIN. The details of this model are also given in Chapter 2. In Chapter 4, results from our investigations on the consequences of soot particles on the plasma remediation of NO_x are discussed. We have performed parameterizations while varying energy deposition, UHC concentration, and soot particle number density on NO_x removal. We found that NO_x remediation improved by nearly 10% in the presence of soot. With soot, higher energies were required for the remediation of a given amount of NO.

In Chapter 5, we report on a computational investigation of the combined effects of repetitive discharge pulses and soot on NO_x remediation and soot oxidation. We investigated the consequences of varying energy deposition, inlet UHC concentration,

soot diameter, and soot particle number density on NO_x remediation and soot oxidation for cases when using a single pulse and when using multiple pulses. In the absence of soot, using repetitive pulses resulted in larger conversion of NO to NO_2 compared to using a single pulse case. The combined effects of multiple pulses and heterogeneous chemistry on NO_x remediation and soot oxidation are twofold. Improved NO_x removal by the increased production of HNO_2, HNO_3, organic nitrates and nitrites due to the more favorable overlap in time of NO_2 and reactive radical densities; and increased soot oxidation because of larger NO_2 densities.

Spatially nonuniform energy deposition in DBDs results in spatial gradients in gas temperature and species densities. These gradients initiate advection and diffusion leading to transport of species to and from the microstreamer region. Previous studies on the dynamics and kinetics of these processes associated with the DBD processing of NO_x showed a significant effect of the transport on the NO_x removal.[42] However, the exhaust gases used in the investigations did not contain UHCs. In this work, we have investigated in detail the consequences of UHCs on the discharge kinetics and transport during the DBD processing of NO_x. For this, we have used the 1-D radial hydrodynamic model. The results are discussed in the Chapter 6.

Another important use of atmospheric pressure plasmas is in the modification of polymer surfaces for improved wettability and adhesion. In these surface treatments, only the top 100s of Å of the material is modified, leaving the bulk polymer largely unaffected.[8] In general, the surface energy of untreated polymers is insufficient for good adhesion. For optimum adhesion, the surface energy of the polymer should be larger than that of the material to be bonded with. Similarly, for effective wetting of a

liquid on a polymer surface, the surface energy of the polymer should exceed the surface tension of the liquid. The surface energies of some common polymers and the surface tensions of a few commonly used inks are shown in Fig. 1.2. For example, the surface energy of untreated PP is ≈ 27 mJ-m^{-2}.[53,54] The typical surface tensions of water-based adhesives are 44-50 mJ-m^{-2} and those of water-based inks are 54-56 mJ-m^{-2}.[55] Plasma surface treatment can increase the surface energy of PP above that of the surface tensions of adhesives and inks, thereby enabling efficient sticking and printing. For example, in studies of atmospheric pressure plasma treatment of PP in He (containing ppm levels of O_2 and H_2O) by Massines and Gouda [53], the surface energy of PP increased from 27 mJ-m^{-2} to as high as 62 mJ-m^{-2}. The increase was attributed primarily to the bonding of O atoms to the PP surface.

A variety of polymers have been treated by plasmas, including polypropylene (PP) [53,56-61], polyethylene (PE) [9,56,62-66], poly(tetrafluoroethylene) [37], polyimide [67,68], polystyrene [66], polycarbonate [69,70], and poly(*p*-phenylene benzobisthiozol) [71]. The aim of these treatments is generally to improve the wetting and adhesion properties of the polymers. For example, Shenton *et al.* [72] observed that atmospheric pressure plasma treatment of low density PE (LDPE) and poly(ethylene terephthalate) (PET) resulted in adhesion enhancements by factors ranging from two to ten.

Plasma surface treatment of polymers primarily results in the oxidation of the surface by generation of functional groups such as C-OH (alcohol), C-O-O-H (hydroperoxide), H-C=O (aldehyde), C=O (carbonyl), C-O-C=O (ester), C-O-O (peroxy), H-O-C=O (acid), OC(O)O (carbonate), and NH_2 (amine). For example, Foerch *et al.* [63]

observed the formation of ester, alcohol, carbonyl, and acid groups by XPS C 1*s* spectra while treating PE with an air plasma. Surface physicochemistry studies of air-corona-discharge-treated PP by O'Hare *et al*. [73] showed the presence of alcohol, peroxide, acid, ester, carbonyl, and carbonate groups on the surface. The relative concentrations of the functional groups generally depend on the operating conditions of the plasma generator such as energy deposition and gas composition for a given polymer being processed. These interrelations can be quite complex. Poncin-Epaillard *et al.* [58] measured 2.5×10^{14} cm^{-2} of amino groups following N_2 microwave plasma treatment of PP using a power of 100 W. Higher concentrations of these groups were observed on PE for treatments with short durations (higher frequency) and powers greater than 50 W.

In addition to functionalization, other phenomena such as erosion of the polymer, chain scission, and cross-linking may occur with corona treatment.[74,75] Clouet and Shi [62] used hexatriacontane ($C_{36}H_{74}$) as a representative for high-density polyethylene (HDPE) to study the gas phase products of plasma surface oxidation and erosion. They found that CO, H_2O, CO_2, and H_2 were the primary products in an oxygen rich plasma. Hansen *et al.* [76] studied the effects of atomic oxygen on polymers such as PE, PP, polyimide, and polysulfide. Emission of CO_2 was observed and correlated with the erosion of the polymer at a rate directly proportional to the duration of the treatment.

The erosion of the polymer occurs through chain scissions and the formation of low molecular weight oxidized materials (LMWOMs). The volatile components of LMWOM can leave the surface.[60,77] LMWOMs have been found to agglomerate into globules at the surface due to a large difference in interfacial free energy between the underlying hydrophobic substrate and the oxygenated overlayer.[78] The role of

LMWOM in the improvement of adhesion is still unresolved. Strobel *et al.* [60] suggest that formation of LMWOM improves adhesion for select conditions whereas Kim *et al*. [6] propose that excessive scission by corona plasma treatment resulting in LMWOM can lead to the formation of weak boundary layers that hinder adhesion.

The gas used for surface treatment determines the surface properties of the polymer. For example, oxygen plasma treatment generally increases the surface energy of polymers, whereas fluorine plasma treatment generally decreases the surface energy thereby making the polymer more hydrophobic and chemically inert.[8,79] Low surface energies can also be obtained by insertion of oriented methyl groups into the polymer chain.[80] In this regard, several gases have been investigated for modifying the surface properties of PP, including He [53], CO_2 [81], N_2 [54,58], NH_3 [82], and air [54,61,83]. CO_2 plasmas have been found to result in less erosion of PP compared to O_2 plasmas.[81] Studies by Massines *et al.* [83] on the role of gas composition in the DBD treatment of PP showed that O_2, even when present in small quantities, can significantly affect the surface chemistry and hence the level of surface transformation. For example, when ≈ 0.2% of O_2 was added to N_2, the percentage of O on the surface doubled while the percentage of N on the surface decreased by a factor of 5.[83] Meiners *et al.* [84] showed that exposure of PP to an Ar plasma followed by exposure to pure acetylene gas (C_2H_2) increased the surface energy from 30 mJ-m^{-2} to 72 mJ-m^{-2}. A thin polymeric film was formed on the PP surface which both increased and stabilized the surface energy. When only an air or Ar plasma was used, the surface energy was 40 mJ-m^{-2}.

The nature of the discharge also affects the surface properties of the polymer. Filamentary discharges, the normal mode of operation of an atmospheric pressure

plasma, result in inhomogeneous treatment on a microscopic scale.[54] Under controlled operating conditions, stable, uniform, nonfilamentary or glow discharges, can be produced,[53] which are often effective compared to filamentary discharges for surface modification. For example, in studies of PP surface treatment at atmospheric pressure by Massines *et al.* [53], the surface energy increased from 27 mJ-m^{-2} to 62 mJ-m^{-2} when using glow (nonfilamentary) discharges, whereas with filamentary discharges the surface energy increased only to 45 mJ-m^{-2}. The contact angle for the glow discharge treated PP was 32^{o} and that for the filamentary discharge treated PP was 57^{o} (The smaller the contact angle, the larger the wettability.).

Power deposition and web speed, which determine the total energy deposition to the surface, largely control the surface properties of the treated film.[75] Other parameters that influence the surface properties include air-gap thickness of the discharge, relative humidity (RH), gas temperature, and the structure of the polymer. For example, Hansen *et al.* [76] found that the rates of oxidation of branched polymers such as PP were considerably higher compared to the relatively unbranched hydrocarbon polymers such as PE for otherwise the same operating conditions.

Plasma modified polymer surfaces tend to age, a process commonly attributed to the migration of groups on the surface after treatment, surface reorientation, and exposure to oxidizing environments.[57] Aging depends on the type of polymer and the process conditions used for its treatment. For example, studies of air-corona-discharge treatment of PP by Strobel *et al.* [57] showed the effects of aging to be minimal. The O/C ratio on the surface did not change with aging while the wettability decreased by < 5% after 30 days. This change in the wettability was attributed to the reorientation of surface groups.

Guimond *et al.* [54] showed that the surface energy of PP produced by a N_2 glow discharge treatment decreased by aging. Immediately after treatment, the surface energy was ≈ 53 mJ-m^{-2}. After 10 days, the surface energy stabilized to ≈ 44 mJ-m^{-2}.

Although plasma processing of polymers is being done in industries on a large scale for more than a decade, the mechanisms responsible for the change in the surface properties of the polymers are unclear. An understanding of the basic processes and their consequences on the surface modification will be of use in arriving at optimal conditions for treatment. To this end, we have developed a pseudo-homogeneous global kinetics model for the study of DBD processing of polymer surfaces. This model is similar to that used for the study of heterogeneous reactions on soot during the plasma remediation of NO_x. The details of this model are given in Chapter 2.

Although the model is capable of handling surface chemistries for any polymer, we have investigated in particular the plasma surface modification of polypropylene (PP), a widely used material. We have developed a surface reaction mechanism for PP and analyzed in detail the consequences of the variations in important process variables such as energy deposition, relative humidity, film speed, and process gas temperature on the surface properties of PP. Results from our computational investigations on the surface modification of PP in humid-air plasmas are in Chapter 7. We found that increasing energy deposition not only results in increased densities of peroxy and acid groups on the PP surface, but also increases byproducts such as N_xO_y and O_3. Increasing the RH resulted in decreased production of O_3. Increasing the gas temperature increased the surface concentration of peroxy radicals and decreased the surface concentrations of alcohol, carbonyl, and acid groups. For a given energy deposition, increasing the web

speed resulted in decreased densities of peroxy, alcohol, carbonyl, and acid groups on the PP surface.

Our concluding remarks are in Chapter 8.

1.2 Figures

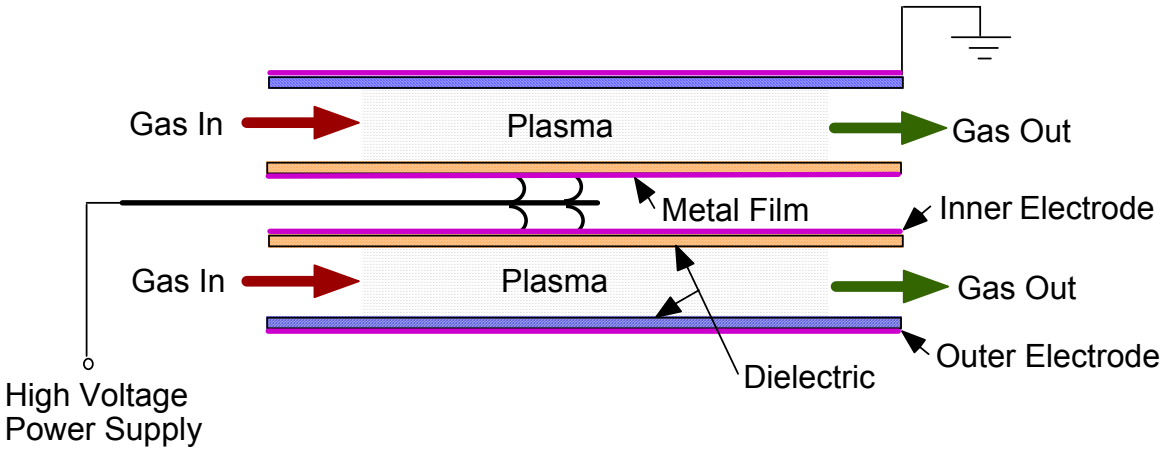

Fig. 1.1. A typical dielectric barrier discharge (DBD) device.

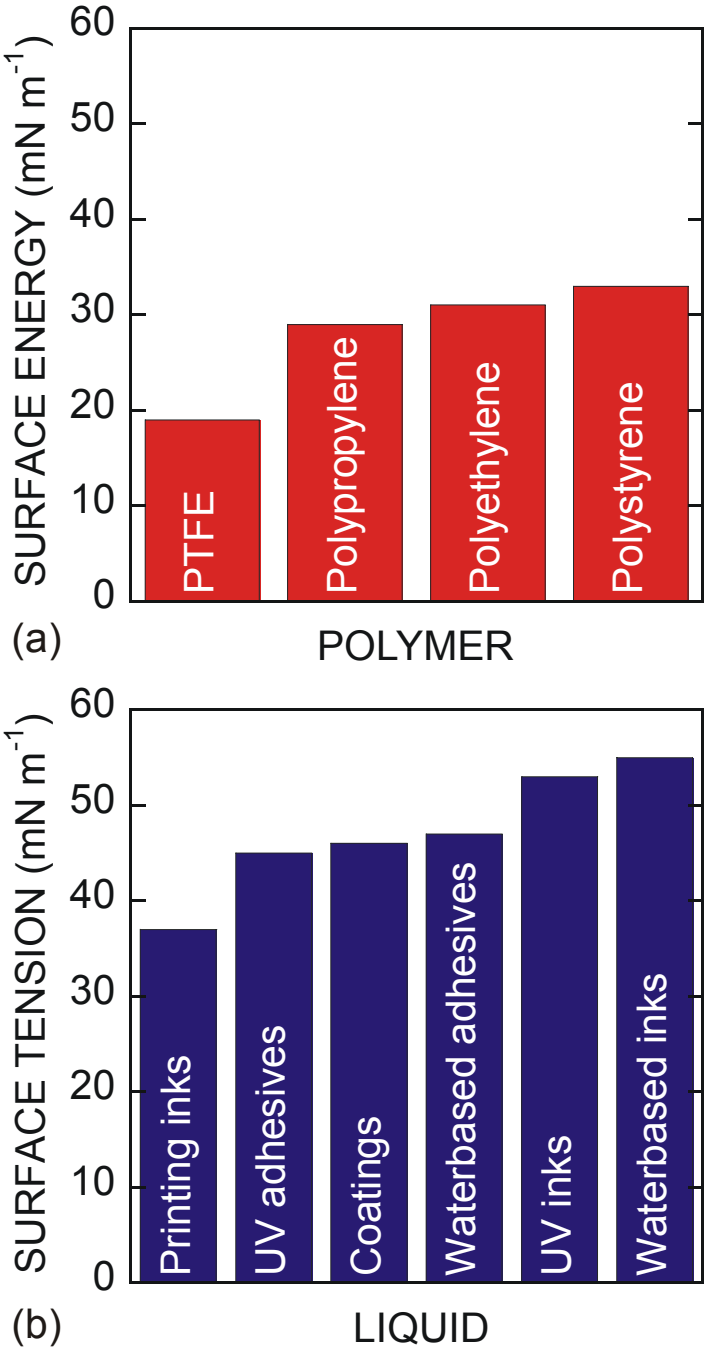

Fig. 1.2. Surface energies of common polymers and surface tensions of liquids. For optimal wetting of a polymer surface, the surface energy of the polymer should exceed the surface tension of the liquid.

1.3 References

1. R. Wegst, M. Neiger, H. Russ, and S. Liu, SAE Technical Paper Series **1999-01-3686,** 1 (1999).
2. C. Fitzsimmons, F. Ismail, J. C. Whitehead, and J. J. Wilman, J. Phys. Chem. A **104,** 6032 (2000).
3. M. B. Chang, M. J. Kushner, and M. J. Rood, Environ. Sci. Technol. **26,** 777 (1992).
4. M. B. Chang, J. H. Balbach, M. J. Rood, and M. J. Kushner, J. Appl. Phys. **69,** 4409 (1991).
5. A. Khacef, J. M. Cormier, and J. M. Pouvesle, J. Phys. D: Appl. Phys. **35,** 1491 (2002).
6. C. Y. Kim, J. Evans, and D. A. I. Goring, J. Appl. Poly. Sci. **15,** 1365 (1971).
7. E. M. Liston, L. Martinu, and M. R. Wertheimer, J. Adhesion Sci. Technol. **7,** 1091 (1993).
8. C.-M. Chan, T.-M. Ko, and H. Hiraoka, Surf. Sci. Rpts. **24,** 1 (1996).
9. J. B. Lynch, P. D. Spence, D. E. Baker, and T. A. Postlethwaite, J. Appl. Poly. Sci. **71,** 319 (1999).
10. T. Hirotsu, T. Tsujisaka, T. Masuda, and K. Nakayama, J. Appl. Poly. Sci. **78,** 1121 (2000).
11. P. Koulik, S. Begounov, and S. Goloviatinskii, Plasma Chem. Plasma Process. **19,** 311 (1999).
12. P. Koulik, Plasma Chem. Plasma Process. **20,** 159 (2000).

13. B. Eliasson, M. Hirth, and U. Kogelschatz, J. Phys. D: Appl. Phys. **20,** 1421 (1987).

14. N. W. Frank, Radiat. Phys. Chem. **45,** 989 (1995).

15. J. C. Person and D. O. Ham, Radiat. Phys. Chem. **31,** 1 (1988).

16. N. W. Frank, S. Hirano, and K. Kawamura, Radiat. Phys. Chem. **31,** 57 (1988).

17. N. W. Frank, K. Kawamura, and G. Miller, Radiat. Phys. Chem. **25,** 35 (1985).

18. P. Fuchs, B. Roth, U. Schwing, H. Angele, and J. Gottstein, Radiat. Phys. Chem. **31,** 45 (1988).

19. S. Jordan, Radiat. Phys. Chem. **31,** 21 (1988).

20. N. W. Frank and S. Hirano, in *Non-thermal plasma techniques for pollution control-Part B: Electron Beam and Electrical Discharge Processing*, edited by B. M. Penetrante and S. Schulthesis (Springer, New York, 1993), p. 1.

21. R. H. Amirov, E. I. Asinovsky, I. S. Samoilov, and A. V. Shepelin, Plasma Sources Sci. Technol. **2,** 289 (1993).

22. E. A. Filimonova, R. H. Amirov, H. T. Kim, and I. H. Park, J. Phys. D: Appl. Phys. **33,** 1716 (2000).

23. Y. S. Mok and I. Nam, Trans. Plasma Sci. **27,** 1188 (1999).

24. G. Naidis, J. Phys. D: Appl. Phys. **30,** 1214 (1997).

25. J. Y. Park, I. Toicic, F. G. Round, and J. S. Chang, J. Phys. D: Appl. Phys. **32,** 1006 (1999).

26. B. M. Penetrante, M. C. Hsiao, B. T. Merritt, G. E. Vogtlin, P. H. Wallman, M. Neiger, O. Wolf, T. Hammer, and S. Broer, Appl. Phys. Lett. **68,** 3719 (1996).

27. M. Tas, R. van Hardeveld, and E. van Veldhuizen, Plasma Chem. Plasma Process. **17,** 371 (1997).

28. G. E. Vogtlin and B. M. Penetrante, in *Non-thermal plasma techniques for pollution control-Part B: Electron Beam and Electrical Discharge Processing*, edited by B. M. Penetrante and S. Schulthesis (Springer, New York, 1993), p. 187.

29. N. Sano, T. Nagamoto, H. Tamon, T. Suzuki, and M. Okazaki, Ind. Eng. Chem. Res. **36,** 3783 (1997).

30. M. Goldman, A. Goldman, and R. S. Sigmond, Pure and Appl. Chem. **57,** 1353 (1985).

31. C. Q. Sun, D. Zhang, and L. C. Wadsworth, Adv. Polym. Technol. **18,** 171 (1999).

32. B. Eliasson and U. Kogelschatz, Trans. Plasma Sci. **19,** 309 (1991).

33. U. Kogelschatz, *Silent discharges and their applications* (International Conference on Gas Discharges and Their Applications, Swansea, U.K., 1992), p. 1.

34. K. Takaki, M. A. Jani, and T. Fujiwara, Trans. Plasma Sci. **27,** 1137 (1999).

35. I. Nagao, M. Nishida, K. Yukimura, S. Kambara, and T. Maruyama, Adv. Appl. Plasma Sci. **3,** 209 (2001).

36. M. Nishida, K. Yukimura, S. Kambara, and T. Maruyama, J. Appl. Phys. **90,** 2672 (2001).

37. S. Ishikawa, K. Yukimura, K. Matsunaga, and T. Maruyama, Jpn. J. Appl. Phys. **39,** 5223 (2000).

38. D. J. Helfritch and P. Feldman, Radiat. Phys. Chem. **24,** 129 (1984).

39. D. J. Helfritch, in *Non-thermal plasma techniques for pollution control-Part B: Electron Beam and Electrical Discharge Processing*, edited by S. Schulthesis (Springer, New York, 1993), p. 33.

40. B. M. Penetrante, M. C. Hsiao, and B. T. Merritt, Trans. Plasma Sci. **23,** 679 (1995).

41. E. P. A. (http://www.epa.gov/ebtpages/airairponitrogenoxidesnox.html), "NOx - How nitrogen oxides affect the way we live and breathe," (1998).

42. A. C. Gentile and M. J. Kushner, J. Appl. Phys. **79,** 3877 (1996).

43. H. Russ, M. Neiger, and J. E. Lang, Trans. Plasma Sci. **27,** 38 (1999).

44. Y. S. Mok, S. W. Ham, and I. Nam, Trans. Plasma Sci. **26,** 1566 (1998).

45. A. C. Gentile and M. J. Kushner, J. Appl. Phys. **78,** 2074 (1995).

46. W. Niessen, O. Wolf, R. Schruft, and M. Neiger, J. Phys. D: Appl. Phys. **31,** 542 (1998).

47. B. M. Penetrante, R. M. Brusasco, B. T. Merritt, W. J. Pitz, G. E. Vogtlin, M. C. Kung, H. H. Kung, C. Z. Wan, and K. E. Voss, SAE Technical Paper Series **982508** (1998).

48. J. P. A. Neeft, M. Makkee, and J. A. Moulijn, Fuel Process. Technol. **47,** 1 (1996).

49. V.-M. Kerminen, T. E. Makela, C. H. Ojanen, R. E. Hillamo, J. K. Vilhunen, L. Rantanen, N. Havers, A. Von Bohlen, and D. Klockow, Environ. Sci. Technol. **31,** 1883 (1997).

50. D. Kayes and S. Hochgreb, Environ. Sci. Technol. **33,** 3968 (2000).

51. M. S. Akhter, A. R. Chughtai, and D. M. Smith, J. Phys. Chem. **88,** 5334 (1984).

52. A. R. Chughtai, W. F. Welch, and D. M. Smith, Carbon **28,** 411 (1990).

53. F. Massines and G. Gouda, J. Phys. D: Appl. Phys. **31,** 3411 (1998).

54. S. Guimond, I. Radu, G. Czeremuszkin, D. J. Carlsson, and M. R. Wertheimer, Plasmas Polym. **7,** 71 (2002).

55. R. P. Wettermann, Medical Device and Diagnostic Industry, October**,** 76 (1990).

56. M. Zenkiewicz, J. Adhesion Sci. Technol. **15,** 63 (2001).

57. J. M. Strobel, M. Strobel, C. S. Lyons, C. Dunatov, and S. J. Perron, J. Adhesion Sci. Technol. **5,** 119 (1991).

58. F. Poncin-Epaillard, B. Chevet, and J.-C. Brosse, J. Adhesion Sci. Technol. **8,** 455 (1994).

59. N. Shahidzadeh-Ahmadi, M. M. Chehimi, F. Arefi-Khonsari, N. Foulon-Belkacemi, J. Amouroux, and M. Delamar, Colloids Surfaces A: Physicochem. Eng. Aspects **105,** 277 (1995).

60. M. Strobel, C. Dunatov, J. M. Strobel, C. S. Lyons, S. J. Perron, and M. C. Morgen, J. Adhesion Sci. Technol. **3,** 321 (1989).

61. M. Strobel, C. S. Lyons, J. M. Strobel, and R. S. Kapaun, J. Adhesion Sci. Technol. **6,** 429 (1992).

62. F. Clouet and M. K. Shi, J. Appl. Poly. Sci. **46,** 1955 (1992).

63. R. Foerch, G. Kill, and M. J. Walzak, J. Adhesion Sci. Technol. **7,** 1077 (1993).

64. E. Foldes, A. Toth, E. Kalman, E. Fekete, and A. Tomasovszky-Bobak, J. Appl. Poly. Sci. **76,** 1529 (2000).

65. N. Sprang, D. Theirich, and J. Engemann, Surf. Coat. Technol. **74-75,** 689 (1995).

66. R. K. Wells, J. P. S. Badyal, I. W. Drummond, K. S. Robinson, and F. J. Street, J. Adhesion Sci. Technol. **7,** 1129 (1993).

67. F. D. Egitto, L. J. Matienzo, K. J. Blackwell, and A. R. Knoll, J. Adhesion Sci. Technol. **8,** 411 (1994).

68. R. Seebock, H. Esrom, M. Charbonnier, and M. Romand, Plasmas Polym. **5,** 103 (2000).

69. A. Hofrichter, P. Bulkin, and B. Drevillon, J. Vac. Sci. Technol. A **20,** 245 (2002).

70. H. Biederman, D. Slavinska, H. Boldyreva, H. Lehmberg, G. Takaoko, J. Matsuo, H. Kinpara, and J. Zemek, J. Vac. Sci. Technol. B **19,** 2050 (2001).

71. Y. Qiu, S. Deflon, and P. Schwartz, J. Adhesion Sci. Technol. **7,** 1041 (1993).

72. M. J. Shenton, M. C. Lovell-Hoare, and G. C. Stevens, J. Phys. D: Appl. Phys. **34,** 2754 (2001).

73. L.-A. O'Hare, S. Leadley, and B. Parbhoo, Surf. Interface Anal. **33,** 335 (2002).

74. M. Gheorghiu, F. Arefi, J. Amouroux, G. Placinta, G. Popa, and M. Tatoulian, Plasma Sources Sci. Technol. **6,** 8 (1997).

75. C.-M. Chan, *Polymer Surface Modification and Characterization*, 1 ed. (Hanser/Gardner Publications, Inc., New York, 1994).

76. R. H. Hansen, J. V. Pascale, R. De Benedictis, and P. M. Rentzepis, J. Polym. Sci.: Part A: Poly. Chem. **3,** 2205 (1965).

77. F. Poncin-Epaillard, J. C. Brosse, and T. Falher, Macromol. Chem. Phys. **200,** 989 (1999).

78. R. D. Boyd, A. M. Kenwright, J. P. S. Badyal, and D. Briggs, Macromolecules **30,** 5429 (1997).

79. S. Mukhopadhyay, P. Joshi, S. Datta, J. Zhao, and P. France, J. Phys. D: Appl. Phys. **35,** 1927 (2002).

80. D. Hegemann, H. Brunner, and C. Oehr, Plasmas Polym. **6,** 221 (2002).

81. F. Poncin-Epaillard and M. Aouinti, Plasmas Polym. **7,** 1 (2002).

82. N. Shahidzadeh, F. Arefi-Khonsari, M. M. Chehimi, and J. Amouroux, Surf. Sci. **352-354,** 888 (1996).

83. F. Massines, G. Gouda, N. Gherardi, M. Duran, and E. Croquesel, Plasmas Polym. **6,** 35 (2001).

84. S. Meiners, J. G. H. Salge, E. Prinz, and F. Forster, Surf. Coat. Technol. **98,** 1121 (1998).

2. DESCRIPTION OF THE MODELS

2.1 Overview

In this chapter, the models used to investigate the atmospheric pressure plasma processing of gases and surfaces are described. The 0-D model, GLOBAL_KIN, used to investigate the volumetric plasma kinetics of NO_x plasma remediation is described in Section 2.2. The modifications made to this model to address the surface kinetics on soot surfaces are discussed in Section 2.3. In Section 2.4, we describe in detail the 1-D hydrodynamic radial model used to investigate the microstreamer discharge dynamics in DBDs. Finally, in Section 2.5, we discuss the modifications made to GLOBAL_KIN to investigate the plasma surface treatment of polymers.

2.2 Zero-Dimensional Plasma Chemistry Model – GLOBAL_KIN

GLOBAL_KIN is a spatially homogenous model and consists of three main modules: a plasma chemistry module, a circuit module and a Boltzmann equation module. A schematic of the modules used in GLOBAL_KIN is given in Fig. 2.1a. From a user-defined reaction mechanism, the plasma chemistry module constructs differential equations for the evolution of the density of species, the electron temperature, and the gas temperature. The circuit module provides the E/N (electric field/number density) in the plasma. The source terms for the gas phase reactions are obtained from the species concentration and reaction rate coefficients using

$$\frac{dn_i}{dt} = \sum_j \left\{ \left(a_{ij}^{(2)} - a_{ij}^{(1)} \right) k_j \prod_l n_l^{a_{lj}^{(1)}} \right\}, \tag{2.1}$$

where $a_{ij}^{(1)}$ and $a_{ij}^{(2)}$ denote the left-hand side (LHS) and right-hand side (RHS) stoichiometric coefficients of species i in reaction j. n_i is the density of species i, k_j is the rate constant of reaction j which depends on the gas temperature and is calculated using Arrhenius expressions for reactions involving only heavy species. The rate constants of electron-impact reactions are obtained as a function of electron temperature by solving the two-term spherical harmonic expansion of Boltzmann's equation for the electron energy distribution and parameterizing them for several values of E/N.[1]

The external discharge circuit used to deposit energy in the plasma is shown in Fig. 2.1b. The discharge region is modeled as a resistor R_p and the dielectrics on the electrodes are represented by the capacitor C_s in series with R_p. The inductor L is added to obtain the desired LC time constant for the circuit. A ballast resistance R_s may be used to control the energy deposition in the plasma. The storage capacitor, C_{sto} is initially charged to the applied voltage. Typical values for the circuit parameters in Fig. 2.1b are:

Applied voltage = 10-20 kV (2.2)

$C_{sto} = 200 \times 10^{-9}$ F (2.3)

$C_p = 20 \times 10^{-9}$ F (2.4)

$C_s = 5.5 \times 10^{-15}$ F (2.5)

$L = 30 \times 10^{-9}$ H. (2.6)

Initially, the voltage across the plasma is equal to the voltage across the storage capacitor. As current flows through the discharge, the capacitor C_s in series with the plasma charges up thereby robbing voltage from the discharge region. When the voltage across the plasma falls below sustaining, the discharge is extinguished.

The electron temperature is determined by the energy gained by Joule heating, and the energy lost in elastic and inelastic collisions,

$$\frac{d}{dt}\left(\frac{3}{2}n_e k_B T_e\right) = \vec{j}\cdot\vec{E} - \sum_i \frac{3}{2} n_e \nu_{mi}\left(\frac{2m_e}{M_i}\right) k_B (T_e - T_i) + \sum_l n_e k_l N_l \Delta\varepsilon_l \,. \qquad (2.7)$$

n_e is the electron density, T_e is the electron temperature, $\vec{j}$ and $\vec{E}$ are the current density and the electric field in the discharge, ν_{mi} is the electron momentum transfer collision frequency with species i, m_e is the electron mass, and M_i and T_i are the mass and temperature of species i. For the l^{th} electron impact process, k_l is the reaction rate coefficient, N_l is the density of the gas phase collision partner, and $\Delta\varepsilon_l$ is the change in the electron energy.

The average gas temperature T_g is obtained by accounting for heating from elastic and inelastic collisions with electrons, enthalpy of heavy particle reactions,

$$\frac{d}{dt}\left(N c_p T_g\right) = \sum_i \frac{3}{2} n_e \nu_{mi}\left(\frac{2m_e}{M_i}\right) k_B (T_e - T_i) + \sum_j n_e k_j N_j \Delta\varepsilon_j - \sum_j \Delta H_j \,, \qquad (2.8)$$

where N is the total gas density, c_p is the specific heat, ΔH_j is the change in enthalpy of the j^{th} reaction, and d_{gap} is the electrode separation. The first and second terms in Eq. 2.8 account for heating due to momentum transfer collisions with electrons and dissociative electron impact processes which produce Frank-Condon heating.

The final set of ordinary differential equations (Eqs. 2.1, 2.7, and 2.8) is then integrated in time using VODE [2], a stiff equation solver. The time steps chosen for integration are dynamically adjusted to capture the dynamics of the system at any particular time and spans > 10^9 orders of magnitude. In order to capture the features of multiple discharges, the model is run for a series of current pulses and afterglow time periods. The total number of pulses is divided equally over the residence time used for the single pulse case. The energy deposition is varied by either changing the applied voltage, the dielectric thickness, or the dielectric permittivity.

2.3 Model for Reaction Kinetics at Soot Surfaces

To investigate the consequences of heterogeneous reactions on soot particles on the plasma remediation of NO_x, a heterogeneous chemistry model was developed and incorporated into GLOBAL_KIN. In this model, the reactive medium around a given soot particle is described using a quasi-homogeneous model which distinguishes two regions in the gas volume surrounding one particle: a homogenous bulk gas phase and a gas-surface boundary layer. (See Fig. 2.2) Using this assumption, the concentration profile in the boundary layer is linear between the gas phase and surface of the particles, and is mainly driven by diffusion and surface reactions. All the particles have the same diameter, d_s, that corresponds to the average of the actual particle diameter distribution.

The soot particles are characterized by their diameter and by the surface density of available adsorption sites. The soot particle number density, n_p, is a constant since additional particle nucleation does not take place. The only physical change that particles undergo is a decrease of their diameter due to oxidation reactions. Gas phase species are characterized by their density in the bulk of the gas phase, n_{sg}, and near the surface of the soot particles, n_{ss}.

The time-evolution of the bulk density of species i is given by

$$\frac{dn_{ig}}{dt} = W_{ig} + W_{is} \tag{2.9}$$

where n_{ig} and W_{ig} are the bulk density and the net production rate by gas-phase reactions of species i. W_{is} denotes the net production term of species i by heterogeneous processes on the soot particles. This term is nonzero only for species involved in the surface reactions.

For large particle diameters, d_s > 80 nm, the continuum approach is valid and the source term W_{is} is directly related to the diffusion rate of species i at the soot surface,

$$W_{is} = \left(- D_i \frac{n_{ig} - n_{is}}{\delta} \right) \left(\pi d_s^2 n_p \right), \tag{2.10}$$

where D_i is the diffusion coefficient of species i and δ the boundary layer thickness. The first term of Eq. 2.10 is the rate of diffusion of species i to the soot particle. The second term is the soot geometric surface per unit volume of the gas phase. The diffusion

boundary layer thickness may be estimated from a standard correlation for mass transfer between a fluid and an immersed sphere. For the conditions of interest,

$$Nu = 2.0 + 0.60\, Re^{1/2}\, Sc^{1/3} \tag{2.11}$$

where, $Nu = d_s/\delta$ is the Nusselt number, $Re = \rho v d_s/\mu$ is the Reynolds number and $Sc = \mu/\rho D_s$ is the Schmidt number.[3] ρ, v and μ denote the mass density, velocity and the viscosity of the gas phase. For the conditions considered in this work Re and Sc are small, and so the boundary layer thickness is nearly equal to the particle radius.

Since gas phase chemistry is neglected in the boundary layer, the time variation of the density near the soot particle is governed by the balance between the flux of species entering the boundary layer by diffusion and the consumption or production of species by heterogeneous reactions at the soot surface. The mass balance in the boundary layer is,

$$\frac{d}{dt}\left[\frac{1}{2}(n_{ig} + n_{is})V_\delta\right] = D_i \frac{n_{ig} - n_{is}}{\delta}\pi d_s^2 + (R_{di} - R_{ai})S_s\,, \tag{2.12}$$

where S_s is the specific surface of the soot particles and V_δ is the volume of the boundary layer. R_{di} and R_{ai} are the rates of desorption and adsorption per unit surface of soot for species i. The consumption rate by adsorption reactions is

$$R_{ai} = \sum_j \left(a_{ij}^{(1)} \gamma_j v_i \frac{n_{is}}{4}\right), \tag{2.13}$$

where γ_j is the adsorption probability for the j^{th} process and v_i the thermal speed of species i at the surface of the soot particle, $v_i = \sqrt{\frac{8kT_g}{\pi m_i}}$. The production rate of species i due to desorption reactions is

$$R_{di} = \sum_j \left(a_{ij}^{(2)} k_j N_{is} \right), \tag{2.14}$$

where k_j is the rate of the j^{th} desorption reaction and N_{is} is the surface density of the adsorbed species. The surface used in the computation of desorption and adsorption rates is the true surface area, S_s, of the soot, $S_s = \pi d_{sp}^2 N_{sp}$, where d_{sp} is the spherule diameter and N_{sp} is the number of spherules contained in each particle. This is consistent with the measurements of the adsorption probability and the surface density of the total adsorption sites.[4-6] The soot specific surface S_s was determined from experiments reporting that the particles are composed of ≈20 nm elementary spherules having a fractal structure.[7] A fractal dimension of $f = 2.8$ was chosen based on work by Mitchell and Frenklach.[8] The number of spherules, N_{sp}, contained in each particle is [9]

$$N_{sp} = \left(\frac{d_s}{d_{sp}} \right)^f. \tag{2.15}$$

The specific surface of the soot particles is assumed to be equal to the total surface of all the spherules. For estimating diffusion fluxes, the geometric surface was used.

The surface densities of the adsorbates are obtained from

$$\frac{dN_{i-s}}{dt} = \sum_j \left(a_{ij}^{(2)} \gamma_j v_i \frac{n_i'}{4} \right) - \sum_j \left(a_{ij}^{(1)} k_j N_{is} \right), \tag{2.16}$$

where the first sum is over adsorption reactions, the second sum is over the desorption reactions and n_i' is the density of the gas-phase species involved in the adsorption reaction.

A single type of adsorption site was used for all adsorbates. The total surface density of adsorption sites for OH and O has been reported to be $\approx 10^{15}$ cm^{-2} [10] which is similar to that for the adsorption sites of NO_2.[5] We therefore used 10^{15} cm^{-2} for the total surface density of the adsorption sites.

When the soot particle diameters are small and produce a Knudsen number, $\lambda_{mfp}/d_s > 1$, the continuum approach is no longer valid. Diffusion is fast enough to insure a constant concentration in the boundary layer, $n_{is} = n_{ig}$.[11] There is consequently no need for an equation for the densities of gas phase species near the soot particles. The rate of surface reactions W_{is} is

$$W_{is} = \left(R_{di} - R_{ai} \right) S_s n_p , \tag{2.17}$$

where the factor $S_s n_p$ is the soot surface per unit volume.

The calculation of R_{ai} is different from that in the continuum regime since the rarefaction around the particle must be taken into account. In this case, R_{ai} is given by [11]

$$R_{ai} = \sum_j \frac{2D_i}{8D_i / \gamma_j v_i + d_s /(1 + 2\Delta / d_s)} \; n_i \,, \tag{2.18}$$

where Δ is the mean distance between the point of last collision in the gas phase and the particle center.

The final set of ordinary differential equations (Eqs. 2.7-2.9, 2.12, and 2.16) are then integrated in time using VODE.[2] At each step during the time integration in the model, the decrease of the soot mass is computed and the corresponding surface and diameter are adjusted assuming that the fractal dimension, and therefore the number of spherules, remain constant. The soot number density also remains constant. When the size of the particle decreases to the point that the flow around the particles is not continuum (Eq. 2.13), Eqs. 2.17 and 2.18 are used to provide the heterogeneous rates.

Soot particle charging by the attachment of charged species may affect the ionization kinetics, and therefore the electron temperature and density, in DBDs. Particle charging in plasmas has been mostly investigated at low pressure where the Orbit Motion Limited (OML) theory may be used.[12] The validity of OML theory requires that $d_p << \lambda_D << \lambda_{mfp}$, where d_p is the particle diameter, λ_D is the Debye length of the plasma and λ_{mfp} is the electron/ion mean free path between collisions. For these conditions, the motion of charged species in the plasma sheath around the particle is collisionless and is

mainly governed by the interaction potential between the particles and electrons or ions. In this case, the sheath potential and currents to the particles are functions only of the plasma density, electron temperature and ion temperature.

Unfortunately, the assumptions for the OML theory are violated by atmospheric plasmas. During the current pulse the electron density n_e and temperature T_e are 10^{12}-10^{13} cm^{-3} and 3-4 eV, which produces a Debye length of the order of 10^{-3} cm. The electron mean free path, based on N_2 is $\approx 3 \times 10^{-5}$ cm and so the sheath is collisional.

To estimate an upper limit to the particle charging during the short current pulse, we considered the charging due to ion collection and electron attachment to the soot. The collection frequency of electrons by the soot is determined by assuming that the electron density in the sheath follows a Boltzmann distribution with respect to the electrical potential. The charging rate is then

$$\frac{dQ_s}{dt} = -q\frac{n_{eg}\exp(qV_s/kT_e)}{4}\sqrt{\frac{8kT_e}{\pi m_e}}\pi d_s^2 + \sum_i q_i \frac{n_{ig}(1-\exp(q_iV_s/kT_i))}{4}\sqrt{\frac{8kT_i}{\pi m_i}}\pi d_s^2 \tag{2.19}$$

where d_s and Q_s denote the diameter and the electrical charge for the soot particles, q is the elementary charge, and k is Boltzmann's constant. m_e, n_{eg} and T_e are the electron mass, density in the bulk plasma, and temperature respectively. m_i, n_{ig}, q_i, and T_i are the ion mass, density in the bulk plasma, charge, and temperature respectively. The sum is over ions. V_s is the particle potential and may be estimated from the particle charge by modeling the particle as a spherical capacitor,

$$V_s = \frac{2qQ_s}{4\pi\varepsilon_0 d_s}. \tag{2.20}$$

2.4 One-Dimensional Plasma Chemistry and Hydrodynamics Model

In the 1-D model, we include the radial dependence of the microstreamers and the surrounding volume and solve for the species densities based on chemical kinetics, and diffusive and advective transport. In actual devices, the streamers have axial variations as well. However, these variations tend to be significant only for times less than a few tens of ns. At processing times of interest for our study, which are at least tens of ms, streamer properties can likely be homogeneous along the axial direction, and hence, their variations in that direction can be neglected. The model developed for this study is based on the 1-D microdischarge simulation described previously in Ref. [13]. The model differs from that in Ref. [13] in that it employs a different technique to obtain the final set of ODEs and a different integration method.

For computational purposes, the DBD is represented as being composed of a uniformly spaced array of identical, radially symmetric microdischarges. Each microdischarge and its surrounding volume is discretized into a set of concentric cylinders (cells) with increasing inter cylinder spacing. Typically, 50-100 radial points are used in the model.

The model is composed of four modules: a circuit module, a Boltzmann's equation solver module, a plasma chemistry module, and a transport module. A schematic of the modules in the 1-D model is given in Fig. 2.3a and the external circuit used to drive the plasma is shown in Fig. 2.3b. The discharge is represented by a parallel set of resistors, each accounting for the cell containing plasma at a particular mesh point.

The circuit module calculates the voltage across the plasma, which is then used to obtain the E/N in each of the cells. The rate coefficients for electron impact reactions are obtained by solving the two-term spherical harmonic expansion of Boltzmann's equation for the electron energy distribution and parameterizing them for several values of E/N.[1] The plasma chemistry module provides the rates for change of species densities based on chemical kinetics. The changes in species densities as a result of motion between the mesh points are addressed in the transport module. The equations we solve in the transport module are:

$$\frac{\partial \rho}{\partial t} = \nabla \cdot (\rho \vec{\mathrm{v}}), \tag{2.21}$$

$$\frac{\partial (\rho \vec{\mathrm{v}})}{\partial t} = -\nabla P - \nabla \cdot (\rho \vec{\mathrm{v}}\vec{\mathrm{v}}) - \nabla \cdot \overline{\overline{\tau}}, \tag{2.22}$$

$$\begin{aligned} \frac{\partial (c_p \rho T)}{\partial t} = {} & \vec{\mathrm{j}} \cdot \vec{\mathrm{E}} - \sum_i \left(\frac{dN_i}{dt} \right) \cdot \Delta H_i + \sum_i \frac{3}{2} n_e \nu_{mi} \left(\frac{2m_e}{M_i} \right) k_B (T_e - T_i) + \\ & + \nabla \cdot \kappa \nabla T - \nabla \cdot (c_p \rho T \vec{\mathrm{v}}) - P(\nabla \cdot \vec{\mathrm{v}}) + 2\mu (\nabla \cdot \vec{\mathrm{v}})^2, \end{aligned} \tag{2.23}$$

where ρ is the mass density, $\vec{\mathrm{v}}$ is the velocity, P is the thermodynamic pressure (assuming ideal gas behavior), $\overline{\overline{\tau}}$ is the viscosity tensor, c_p is the heat capacity, and κ is the thermal conductivity. $\vec{\mathrm{j}} = \sigma \vec{\mathrm{E}}$ (σ is the plasma conductivity) is the current density, H_i is the enthalpy of heavy particle species i, and μ is the viscosity. The viscosity and thermal conductivity of the gas are obtained using Lennard-Jones parameters and applying the mixture rules as described in Hirshfelder *et al.*[14]

The densities of individual species are obtained by solving separate continuity equations,

$$\frac{\partial N_i}{\partial t} = -\nabla \cdot \left(N_i \vec{\mathrm{v}} - \rho D_i \nabla \left(\frac{N_i}{\rho} \right) \right) + W_{0D} \quad , \tag{2.24}$$

where D_i is its diffusion coefficient, and W_{0D} is the source function due to electron impact and heavy particle reactions. For charged heavy species, we used ambipolar diffusion coefficients. Spatially dependent time derivatives are constructed using conservative finite difference donor cell techniques on a staggered mesh (ρ, N_i, and T are obtained at cell vertices whereas $\rho\vec{\mathrm{v}}$ is obtained at cell boundaries). The resulting ordinary differential equations for electron temperature (Eq. 2.7), continuity (Eq. 2.21), momentum (Eq. 2.22), gas energy (Eq. 2.23), and species densities (Eqs. 2.24) along with those for circuit parameters are integrated in time using VODE.[2] Typically the effect of advection is significant only during and slightly after the current pulse. At times later than 1 μs (typically, the current pulses last a few 10s of ns), the effects of advection are minimal and are neglected. At such times, species transport is by diffusion only. To capture the features of repetitive pulses, the model is run for a series of current pulses and afterglow periods.

2.5 Model for Reaction Kinetics on Polymer Surfaces

A schematic of a typical corona device used for plasma surface modification is shown in Fig. 2.4a. The device consists of two parallel dielectric plates backed by metal

electrodes across which typically 10s of kV sinusoidal pulses at 10s of kHz are applied to produce discharges in air. The discharges are in the form of microstreamers which are typically 10s – 100s of μm in diameter, lasting a few – 100s of ns.[13] Typical web speeds are 10s – 100s m-min^{-1} and the polymer usually spends a maximum of a few seconds in the discharge. Energy depositions are usually 0.1 – a few J-cm^{-2}. Although the plasma equipment used industrially for polymer processing are typically called corona discharges, due to the dielectrics on the electrodes and the capacitance of the polymer, the devices function as DBDs.

To address the reactions on and near the polymer surface, a heterogeneous model was developed and incorporated into GLOBAL_KIN. The reaction set typically includes: electron-impact processes in the gas phase which result in ionization, dissociation, excitation, electron-ion recombination, and attachment; heavy species reactions in the gas phase that result in neutral chemistry, charge exchange, and ion-ion neutralization; reactions of gas phase species with species on the surface; and reactions between surface species.

In addition to the terms used in the estimation of the average gas temperature as given in Eq. 2.8, a term for heat transfer to surfaces is now included,

$$\frac{d}{dt}\left(Nc_pT_g\right)=\sum_i\frac{3}{2}n_e\nu_{mi}\left(\frac{2m_e}{M_i}\right)k_B\left(T_e-T_i\right)+\sum_j n_e k_j N_j\Delta\varepsilon_j-\sum_j\Delta H_j-h_{eff}\frac{T_g-T_w}{d_{gap}}, \tag{2.25}$$

where h_{eff} is the effective heat transfer coefficient with the discharge walls having temperature T_w. We approximated that h_{eff} = 2.3 W-cm^{-2}-K^{-1}, based on flow over a flat plate.[3]

The reaction mechanism for plasma-polymer interactions is implemented using a quasi-homogeneous model which distinguishes two regions above the polymer surface; a homogeneous bulk gas phase and a gas-surface boundary layer, as shown in Fig. 2.4b. The radical concentration profile in the boundary layer is mainly driven by diffusion and surface reactions. A gas phase species i is characterized by its density in the bulk of the gas phase, n_{ig}, and near the surface of the polymer, n_{is}. The state of the polymer is characterized by the fractional occupancy of its surface sites by different species.

The time-evolution of the bulk density of species i is given by

$$\frac{dn_{ig}}{dt} = W_{ig} + W_{id}\,, \tag{2.26}$$

where W_{ig} and W_{id} are the net rate of production of species i by gas phase reactions and the rate of accumulation of species i in the bulk gas phase by diffusion from the polymer surface. W_{id} is nonzero only for species involved in the surface reactions.

The source term W_{id} is proportional to the rate of diffusion to the polymer surface,

$$W_{id} = \left(-D_i \frac{n_{ig} - n_{is}}{\delta} \right)\left(\frac{S}{V}\right), \tag{2.27}$$

where D_i is the diffusion coefficient, δ the boundary layer thickness, S is the polymer geometric surface area, and V is the volume of the bulk plasma. The diffusion boundary layer thickness may be taken to be a few mean free paths (≈ μm for air at 1 atm). For the conditions of this study, diffusion is not the rate limiting step and hence the thickness of the diffusion boundary layer is not critical.

Since gas phase chemistry is neglected in the boundary layer, the time variation of the density near the polymer surface is governed by the balance between the flux of species entering the boundary layer by diffusion and the consumption or production of species by heterogeneous reactions at the polymer surface. The mass balance in the boundary layer is

$$\frac{d}{dt}\left[\frac{1}{2}(n_{ig}+n_{is})V_B\right] = D_i\frac{n_{ig}-n_{is}}{\delta}S + \left(R_{di}-R_{ai}\right)S\,, \tag{2.28}$$

where V_B is the volume of the boundary layer. R_{di} and R_{ai} are the rates of desorption and adsorption (or abstraction) per unit surface of polymer for species i. The rate of consumption by adsorption (or abstraction) reactions is

$$R_{ai} = \sum_j \left(a_{ij}^{(1)} - a_{ij}^{(2)}\right)\gamma_j v_i \frac{n_{is}}{4}, \qquad \gamma_j = \gamma_{j0}\frac{\rho_j}{\rho_o}, \tag{2.29}$$

where γ_j is the adsorption probability for the j^{th} process, and v_i the thermal speed of species i at the surface of the polymer, $v_i = \sqrt{\dfrac{8kT_g}{\pi M_i}}$. γ_{j0} is the adsorption probability per

unit area, ρ_j is the density of surface sites available to reaction j and ρ_o is the density of surface sites on a virgin polymer surface. $a_{ij}^{(1)}$ and $a_{ij}^{(2)}$ denote the LHS and RHS stoichiometric coefficients of species i in reaction j. The production rate of species i due to desorption reactions is

$$R_{di} = \sum_j \left(a_{ij}^{(2)} k_j N_{is} \right), \tag{2.30}$$

where k_j is the rate of the j^{th} desorption reaction, and N_{is} is the surface density of the adsorbed species.

The densities of the surface species are obtained from

$$\frac{dN_{is}}{dt} = \sum_j \left(a_{ij}^{(2)} \gamma_j v_i \frac{n_i}{4} \right) - \sum_j \left(a_{ij}^{(1)} k_j N_{is} \right) + \sum_j \left((a_{ij}^{(2)} - a_{ij}^{(1)}) k_j \prod_l N_{ls}^{a_{lj}^{(1)}} \right), \tag{2.31}$$

where the first sum is over adsorption or abstraction reactions, the second is over desorption reactions, and the third is over reactions between surface species. n_i is the density of the gas phase species involved in the adsorption or abstraction reaction.

The ordinary differential equations for electron temperature (Eq. 2.7), gas temperature (Eq. 2.25), species densities (Eqs. 2.26, 2.28, and 2.31) along with those for circuit parameters are integrated in time using VODE.[2]

2.6 Figures

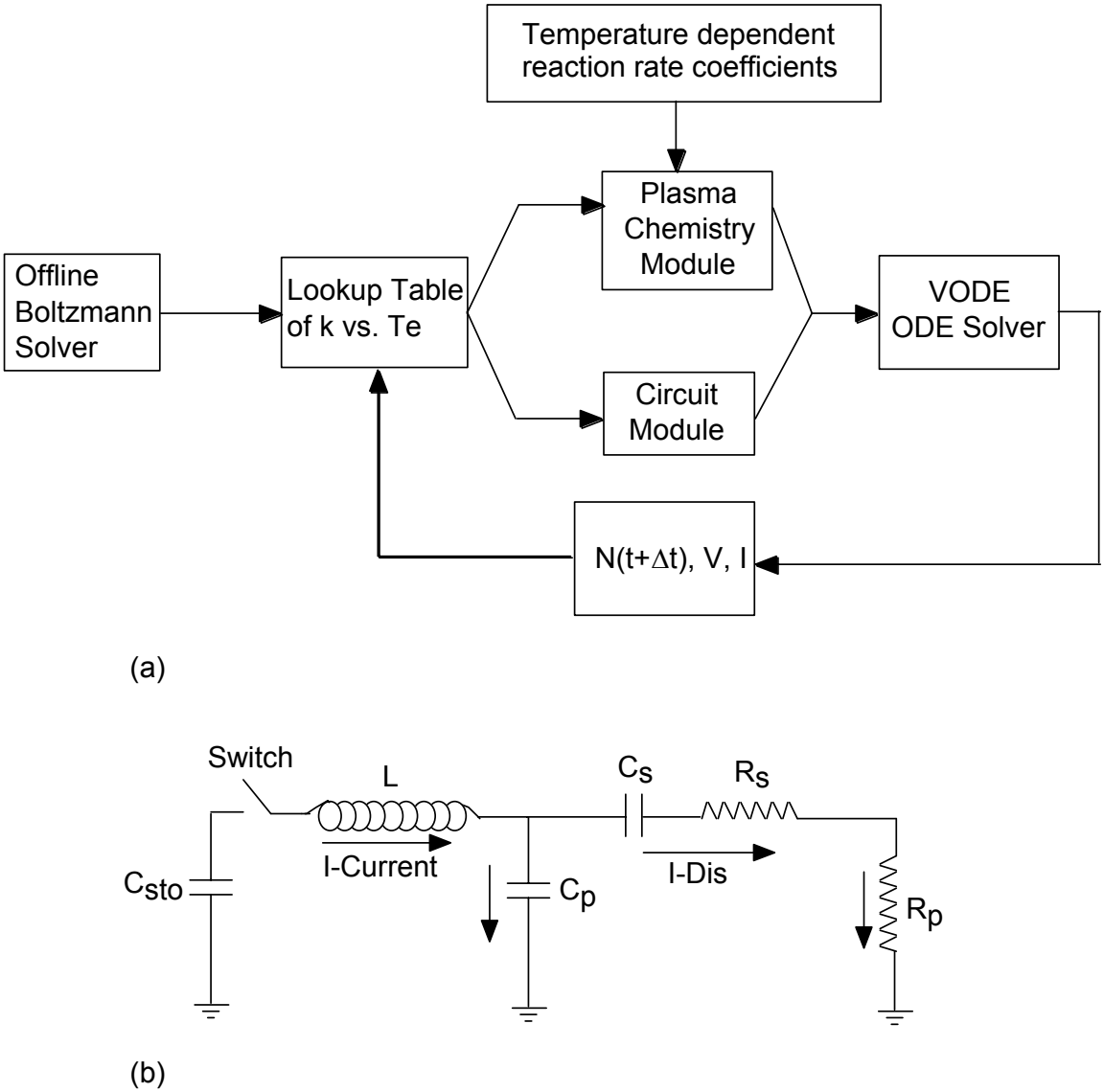

Fig. 2.1. (a) Block diagram of the 0-D model – GLOBAL_KIN. (b) Schematic of the circuit used in the 0-D model. The plasma created in the DBD is represented by the resistor R_p and the dielectrics on the electrodes are represented by the capacitor C_s in series with R_p. R_s is a ballast resistor. C_{sto} is a storage capacitor, C_p is a peaking capacitor in parallel with R_p, and L is an inductor.

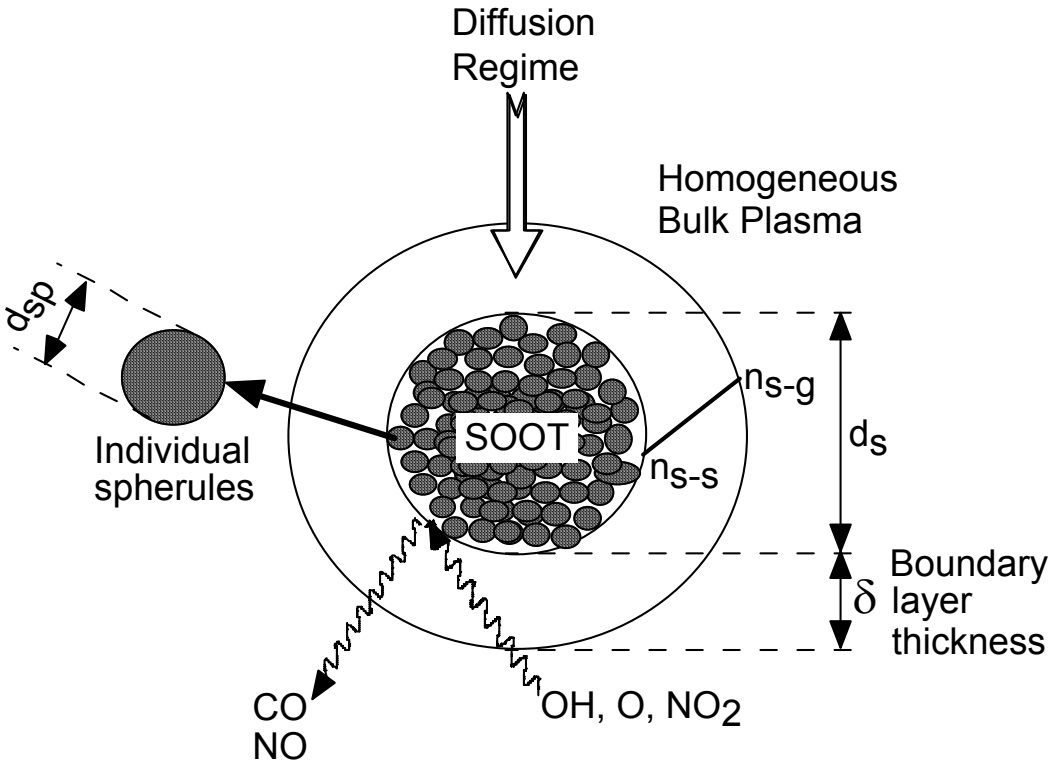

Fig. 2.2. Schematic of the quasi-homogeneous gas-phase model used in GLOBAL_KIN to account for soot particles. The region surrounding the soot is divided into two zones – a homogeneous bulk gas phase and a gas-surface boundary layer. Species in the bulk plasma diffuse to the soot surface through the boundary layer. Gaseous products of the heterogeneous reactions desorb from the soot surface to return to the bulk through the boundary layer.

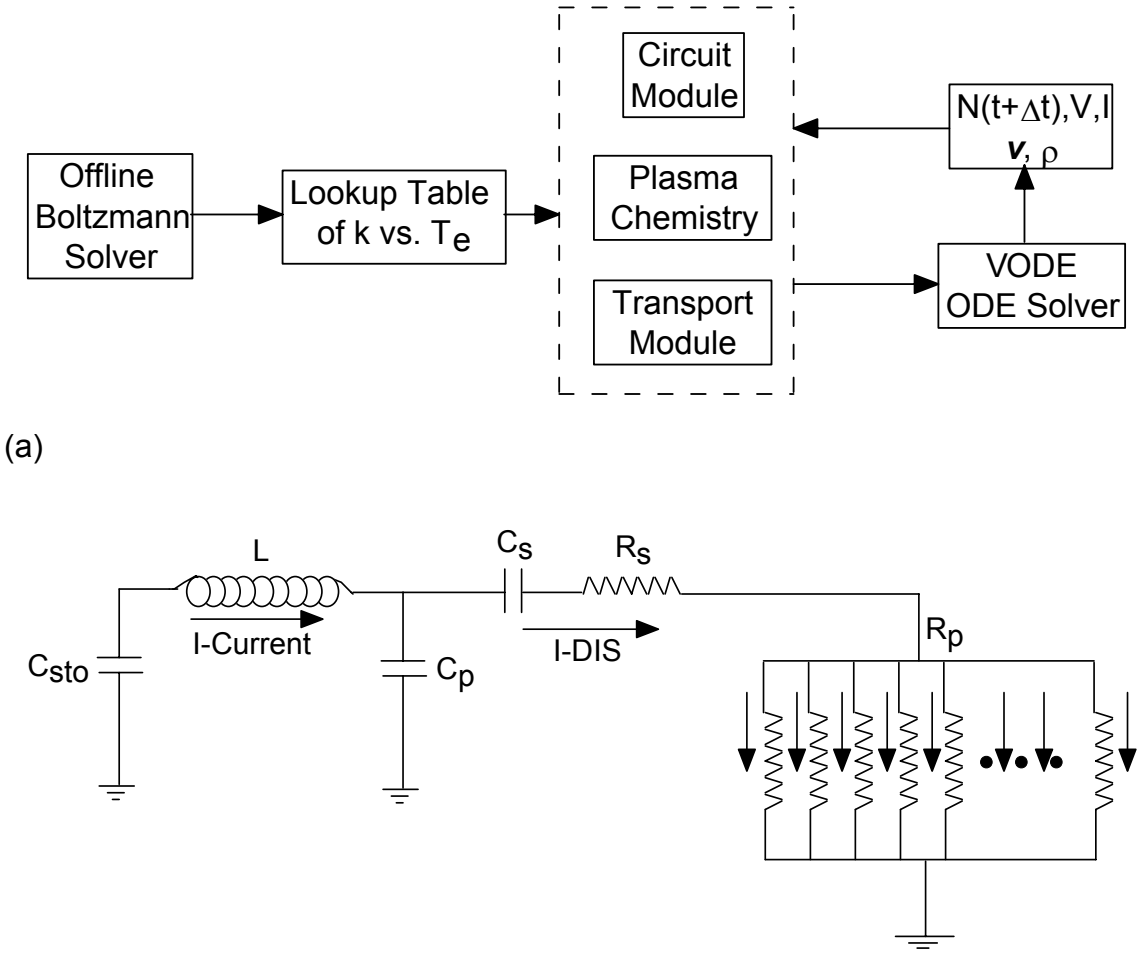

Fig. 2.3. 1-D Model. (a) Modules in the 1-D radial hydrodynamic and plasma chemistry model. (b) External circuit. The discharge region and its surrounding area are represented by a set of resistors in parallel.

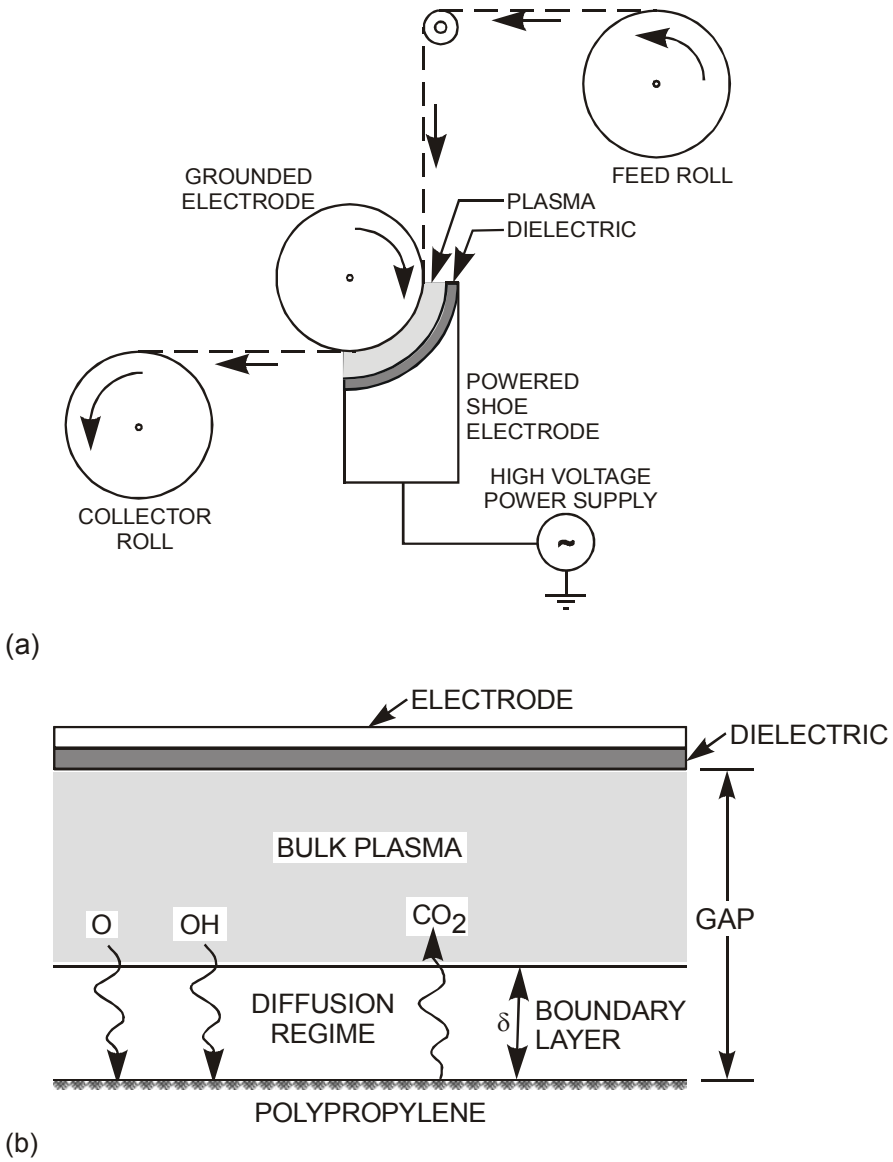

Fig. 2.4. Model for plasma polymer surface treatment. (a) Schematic of the plasma polymer surface treatment process. A plasma is created in air by applying 10s of kV sinusoidal pulses at 10s kHz across a few mm gap. The polymer web traverses the plasma region at speeds of 10s - a few 100s of m-min^{-1}. Typically, the residence time of the polymer in the plasma is at most a few s. (b) Quasi homogeneous model for species transport to the polymer surface. Two zones above the PP surface are considered – a diffusion boundary layer and homogeneous bulk plasma. Species produced in the bulk plasma diffuse through the boundary layer, react with the polymer surface, and the products diffuse back to the bulk through the boundary layer.

2.7 References

1. S. D. Rockwood, Phys. Rev. A **8,** 2348 (1973).
2. P. N. Brown, A. Hindmarsh, and G. D. Byrne, VODE - Variable-coefficient Ordinary Differential Equation solver (1998).
3. R. B. Bird, W. E. Stewart, and E. N. Lightfoot, *Transport Phenomena* (John Wiley & Sons, Singapore, 1994).
4. M. S. Akhter, A. R. Chughtai, and D. M. Smith, J. Phys. Chem. **88,** 5334 (1984).
5. K. Tabor, L. Gutzwiller, and M. J. Rossi, J. Phys. Chem. **98,** 6172 (1994).
6. M. Kalberer, K. Tabor, M. Ammann, Y. Parrat, E. Weingartner, D. Piguet, E. Rossler, D. T. Jost, A. Turler, H. W. Gaggeler, and U. Baltensperger, J. Phys. Chem. **100,** 15487 (1996).
7. J. P. A. Neeft, M. Makkee, and J. A. Moulijn, Fuel Process. Technol. **47,** 1 (1996).
8. P. Mitchell and M. Frenklach, The Combustion Institute, 27th Symposium (International) on Combustion**,** 1507 (1998).
9. J. Magill, J. Aerosol Sci. **22,** S165 (1991).
10. P. Markatou, H. Wang, and M. Frenklach, Combust. Flame **93,** 467 (1993).
11. J. Porstendorfer, G. Robig, and A. Ahmed, J. Aerosol Sci. **10,** 21 (1979).
12. J. Goree, Plasma Sources Sci. Technol. **3,** 400 (1994).
13. A. C. Gentile and M. J. Kushner, J. Appl. Phys. **79,** 3877 (1996).
14. J. Hirschfelder, C. Curtiss, and R. B. Bird, in *Molecular Theory of Gases and Liquids* (Wiley, New York, 1954), Chap. 8.

3. REPETITIVELY PULSED PLASMA REMEDIATION OF NO_X IN THE PRESENCE OF UNBURNED HYDROCARBONS

3.1 Introduction

We previously established that unburned hydrocarbons (UHCs), inevitably present in diesel exhausts, significantly affect the NO_x chemistry during the plasma remediation of NO_x in diesel exhausts.[1] Industrial systems for plasma processing of toxic gases typically operate at sufficiently high repetition rates that a given sample of gas is subjected to several discharge pulses. Pulses with short rise-time and high amplitude voltage have been found to be advantageous due to their ability to rapidly produce high E/N (electric field/number density).[2] It has also been found that it is more efficient with respect to remediation to deposit a given amount of energy in a large number of shorter duration pulses.[3] With each pulse, radicals initiating the plasma chemistry are generated and during the interpulse period, these radicals undergo reactions thereby changing the composition of the plasma. The reaction chemistry for the follow-on pulses is different from that which would be obtained from an equivalent energy deposition in a single or smaller number of pulses due to the accumulation of these interpulse products.

In this chapter, we discuss the consequences of interpulse chemistry on the plasma remediation of NO_x in a DBD reactor. The reaction mechanism for the NO_x-propene-propane mixture is summarized in Section 3.2. NO_x processing with multiple pulse formats is discussed in Section 3.3. Briefly, we found that with multiple pulses, approximately 10 ppm of methyl nitrate (CH_3ONO_2) and 16 ppm of ethyl nitrate ($C_2H_5ONO_2$) was formed, whereas less than 1 ppm of each were produced with a single

pulse. The efficiency of NO_x remediation improved from 240 eV per molecule for a single pulse to 185 eV per molecule when the same energy (58 J/L) was distributed over 20 pulses. Concluding remarks are in Section 3.4.

3.2 Reaction Mechanism for NO_x-C_3H_6-C_3H_8

For this study, we considered nearly 80 electron impact reactions and 360 reactions involving heavy species. The species used in the model are listed in Appendix A. The reactions for NO_x both in the absence and in the presence of propane and propene are given in Appendix B. The reaction mechanism for NO_x remediation can be described by two trees; reactions with and without UHCs. The detailed mechanism for NO_x in the absence of UHCs is described in Ref. 3. In summary, in the absence of UHCs, NO_x is remediated primarily by two channels,

Reduction :

$$NO + N \rightarrow N_2 + O, \qquad k = 3.41\times10^{-11}\exp(-24/T)\,cm^3s^{-1},$$

$$k_{298} = 3.2\times10^{-11}\,cm^3s^{-1}, \tag{3.1}$$

Oxidation :

$$NO + O_3 \rightarrow NO_2 + O_2, \qquad k = 4.3\times10^{-12}\exp(-1598/T)\,cm^3s^{-1},$$

$$k_{298} = 2.1\times10^{-14}\,cm^3s^{-1}, \tag{3.2a}$$

$$NO + O + M \rightarrow NO_2 + M, \qquad k = 6.71\times10^{-32}(T/298)^{-1.41}\,cm^6s^{-1}, \tag{3.2b}$$

$$NO + HO_2 \rightarrow NO_2 + OH, \qquad k = 3.5\times10^{-12}\exp(+240/T)\,cm^3s^{-1},$$

$$k_{298} = 7.8\times10^{-12}\,cm^3s^{-1}, \tag{3.2c}$$

$$NO + OH + M \rightarrow HNO_2 + M,$$

$$k = 8.64\times10^{-31}(T/298)^{-2.51}\exp(34/T)\,cm^6s^{-1},\ k_{298} = 9.7\times10^{-31}cm^6s^{-1}, \quad (3.2d)$$

$$NO_2 + OH + M \rightarrow HNO_3 + M,$$

$$k = 4.62\times10^{-29}(T/298)^{-5.49}\exp(-1183/T)\,cm^6s^{-1},\ k_{298} = 8.7\times10^{-31}cm^6s^{-1}. \quad (3.3)$$

k is the rate coefficient and k_{298} is its value at $T = 298$ K. O, N, and OH are produced by electron impact reactions with O_2, N_2, and H_2O respectively.

$$e + O_2 \rightarrow O + O + e, \quad (3.4)$$

$$e + N_2 \rightarrow N + N + e, \quad (3.5)$$

$$e + H_2O \rightarrow OH + H + e. \quad (3.6)$$

O_3 is produced by the reaction of O with O_2,

$$O + O_2 + M \rightarrow O_3 + M, \qquad k = 3.4\times10^{-34}(T/298)^{-1.2}\,cm^6s^{-1}. \quad (3.7)$$

HO_2 is produced by the reaction of H with O_2,

$$H + O_2 + M \rightarrow HO_2 + M, \qquad k = 1.78\times10^{-32}(T/298)^{-0.8}\,cm^6s^{-1}. \quad (3.8)$$

H by itself is formed by the electron impact dissociation of H_2O (Eq. 3.6) and by the reaction of O with OH,

$$O + OH \rightarrow O_2 + H, \qquad k = 4.55\times10^{-12}(T/298)^{0.4}\exp(372/T)\,cm^3s^{-1},$$

$$k_{298} = 1.6\times10^{-11}\,cm^3s^{-1}. \tag{3.9}$$

In the absence of UHCs, the consumption of NO_x mainly occurs through the oxidation channel. This is due to the fact that the rates of producing O and OH are higher compared to N because of the lower dissociation energy of H_2O and O_2 compared to N_2.

For example, the contributions of each of the above channels to NO remediation in a mixture with 8% O_2, 6% H_2O, 7% CO_2, 400 ppm CO, 260 ppm NO, 133 ppm H_2 and balance N_2 are given in Fig. 3.1. At 30 J/L, the reduction channel (Eq. 3.1) accounts for only 8% of the total NO remediation. Oxidation by O_3 is the dominant consumption pathway for NO (Eq. 3.2a).

The reaction mechanism for NO_x in the presence of propane (C_3H_8) and propene (C_3H_6) is discussed in detail in Ref. 1 and is summarized in Fig. 3.2. In the presence of the UHCs, C_3H_6 and C_3H_8, new pathways for NO oxidation are introduced, most of which primarily result in the formation of NO_2. The reactivity of propane is smaller compared to propene as approximately only 5% propane is consumed at the end of a typical process [40 J/L] compared to 50% for propene. Briefly, the initiating processes for the C_3H_6 and C_3H_8 chains are reactions with O and OH.

$$OH + H_3C{-}CH{=}CH_2 \rightarrow (0.35)\ H_3C{-}CH(OH){-}CH_2$$

$$+ (0.65)\ H_3C{-}CH{-}CH_2OH,$$

$$k = 4.85\times10^{-12}\exp(504/T)\,cm^3s^{-1}, \qquad k_{298} = 2.6\times10^{-11}\,cm^3s^{-1}, \tag{3.10}$$

$$O + H_3C{-}CH{=}CH_2 \rightarrow CH_3{-}CH{-}CH_2 \quad (30\%) \tag{3.11}$$

$$\rightarrow CH_3CH_2CHO \quad (30\%) \tag{3.12}$$

$$\rightarrow CH_2CHO + CH_3 \quad (20\%) \tag{3.13}$$

$$\rightarrow HCO + C_2H_5 \quad (20\%), \tag{3.14}$$

$$k = 4\times10^{-12}\, cm^3 s^{-1},$$

$$OH + H_3C{-}CH_2{-}CH_3 \rightarrow H_3C{-}CH_2{-}CH_2 + H_2O,$$

$$k = 7.95\times10^{-13}(T/298)^2 \exp(-227/T)\, cm^3 s^{-1},\ k_{298} = 3.7\times10^{-13}\, cm^3 s^{-1}. \tag{3.15}$$

$$\rightarrow H_3C{-}CH{-}CH_3 + H_2O,$$

$$k = 1.44\times10^{-12}(T/298)\exp(130/T)\, cm^3 s^{-1}, \quad k_{298} = 2.2\times10^{-12}\, cm^3 s^{-1}. \tag{3.16}$$

The hydroxyalkyl and alkyl radicals formed by the reactions in Eqs. 3.10, 3.15 and 3.16 then quickly react with O_2 to form the peroxy radicals,

$$H_3C{-}CH(OH){-}CH_2 + O_2 \rightarrow H_3C{-}CH(OH){-}CH_2OO, \quad k = 3.82\times10^{-12}\, cm^3 s^{-1}, \tag{3.17}$$

$$H_3C{-}CH{-}CH_2OH + O_2 \rightarrow H_3C{-}CH(OO){-}CH_2OH, \quad k = 1.16\times10^{-11}\, cm^3 s^{-1}, \tag{3.18}$$

$$H_3C{-}CH_2{-}CH_2 + O_2 \rightarrow H_3C{-}CH_2{-}CH_2OO, \quad k = 8\times10^{-12}\, cm^3 s^{-1}, \tag{3.19}$$

$$H_3C{-}CH{-}CH_3 + O_2 \rightarrow H_3C{-}CH(OO){-}CH_3, \quad k = 1.1\times10^{-11}\, cm^3 s^{-1}. \tag{3.20}$$

These peroxy radicals (R–OO) then react with NO to convert it into NO_2,

$$R{-}OO + NO \rightarrow R{-}O + NO_2, \tag{3.21}$$

where R is the alkyl or hydroxyalkyl part of the peroxy radical.

Some amount of NO remediation is also achieved through the formation of organic nitrates and nitrites. For example, CH_3O, formed from a two-step reaction beginning with CH_3, reacts with NO to form CH_3ONO (methyl nitrite).

$$CH_3 + O_2 + M \rightarrow CH_3O_2 + M, \qquad k = 4.41\times10^{-31}(T/298)^{-3}\ cm^6 s^{-1}, \quad (3.22)$$

$$CH_3O_2 + NO \rightarrow CH_3O + NO_2, \qquad k = 4.2\times10^{-12}\exp(180/T)\, cm^3 s^{-1},$$

$$k_{298} = 7.7\times10^{-12}\, cm^3 s^{-1}, \quad (3.23)$$

$$CH_3O + NO \rightarrow CH_3ONO, \qquad k = 2.0\times10^{-11}\, cm^3 s^{-1}. \quad (3.24)$$

CH_3 is primarily produced by the reaction in Eq. 3.13. CH_3O also reacts with NO_2 to form CH_3ONO_2 (methyl nitrate).

$$CH_3O + NO_2 \rightarrow CH_3ONO_2, \qquad k = 8.32\times10^{-12}\, cm^3 s^{-1}. \quad (3.25)$$

Similar chemistry is observed when C_2H_5O, formed from C_2H_5, reacts with NO to generate C_2H_5ONO (ethyl nitrite),

$$C_2H_5 + O_2 + M \rightarrow C_2H_5O_2 + M, \quad k = 8.02\times10^{-26}(T/298)^{-8.24}\exp(-2150/T)\ cm^6 s^{-1},$$

$$k_{298} = 5.0\times10^{-29}\, cm^6 s^{-1}, \quad (3.26)$$

$$C_2H_5O_2 + NO \rightarrow C_2H_5O + NO_2, \quad k = 3.1\times10^{-12}\exp(330/T)\ cm^3 s^{-1},$$

$$k_{298} = 9.4 \times 10^{-12}\, cm^3 s^{-1}, \tag{3.27}$$

$$C_2H_5O + NO \rightarrow C_2H_5ONO, \qquad k = 2.0 \times 10^{-11}\, cm^3 s^{-1}. \tag{3.28}$$

C_2H_5 is produced by the reaction of O with C_3H_6 (Eq. 3.14). C_2H_5O also reacts with NO_2 to form $C_2H_5ONO_2$ (ethyl nitrate).

$$C_2H_5O + NO_2 \rightarrow C_2H_5ONO_2, \qquad k = 1.32 \times 10^{-11}\, cm^3 s^{-1}. \tag{3.29}$$

3.3 Plasma Processing of NO_x in the Presence of UHCs Using Single and Multiple Pulse Formats

To validate the model, comparisons were made of computed results to experiments conducted by Khacef *et al*. [4] for DBD processing of NO in the presence of hydrocarbons. The 1 atm, 530 K gas feed contained 500 ppm NO, 500 ppm C_3H_6, 10% O_2 and 10% H_2O, with the balance being N_2. The reactor was a cylindrical wire-to-cylinder apparatus with a 0.5 cm gap. Comparison conditions were a repetition rate of 100 Hz and residence time of 0.1 s. Exit NO and NO_2 densities as a function of energy deposition are shown in Fig. 3.3(a). With increasing energy deposition, the NO density decreases while that of NO_2 initially increases and then decreases. The decrease is attributable to a decrease in its rate of formation from reactions involving NO. The computed NO densities agree well with the experiments whereas agreement for the case of NO_2 is within 15–20%. Given the agreement with the NO density, the less good agreement for NO_2 is attributable to the disposition of N atoms from NO forming NO_2 and other N containing products, and the destruction of NO_2. For example, the density of

the dominant N-containing products HNO_3, HNO_2, CH_3ONO_2 and CH_3ONO, are shown in Fig. 3.3(b). The rate coefficient for formation of the major product, HNO_3, has an uncertainty of ≈25% [5], and this uncertainty accounts for a large proportion of the disagreement.

The gas mixture discussed in the remainder of this chapter contains 8% O_2, 6% H_2O, 7% CO_2, 400 ppm CO, 260 ppm NO, 133 ppm H_2, 500 ppm propene (C_3H_6) and 175 ppm propane (C_3H_8) with the balance being N_2. This composition was chosen to assist comparison to experiments conducted at Ford Research Laboratories using a DBD device. [6] The processed gas in the experiments was analyzed with a chemiluminescent NO_x analyzer and a Fourier transform infrared (FTIR) spectrometer.

A baseline was obtained by performing simulations for a single pulse having a duration ≈ 10^{-7}s. The electron density (n_e) and temperature (T_e) as a function of time for the base case are shown in Fig. 3.4a. The maximum electron density is ≈ 10^{13} cm^{-3} at which time T_e ≈ 3 eV. When the voltage is switched off, electron densities decay due to dissociative attachment with H_2O (69%), O_2 (20%), CO_2 (3%), dissociative recombination with $H_3O^+ \cdot H_2O$ (2%) and nondissociative attachment with O_2 (6%).

$$e + H_2O \rightarrow H^- + OH, \tag{3.30}$$

$$e + O_2 \rightarrow O^- + O, \tag{3.31}$$

$$e + CO_2 \rightarrow CO + O^-, \tag{3.32}$$

$$e + H_3O^+ \cdot H_2O \rightarrow H + H_2O + H_2O, \tag{3.33}$$

$$e + O_2 + M \rightarrow O_2^- + M. \tag{3.34}$$

O^-, H^- and O_2^- then neutralize with positive ions, dominated by $H_3O^+ \cdot H_2O$ to form neutral products,

$$O^- + H_3O^+ \cdot H_2O \rightarrow OH + H_2O + H_2O, \qquad k = 3.0 \times 10^{-6}\, cm^3 s^{-1}, \tag{3.35}$$

$$H^- + H_3O^+ \cdot H_2O \rightarrow H_2 + H_2O + H_2O, \qquad k = 3.0 \times 10^{-6}\, cm^3 s^{-1}, \tag{3.36}$$

$$O_2^- + H_3O^+ \cdot H_2O \rightarrow O_2 + H + H_2O + H_2O, \qquad k = 3.0 \times 10^{-6}\, cm^3 s^{-1}. \tag{3.37}$$

After approximately 3×10^{-7} s, ions have neutralized and recombined, and the chemistry is dominantly driven by neutral radicals, mostly OH, O, N, and HO_2. The densities of OH, O, N, and HO_2 are shown in Fig. 3.4b for the base case. O, N, and OH are mainly generated by electron impact reactions (Eqs. 3.4-3.6). HO_2 is mainly produced as an end product of the NO - R–OO radical reactions (67%), by the reaction of H with O_2 (11%) (Eq. 3.8) and by the reaction of HCO with O_2 (22%),

$$HCO + O_2 \rightarrow HO_2 + CO, \qquad k = 2.0 \times 10^{-14} (T/298)^{2.38} \exp(768/T)\, cm^3 s^{-1},$$

$$k_{298} = 2.6 \times 10^{-13}\, cm^3 s^{-1}. \tag{3.38}$$

NO is dominantly consumed by conversion to NO_2 by the reactions with O, O_3, HO_2, and R–OO in proportions 2%, 1%, 38%, and 45% (Eqs. 3.2 and 3.21). Some amount of NO remediation also occurs by the reaction with OH to form HNO_2 (2%) (Eq. 3.2d) and by the formation of organic nitrites (8%) (Eqs. 3.24 and 3.28).

To investigate multiple pulse excitation, 20 pulses were applied over the residence time of 0.2 s at 100 Hz while keeping the total energy deposition constant. The electron

density and temperature during the first pulse and the last pulse for the base case are shown in Fig. 3.5. The lower energy deposition/pulse was obtained by decreasing the voltage. The electron density reaches a maximum of 5×10^{11} cm^{-3} at which time T_e peaks to 3 eV. The current pulses are longer compared to the single pulse case in spite of the lower peak electron density because of the longer time required to avalanche due to the lower applied voltage. The lower energy deposition per pulse results in a peak electron density approximately 3% that of the single pulse which is less than 1/20 of the single pulse due to the lower ionization efficiency at lower voltage. The electron temperature does not significantly change since multistep excitation is not important for these conditions and so the ionization source is dominated by electron impact with ground state species. The electron density and the temperature for the 20th pulse are essentially the same as for the 1st pulse because of the almost constant composition of the background gas mixture.

The densities of O, N, OH, and HO_2 during the first pulse are shown in Fig. 3.6a and for the 20th pulse in Fig. 3.6b. The maximum densities of O, N, OH, and HO_2 are ≈ 4.6% that of the single pulse because of the lower energy deposition and lower excitation efficiency of the lower voltage. The maximum O, N, and OH densities are nearly unchanged for each of the 20 pulses since the density of the feedstock gases for the generation of O, N and OH, O_2, N_2 and H_2O do not change significantly. The rate of decay of O is essentially the same for the 1st and the 20th pulse whereas the rate of decay of N is slower for the 20th pulse because the density of NO, the main consumer of N atoms, has decreased by that time, as shown in Fig. 3.7. The decay of OH is more rapid during the 20th pulse compared to the 1st pulse because of the increased rate of reaction of

OH with NO_2, (Eq. 3.3) which has a higher density by the 20th pulse. The rate of decay of HO_2 is significantly smaller for the 20th pulse because the density of NO, which is the main consumer of HO_2, has decreased significantly. Unresolved HO_2 radical densities are shown in Fig. 3.6c. As the NO density decreases with each pulse, the density of HO_2 increases as its rate of consumption with NO decreases (Eq. 3.2c).

The densities of NO and NO_2 for single and multiple pulse excitation are compared in Fig. 3.7. With a single pulse, the NO density decreases from 4.2×10^{15} cm^{-3} to 1.0×10^{14} cm^{-3} at t = 0.2 s resulting in approximately 98% NO remediation. With multiple pulses, the exit densities of NO are higher than with a single pulse. This is due to the regeneration of NO from NO_2 by,

$$\mathrm{NO_2 + O \rightarrow NO + O_2}, \qquad k = 6.5\times10^{-12}\exp(120/T)\ cm^3 s^{-1},$$

$$k_{298} = 9.7\times10^{-12}\, cm^3 s^{-1}. \qquad (3.39)$$

CH_3O is a transient species as shown in Fig. 3.8. It is generated by the reaction of CH_3O_2 with NO (Eq. 3.23) and consumed by reactions with NO and NO_2 (Eqs. 3.24 and 3.25) to produce CH_3ONO and CH_3ONO_2 respectively. The reaction rate coefficients for these processes are approximately the same and so their relative rates are determined by the relative concentrations of NO and NO_2. With a single pulse, the density of NO greatly exceeds NO_2 when the density of CH_3O is maximum. Hence, most of the CH_3O is lost in the reaction with NO forming CH_3ONO and the production of CH_3ONO_2 is low. With multiple pulses, CH_3O is produced during each pulse. With each successive pulse, the concentration of NO decreases and that of NO_2 increases. When the concentration of

NO_2 exceeds that of NO, CH_3O is consumed preferentially by NO_2 forming CH_3ONO_2 as opposed to reacting with NO. This leads to an increase in NO_x remediation since CH_3ONO_2 is a terminal product.

With a single pulse, NO remediation is almost 98%, whereas with multiple pulses, the exit densities of NO are higher due to the regeneration from NO_2 through the reaction in Eq. 3.39. With a single pulse, the density of O decays before the density of NO_2 increases to a significant level. As a result, the regeneration process is not important. For later pulses, the densities of O and NO_2 are high at the same time, resulting in NO_2 reduction and formation of NO. This trend is shown in Fig. 3.9. During the initial pulses, NO is mainly converted to NO_2 ($t < 0.05$ s) and the density of NO_2 increases. At later times, as the concentration of NO_2 increases, NO and NO_2 come into a pulse-to-pulse equilibrium. After approximately 0.05 s, at the start of each pulse, NO_2 is converted to NO by the reaction with O atoms (Eq. 3.39) and at later times during the same pulse, the NO is converted back into NO_2 (Eqs. 3.2 and 3.21).

The densities of CH_3ONO_2 for single and multiple pulse formats for an energy deposition of 70 J/L are shown in Fig. 3.10. The final concentration with multiple pulses is ≈ 2.5 times that produced with a single pulse. This difference is due to the increased temporal overlap of CH_3O and NO_2 in the multiple pulse case in comparison with the single pulse.

The exit densities of NO as a function of energy deposition are shown in Fig. 3.11a. For energy depositions > 40 J/L, almost 100% of the NO is removed with a single pulse, a major fraction of (~65%) which reappears as NO_2. With increasing energy deposition, a larger fraction of this NO_2 is converted to HNO_3. With multiple pulses, NO

conversion is lower compared to the single pulse case due to the regeneration of NO from NO_2 (Eq. 3.39). The exit NO densities obtained using multiple pulses agree more closely with experimental results than with sinlge pulses. The efficiency of these processes can be quantified by *W*-values. (*W*-value [eV/molecule] is the amount of energy required to remove one molecule of the compound. Lower values correspond to more efficient processes.) The *W*-values for NO_x as a function of energy deposition are also shown in Fig. 3.11a. The *W*-values for NO_x are lower (more efficient) with multiple pulses. At low energy deposition (≈20 J/L), *W*-values are ≈ 110 eV for multiple pulses compared to 153 eV for a single pulse. At high energy deposition (≈60 J/L), *W*-values for multiple pulses are ≈ 185 eV compared to 240 eV for a single pulse. The decrease in the *W*-values is a result of the additional removal of NO_x through the formation of larger amounts of HNO_2, HNO_3 and CH_3ONO_2.

The densities of NO_2 and CH_3ONO_2 as a function of energy deposition with single and multiple pulses are shown in Fig. 3.11b. As before, the values obtained using multiple pulses agree more closely with those with experimental results. With multiple pulses, more NO_2 is channeled into reactions with OH, CH_3O and O (Eqs. 3.3, 3.25 and 3.39) because, with each pulse, NO_2 is present when O, OH and CH_3O have large densities. As a result, the NO_2 densities are lower. With increasing energy deposition, the exit concentrations of NO_2 initially increase and then decreases. The decrease is due to the increased production of O, OH and CH_3O at higher energy deposition, which then consume NO_2 to produce NO, HNO_3 and CH_3ONO_2 respectively. The difference in CH_3ONO_2 densities between single and multiple pulse formats increases with increasing energy deposition. This is because, at high energy deposition, larger quantities of CH_3O

and NO_2 are produced which results in more CH_3ONO_2 when their peak densities coincide.

The exit densities of N-containing products, HNO_2 and HNO_3 as a function of energy deposition are shown in Fig. 3.12a. The densities with multiple pulses are generally higher. HNO_2 is produced by the reaction of OH with NO (Eq. 3.2d). The higher HNO_2 density with multiple pulses is due to increase in the rate of the reaction,

$$HO_2 + NO_2 \rightarrow HNO_2 + O_2, \qquad k = 1.2\times10^{-13}\, cm^3 s^{-1}. \tag{3.40}$$

Since the concentration of NO_2 increases with each pulse, high densities of HO_2 and NO_2 can coincide, a condition which does not significantly occur with a single pulse. As a result, the contribution from this reaction to HNO_2 production also increases. HNO_3 is produced by the reaction of NO_2 and OH (Eq. 3.3). With the increase in NO_2, the HNO_3 density also increases as OH and NO_2 also have high densities at the same time with multiple pulses.

The consumption of C_3H_6 as a function of energy deposition is shown in Fig. 3.12b. At higher energy deposition, C_3H_6 consumption is higher with multiple pulses due to the increased production of OH by the reaction of HO_2 with NO (Eq. 3.2c). HCO production also increases with multiple pulses due to the reaction of OH with the increasing density of HCHO,

$$OH + HCHO \rightarrow HCO + H_2O, \qquad k = 4.73\times10^{-12}\,(T/298)^{1.18}\exp(225/T)\ cm^3s^{-1},$$
$$k_{298} = 1.0\times10^{-11}\, cm^3 s^{-1}. \tag{3.41}$$

The production of CO therefore also increases with multiple pulses due to the increase in the production of HCO radicals, which then reacts with O_2 to produce CO (Eq. 3.38).

The final C-containing products HCHO, CH_3CHO, methyl oxirane and CHO-CHO are shown in Fig. 3.13. HCHO and CH_3CHO are generated as the end-products of the OH-initiated reactions with C_3H_6. With multiple pulses, the NO density is higher (because of the $NO_2 \rightarrow NO$ conversion) which results in higher rates of reactions with peroxy radicals (Eq. 3.21). This increases the production of HCHO and CH_3CHO. The pathway leading to the production of HCHO and CH_3CHO is described in detail in Ref. 1. Briefly, the product RO of the reaction of peroxy radicals with NO (Eq. 3.21) decomposes to produce HCHO, CH_3CHO and hydroxyalkyl radicals. These hydroxyalkyl radicals further react with O_2 to produce HO_2 and more HCHO, and CH_3CHO. Methyl oxirane and CHO-CHO are products of the O atom initiated reactions with C_3H_6. Only small differences are observed in the densities of these species between single and multiple pulses because the initiating species, O, is not significantly affected by multiple pulses.

3.4 Concluding Remarks

The consequences of multiple discharge pulses on the plasma remediation of NO_x in the presence of hydrocarbons was numerically investigated. When using multiple pulses, reactions occur in the latter pulses with reaction products from previous pulses which are not accessible with a single pulse. For example, less than 1 ppm of CH_3ONO_2 was formed with a single pulse whereas nearly 10 ppm was produced when the same

energy was distributed over 20 pulses. Comparison of the products of single and multiple pulse discharges showed marked differences in final concentrations of NO_2, HNO_x, C_3H_6 and CO. *W*-values for NO_x decreased from 240 eV for a single pulse to 185 eV when the same energy was distributed over 20 pulses.

3.5 Figures

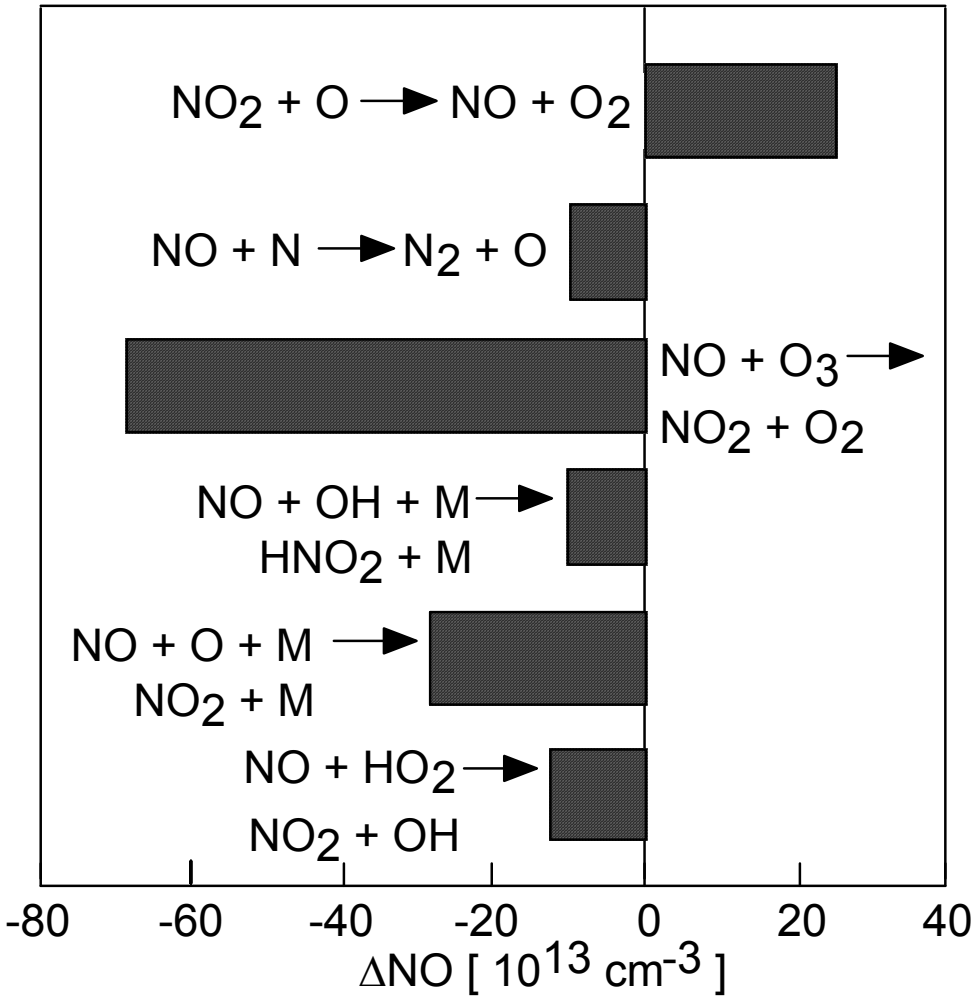

Fig. 3.1. Individual contributions of various reaction channels towards the remediation of NO during the DBD processing of NO_x in the absence of UHCs. The base gas mixture contains $N_2/O_2/H_2O/CO_2$ = 79/8/6/8 with 260 ppm of NO, 400 ppm of CO and133 ppm of H_2. The energy deposition is 30 J/L. The reactor temperature and pressure are 453 K and 1atm. In the absence of UHCs, the dominant reaction channels result in the oxidation of NO to NO_2. The reduction channel, $NO + N \rightarrow N_2 + O$, accounts for only 8% of the NO remediation.

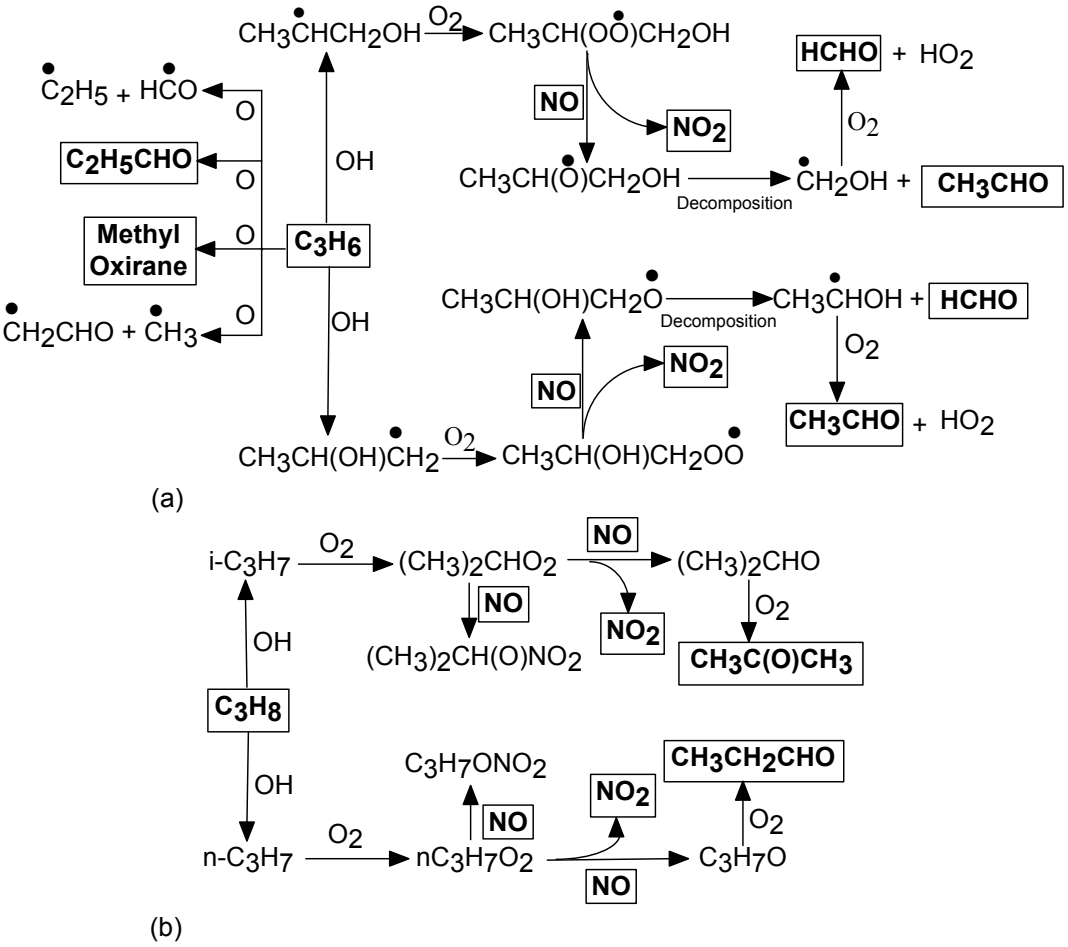

Fig. 3.2. Reaction mechanism for NO_x in the presence of C_3H_6 and C_3H_8.

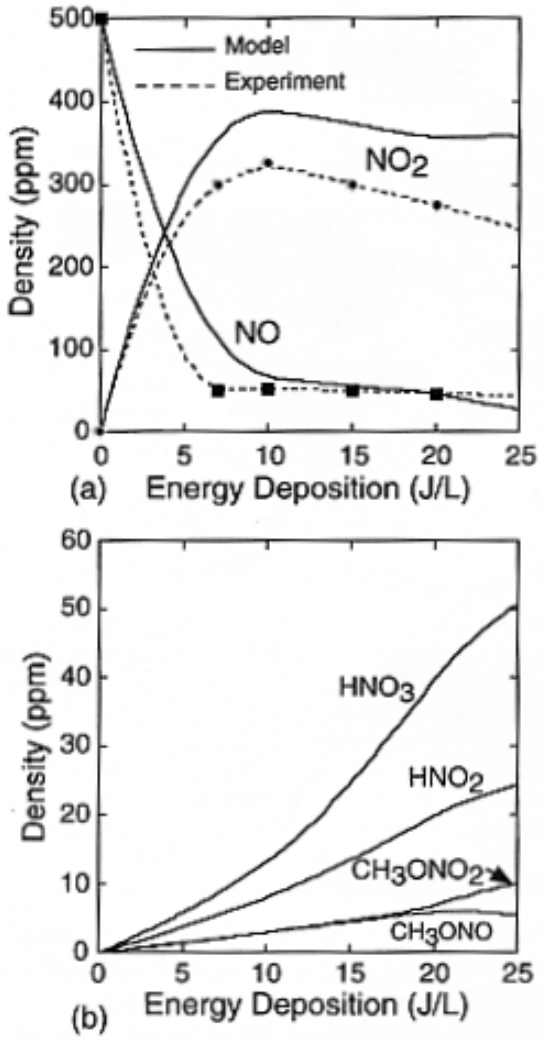

Fig. 3.3. NO and NO_2 exit densities as a function of energy deposition. Feed gas is at 260 ^{o}C and contains 500 ppm NO, 500 ppm C_3H_6, 10% O_2, 10% H_2O and balance N_2: (a) Experiment [4] and model results; (b) exit densities of major N-containing products.

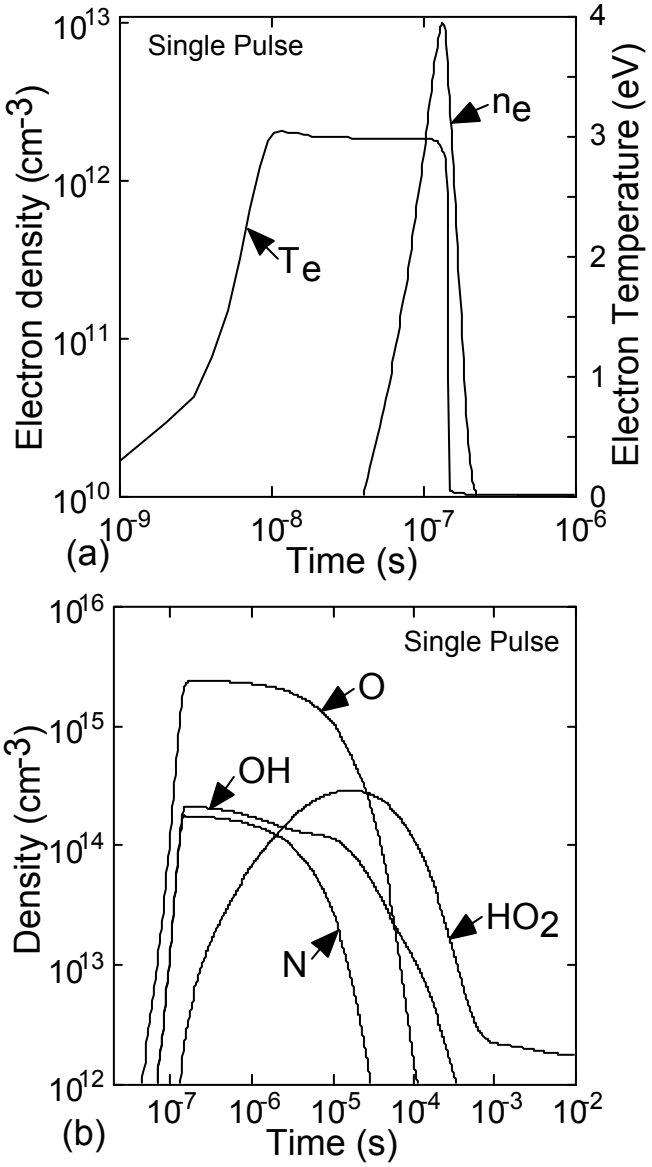

Fig. 3.4. Plasma properties during the single pulse discharge processing of NO_x. a) n_e and T_e. b) O, OH, N and HO_2. The background gas mixture is the same as in Fig. 3.1 with 500 ppm C_3H_6 and 175 ppm C_3H_8.

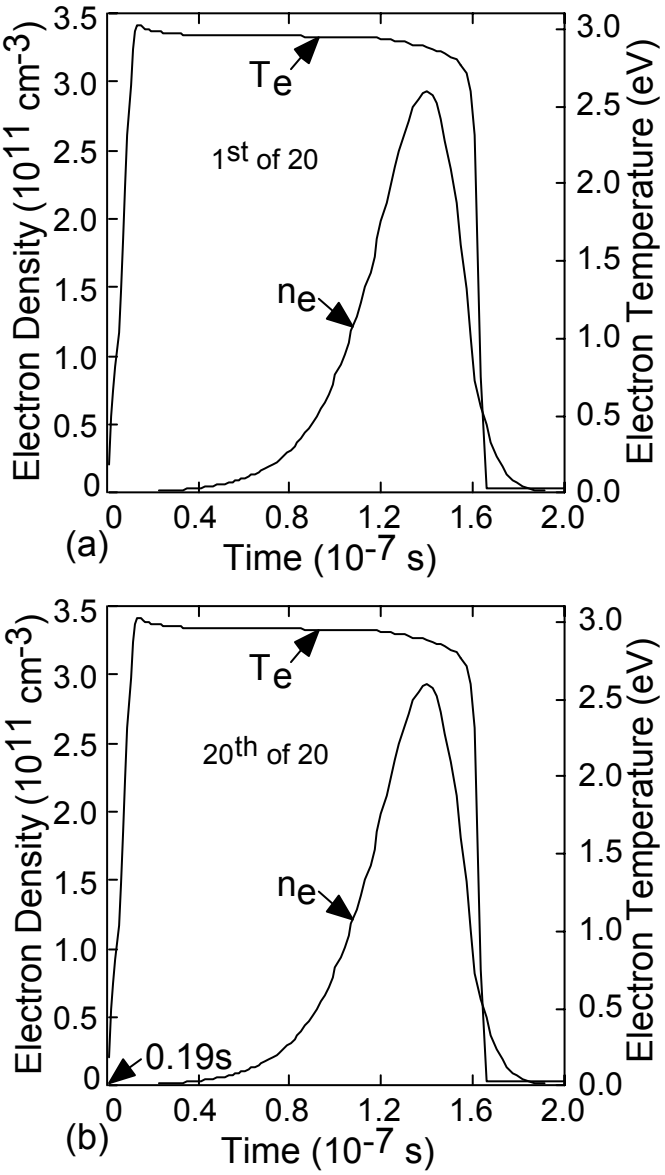

Fig. 3.5. Electron density and temperature during the multiple pulse discharge processing of NO_x. a) 1st of 20 pulses. b) 20th of 20 pulses. Electron densities and temperature are almost the same for all the pulses because the background gas mixture does not significantly change during the previous pulses. The gas mixture is the same as in Fig. 3.4.

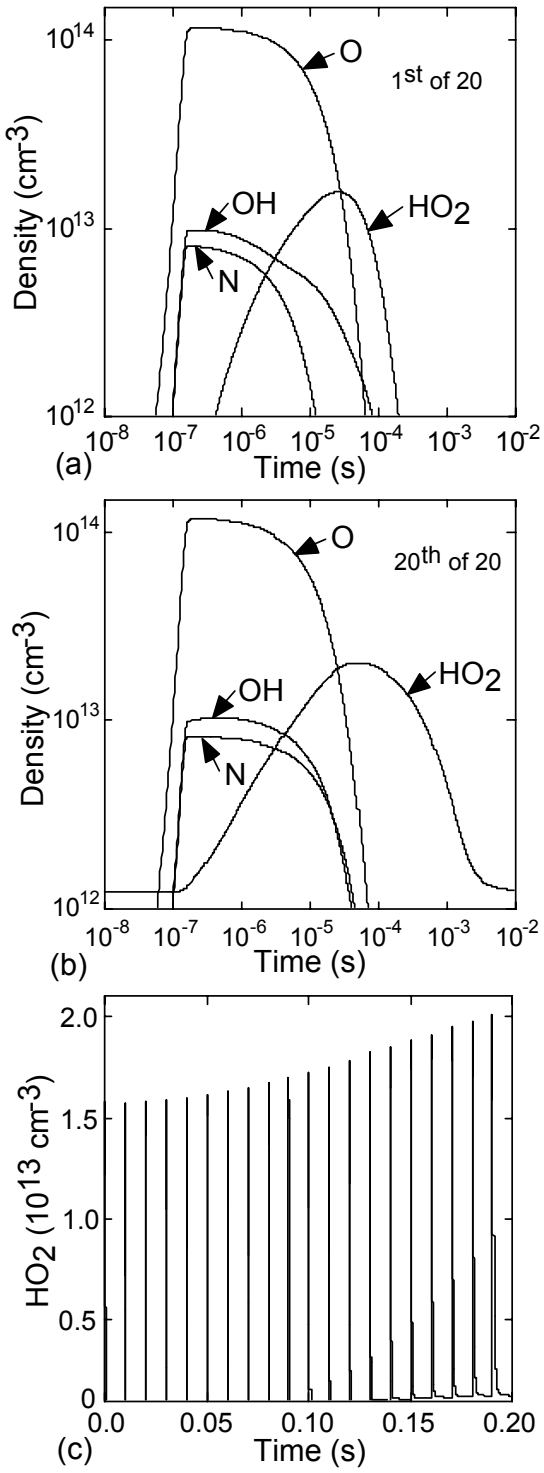

Fig. 3.6. Atom and radical densities during the multiple pulse plasma processing of NO_x. a) O, OH, HO_2 and N during the first pulse. b) O, OH, HO_2 and N for the 20th pulse. c) Unresolved HO_2 densities during the full length of the residence time. Peak HO_2 densities increase with time owing to the decreased consumption from NO, the main consumer of HO_2. Conditions are the same as in Fig. 3.4.

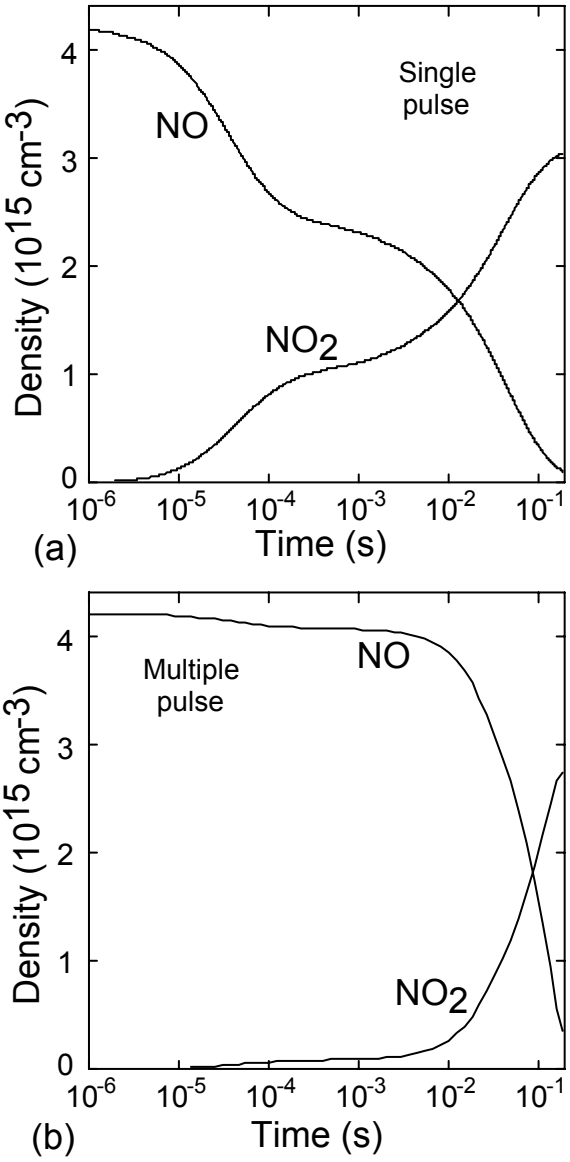

Fig. 3.7. Comparison of NO, and NO_2 densities during the single and multiple discharge processing of NO_x. Conditions are the same as in Fig. 3.4. a) Single pulse. b) Multiple pulse.

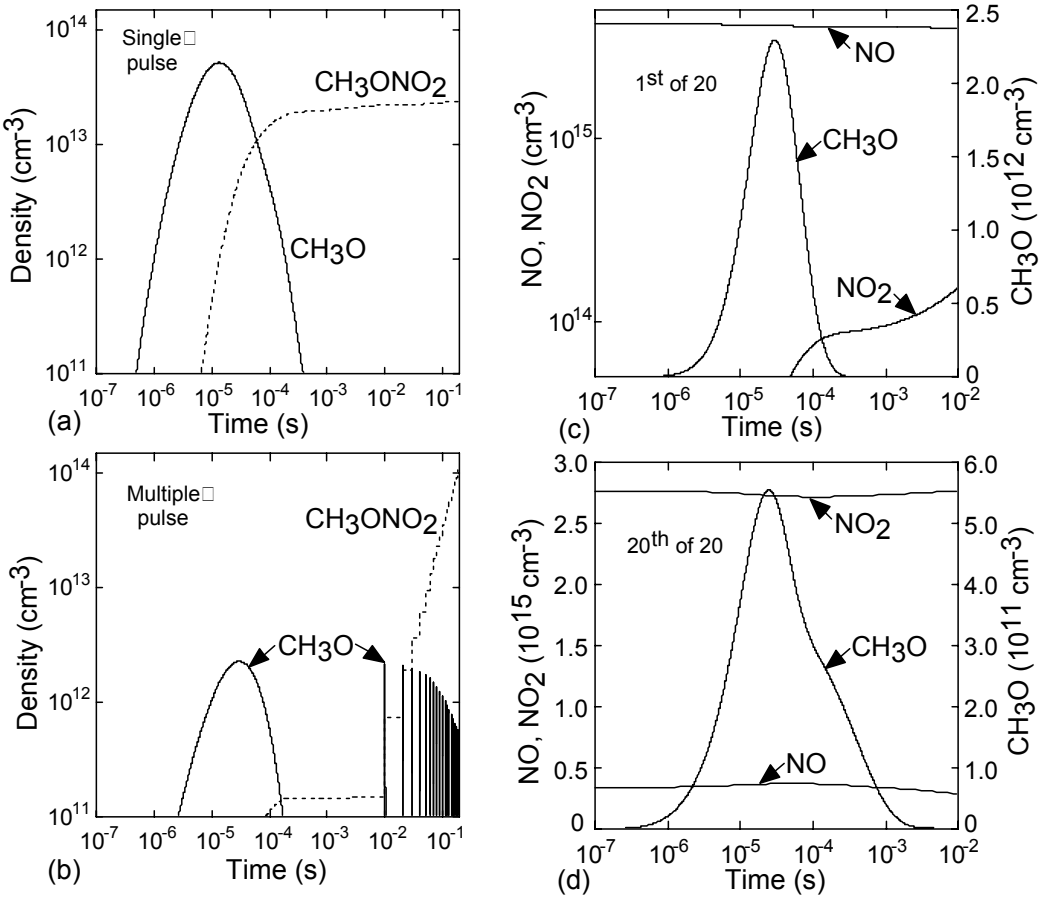

Fig. 3.8. CH_3O, CH_3ONO_2, NO and NO_2 densities for single and multiple pulse discharge processing of NO_x. Conditions are the same as in Fig. 3.4. CH_3O and CH_3ONO_2 densities for a) Single pulse, b) Multiple pulse. NO, NO_2 and CH_3O densities for c) 1st of 20 pulses, d) 20th of 20 pulses. With multiple pulses, NO densities are gradually lowered and NO_2 densities are gradually increased. CH_3O is produced during each pulse and there comes a time when $[NO_2]>[NO]$ and the formation of CH_3ONO_2 commences. CH_3O density decreases with each pulse, because the source of CH_3O, C_3H_6, decreases with each pulse.

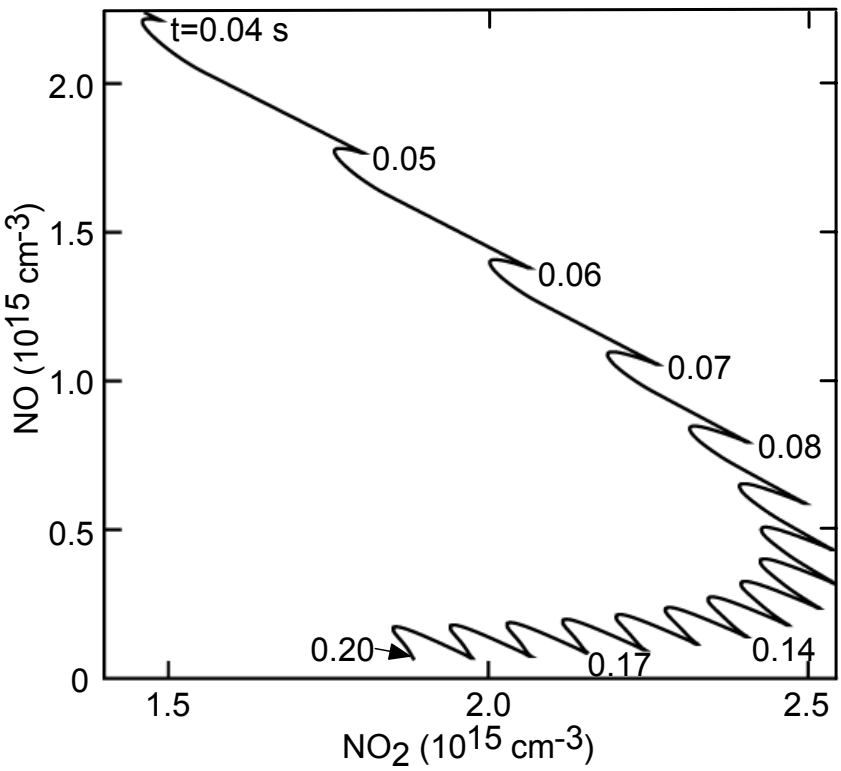

Fig. 3.9. Variation of NO with NO_2. The curve corresponds to a time evolution. At t < 0.05 s, NO + O$\rightarrow$$NO_2$ dominates over NO_2 + O $\rightarrow$NO + O_2 due to the smaller density of NO_2. As a result, in each of the pulse periods after 0.05 s, there is an initial back conversion of NO_2 to NO and a later conversion of NO to NO_2. The contribution to NO formation from the initial back conversion of NO_2 becomes larger as the concentration of NO_2 increases.

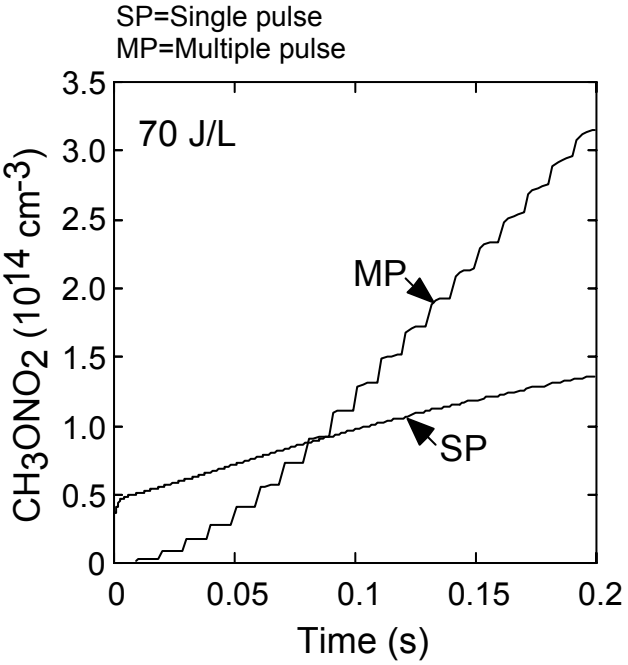

Fig. 3.10. CH_3ONO_2 density as a function of time for single and multiple pulse formats. The energy deposition is 70 J/L and other conditions are the same as in Fig. 3.4.

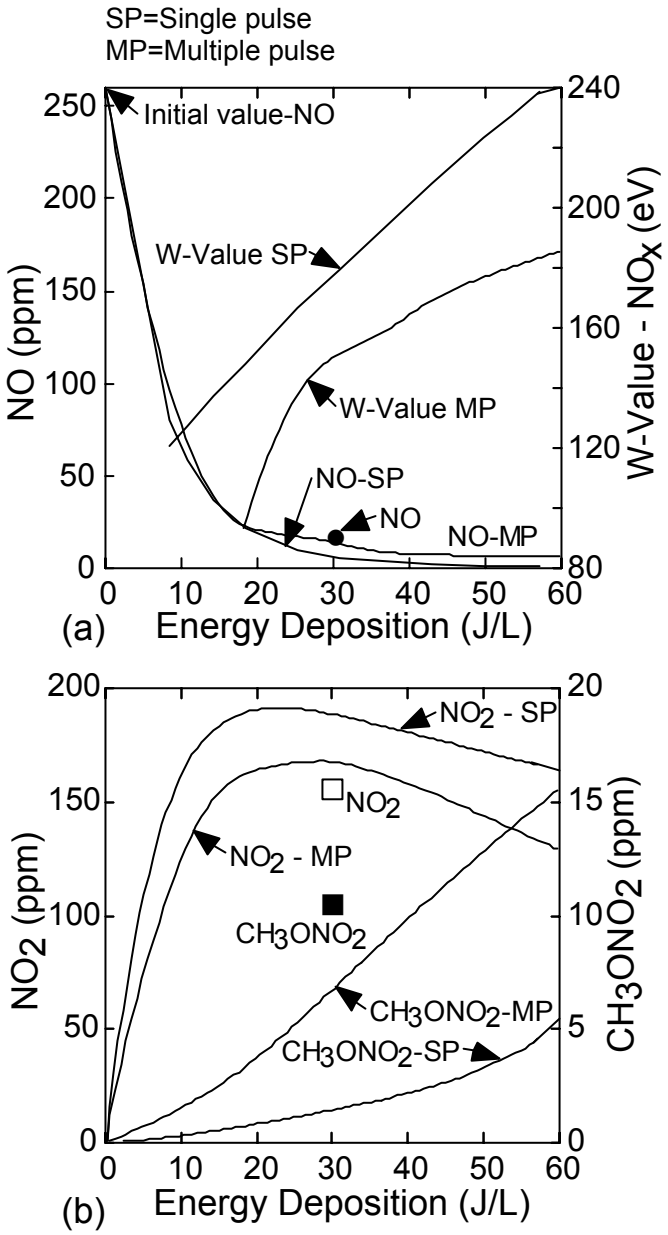

Fig. 3.11. Effect of energy deposition on NO_x remediation. a) NO and W-value for NO_x. b) NO_2 and CH_3ONO_2. Experimental values for NO (solid circles), NO_2 (empty squares) and CH_3ONO_2 (filled squares) are also shown.[6] In general, the *W*-values for multiple discharge formats are lower, indicating higher efficiencies of remediation. NO_2 densities in the case of multiple discharge formats are lower because of the back conversion to NO ($NO_2 + O \rightarrow NO + O_2$). The differences in CH_3ONO_2 between single and multiple pulse formats increases with energy deposition because of the increased production of CH_3O and NO_2.

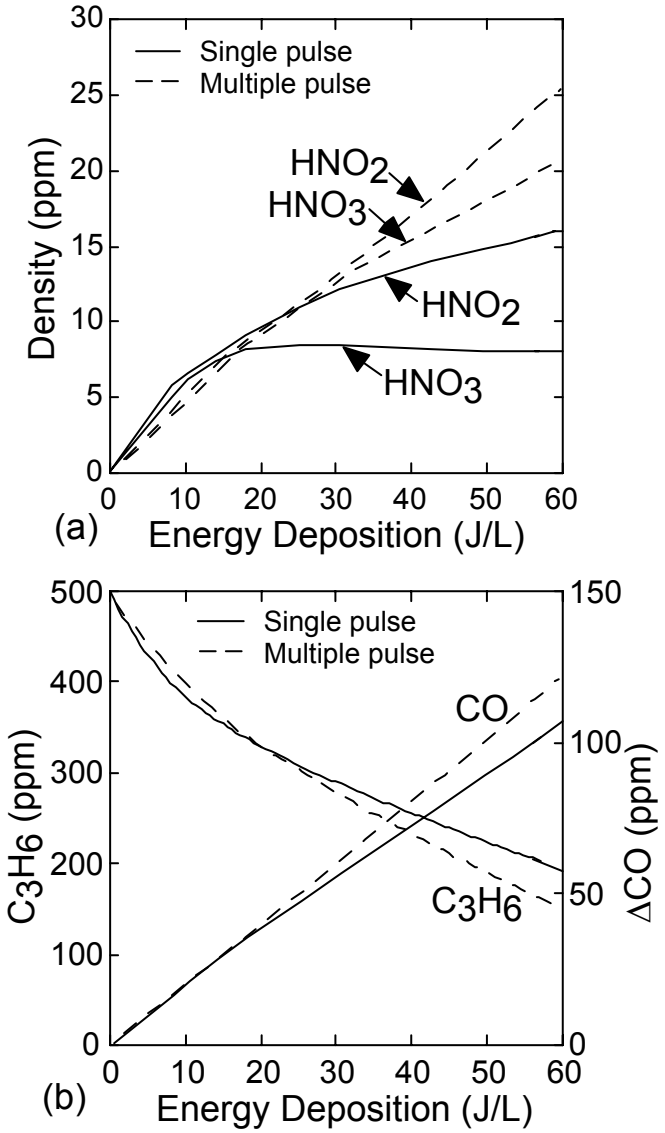

Fig. 3.12. Exit UHC and end product densities as a function of energy deposition. a) HNO_2 and HNO_3. b) C_3H_6 and CO. Single pulse (solid lines) and multiple pulse (dashed lines). HNO_x densities are higher with multiple pulse formats due to the increased production from NO_2. Higher C_3H_6 conversion is observed with multiple pulse formats due to the increased production of OH from HO_2 ($HO_2 + NO \rightarrow NO_2 + OH$). CO production increases with multiple pulse formats due to the increase in the production of HCO from HCHO ($HCHO + OH \rightarrow HCO + H_2O$; $HCO + O_2 \rightarrow CO + HO_2$).

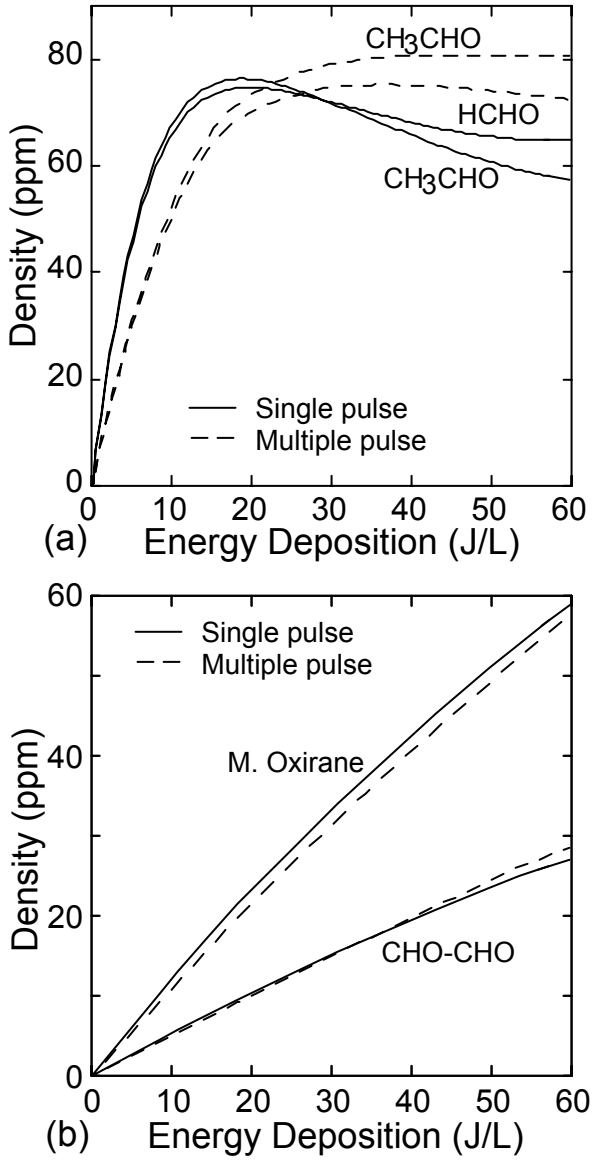

Fig. 3.13. Exit hydrocarbon end product densities as a function of energy deposition. a) HCHO and CH_3CHO. b) Methyl oxirane and CHO-CHO. Single pulse (solid lines) and multiple pulse (dashed lines).

3.6 References

1. R. Dorai, M. S. Thesis, University of Illinois, 2000 <http://uigelz.ece.uiuc.edu>.
2. P. Vitello, B. M. Penetrante, and J. Bardsley, Phys. Rev. E **49,** 5575 (1994).
3. A. C. Gentile and M. J. Kushner, J. Appl. Phys. **78,** 2074 (1995).
4. A. Khacef, M. Nikravech, O. Motret, P. Lefaucheux, R. Viladrosa, J. M. Pouvesle and J. M. Cormier, Private communications (2000).
5. D. Fulle, H. F. Hamann, H. Hippler and J. Troe, J. Chem. Phys. **108**, 5391 (1998).
6. J. Hoard, Private communications (2000).

4. INTERACTIONS BETWEEN SOOT PARTICLES AND NO_X DURING PLASMA REMEDIATION OF SIMULATED DIESEL EXHAUST

4.1 Introduction

In this chapter, we present results from a modeling investigation of the consequences of soot particles on the plasma chemistry in simulated diesel exhaust gas processed in a DBD reactor. The modified form of the zero-dimensional global kinetics simulation GLOBAL_KIN, as described in Section 2.3, is used to address the heterogeneous chemistry on the soot surface. In this investigation, we address NO_x-soot interactions, heterogeneous reactions of radicals such as O and OH with soot and the effects of soot on the ionization kinetics. We found that in the presence of soot, NO_x remediation improved by nearly 10%. With soot, higher energies were required for the remediation of a given amount of NO. Since we have already discussed in detail the reaction mechanism for NO_x-propene-propane in Section 3.2, only those reactions particularly germane to this study will be summarized in Section 4.2. The surface chemistry on soot particles is discussed in detail in Section 4.3. Results from our parametric studies on the NO_x chemistry in the presence of soot are in Section 4.4. Section 4.5 contains our concluding remarks.

4.2 Reaction Mechanism for Gas Phase Chemistry in Simulated Diesel Exhaust

The base gas mixture contained $N_2/O_2/H_2O/CO_2$ = 79/8/6/7 with 400 ppm of CO, 260 ppm of NO, 133 ppm of H_2, 500 ppm of propene (C_3H_6) and 175 ppm of propane (C_3H_8). The last two gases are used as model UHCs. The list of species used for the simulations is given in Appendix A. All the reactions in Appendix B which involve the

species for this study are considered in the model. The reaction mechanism used in the absence of soot is discussed in detail in Chapter 3 and in Refs. 1 and 2.

The NO_x chemistry is mainly driven by oxidation processes that result in the conversion of NO to NO_2. The radicals initiating the chemistry, O, N and OH are produced by electron impact processes.

$$e + O_2 \rightarrow O + O + e \quad (4.1)$$

$$e + N_2 \rightarrow N + N + e \quad (4.2)$$

$$e + H_2O \rightarrow OH + H + e \quad (4.3)$$

NO reduction occurs through the reaction with N atoms.

$$N + NO \rightarrow N_2 + O \quad (4.4)$$

Reactions with O atoms and OH radicals results in NO oxidation,

$$NO + O + M \rightarrow NO_2 + M \quad (4.5)$$

$$NO_2 + OH + M \rightarrow HNO_3 + M \quad (4.6)$$

In the presence of UHCs, the key oxidant-species are the OH and HO_2 radicals and the β-hydroxyalkyl peroxy radicals (βHAPs) $CH_3CH(OO)CH_2OH$ and $CH_3CH(OH)CH_2OO$. HO_2 is an intermediate produced by reactions of βHAPs. The βHAP radicals are produced through a two-step oxidation of propene initiated by OH, which is initially

produced by electron impact of H_2O (Eq. 4.3). The β-hydroxyalkyl radicals CH_3CHCH_2OH and $CH_3CH(OH)CH_2$ are intermediate species.

$$C_3H_6 + OH \rightarrow CH_3CHCH_2OH \quad (4.7)$$

$$C_3H_6 + OH \rightarrow CH_3CH(OH)CH_2 \quad (4.8)$$

$$CH_3CHCH_2OH + O_2 \rightarrow CH_3CH(OO)CH_2OH \quad (4.9)$$

$$CH_3CH(OH)CH_2 + O_2 \rightarrow CH_3CH(OH)CH_2OO \quad (4.10)$$

The oxidation of NO then takes place following two pathways. The first one is a simple oxidation involving HO_2,

$$HO_2 + NO \rightarrow NO_2 + OH. \quad (4.11)$$

The second channel involves the βHAP radicals,

$$CH_3CH(OO)CH_2OH + NO \rightarrow CH_3CH(O)CH_2OH + NO_2 \quad (4.12)$$

$$CH_3CH(OH)CH_2OO + NO \rightarrow CH_3CH(OH)CH_2O + NO_2 \quad (4.13)$$

The radicals produced through the reactions of βHAPs with NO undergo thermal decomposition which ultimately leads to the formation of HO_2, formaldehyde (HCHO) and acetaldehyde (CH_3CHO).

$$CH_3CH(O)CH_2OH \rightarrow CH_2OH + CH_3CHO \quad (4.14)$$

$$CH_2OH + O_2 \rightarrow HCHO + HO_2 \quad (4.15)$$

$$CH_3CH(OH)CH_2O \rightarrow CH_3CHOH + HCHO \quad (4.16)$$

$$CH_3CHOH + O_2 \rightarrow CH_3CHO + HO_2 \quad (4.17)$$

These reactions lead to $NO \rightarrow NO_2$ conversion. The actual NO_x remediation from the exhaust is mainly due to the oxidation of NO_2 to HNO_3 (Eq. 4.6) and

$$NO + OH + M \rightarrow HNO_2 + M. \quad (4.18)$$

The fraction of NO_x that is actually converted to HNO_2 and HNO_3 ranges between 10 and 20%.[2]

4.3 NO_x-Soot Interactions

The gas temperatures of interest are ≈453 K and the gas residence time is usually a few tenths of a second. Under these conditions soot growth and soot nucleation are kinetically limited and may be neglected. Similarly, the soot oxidation by molecular oxygen usually observed in combustion does not take place in DBDs since gas temperatures above 700 K are typically required for such processes to be important.[3] However, soot particles may undergo oxidation when reacting with plasma generated radicals such as O and OH which are effective oxidants for carbonaceous particles even at low temperature (T≈300 K).[4,5] The oxidation of soot by OH is one of the major soot consumption processes in flames, and occurs with a reaction probability of ≈ 0.1

producing CO and H_2.[4] The oxidation of solid carbon by O atoms at low temperatures producing CO has been investigated only for solid graphite films. Reaction probabilities as high as 0.12 have been reported at 300 K.[5]

The interaction between NO_x and soot takes place through adsorption and reduction processes involving NO_2. The interaction of NO_x with carbonaceous particles was first considered in the context of atmospheric chemistry.[6-10] These studies indicated that reactions of soot with NO_2 leads to the formation of NO [8,9] and HNO_2 [10]. At low temperatures (T < 333 K) NO_2 once adsorbed tends to remain on the soot. The adsorption of NO_2 on n-hexane soot particles was investigated by Smith and coworkers who showed that, at 300 K, two adsorbates are formed, C-ONO and C-NO_2.[6,7,11] For temperatures higher than 350 K, a redox reaction of NO_2 occurs resulting in the desorption of NO and CO to the gas phase.

In principle, soot particles can also react with other radicals in the NO_x chemistry. However the homogeneous gas phase chemistry of these radicals, with the exception of the βHAPs, produces loss frequencies several orders of magnitudes greater than their collision frequencies with soot particles. For example, the loss frequency of β hydroxyalkyl radicals by reaction with O_2 is approximately 10^8 s^{-1} compared to the collision frequency with soot particles of ≈ 10^4 s^{-1} for a particle density of 5 x 10^8 cm^{-3} and a particle diameter of 150 nm. Consequently, the concentration of these radicals is mainly governed by the gas phase chemistry and their interaction with soot may be neglected.

An exception is the βHAP radical which is consumed by NO with a frequency of $\approx 10^3$ s^{-1} for a NO density of 10^{16} cm^{-3}. Since there is little data on the reaction of βHAP radicals on soot particles, parametric studies on these rate coefficients were performed.

To take into account these heterogeneous processes, we developed the following surface reaction mechanism for soot particles (denoted by C_xH_y):

$$(C_xH_y) + NO_2 \rightarrow (C_{x-1}H_y)\text{-}C\text{-}NO_2 \quad (4.19)$$

$$(C_xH_y) + NO_2 \rightarrow (C_{x-1}H_y)\text{-}C\text{-}ONO \quad (4.20)$$

$$(C_xH_y) + O \rightarrow (C_{x-1}H_y)\text{-}C\text{-}O \quad (4.21)$$

$$(C_xH_y) + OH \rightarrow (C_{x-1}H_y)\text{-}C\text{-}OH \quad (4.22)$$

$$(C_{x-1}H_y)\text{-}C\text{-}NO_2 \rightarrow (C_{x-1}H_y) + NO + CO \quad (4.23)$$

$$(C_{x-1}H_y)\text{-}ONO \rightarrow (C_{x-1}H_y) + NO + CO \quad (4.24)$$

$$(C_{x-1}H_y)\text{-}C\text{-}O \rightarrow (C_{x-1}H_y) + CO \quad (4.25)$$

$$(C_{x-1}H_y)\text{-}C\text{-}OH \rightarrow (C_{x-1}H_{y-1}) + CO + 1/2\ H_2 \quad (4.26)$$

$$\beta HAP + (C_xH_y) \rightarrow \beta HAP\text{-}(C_xH_y) \quad (4.27)$$

$$\beta HAP\text{-}(C_xH_y) \rightarrow C_xH_y + \text{Gas-phase decomposition products.} \quad (4.28)$$

The soot is assumed to contain only H and C atoms, though actual soot may also contain O, N and S. The reaction mechanism begins with the adsorption of NO_2 on soot forming $-C\text{-}NO_2$ and –C-ONO complexes. Adsorption of O and OH produces –C-O and –C-OH complexes. Spontaneous desorption produces CO (and a reduction of soot mass) and NO or H_2. The reaction of βHAPs with soot is what we call a deactivation process. The resulting desorption products are not further important to the process and so the reactivity

of the βHAPs has been decreased. The kinetics of the adsorption reactions in Eqs. 4.19-4.22 and 4.27 is described in terms of reaction probability γ_i (i = 19-22, 27 for reactions 4.19-4.22, 4.27). These probabilities depend on the surface density of free adsorption sites [s]. We assumed a simple linear dependence of the form $\gamma_i = \gamma_{i\text{-}0}$ [s]/$[s]_0$ where $\gamma_{i\text{-}0}$ and $[s]_0$ are the reaction probability and the surface density of free adsorption sites at zero coverage of adsorbates. We chose $\gamma_{21\text{-}0} = 0.12$ and $\gamma_{22\text{-}0} = 0.1$ for O and OH based on Refs. 4 and 5. There is more uncertainty on the reaction probabilities for NO_2 ($\gamma_{19\text{-}0}$ or $\gamma_{20\text{-}0}$). Experimental studies of different carbonaceous particles have produced $\gamma_{20\text{-}0}$ of 5 x 10^{-3} - 0.5. We used $\gamma_{20\text{-}0} = 0.1$ from the experimental measurements of Smith and Chughtai for hexane soot as a base value.[6] The choice of this value was motivated by the fact that n-hexane soot is a good model for the soot found in diesel exhausts. However, since $\gamma_0(NO_2)$ may vary with the soot structure and the exhaust composition, we performed a parametric study of this parameter.

The rate constants of the desorption reactions in Eqs. 4.23 and 4.24 were deduced from the experiments of Tabor *et al*.[8] Frequencies of 100-500 s^{-1} were determined for NO desorption following NO_2 adsorption on different carbonaceous particles at 300 K taking into account both the (C_xH_y)-NO_2 and (C_xH_y)-ONO channels. These values represent a lower limit since the gas temperature in exhausts at the point of processing is around 453 K which should result in higher desorption frequencies. Consequently, a parametric study was performed on the NO desorption frequency. Since the rate limiting step of the oxidation of soot by either O-atoms or OH-radicals is the adsorption step, an arbitrary value of 10^8 s^{-1}, consistent with a fast desorption process, was used for the frequency of reactions in Eqs. 4.25, 4.26, and 4.28.

4.4 Plasma Remediation of NO_x in the Presence of Soot

The gas is treated by a single discharge pulse having a duration $\approx 10^{-7}$s consistent with DBDs. The time evolution of the exhaust is followed for a reactor gas residence time of 0.2 s. The initial composition of the exhaust gas is $N_2/O_2/H_2O/CO_2$ = 79/8/6/7 with 400 ppm of CO, 260 ppm of NO, 133 ppm of H_2, 500 ppm of propene and 175 ppm of propane. The base case values are an energy deposition of 38 J/L, soot particle density of 10^8 cm^{-3}, and soot particle diameters of 100 nm. The adsorption probability of NO_2 and the desorption rate constants are $\gamma_{20\text{-}0} = 0.1$ and $k_d = 500$ s^{-1} respectively.

The fundamental processes initiating the plasma chemistry are the electron impact dissociation of O_2, N_2, H_2O and CO_2. The electron density, n_e and temperature, T_e are shown in Fig. 4.1a for the base case conditions. T_e rises to 3 eV until electron avalanche increases the conductivity of the plasma and T_e begins to decrease. n_e reaches 10^{13} cm^{-3} at which time the dielectric charges, thereby removing voltage from the gap. This reduces the electric field and T_e below the self sustaining value. The electron density then quickly decays by attachment and recombination. The densities of O, OH and N are shown in Fig. 4.1b. Electron impact on O_2, N_2 and H_2O produce O, N and OH respectively (Eqs. 4.1-4.3). O is also produced by the electron impact dissociation of CO_2.

$$e + CO_2 \rightarrow CO + O + e \tag{4.29}$$

The peak O density is $\approx 10^{15}$ cm^{-3}. O is quickly consumed by O_2 to form ozone.

$$O + O_2 + M \rightarrow O_3 + M \tag{4.30}$$

N densities are smaller, $\approx 8 \times 10^{13}$ cm^{-3}, due to the higher threshold energy for the dissociation of N_2. N is dominantly consumed by the reaction with NO (Eq. 4.4). The peak OH density is $\approx 10^{14}$ cm^{-3}. OH is dominantly consumed by reactions with UHCs (Eqs. 4.7 and 4.8). Other nonhydrocarbon species that convert NO to NO_2 are HO_2 (Eq. 4.11) and O_3,

$$O_3 + NO \rightarrow NO_2 + O_2. \tag{4.31}$$

The time-evolution of HO_2 and O_3 are shown in Fig. 4.1c. HO_2 is sustained as an intermediate of the reactions of NO with the βHAPs (Eqs. 4.15 and 4.17) and by the reaction of HCO with O_2.

$$HCO + O_2 \rightarrow HO_2 + CO \tag{4.32}$$

The densities of NO and NO_2 with and without heterogeneous reactions on the soot particles are shown in Fig. 4.2. The densities of OH and βHAP radicals are shown in Fig. 4.3. For $t < 10^{-6}$ s, the species that initiate the NO_x chemistry, HO_2, O_3 and the βHAP radicals, have a low density and NO and NO_2 densities remain nearly constant. For $t > 10^{-6}$ s, homogenous reactions dominate and result in an almost total conversion of NO to NO_2 when heterogeneous processes are not taken into account. When surface reactions are included, the densities of NO and NO_2 critically depend on the probability of reaction

with βHAP radicals. In the absence of βHAP deactivation, heterogeneous reactions slow down the total rate of NO→NO_2 conversion by the generation of NO on the particles. For example, the exit NO density is ≈50 ppm compared to ≈5 ppm when soot particles are not considered. The heterogeneously generated NO comes from the adsorption of NO_2 on the particles, followed by reduction of NO_2 and desorption. This is accompanied by a 35% decrease in NO_2 concentration.

When the adsorption of βHAPs is included with $\gamma_{27\text{-}0} = 1.0$, the effect of soot is more pronounced. The NO→NO_2 homogeneous conversion produces a minimum in the density of NO of 1.9×10^{15} cm^{-3} at $t \approx 10^{-2}$ s and then increases to 3.3×10^{15} cm^{-3}, keeping NO as the major NO_x species. As a result of βHAP deactivation on soot, βHAP densities decrease to 2.8×10^{14} cm^{-3} by 10^{-2} s (see Fig. 4.3). This decreases the rate of oxidation of NO by βHAP (Eqs. 4.12 and 4.13) which in turn decreases the rate of production of NO_2. The end result is a rebound in the density of NO.

The change in total NO_x concentration is shown in Fig. 4.4c. The unresolved drop in NO_x of ≈15 ppm when including soot chemistry without βHAP deactivation is due to the increased conversion of NO to HNO_2. This is facilitated by an increase of OH density when soot is included, as shown in Fig. 4.3b. When both NO_2-soot reactions and βHAP radical deactivation are taken into account, NO_x removal decreases by ≈10%. This change is mainly due to the decrease of OH radical concentration, as shown in Fig. 4.3b. This decrease in OH is due to the decrease in the production of OH from βHAPs [pathways (4.12)-(4.14)-(4.15)-(4.11) and (4.13)-(4.16)-(4.17)-(4.11)]. Since βHAP deactivation decreases the gas-phase concentration of βHAP, the rates of the subsequent reactions in the pathways are also decreased. The rate of NO→HNO_2 conversion (Eq.

4.18) is proportional to the density of OH which is dominantly produced from HO_2 through the reaction in Eq. 4.11. The main sources of HO_2 are the reactions between βHAP radicals and NO through the reaction pathways (4.12)-(4.14)-(4.15) and (4.13)-(4.16)-(4.17). Therefore the deactivation of βHAPs leads to the decrease in HO_2 and OH densities, which in turn slows the rate of homogeneous oxidation of NO and NO_2.

The reaction of soot with NO_2 also affects the C_3H_6, HCHO and CH_3CHO densities as shown in Fig. 4.4. When $\gamma_{27\text{-}0} = 0$ for βHAPs, the C_3H_6 density decreases by ≈25% compared to the no soot case. This is due to the increase of the OH concentration (see Fig. 4.3b) which produces an increase in the consumption of C_3H_6 through the reactions in Eqs. 4.7 and 4.8. Simultaneously, the densities of formaldehyde and acetaldehyde increase by factors of 2 and 3. This is due to the higher NO density which leads to an increase in production of HCHO and CH_3CHO through the reaction pathways (4.12)-(4.14)-(4.15) and (4.13)-(4.16)-(4.17). When $\gamma_{27\text{-}0} = 1$ for βHAPs, the decrease of the OH density lowers the reaction rate between OH and C_3H_6. Consequently, the C_3H_6 density is 12% higher than the case without soot. Smaller densities for HCHO and CH_3CHO are also generated due to the lower rate of reaction of OH with C_3H_6, the initiating reaction for the production of these species.

The heterogeneous interaction of NO_2, O and OH with soot particles leads to the formation of CO. The densities of CO with and without soot particles are shown in Fig. 4.5a. The heterogeneous production of CO starts at $t \approx 10^{-4}$ s when desorption of NO from the particles becomes important. Consequently, without βHAP deactivation, the exit CO concentration is ≈65% larger than the case without soot. The production of CO is assisted by the dynamics of $NO \leftrightarrow NO_2$ exchange involving homogeneous $NO \rightarrow NO_2$

conversion in the gas phase and heterogeneous $NO_2 \rightarrow NO$ conversion on soot. For each cycle of this exchange ($NO_{2(gas)} \rightarrow NO_{2(soot)} \rightarrow NO_{(gas)}$), one CO molecule is generated. When $\gamma_{27\text{-}0} = 1$ for βHAP, the increase of CO concentration is ≈20% since the $NO \leftrightarrow NO_2$ exchange rate is slower due to the decrease of βHAP and HO_2 densities.

The desorption of CO produces a loss of soot mass shown in Fig. 4.5b. The mass of soot is decreased by a factor 3.5 with a diameter reduction of ≈45%. The mass loss is initiated by reactions with NO_2 which account for ≈99.9% of the loss. Less soot is consumed when $\gamma_{27\text{-}0} = 1$ for βHAP. In this case, the βHAPs are mainly consumed through deactivation on soot particles, which leads to a decrease of the $NO \rightarrow NO_2$ conversion rate and slower $NO \leftrightarrow NO_2$ exchange dynamics.

The densities of adsorbed species are shown in Fig. 4.6 for the case with no βHAP deactivation. The adsorption sites are not saturated. The surface densities of NO_2 adsorbates reaches a quasi-steady state value of ≈6 x 10^{14} cm^{-2} at $t \approx 10^{-3}$s at which time the limiting step for the $NO_2 \rightarrow NO$ heterogeneous conversion is the desorption of NO. The surface densities of O and OH are smaller compared to NO_2 due to the higher homogeneous loss frequencies of O and OH and the spontaneous desorption of $O_{(ads)}$ and $OH_{(ads)}$.

In the simulations discussed thus far, electron and ion attachment to soot were not considered. n_e and T_e are shown for particle density of 10^9 cm^{-3} and soot diameter of 150 nm in Fig. 4.7 with and without particle charging. At this higher surface density of soot, there is ≈5% decrease in n_e and a small increase in T_e to increase the ionization rate to offset the electron loss to the particles. The effect is proportionally smaller for the smaller soot surface density of the base case. The consequence of these changes on the

active species in NO_x chemistry is small and does not appreciably affect the results reported in this section.

The soot affects NO_x chemistry through the kinetics of NO_2 adsorption and NO desorption. Since the adsorption probability and the soot surface may change during the treatment of the exhaust, it is instructive to parameterize the initial NO_2 adsorption probabilities, [$\gamma_{19\text{-}0}$ and $\gamma_{20\text{-}0}$ collectively called $\gamma_0(NO_2)$], the NO desorption frequency [k_d(-C-ONO) and k_d(-C-NO_2) collectively called k_d(NO)] and the initial active soot surface per unit gas phase volume (the product of the soot active surface and the soot particle density, $S_s n_p$).

The exit densities of NO and NO_2 as a function of $\gamma_0(NO_2)$ for different values of k_d(NO), with $\gamma_{27\text{-}0} = 0$ for βHAPs, are shown in Fig. 4.8. For low k_d, NO increases monotonically with $\gamma_0(NO_2)$. Larger rates of NO_2 adsorption produce more NO generation. Most of the NO is converted to NO_2 in the gas-phase thereby showing a monotonic decrease with $\gamma_0(NO_2)$. For $k_d(NO) \geq 1000$ s^{-1}, the density of NO first increases with $\gamma_0(NO_2)$, reaches a maximum and then decreases at high $\gamma_0(NO_2)$ values. In the low $\gamma_0(NO_2)$ range, the soot particles diameter does not change significantly, and the main consequence of increasing the adsorption probability is the production of more NO. Above a critical adsorption probability, the NO_2-soot reaction results in a decrease of soot particle diameter as shown in Fig. 4.9a. This reduction in the specific surface area reduces the rate of $NO_2 \rightarrow NO$ heterogeneous conversion. Consequently, the homogenous $NO \rightarrow NO_2$ conversion dominates over the heterogeneous $NO_2 \rightarrow$ NO conversion, which leads to a smaller density for NO. The final NO concentration as a function of $\gamma_0(NO_2)$ is not affected by the desorption frequency when $k_d > 10^4$ s^{-1}. This indicates that the

limiting step in $NO_2 \rightarrow NO$ heterogeneous conversion is the adsorption step. The decrease in soot diameter with increasing $\gamma_0(NO_2)$ is a result of the more rapid rate of heterogeneous reactions which bind with C in the soot, ultimately leading to the production of CO. As $k_d(NO)$ increases, the fraction of unoccupied surface sites increases, as shown in Fig. 4.9b, thereby enabling more rapid adsorption of NO_2. When $k_d(NO) > 10^4\ s^{-1}$, the adsorption of NO_2 becomes the rate-limiting step in the oxidation of soot. This results in low surface densities of NO_2 and so the oxidation of soot saturates.

The variation of the total NO_x density with $\gamma_0(NO_2)$ closely follows that of NO_2. In particular, a 15% increase in NO_x remediation is obtained when $\gamma_0(NO_2)$ increases from 10^{-4} to 0.1. The increase in $\gamma_0(NO_2)$ also produces significant changes in CO, C_3H_6, HCHO and CH_3CHO densities, as shown in Fig. 4.10. These densities are almost independent on the NO_2 desorption frequency and values are shown for $k_d(NO_2)=10^3 s^{-1}$. The increase of $\gamma_0(NO_2)$ in the range 10^{-4} - 0.1 leads to a 50% increase of CO and more than a 100% increase for HCHO and CH_3CHO. The concentration of C_3H_6 decreases by almost 25%. The increase of CO is a direct consequence of the increase of adsorption of NO_2 leading to NO and CO desorption. The increase in HCHO and CH_3CHO when increasing $\gamma_0(NO_2)$ is a consequence of the enhancement of NO-βHAP reactions in Eqs. 4.12 and 4.13 resulting from the increase in NO. These reactions also ultimately increase the OH density which increases the rate of reactions between OH and C_3H_6 (Eqs. 4.7 and 4.8), which then decreases the C_3H_6 density.

When $\gamma_{27\text{-}0}=1$ for βHAP, the densities of NO and NO_2 as a function of $\gamma_0(NO_2)$ have a weak dependence on k_d. The NO concentration increases by almost 90% when $\gamma_0(NO_2)$ is varied from 10^{-4} to 0.1 as shown in Fig. 4.11 while the NO_2 concentration

decreases. When βHAP radicals are totally quenched by the soot, the NO_x chemistry is similar to that in the absence of UHCs. This results in a slower rate of $NO \rightarrow NO_2$ homogenous conversion, which also leads to a slower $NO_2 \leftrightarrow NO$ exchange dynamics. As a result, the effect of the NO released from the soot is less pronounced on the densities of the other species (e.g., C_3H_6) as compared to the $\gamma_{27\text{-}0} = 0$ case. The densities of HCHO and CH_3CHO, which are produced by NO-βHAP reactions, are almost one order of magnitude smaller than in the case for $\gamma_{27\text{-}0} = 0$ for βHAP. The production of CO is commensurately smaller.

The surface of soot particles per unit volume is one of the key-parameters in the model. The average diameter of soot particles in diesel exhaust is usually 90-120 nm while the particle density can vary by orders of magnitude depending on the combustion regime or the type of engine.[12-14] The variation of the exit NO and NO_2 concentration as a function of particle density are shown in Fig. 4.12a for $\gamma_o(NO_2) = 0.1$. The increase of n_p leads to an increase of NO and a decrease of NO_2 due to the larger surface area available for NO_2 adsorption. The heterogeneous reaction chemistry becomes significant for $n_p > 5 \times 10^7$ cm^{-3}. NO becomes the major exit NO_x species when $n_p > 2 \times 10^8$ cm^{-3}. The NO density saturates for $n_p > 10^9$ cm^{-3} due to depletion of NO_2. Except for $n_p > 5 \times 10^9$ cm^{-3}, the increase of NO leads to a small increase in the remediation of NO_x and an increase of HNO_2. The higher production of HNO_2 is due to the increase of the densities of HO_2 and OH whose production is assisted by the $NO_2 \leftrightarrow NO$ exchange dynamics. The increase of NO results in higher rates of reactions with βHAPs (Eqs. 4.12 and 4.13). This ultimately results in the increase in the densities of HO_2, HCHO and CH_3CHO through the reaction pathways (4.12)-(4.14)-(4.15) and (4.13)-(4.16)-(4.17) as shown in Fig.

4.12b. The increase of NO and HO_2 leads to an increase in OH production (Eq. 4.11) which results in more propene consumption (Eqs. 4.7 and 4.8). The increase in total particle surface area increases the concentration of carbon monoxide by a factor of 2.2 for n_p=10^7 cm^{-3} to 10^9 cm^{-3}.

The results just discussed had $\gamma_{27\text{-}0}$ = 0 for βHAP. When $\gamma_{27\text{-}0}$ = 1 for βHAP, the results obtained are similar to those for $\gamma_0(NO_2)$ variation. In particular, the dynamics of the $NO_2 \leftrightarrow NO$ exchange slow down and there is no indirect effect of soot on the production of HO_2 and OH as observed for the $\gamma_{27\text{-}0}$ = 0 case.

The consequences of energy deposition by the plasma on the NO_x chemistry with and without soot are shown in Fig. 4.13. The peak O and OH densities increase linearly with increasing energy deposition. The increase in the production of these radicals increases the remediation of NO and NO_x. The decrease of NO with energy deposition is larger without soot particles due to the heterogeneous generation of NO with soot. Soot however, generally improves NO_x remediation. This is due to the conversion of NO to HNO_2 through the reaction with OH (Eq. 4.18). As energy deposition increases, the exit HCHO and CH_3CHO densities decrease, both with and without soot, as shown in Fig. 4.13b. This is due to the fact that with increasing energy more OH is generated which consumes more NO to form HNO_2. Thus the amount of NO reacting with βHAPs decreases and consequently, HCHO and CH_3CHO which are formed from the products of the reaction of βHAP with NO also decrease.

The energy required for converting a given amount of NO to NO_2 before performing a catalytic reduction strongly depends on the soot particle density and is shifted to higher values when n_p is increased. Plasma treatment cannot generally reduce

the NO concentration below a lower limit of ≈20-40 ppm if a large amount of soot is present in exhausts.

4.5 Concluding Remarks

Results from a computational investigation of NO_x plasma remediation were used to discuss the consequences of heterogeneous chemistry on soot particles. For particle densities typical of diesel exhausts, n_p =10^7-10^9 cm^{-3}, the heterogeneous chemistry maintains the dynamic NO density which ultimately enables a higher NO_x remediation rate. The heterogeneous reactions also increase the production of carbon monoxide, formaldehyde and acetaldehyde. When the particle density is greater than 10^8 cm^{-3}, there may also be additional remediation of UHCs such as propene.

The effects of soot on the NO_x reaction mechanism is summarized in Fig. 4.14. Soot influences the NO_x chemistry by changing the NO/NO_2 ratio in the plasma. By regenerating the NO from NO_2 and by indirectly leading to the increase of OH radicals (Eq. 4.11), soot increases the formation of HNO_2. This leads to an increased NO_x remediation. The increase in OH density also increases UHC consumption (Eqs. 4.7 and 4.8). The effect of soot strongly depends on the disposition of βHAP radicals on particles. If βHAP adsorb on the particles with high probability, the homogeneous chemistry is similar to that taking place without UHCs since these important intermediate radicals are consumed by the soot (or deactivated). The soot particles affect the NO_x chemistry mainly through the $NO_2 \rightarrow NO$ heterogeneous conversion. The effect of soot is much more complex in the case when the reactivity of βHAP radicals on the particles is small. In such a case, the combined effect of the heterogeneous NO_2 reactions and the

homogeneous reactions in Eqs. 4.12 and 4.13 are reflected in the production of HNO_2 (Eq. 4.18), formaldehyde [pathways (4.12)-(4.14)-(4.15) and (4.13)-(4.16)] and acetaldehyde [pathways (4.12)-(4.14) and (4.13)-(4.16)-(4.17)]. These dynamics also result in the remediation of UHCs and to the increase of CO in the exhaust.

The CO production is accompanied by a decrease in soot mass which, for most of the conditions discussed here, does not lead to a complete removal of soot particles. The soot particles also do not contain a significant amount of adsorbed NO_x for the desorption frequencies used in this work. Consequently, posttreatment of these particles would not lead to regeneration of NO_x. The presence of soot increases the amount of energy required for a given $NO \rightarrow NO_2$ conversion. For exhausts with high densities of soot particles, the variation of NO conversion with energy density shows a higher asymptotic value compared to the no soot case.

This work has clarified weakness in the database which should be addressed to more accurately investigate soot dynamics. In particular, a better description of the soot structure is necessary to more accurately model the surface reaction kinetics. The effect of the heterogeneous chemistry of water adsorption on soot particles should also be investigated, and the possible interactions between different adsorbates should be taken into account. The disposition of βHAP radicals on soot is a major issue which requires further investigation.

4.6 Figures

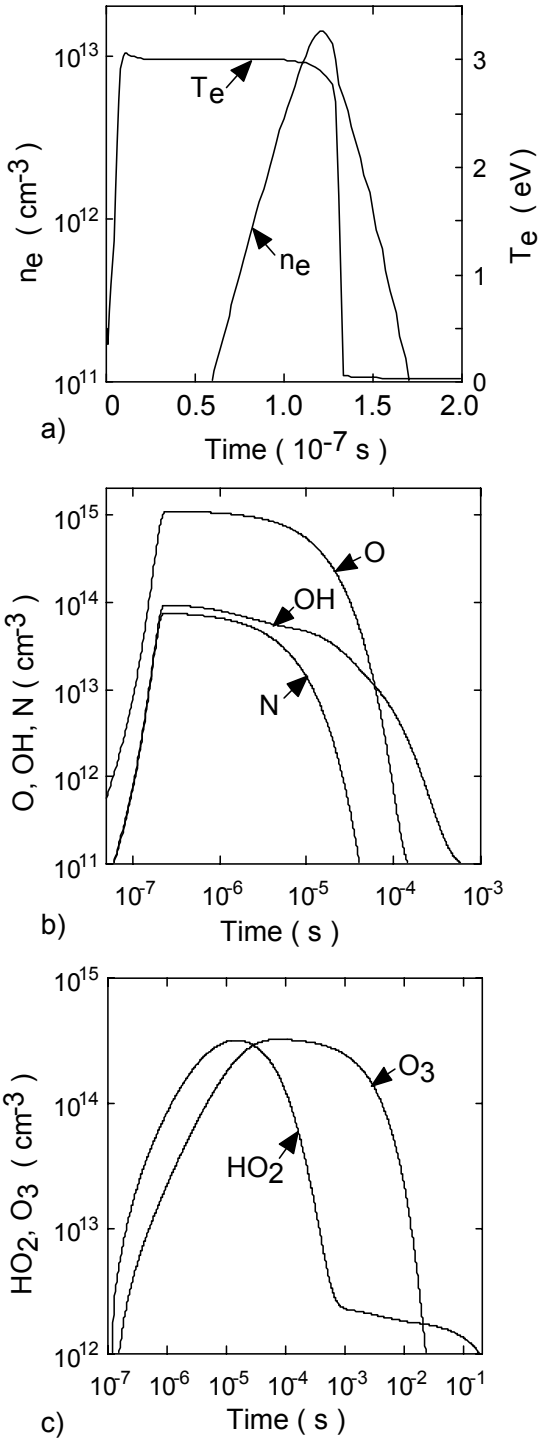

Fig. 4.1. Time evolution of plasma parameters and plasma chemistry initiating species. a) n_e and T_e. b) N, OH and O. c) HO_2 and O_3. Figures correspond to the base case conditions – Energy deposition of 38 J/L, initial gas mixture of $N_2/O_2/H_2O/CO_2$=79/6/8/7 with 400 ppm CO, 133 ppm H_2 and 260 ppm NO (1 atm, 453 K), soot particle number density of 10^8 cm^{-3} and diameter of 100 nm.

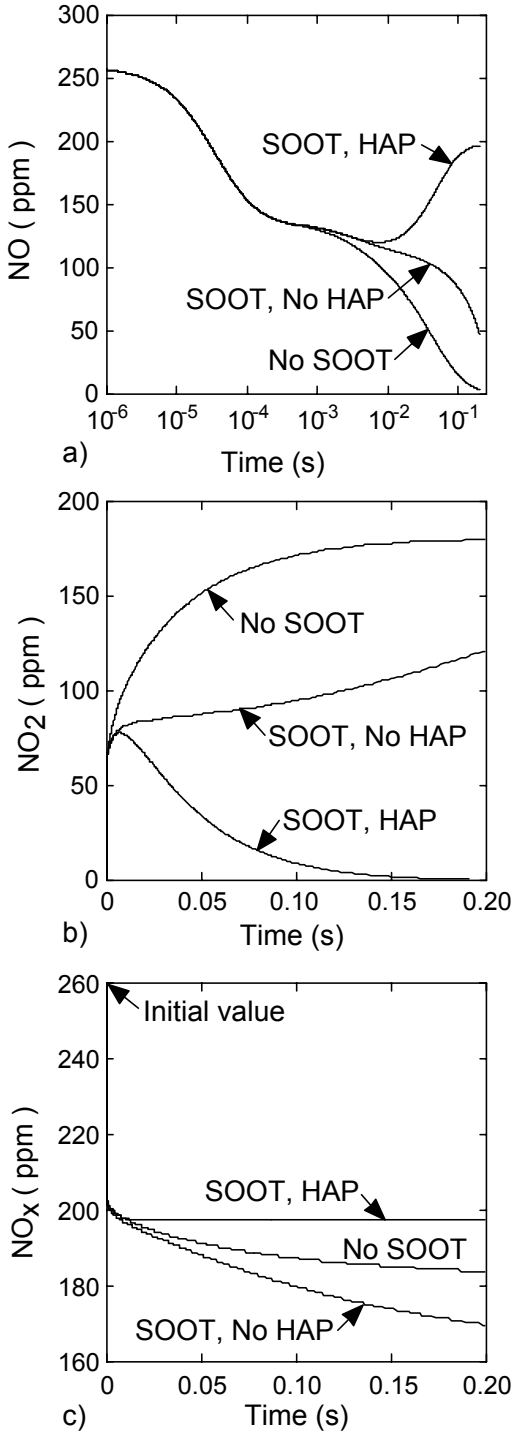

Fig. 4.2. Time evolution of NO_x species without soot (No SOOT), with soot (SOOT, No HAP) and with soot + βHAP deactivation on soot (SOOT, HAP). a) NO. b) NO_2. c) NO_x. The presence of soot improves NO_x remediation through the increased production of HNO_2. With βHAP deactivation on soot, the exit concentration of NO_x is higher compared to the no-soot case because of the decreased production of OH. Conditions are the same as for Fig. 4.1.

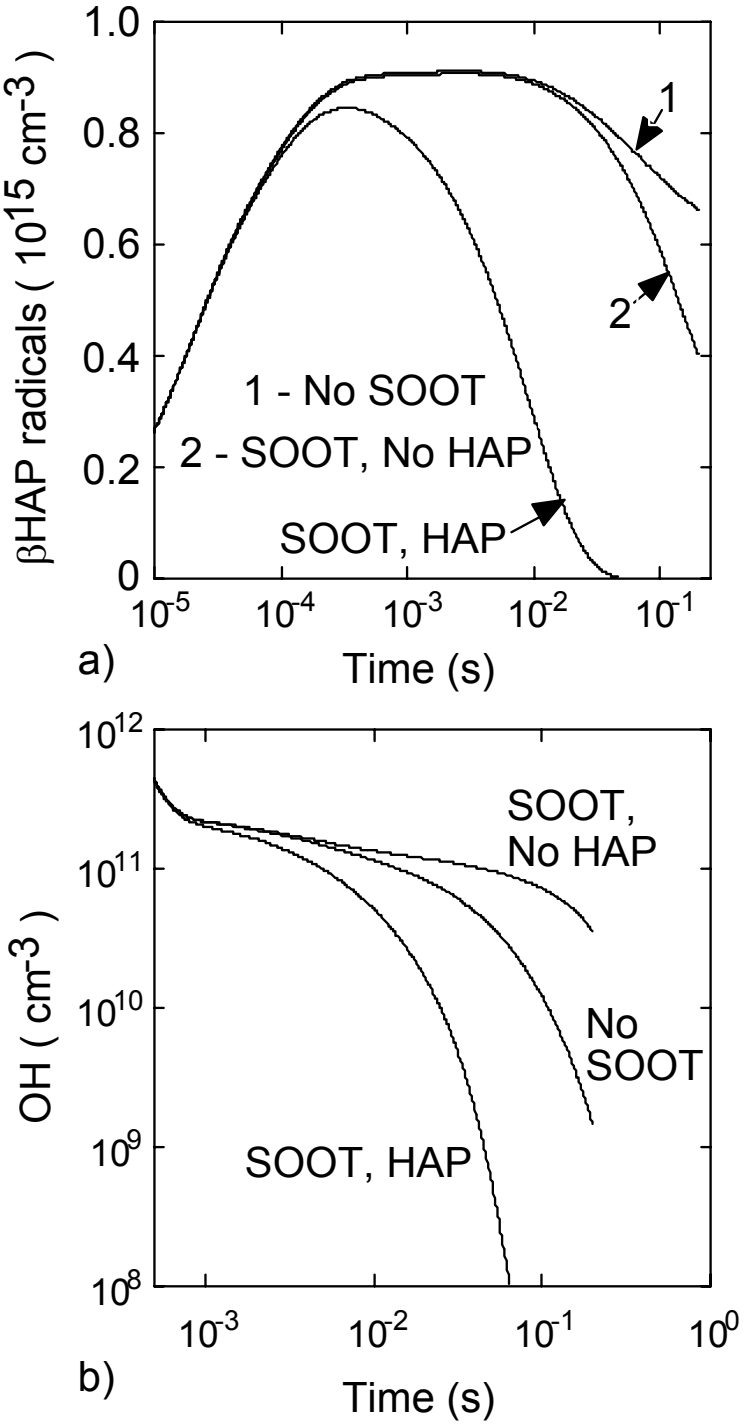

Fig. 4.3. Time evolution of radicals involved in NO remediation. a) βHAPs and b) OH for the cases without soot, with soot and with soot + βHAP deactivation. In the presence of soot and without βHAP deactivation, OH densities are higher and as a result aid in NO_x remediation through the formation of HNO_2. With βHAP deactivation, the rate of reactions in the NO_x-soot reaction cycle is decreased leading to a decreased production of OH. Conditions are the same as for Fig. 4.1.

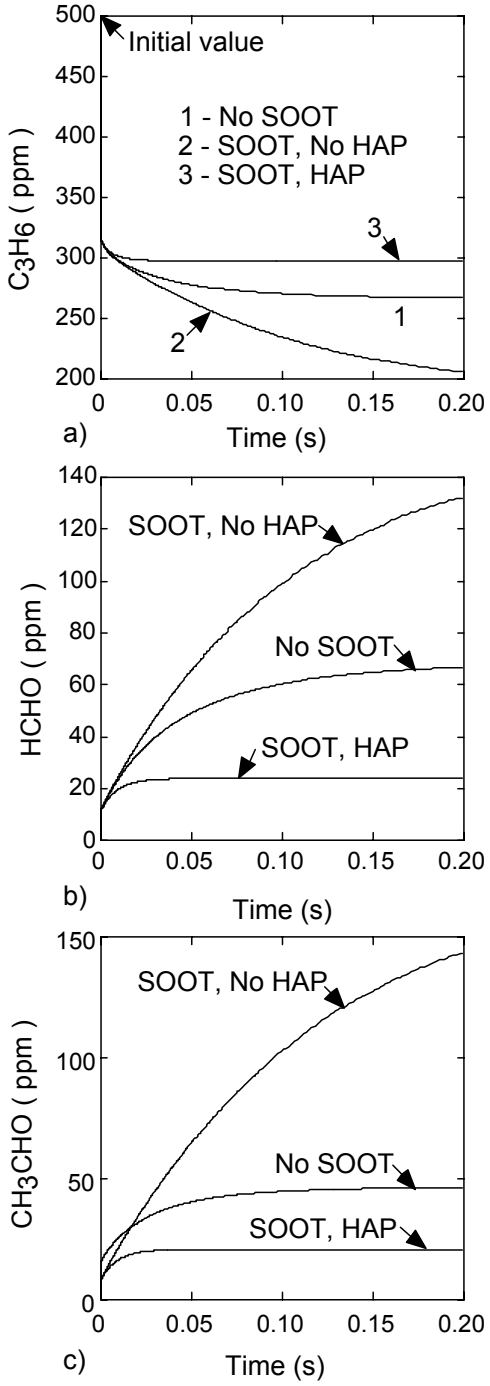

Fig. 4.4. Time evolution of UHCs and end-products of the remediation process. a) C_3H_6 b) HCHO and c) CH_3CHO for the cases without soot, with soot and with soot + βHAP deactivation. In the presence of soot and no βHAP deactivation, C_3H_6 concentrations are smaller due to the increased consumption by reactions with OH. This in turn, leads to increased production of HCHO and CH_3CHO, the final products of NO-βHAP reaction. With βHAP deactivation, OH production decreases leading to lesser C_3H_6 consumption and a lower production of HCHO and CH_3CHO. Conditions are the same as for Fig. 4.1.

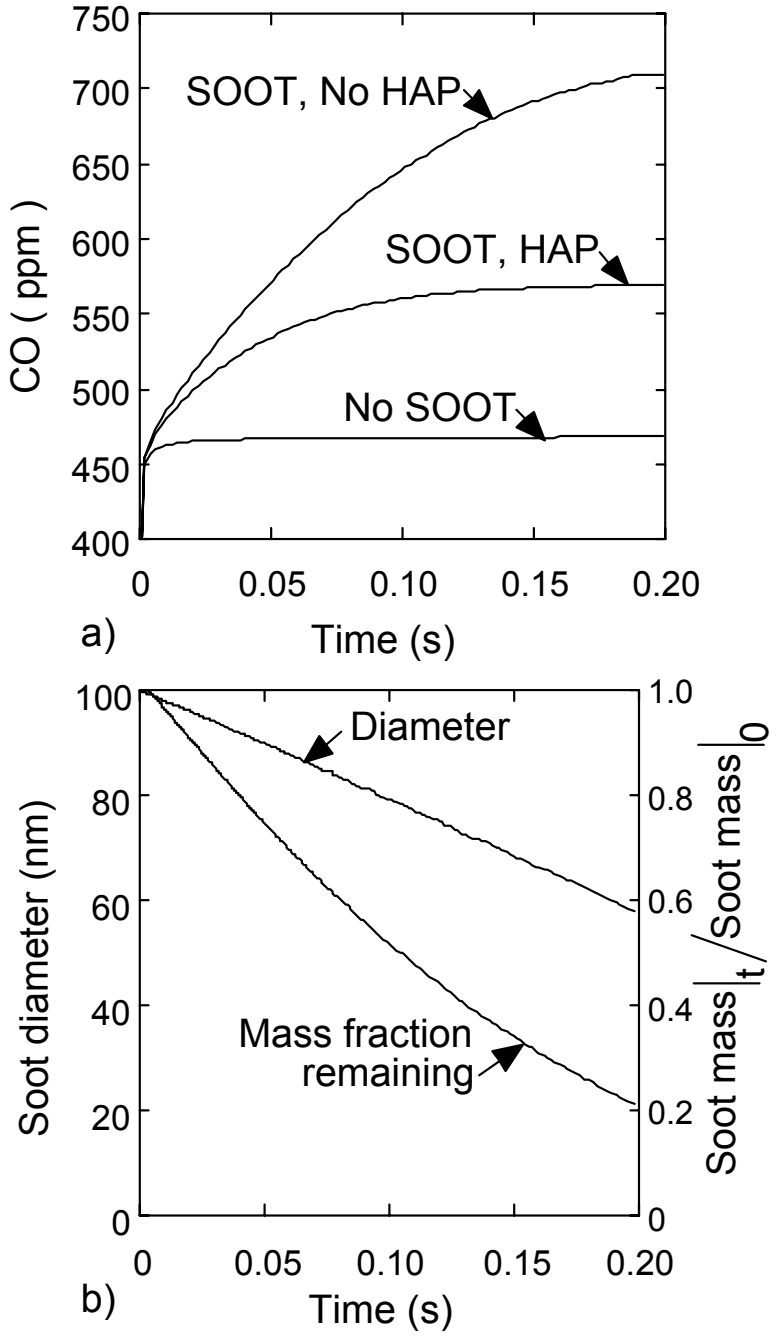

Fig. 4.5. Time variation of soot oxidation products and soot properties. a) CO production for the cases without soot, with soot and with soot + βHAP deactivation. b) soot diameter and fractional reduction in soot mass. Conditions are the same as for Fig. 4.1. In the presence of soot, more CO is produced due to the oxidation of soot by NO_2. With βHAP deactivation, less NO_2 is produced due to the heterogeneous loss of βHAP on soot. As a result, less CO is produced compared to the soot-no βHAP case. However, compared to the no-soot case, CO production is increased due to the additional heterogeneous CO source by NO_2 adsorption.

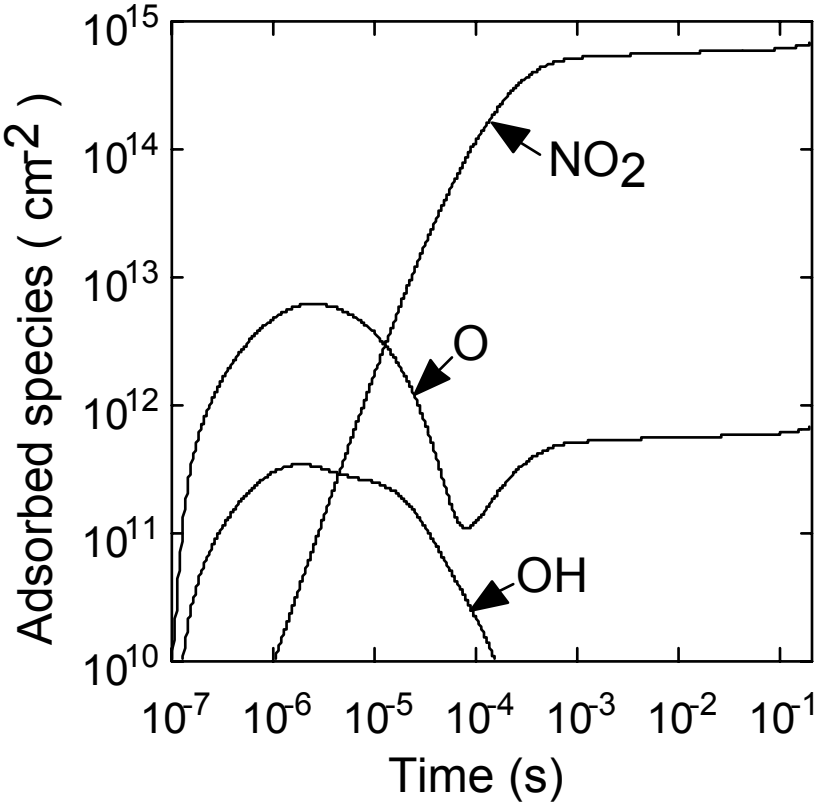

Fig. 4.6. Time evolution of the adsorbed species, O, OH and NO_2. Conditions are same as for Fig. 4.1.

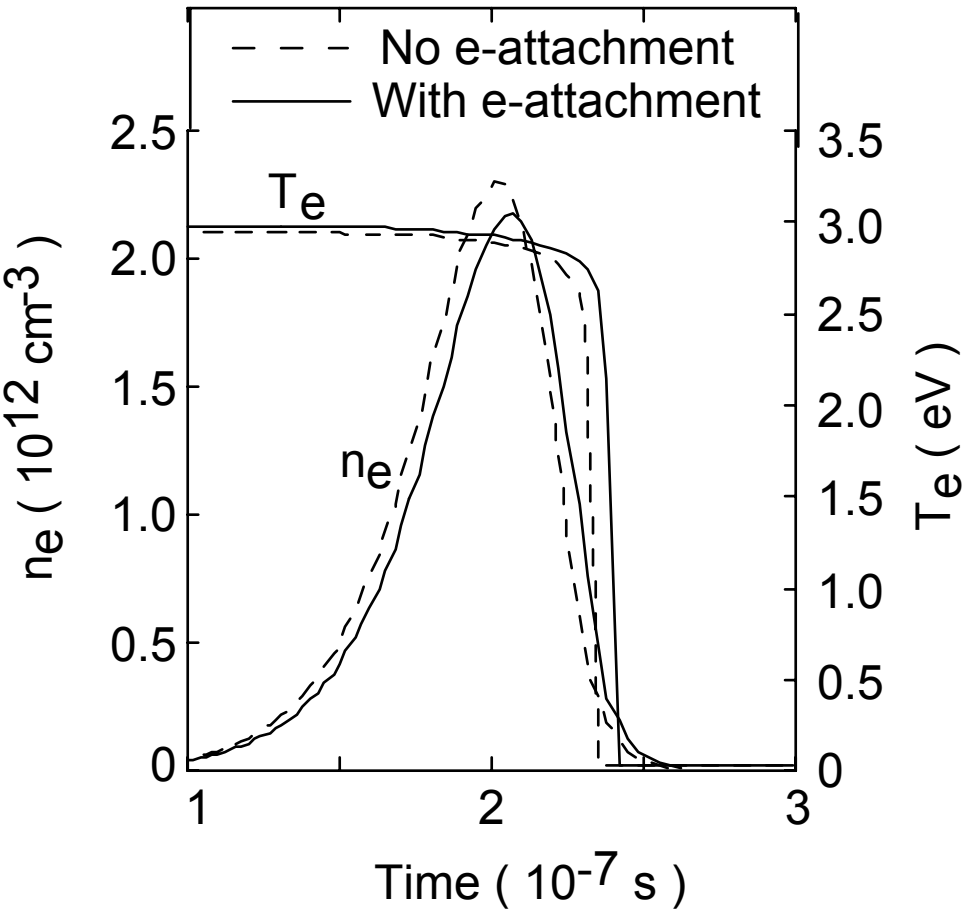

Fig. 4.7. Electron attachment to soot. n_e and T_e for a soot particle density of 10^9 cm^{-3} and an initial particle diameter of 150 nm. Other conditions are same as for Fig. 4.1. The electron temperature increases slightly in the presence of soot to increase ionization rates to account for losses to the soot.

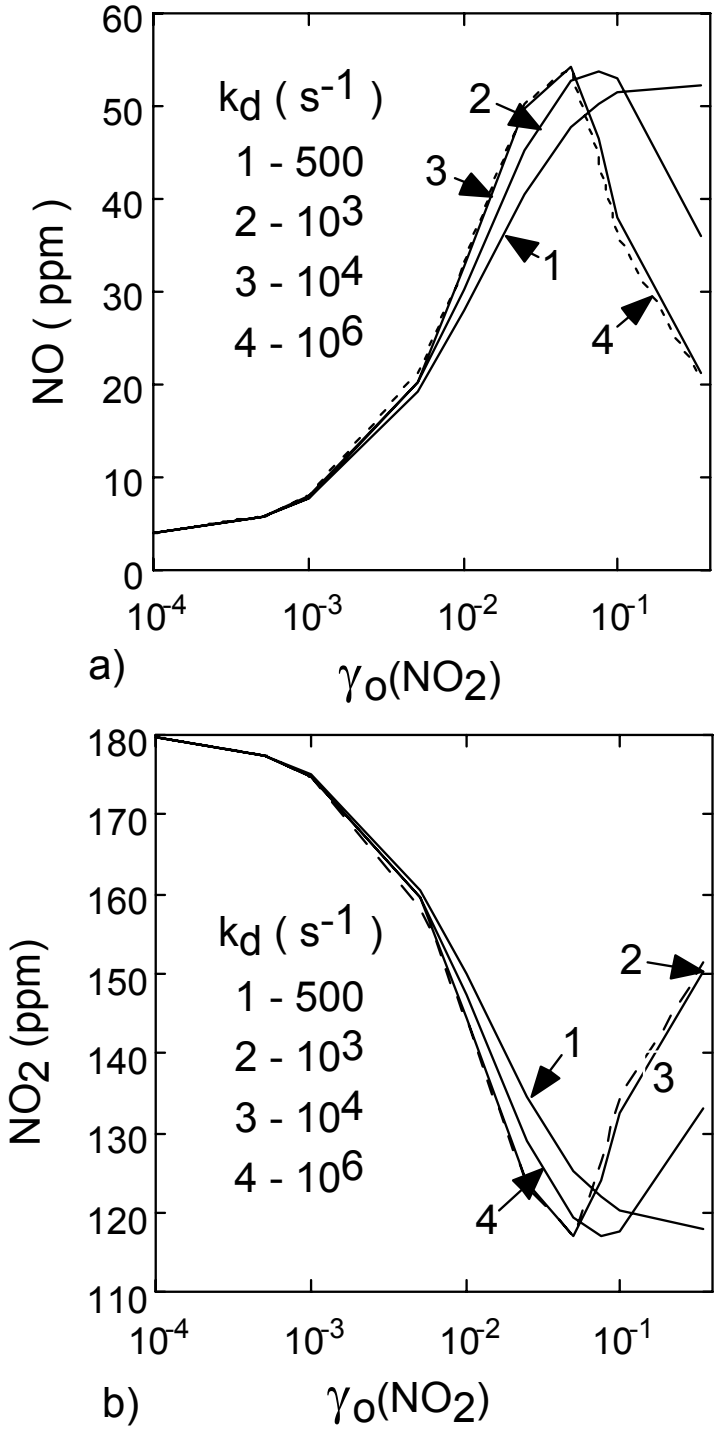

Fig. 4.8. Exit concentrations as a function of $\gamma_o(NO_2)$ for different values of $k_d(NO_2)$. a) NO. b) NO_2. Conditions are the same as for Fig. 4.1 with no βHAP deactivation.

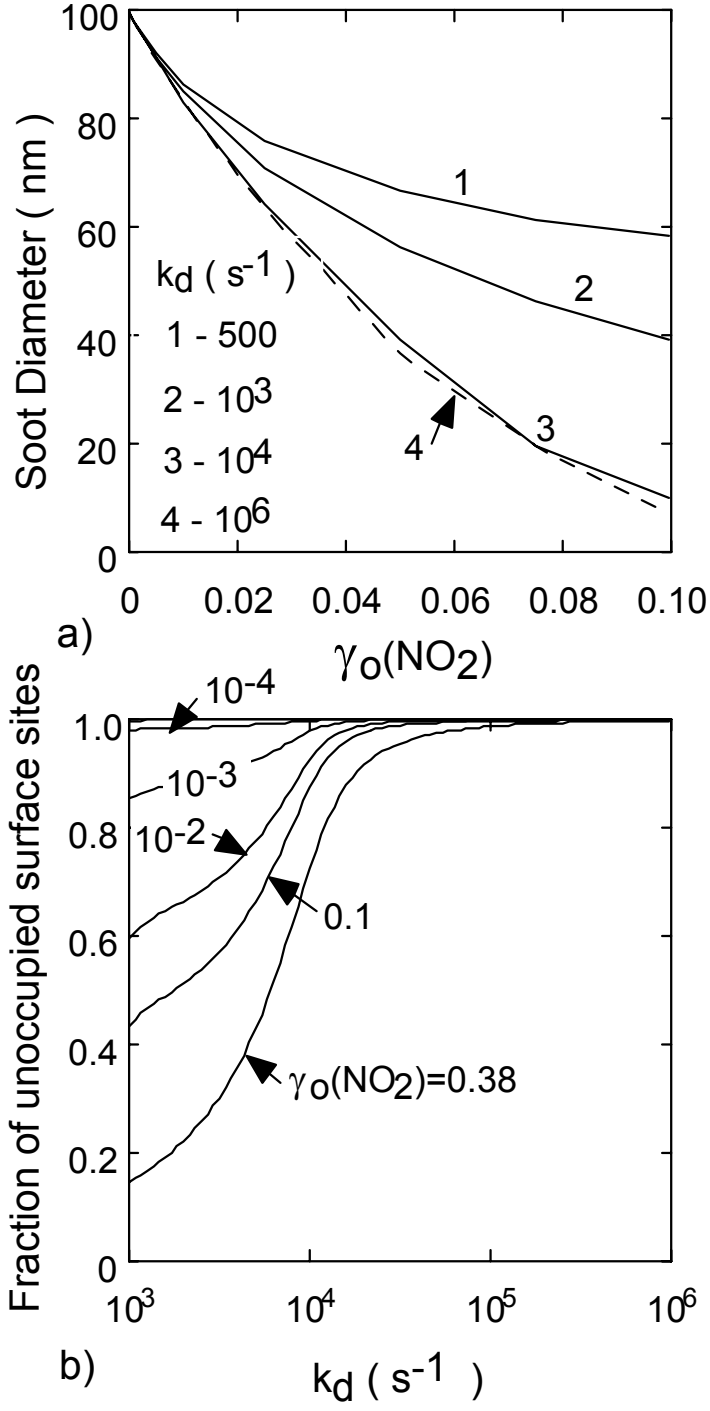

Fig. 4.9. Change in soot properties as a function of $\gamma_o(NO_2)$ and $k_d(NO_2)$. a) Soot diameter. b) Fraction of unoccupied surface sites.

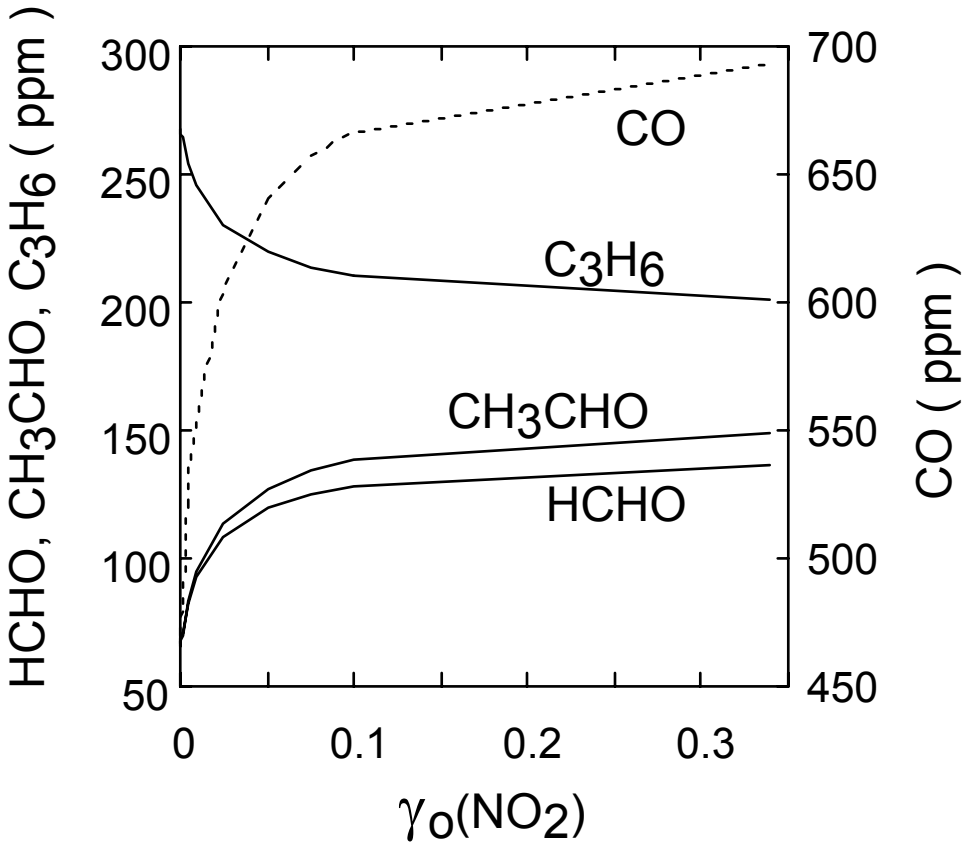

Fig. 4.10. Exit densities of HCHO, CH_3CHO, C_3H_6 and CO as a function of $\gamma_o(NO_2)$. With increasing adsorption probabilities of NO_2, the production of HCHO, CH_3CHO and CO increase and the consumption of C_3H_6 also increases due to the indirect increase in OH production.

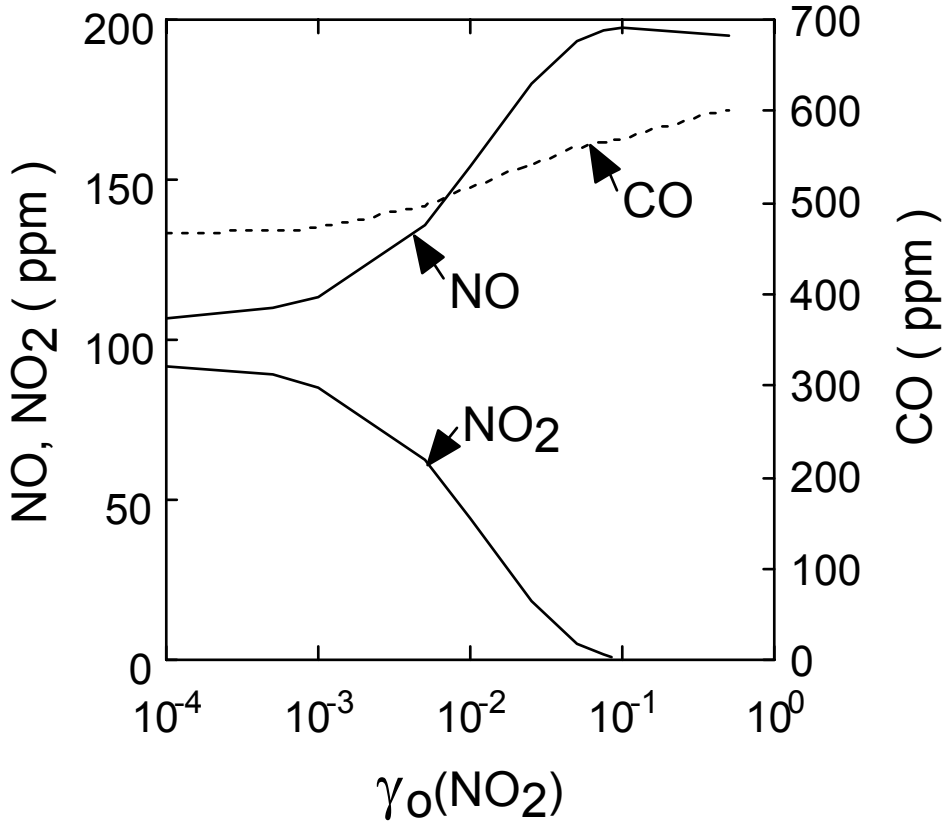

Fig. 4.11. Variation of NO, NO_2 and CO with $\gamma_o(NO_2)$ for full βHAP deactivation. As $\gamma_o(NO_2)$ increases, more NO_2 is adsorbed leading to an increased gas-phase concentration of NO. This also leads to an increased oxidation of soot resulting in increased CO production. Other conditions are the same as for Fig. 4.1.

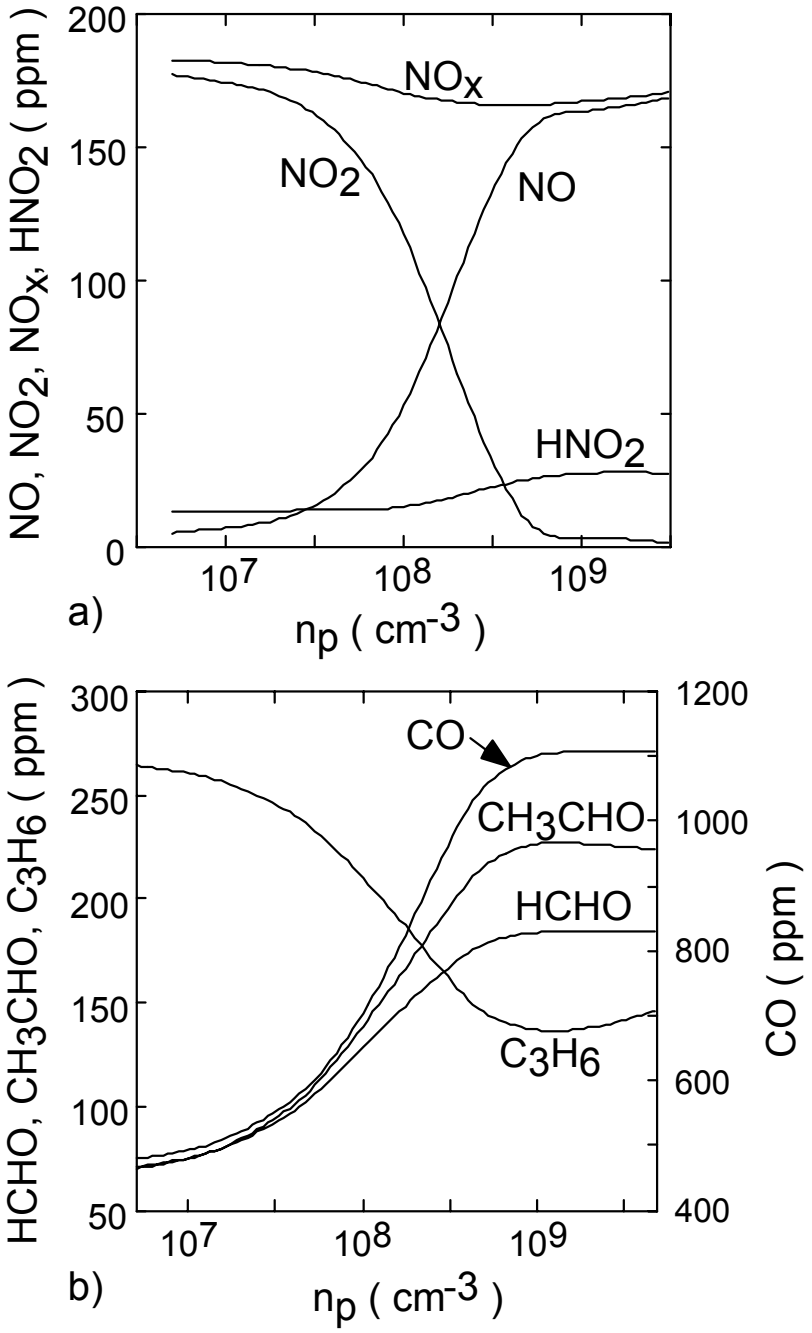

Fig. 4.12. Effect of soot particle number density on NO_x / $C_xH_yO_z$. a) NO, NO_2, NO_x and HNO_2. Increased soot number density increases the rate of heterogeneous $NO_2 \rightarrow$ NO conversion resulting in higher NO concentrations. NO_x densities decrease with n_p due to the increased production of HNO_2. b) HCHO, CH_3CHO, C_3H_6 and CO. Increasing n_p increases the surface area for heterogeneous reactions resulting in increased production of OH which increases the rate of reaction with C_3H_6. As a result more of HCHO and CH_3CHO are produced. CO increases due to the increased rate of soot oxidation.

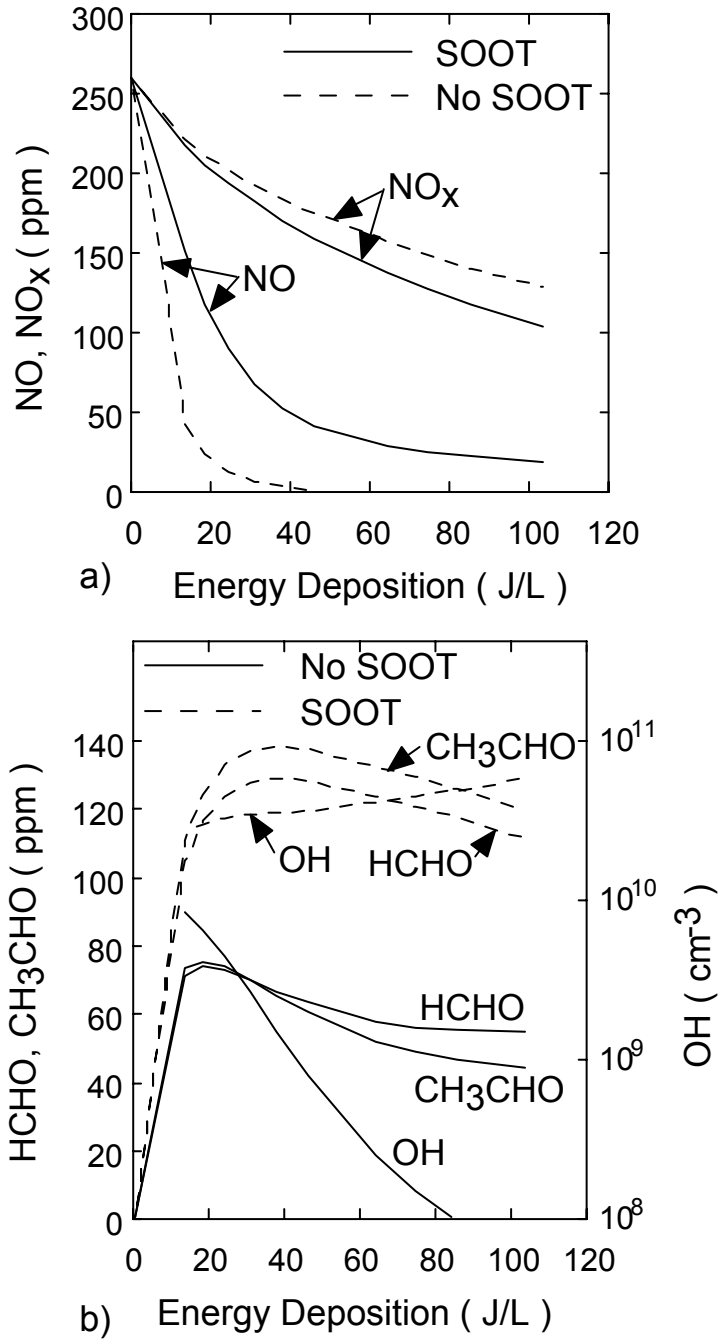

Fig. 4.13. Effect of energy deposition on NO_x / $C_xH_yO_z$. a) Exit concentrations of NO, NO_x with and without soot. NO_x remediation improves in the presence of soot due to the increased production of HNO_2. In the presence of soot NO is not completely remediated due to the heterogeneous back-conversion of NO_2 to NO. b) Exit concentrations of HCHO, CH_3CHO and OH with and without soot. With increasing energy deposition, more OH is produced due to the increased rates of the dissociation of H_2O. However, in the presence of soot, higher OH densities are sustained due to the increased production of HO_2.

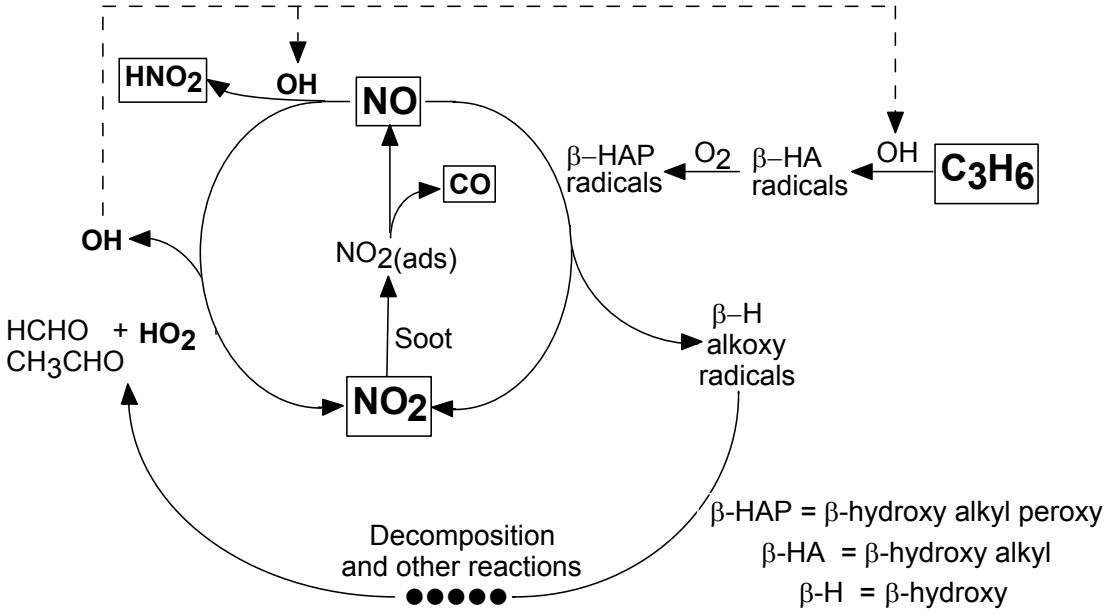

Fig. 4.14. Summary of the effects of soot on homogeneous NO_x chemistry. Heterogeneous reactions on soot surfaces result in higher NO densities in the gas-phase which increases the rates of the reactions with βHAPs. This leads to increased production of aldehydes and HO_2. HO_2 further reacts with NO by $HO_2 + NO \rightarrow NO_2 + OH$ to increase the production of OH. This increases the production of HNO_2 and the conversion of C_3H_6 thereby improving NO_x remediation and UHC consumption.

4.7 References

1. A. C. Gentile and M. J. Kushner, J. App. Phys. **78**, 2074 (1995).

2. R. Dorai and M. J. Kushner, J. Appl. Phys. **88**, 3739 (1999).

3. J. P. A. Neeft, T. Xander Nijhuis, E. Smakman, M. Makkee, and J. A. Moulijn, Fuel **76**, 1129 (1997).

4. A. Harano, M. Sadakata, and M. Sato, J. Chem. Eng. Japan **24**, 100 (1991).

5. T. Ngo, E. J. Sander, W. M. Tong, R. S. Williams, and M. S. Anderson, Surf. Sci. **314**, L817 (1994).

6. M. S. Akhter, A. R. Chughtai, and D. M. Smith, J. Phys. Chem. **88**, 5334 (1984).

7. A. R. Chughtai, W. F. Welch, and D. M. Smith, Carbon **28**, 411 (1990).

8. K. D. Tabor, L. Gutzviller, and M. J. Rossi, J. Phys. Chem. **98**, 6172 (1994).

9. M. Kalberer, K. Tabor, M. Ammann, Y. Parrat, E. Weingartner, D. Piguet, E. Rössler, D. T. Jost, A. Türler, H. W. Gäggeler, and U. Baltensperger, J. Phys. Chem. **100**, 15487 (1996).

10. B. Aumont, S. Madronich, M. Ammann, M. Kalberer, U. Baltensperger, D. Hauglustaine, and F. Brocheton, J. Geophys. Res. **104**, 1729 (1999).

11. D. M. Smith and A. R. Chughtai, Colloids Surf., A **105**, 47 (1995).

12. J. P. A. Neeft, M. Makkee, and J. A. Moulijn, Fuel Process. Technol., **47**, 1 (1996).

13. V. T. Kerminen, T. E. Makela, C. H. Ojanen, R. E. Hillamo, J. K. Vilhunen, L. Rantanen, N. Havers, A. Von Bohlen, and D. Klockow, Environ. Sci. Technol. **31**, 1883 (1997).

14. D. Kayes and S. Hochgreb, Environ. Sci.Technol. **33**, 3968 (1999).

5. REPETITIVELY PULSED PLASMA REMEDIATION OF NO_X IN SOOT LADEN EXHAUST

5.1 Introduction

In Chapter 3, we saw that interpulse chemistry significantly affects the plasma remediation of NO_x and in fact, was more efficient for NO_x remediation. We found that the interaction of products of previous pulses with the species during the current pulse allowed for a different chemistry in the repetitively pulsed case which ultimately improved remediation. In Chapter 4, we showed that soot particles significantly affect the NO_x chemistry during plasma remediation. In this chapter, we report on a computational investigation of the combined effects of repetitive discharge pulses and soot on NO_x remediation and soot oxidation. For this study, we used the modified version of GLOBAL_KIN as described in Section 2.3 to address the reaction kinetics on the soot surface. We investigated the consequences of varying energy deposition, inlet UHC concentration, soot diameter, and soot particle number density on NO_x remediation and soot oxidation for cases when using a single pulse and when using multiple pulses. Results for repetitively pulsed plasma processing of NO_x and oxidation of soot are discussed in Section 5.2. Concluding remarks are in Section 5.3.

5.2 Repetitively Pulsed Plasma Processing of NO_x and Oxidation of Soot

The base case operating conditions are 1 atm, 453 K, gas residence time of 0.2 s (space velocity of 18,000 hr^{-1}) and an electrode spacing of 0.25 cm. The gas mixture is $N_2/O_2/H_2O/CO_2$ = 79/8/6/7 with 260 ppm NO, 400 ppm CO, 133 ppm H_2, and 500 ppm C_3H_6. The reaction set used for this study is the same as that in Chapter 4. The soot

density and diameter are 10^8 cm^{-3} and 100 nm. The energy deposition is 30 J/l (10% fuel economy for a diesel engine [1]) which, for a single pulse, corresponds to a discharge voltage of 18 kV. To address repetitively pulsed discharges, 100 Hz here, the model is executed for a series of current pulses and afterglow periods (20 for the 0.2 s residence time). The initial conditions for a discharge pulse are given by the species densities at the end of the previous afterglow. To achieve the same energy deposition with repetitive pulses, the applied voltage is 13 kV. Although there are differences in excitation rates resulting from the different voltages, these differences do not prejudice any comparisons. When varying energy deposition, either the voltage or the permittivity of the dielectric was changed.

Electron density (n_e) and temperature (T_e) are shown in Fig. 5.1 for the base case conditions when using single and multiple pulses. The current pulse lasts approximately 145 ns for the single pulse case and approximately 165 ns for the multiple pulse case. The longer current pulse when using repetitive pulses is because of the slower avalanche resulting from the lower applied voltage. Electrons, accelerated by the electric field, collide with the background gases producing positive ions and secondary electrons, dominantly by,

$$e + N_2 \rightarrow N_2^+ + e + e, \tag{5.1}$$

$$e + O_2 \rightarrow O_2^+ + e + e, \tag{5.2}$$

$$e + H_2O \rightarrow H_2O^+ + e + e, \tag{5.3}$$

$$e + CO_2 \rightarrow CO_2^+ + e + e. \tag{5.4}$$

For a single discharge pulse, the peak electron density is $\approx 10^{13}$ cm^{-3} and the peak electron temperature is ≈3 eV. With repetitive pulses, less energy is deposited per pulse and, as a result, the peak electron density is $\approx 0.03 \times 10^{13}$ cm^{-3}, while the peak electron temperature is ≈3 eV. Since the current pulse is wider (165 ns) with repetitive pulses than with a single pulse (145 ns) the peak n_e at high pulse repetition frequency (PRF) is less than $1/20^{th}$ of the single pulse value. The time dependences of n_e and T_e for the first and last pulse of the repetitive pulse case do not differ appreciably because the mole fractions of the major background gases do not change significantly.

Although the chemistry of interest is dominantly through free-radical reactions, it is nevertheless instructive to also discuss the ion chemistry. Since the ion chemistry does not significantly differ between single and repetitive pulses due to the shorter time scales for ion reactions (100s of ns), we will discuss the ion chemistry for single pulses.

The initiating reactions for ion chemistry are electron impact ionizations producing N_2^+, O_2^+, H_2O^+, and CO_2^+ (Eqs. 5.1-5.4). Nearly 46% of the N_2^+ formed undergoes charge exchange reactions with H_2O to form H_2O^+,

$$N_2^+ + H_2O \rightarrow H_2O^+ + N_2, \qquad k = 2.0 \times 10^{-9}\ cm^3 s^{-1}\ [2], \qquad (5.5)$$

where k is the rate coefficient for the reaction. Most of the remaining N_2^+ (52%) dimerizes with N_2 to form N_4^+ which then charge exchanges with O_2 to form O_2^+,

$$N_2^+ + N_2 + M \rightarrow N_4^+ + M, \qquad k = 1.1 \times 10^{-29}\ cm^6 s^{-1}\ [3], \qquad (5.6)$$

$$N_4^+ + O_2 \rightarrow O_2^+ + N_2 + N_2, \qquad k = 2.5\times10^{-10}\ cm^3 s^{-1}\ [3]. \qquad (5.7)$$

O_2^+ is also formed by charge exchange reactions of H_2O^+ and CO_2^+ with O_2,

$$H_2O^+ + O_2 \rightarrow O_2^+ + H_2O, \qquad k = 4.3\times10^{-10}\ cm^3 s^{-1}\ [3], \qquad (5.8)$$

$$CO_2^+ + O_2 \rightarrow O_2^+ + CO_2, \qquad k = 5.6\times10^{-11}\ cm^3 s^{-1}\ [3]. \qquad (5.9)$$

About 66% of the CO_2^+ is consumed by the above reaction. The remainder is lost by charge neutralization reactions with O^- and H^-.

Almost all of the O_2^+ formed by the above reactions associates with H_2O to form $O_2^+ \cdot H_2O$, which further reacts with H_2O to form H_3O^+,

$$O_2^+ + H_2O + M \rightarrow O_2^+ \cdot H_2O + M, \qquad k = 2.5\times10^{-28}\ cm^6 s^{-1}\ [3], \qquad (5.10)$$

$$O_2^+ \cdot H_2O + H_2O \rightarrow H_3O^+ + OH + O_2, \quad k = 1.2\times10^{-9}\ cm^3 s^{-1}\ [3]. \qquad (5.11)$$

H_3O^+ is also formed from H_2O^+,

$$H_2O^+ + H_2O \rightarrow H_3O^+ + OH, \qquad k = 1.7\times10^{-9}\ cm^3 s^{-1}\ [3]. \qquad (5.12)$$

H_3O^+ reacts with H_2O to form the complex ion, $H_3O^+ \cdot H_2O$,

$$H_3O^+ + H_2O + M \rightarrow H_3O^+ \cdot H_2O + M, \qquad k = 5.0 \times 10^{-27}\ cm^6 s^{-1}\ [3]. \quad (5.13)$$

Electrons are dominantly lost by dissociative attachment to H_2O (73%), CO_2 (3%), and O_2 (24%) (both dissociative and nondissociative),

$$e + H_2O \rightarrow H^- + OH, \quad (5.14)$$

$$e + CO_2 \rightarrow O^- + CO, \quad (5.15)$$

$$e + O_2 \rightarrow O^- + O, \quad (5.16)$$

$$e + O_2 + M \rightarrow O_2^- + M. \quad (5.17)$$

The densities of $H_3O^+ \cdot H_2O$, N_4^+, O^- and H^- as a function of time are shown in Fig. 5.2. The rapid decay of N_4^+ is by reaction with O_2 forming O_2^+ (Eq. 5.7). O^- and H^- neutralize less rapidly by collisions with $H_3O^+ \cdot H_2O$ to produce H_2O, OH and H_2,

$$H_3O^+ \cdot H_2O + O^- \rightarrow H_2O + H_2O + OH, \qquad k = 3.0 \times 10^{-6}\ cm^3 s^{-1}\ [3], \quad (5.18)$$

$$H_3O^+ \cdot H_2O + H^- \rightarrow H_2O + H_2O + H_2, \qquad k = 3.0 \times 10^{-6}\ cm^3 s^{-1}\ [3]. \quad (5.19)$$

The free-radical reactions are initiated by the electron impact dissociation of the background gases producing N, O, OH, and H,

$$e + N_2 \rightarrow N + N + e, \quad (5.20)$$

$$e + O_2 \rightarrow O + O + e, \quad (5.21)$$

$$e + H_2O \rightarrow OH + H + e, \tag{5.22}$$

$$e + CO_2 \rightarrow O + CO + e. \tag{5.23}$$

The densities of N, O, OH and H as a function of time are shown in Fig. 5.3 for a single pulse, and for the first and the last pulse of the multiple pulse case. Recalling that the current pulse is ≈150 ns, the production of these primary radicals is dominantly from electron impact reactions. Reactions with neutral species then determine the disposition of this initial inventory of radicals. N atoms are dominantly consumed by reactions with NO, NO_2, CO_2 and O_2,

$$N + NO \rightarrow N_2 + O, \qquad k = 3.4\times10^{-11}\exp(-24/T)\ cm^3s^{-1},$$

$$k_{298} = 3.2\times10^{-11}\ cm^3s^{-1}\ [3], \tag{5.24}$$

$$N + NO_2 \rightarrow N_2O + O, \qquad k = 2.4\times10^{-12}\ cm^3s^{-1}\ [3], \tag{5.25}$$

$$N + NO_2 \rightarrow NO + NO, \qquad k = 9.9\times10^{-13}\ cm^3s^{-1}\ [3], \tag{5.26}$$

$$N + CO_2 \rightarrow CO + NO, \qquad k = 3.2\times10^{-13}\exp(-1710/T)\ cm^3s^{-1},$$

$$k_{298} = 1.0\times10^{-15}\ cm^3s^{-1}\ [4], \tag{5.27}$$

$$N + O_2 \rightarrow NO + O, \qquad k = 4.4\times10^{-12}\exp(-3220/T)\ cm^3s^{-1},$$

$$k_{298} = 7.7\times10^{-17}\ cm^3s^{-1}\ [5], \tag{5.28}$$

where k_{298} is the rate constant at 298 K. When using a single pulse, the contribution to N consumption from the reactions with NO, NO_2, CO_2 and O_2 (Eqs. 5.24-5.28) are 89.0%,

0.2%, 5.0% and 3.0% respectively. With repetitive pulses, the contributions are 63.0%, 14.0%, 14.0% and 8.0%. The higher contribution from NO_2 for N consumption with multiple pulses is a result of an increased overlap in time of the NO_2 and N atom densities. The density of NO, a major consumer of N atoms, decreases during later pulses (explained below). As a result, the N atom densities are sustained for longer periods during the latter pulses compared to the first pulse when using repetitive pulses.

With repetitive pulses, the peak O density is $\approx 10^{14}$ cm^{-3} in any given pulse as compared with 2×10^{15} cm^{-3} for a single pulse. The peak O atom densities for the first and last of 20 pulses, determined largely by electron impact, are similar because the density of O_2 remains nearly a constant. O atoms are primarily consumed by reactions with C_3H_6, NO_2 and O_2,

$$O + C_3H_6 \rightarrow \text{Methyl Oxirane}, \quad k = 1.2\times10^{-12}\ cm^3 s^{-1}\ [6], \tag{5.29}$$

$$\rightarrow C_2H_5CHO, \quad k = 1.2\times10^{-12}\ cm^3 s^{-1}\ [6], \tag{5.30}$$

$$\rightarrow CH_2CHO + CH_3, \quad k = 0.8\times10^{-12}\ cm^3 s^{-1}\ [6], \tag{5.31}$$

$$\rightarrow C_2H_5 + HCO, \quad k = 0.8\times10^{-12}\ cm^3 s^{-1}\ [6], \tag{5.32}$$

$$O + NO_2 \rightarrow NO + O_2, \quad k = 6.5\times10^{-12}\exp(120/T)\ cm^3 s^{-1},$$

$$k_{298} = 9.7\times10^{-12}\ cm^3 s^{-1}\ [5], \tag{5.33}$$

$$O + O_2 + M \rightarrow O_3 + M, \quad k = 3.4\times10^{-34}(T/298)^{-1.2}\ cm^6 s^{-1}\ [4]. \tag{5.34}$$

Using single pulses, the contributions of the reactions with C_3H_6, NO_2 and O_2 (Eqs. 5.29-5.34) towards O consumption are 56%, 4% and 11% respectively. When using repetitive pulses, the contributions are 56%, 25% and 12%. The larger contribution to O consumption by the reaction with NO_2 with multiple pulses is due to the increased overlap in time of NO_2 and O atom densities. The more rapid consumption of O in the first pulse is due to the higher densities of C_3H_6 during the first pulse compared to the last.

OH radicals are consumed primarily by reactions with C_3H_6 forming C_3H_6OH (hydroxy alkyl radicals), HCHO forming HCO, NO_2 forming HNO_3 and NO forming and HNO_2,

$$\mathrm{OH} + \mathrm{C_3H_6} \rightarrow 0.65\ \mathrm{CH_3CHCH_2OH} + 0.35\ \mathrm{CH_3CH(OH)CH_2}, \quad k = 4.9\times10^{-12}\exp(504/T)\ cm^3 s^{-1}, \quad k_{298} = 2.6\times10^{-11}\ cm^3 s^{-1}\ [6], \tag{5.35}$$

$$\mathrm{OH} + \mathrm{HCHO} \rightarrow \mathrm{HCO} + \mathrm{H_2O}, \quad k = 4.7\times10^{-12}(T/298)^{1.2}\exp(225/T)\ cm^6 s^{-1}, \quad k_{298} = 1.0\times10^{-11}\ cm^3 s^{-1}\ [7], \tag{5.36}$$

$$\mathrm{OH} + \mathrm{NO_2} + \mathrm{M} \rightarrow \mathrm{HNO_3} + \mathrm{M}, \quad k = 4.6\times10^{-29}(T/298)^{-5.5}\exp(-1183/T)\ cm^6 s^{-1}, \quad k_{298} = 8.7\times10^{-31}\ cm^6 s^{-1}\ [8], \tag{5.37}$$

$$\mathrm{OH} + \mathrm{NO} + \mathrm{M} \rightarrow \mathrm{HNO_2} + \mathrm{M}, \quad k = 8.6\times10^{-31}(T/298)^{-2.5}\exp(34/T)\ cm^6 s^{-1}, \quad k_{298} = 9.7\times10^{-31}\ cm^6 s^{-1}\ [8]. \tag{5.38}$$

The contributions of reactions of C_3H_6, HCHO, NO_2 and NO (Eqs. 5.35-5.38) to OH consumption are 66%, 5%, 7% and 4% when using a single pulse. With multiple pulses, the contributions are 72%, 11%, 10% and 4%. OH consumption is more rapid in the last pulse compared to the first due to increased rates of reactions with HCHO and NO_2 which have larger densities during the last pulse.

In the absence of UHCs, the radicals primarily responsible for the oxidation of NO to NO_2 in the gas phase are HO_2 and O_3. With UHCs, radicals such as $CH_3CH(OH)CH_2OO$ and $CH_3CH(OO)CH_2OH$ (β-hydroxy alkyl peroxies, in short βHAPs) are produced, which oxidize NO to NO_2. The reactions of HO_2, O_3 and βHAPs with NO produces NO_2, OH and O_2. Products also include $CH_3CH(OH)CH_2O$ and CH3CH(O)CH_2OH (β-hydroxy alkoxy radicals, in short βHAs),

$$\mathrm{NO} + \mathrm{CH_3CH(OH)CH_2OO} \rightarrow$$

$$\mathrm{NO_2} + \mathrm{CH_3CH(OH)CH_2O}, \qquad k = 2.7\times10^{-12}\exp(360/T)\,cm^3s^{-1},$$

$$k_{298} = 9.0\times10^{-12}\,cm^3s^{-1}\ [6], \tag{5.39}$$

$$\mathrm{NO} + \mathrm{CH_3CH(OO)CH_2OH} \rightarrow$$

$$\mathrm{NO_2} + \mathrm{CH3CH(O)CH_2OH}, \qquad k = 2.7\times10^{-12}\exp(360/T)\,cm^3s^{-1},$$

$$k = 9.0\times10^{-12}\,cm^3s^{-1}\ [6], \tag{5.40}$$

$$\mathrm{NO} + \mathrm{HO_2} \rightarrow \mathrm{NO_2} + \mathrm{OH}, \qquad k = 3.5\times10^{-12}\exp(240/T)\,cm^3s^{-1},$$

$$k_{298} = 7.8\times10^{-12}\,cm^3s^{-1}\ [6], \tag{5.41}$$

$$\mathrm{NO} + \mathrm{O_3} \rightarrow \mathrm{NO_2} + \mathrm{O_2}, \qquad k = 4.3\times10^{-12}\exp(-1598/T)\,cm^3s^{-1},$$

$$k_{298} = 2.1\times10^{-14}\ cm^3 s^{-1}\ [6]. \qquad (5.42)$$

The time dependence of the densities of the βHAPs, HO_2 and O_3 for a single pulse and for the first and the last pulse of the high PRF case are shown in Fig. 5.4. βHAPs are produced by the reaction of O_2 with hydroxy alkyl radicals (produced by the reaction in Eq. 5.35),

$$CH_3CHCH_2OH + O_2 \rightarrow CH_3CH(OO)CH_2OH, \quad k = 1.2\times10^{-11}\ cm^3 s^{-1}\ [6], \quad (5.43)$$

$$CH_3CH(OH)CH_2 + O_2 \rightarrow CH_3CH(OH)CH_2OO, \quad k = 3.8\times10^{-12}\ cm^3 s^{-1}\ [6], \quad (5.44)$$

and are mainly consumed reactions with NO to form NO_2 and βHA radicals. Further reactions of βHA radicals then result in the formation of HCHO, CH_3CHO and HO_2,

$$CH_3CH(OH)CH_2O \rightarrow CH_3CHOH + HCHO, \quad k = 7.9\times10^{13}\exp(-10517/T)\ s^{-1},$$

$$k_{298} = 3.7\times10^{-2}\ s^{-1}\ [4], \quad (5.45)$$

$$CH_3CHOH + O_2 \rightarrow CH_3CHO + HO_2, \quad k = 1.9\times10^{-11}\ cm^3 s^{-1}\ [9], \quad (5.46)$$

$$CH_3CH(O)CH_2OH \rightarrow CH_2OH + CH_3CHO, \quad k = 9.1\times10^{4}\ s^{-1}\ [4], \quad (5.47)$$

$$CH_2OH + O_2 \rightarrow HCHO + HO_2, \quad k = 2.0\times10^{-12}\ cm^3 s^{-1}\ [10]. \quad (5.48)$$

The peak βHAP radical density during the first pulse of 20 pulses is $\approx 2 \times 10^{13}$ cm^{-3}. The decrease in this peak density during the 20th pulse (to 1.5×10^{13} cm^{-3}) is primarily a result of the decrease in the density of C_3H_6, its precursor (discussed below).

The contributions of the reactions of O_2 with CH_3CHOH and CH_2OH (Eqs. 5.46 and 5.48) to the formation of HO_2 when using multiple pulses are 27% and 50% respectively. Other reactions which produce HO_2 include,

$$H + O_2 + M \rightarrow HO_2 + M, \qquad k = 1.8 \times 10^{-32} (T/298)^{-0.8}\ cm^6 s^{-1}\ [11], \tag{5.49}$$

$$HCO + O_2 \rightarrow HO_2 + CO, \qquad k = 2.0 \times 10^{-14} (T/298)^{2.4} \exp(768/T)\ cm^3 s^{-1},$$

$$k_{298} = 2.6 \times 10^{-13}\ cm^3 s^{-1}\ [4], \tag{5.50}$$

with their contributions being 2% (Eq. 5.49) and 21% (Eq. 5.50). With single pulses, the contributions to HO_2 production by O_2 reactions with CH_3CHOH, CH_2OH, H and HCO are 24%, 46%, 10% and 20%. The primary loss process for HO_2 radicals is the reaction with NO forming NO_2 and OH (Eq. 5.41).

O_3 is produced by the reaction of O with O_2 (Eq. 5.34) and is dominantly consumed by reaction with NO forming NO_2 (Eq. 5.42) and by reaction with $O_2(^1\Delta)$ forming O,

$$e + O_2 \rightarrow O_2(^1\Delta) + e, \tag{5.53}$$

$$O_3 + O_2(^1\Delta) \rightarrow O + O_2 + O_2, \qquad k = 5.2 \times 10^{-11} \exp(-2840/T)\, cm^3 s^{-1},$$

$$k_{298} = 3.8 \times 10^{-15}\ cm^3 s^{-1}\ [9]. \tag{5.54}$$

Due to the larger rate coefficients for reactions of NO with HO_2 and βHAP radicals compared to O_3, HO_2 and βHAP radicals are more rapidly consumed than ozone. As a consequence, the O_3 density accumulates pulse to pulse, as shown in Fig. 5.4c.

The densities of NO and NO_2 as a function of time with and without soot for a single pulse are shown in Fig. 5.5. Without soot NO is mainly consumed by reactions with βHAP radicals (34%), HO_2 (36%), CH_3O_2 (3%), and $C_2H_5O_2$ (6%) to produce NO_2 by the reactions in Eqs. 5.39-5.41. The reaction of NO with CH_3O_2 and $C_2H_5O_2$ are,

$$\mathrm{NO + CH_3O_2 \rightarrow NO_2 + CH_3O}, \qquad k = 4.2\times10^{-12}\exp(180/T)\,cm^3s^{-1},$$

$$k_{298} = 7.7\times10^{-12}\,cm^3s^{-1}\ [9], \qquad (5.55)$$

$$\mathrm{NO + C_2H_5O_2 \rightarrow NO_2 + C_2H_5O}, \qquad k = 3.1\times10^{-12}\exp(330/T)\,cm^3s^{-1},$$

$$k_{298} = 9.4\times10^{-12}\,cm^3s^{-1}\ [4]. \qquad (5.56)$$

CH_3O_2 and $C_2H_5O_2$ are formed by the reactions of CH_3 and C_2H_5 with O_2,

$$\mathrm{CH_3 + O_2 + M \rightarrow CH_3O_2 + M}, \qquad k = 4.4\times10^{-31}(T/298)^{-3}\,cm^6s^{-1}\ [4], \qquad (5.57)$$

$$\mathrm{C_2H_5 + O_2 + M \rightarrow C_2H_5O_2 + M}, \qquad k = 8.0\times10^{-26}(T/298)^{-8.2}\exp(-2150/T)\,cm^6s^{-1},$$

$$k_{298} = 5.0\times10^{-29}\,cm^6s^{-1}\ [12]. \qquad (5.58)$$

CH_3 and C_2H_5 are produced by the reactions of O atoms with C_3H_6 (Eqs. 5.31 and 5.32).

With soot particles, NO_2 undergoes heterogeneous reactions on their surface to form NO and CO,

$$NO_{2(g)} \rightarrow NO_{2(ads)}, \qquad \gamma_o(NO_2)=0.1 \text{ [13]}, \tag{5.59}$$

$$NO_{2(ads)} \rightarrow NO_{(g)} + CO_{(g)}, \qquad k = 10^3\ s^{-1} \text{ [14]}, \tag{5.60}$$

resulting in an increase in the NO density at later times.

The time dependences of the densities of NO and NO_2 with and without soot for multiple pulses are shown in Fig. 5.6a. Without soot, most of the NO is converted to NO_2 by reactions with βHAP radicals (42%), HO_2 (44%), O_3 (2%), CH_3O_2 (5%) and $C_2H_5O_2$ (2%) (Eqs. 5.39-5.42, 5.55, and 5.56). After the fifth pulse, the density of NO is less than that of NO_2. Since radicals such as N, O, OH, HO_2 and CH_3O are produced (Eqs. 5.20-5.22, 5.49, and 5.55) with every discharge pulse, the rate of reaction of these radicals with NO_2 increases relative to NO whose density decreases with each pulse. Without NO, the source of NO_2 removed and the density of NO_2 decreases with each pulse. The end products of the NO_2 conversion include NO (Eqs. 5.26 and 5.33), HNO_3 (Eq. 5.37), HNO_2 and CH_3ONO_2. HNO_2 is formed by the reaction of HO_2 with NO_2,

$$HO_2 + NO_2 \rightarrow HNO_2 + O_2, \qquad k = 1.2\times10^{-13}\ cm^3 s^{-1} \text{ [4]}. \tag{5.61}$$

CH_3ONO_2 is formed by the reaction of CH_3O with NO_2,

$$CH_3O + NO_2 \rightarrow CH_3ONO_2, \qquad k = 8.3\times10^{-12}\ cm^3 s^{-1} \text{ [4]}. \tag{5.62}$$

With multiple pulses and soot, NO densities are generally higher and NO_2 densities are generally lower than without soot because of the heterogeneous conversion of NO_2 to NO on the soot surface. In any given pulse, there are three distinct phases for the evolution of the NO density as shown in Fig. 5.6b for the 12^{th} pulse. In the first phase during the current pulse, there is a small and rapid production of NO from NO_2. In the second phase following the current pulse and lasting approximately 3 ms, the NO density decreases primarily due to gas phase reactions with βHAP radicals and HO_2 (Eqs. 5.39-5.41), resulting in conversion to NO_2. During the third phase, the NO density increases due to its heterogeneous production from the reaction of NO_2 with soot (Eqs. 5.59 and 5.60). For any given pulse, the gas phase consumption of NO is larger than its heterogeneous production, and so the NO density decreases. For pulses later than the 5^{th}, the density of NO_2 is greater than NO. As a result, immediately following the current pulse, there is a rapid decrease in the density of NO_2 and a corresponding increase in the NO density as shown in Figs. 5.7b and 5.7c. This is due to the conversion of NO_2 to NO by reactions with O and N atoms (Eqs. 5.26 and 5.33) which are produced by electron impact reactions (Eqs. 5.20 and 5.21).

Since the density of NO decreases with every pulse, the rates of reaction of NO with βHAP radicals, O_3 and HO_2 decrease with each pulse. As a result, the rates of consumption of βHAP radicals, O_3 and HO_2 decrease with each pulse and so their densities at the end of a pulse increase with time. These trends are shown in Fig. 5.7.

In Chapter 4, we showed that the surface densities of O and OH on the soot are at least two orders of magnitude smaller than that of NO_2 and hence do not significantly

influence the heterogeneous chemistry. The time dependencies of the fraction of sites occupied by NO_2 when using single and multiple pulses are shown in Fig. 5.8a. With a single pulse, most of the adsorbed NO_2 desorbs to NO and CO. However, after a residence time of 0.2 s a significant fraction (15%) of the sites on the soot surface are still occupied by NO_2. When using multiple pulses, due to the smaller rate of production of NO_2 during any given pulse compared to a single pulse, a smaller fraction of the sites are occupied by NO_2. However, due to the larger densities of NO_2 at later times when using multiple pulses (See Fig. 5.6a.), there is an increased flux of NO_2 to the soot. The end result is an increased rate of soot oxidation.

The mass fractions of soot remaining as a function of time are shown in Fig. 5.8b for single and multiple pulses. The initial rates of oxidation are higher with single pulses because of the larger flux of NO_2 to the soot resulting from the initially larger NO_2 densities in the gas phase. At later times, there is a larger flux of NO_2 to the soot with multiple pulses (compare Figs. 5.6 and 5.7a) and, as a result, more soot oxidation occurs. This higher flux results from the conversion of NO to NO_2 by βHAP radicals and HO_2 (Eqs. 5.39-5.41). The diameters of the soot particles as a function of time for single and multiple pulses are shown in Fig. 5.8c. As a result of oxidation the diameter of the soot particles decreases to approximately 58 nm at the end of 0.2 s with a single pulse while with repetitive pulses, the exit soot diameter is 38 nm.

To investigate the consequences of complete desorption of NO_2 from the soot, the residence time of the gas was increased to 3 s while keeping the energy deposition and the number of pulses a constant. To maintain the 20 pulse format, the repetition rate was decreased to 7 Hz. With a single pulse almost all of the NO_2 desorbs from the surface as

shown in Fig. 5.9a. Due to the smaller production of NO_2 per pulse with multiple pulses, less NO_2 is adsorbed during the early pulses as shown in Fig. 5.9b. However, due to the larger flux of NO_2 at later times, more soot is ultimately oxidized using multiple pulses. For example, the diameters of the soot as a function of time for the single and repetitive pulse cases (7 Hz) are shown in Fig. 5.9c. With multiple pulses the NO_2 densities are sustained for longer times and so almost complete soot oxidation occurs. With single pulses, most of the NO_x for times > 0.1 s is NO and so less soot oxidation occurs. The soot diameter decreases by only ≈55% for the same energy deposition.

Soot leads to circular chemistry involving interconversion between NO and NO_2, as shown in Fig. 5.10. In the absence of soot, the conversion of NO to NO_2 occurs by the reaction of NO with HO_2 which produces OH (Eq. 5.41) and by the reactions of NO with βHAP radicals which lead to HO_2 formation (Eqs. 5.39, 5.40, 5.45-5.48). The reaction of OH with C_3H_6 starts a chain reaction resulting in the formation of βHAP radicals (Eqs. 5.35, 5.43, and 5.44). Thus, the reaction of HO_2 with NO leads to the formation of βHAP radicals and that of βHAPs with NO produces HO_2. The products of the gas phase reactions converting NO to NO_2 are reactants for further NO to NO_2 conversion. With soot, heterogeneous conversion of NO_2 produces NO and as a result NO densities are sustained for longer periods of time. This leads to increased rates for the conversion of NO to NO_2 in the gas phase and a prolonged production of OH, HO_2 and βHAP radicals.

Due to the larger production of OH with soot more C_3H_6 is consumed (Eq. 5.35), as shown in Fig. 5.11a. Soot does not significantly affect C_3H_6 consumption when using single pulses as the heterogeneous conversion of NO_2 to NO occurs on time scales > 1 ms by which time most of the radicals required for the conversion of NO to NO_2 have been

consumed. As a result, the circular chemistry is less efficient. NO oxidizing radicals (for example, HO_2, O_3 and βHAP radicals) are produced during each pulse of the repetitive pulse case and so there is an increased overlap in time of the densities of NO and the oxidizing species. There is also a higher density of NO with soot. The combined effect of multiple pulses and soot is production of more OH (by the circular chemistry) which then results in increased consumption of C_3H_6, as shown in Figs. 5.12b and 5.12c.

In order to track the large dynamic ranges in densities of radicals over large dynamic ranges in time, the densities have to this point to be expressed in cm^{-3}. However, it is typical for measures of remediation to be expressed in ppmv (parts per million by volume) or simply ppm for comparison with the emission standards expressed in such units. These units will be used in the following discussion. For the operating conditions of interest (1 atm, 453 K), 1 ppm = 1.62×10^{13} cm^{-3} (initial NO density = 260 ppm = 4.2×10^{15} cm^{-3}).

Increasing energy deposition with single pulses results in increased NO conversion, as shown in Fig. 5.12a. (Energy deposition was varied by changing the applied voltage.) At 60 J/l, NO densities decrease to approximately 125 ppm resulting in an NO conversion of 52%. This higher rate of NO consumption at larger energy deposition is primarily due to the chain chemistry producing N_2 and HNO_2 by the reactions in Eqs. 5.24 and 5.38. At higher energy deposition, there is also an increased production of O atoms which generates more CH_3 and C_2H_5 by reactions with C_3H_6 (Eqs. 5.31 and 5.32). This results in increased formation of CH_3O and C_2H_5O (Eqs. 5.55 and 5.56), which then consume NO by

$$CH_3O + NO \rightarrow CH_3ONO, \qquad k = 2.0\times10^{-11}\ cm^3 s^{-1}\ [4], \qquad (5.63)$$

$$C_2H_5O + NO \rightarrow C_2H_5ONO, \qquad k = 2.0\times10^{-11}\ cm^3 s^{-1}\ [4]. \qquad (5.64)$$

The exit composition of NO_x is primarily NO because of the heterogeneous conversion of NO_2 to NO on the soot (Eqs. 5.59 and 5.60). The fraction of sites on the soot occupied by NO_2 is maximum at approximately 0.15 when the NO_2 density peaks and subsequently decreases as the NO_2 flux decreases at higher energy deposition. This decrease in NO_2 density is largely a result of reactions with radicals such as OH, HO_2, and CH_3O to produce HNO_3, HNO_2, and CH_3ONO_2 (Eqs. 5.37, 5.61, and 5.62). The decrease is also attributable to reactions of NO_2 with $C_2H_5O_2$ to form $C_2H_5OONO_2$,

$$C_2H_5O_2 + NO_2 \rightarrow C_2H_5OONO_2, \quad k = 2.6\times10^{-10}(T/298)^{-3.7}\exp(-1029/T)\ cm^3 s^{-1},$$
$$k_{298} = 8.2\times10^{-12}\ cm^3 s^{-1}\ [4]. \qquad (5.65)$$

With increasing energy deposition with repetitive pulses, HO_2, O_3 and βHAP radicals are produced on every pulse and so the heterogeneously generated NO is more effectively converted to NO_2. As a result, NO densities decrease more rapidly with energy deposition, as shown in Fig. 5.12b. The reactions responsible for the decrease in the NO_2 density with energy deposition are similar to those for a single pulse, however the decrease is more pronounced because of the increased overlap in time of NO_2 and OH, CH_3O, $C_2H_5O_2$ and HO_2 densities following each pulse. The fraction of sites

occupied by adsorbed NO_2 is in general larger with multiple pulses due to the larger NO_2 density.

The *W*-values for NO_x with single and multiple pulses are shown in Fig. 5.12c. In general repetitive pulses are more efficient (lower *W*-value) compared to single pulses. At the base case energy of 30 J/l, the W-value for NO_x for a single pulse is 152 eV and for multiple pulses is 120 eV. The increase in efficiency is primarily a result of increased conversion of NO_2 to HNO_3, CH_3ONO_2, $C_2H_5OONO_2$ and HNO_2. The densities of these nitrogen-containing products, shown in Fig. 5.13, are higher for multiple pulses as a result of the increased overlap in time of the densities of NO_2 and the participating radical species (for example, OH, CH_3O, $C_2H_5O_2$ and HO_2). At 60 J/l, approximately 70 ppm of HNO_2 is produced using repetitive pulses whereas only 35 ppm is formed using single pulses. At the same energy deposition, repetitive multiple pulses produce approximately 40 ppm of organic nitrates ($C_2H_5OONO_2$ and CH_3ONO_2) while with single pulses only 10 ppm are produced.

Important hydrocarbon products of C_3H_6 dissociation include aldehydes such as HCHO and CH_3CHO. The exit densities of HCHO and CH_3CHO as a function of energy deposition are shown in Fig. 5.13c. HCHO and CH_3CHO are produced from the reactions of the βHA radicals (Eqs. 5.45-5.48). More C_3H_6 is consumed (see Fig. 5.10) with repetitive pulses leading to an increased production of βHAP radicals (Eqs. 5.35, 5.43, and 5.44). This results in increased formation of βHA radicals (Eqs. 5.39 and 5.40) which are the precursors to HCHO and CH_3CHO production (Eqs. 5.45-5.48). The HCHO density decreases at higher energy depositions owing to consumption by reaction with OH (Eq. 5.36).

The mass fractions of soot remaining as a function of energy deposition for single and repetitive pulses are shown in Fig. 5.14a. At energy depositions > 20 J/l, the NO_2 density in the gas phase for single pulses decreases because of increased NO_2 consumption by the reactions in Eqs. 5.37, 5.61, 5.62, and 5.65. As a result, a smaller amount of soot is oxidized at higher energies. The larger NO_2 densities obtained with increasing energy deposition with repetitive pulses result in higher rates of adsorption on the soot. Consequently, more soot is oxidized. The *W*-values for soot removal (J/μg) are shown as a function of energy deposition in Fig. 5.14b. Using multiples pulse in general results in more efficient soot removal due to the sustained densities of NO_2 which oxidize the soot. The *W*-value for soot at 30 J/l is about 0.3 J/μg for multiple pulses and 0.5 J/μg for single pulses.

CO is an end product not only of soot oxidation (Eq. 5.60) but also of gas phase reactions such as the electron impact dissociation of CO_2 (Eq. 5.23) and the reaction of HCO with O_2,

$$\text{HCO} + \text{O}_2 \rightarrow \text{CO} + \text{HO}_2, \qquad k = 2.0\times10^{-14}(T/298)^{2.4}\exp(768/T)\ cm^3 s^{-1},$$

$$k = 2.6\times10^{-13}\ cm^3 s^{-1}\ [4]. \tag{5.66}$$

HCO is formed by the reactions of O with C_3H_6 (Eq. 5.32) and OH with HCHO (Eq. 5.36). CO exit densities as a function of energy deposition are shown in Fig. 5.14c. Increasing energy deposition leads to increased rates of CO_2 dissociation and HCO formation (due to higher O and OH production) resulting in higher CO densities. Larger

densities of HCO are generated with repetitive pulses due to the larger production of OH. These larger densities also result in increased CO formation (Eq. 5.66).

Due to the variations in the composition of diesel fuel, the UHC concentration in exhaust gas can fluctuate. To this end, we investigated the sensitivity of NO_x removal to the inlet UHC concentration when using multiple pulses. All other conditions are the same as the base case. The removal of NO_x improves with increasing C_3H_6, as shown in Fig. 5.15. This trend is a result of increased nitrate and HNO_x formation by the reactions in Eqs. 5.37, 5.61-5.65. For example, the increasing densities of HNO_2 with increasing C_3H_6 are also shown in Fig. 5.15. Increased production of OH and HO_2 occur with soot by increased cyclic conversion between NO and NO_2 resulting in larger rates of HNO_2 formation (Eqs. 5.38 and 5.61).

The effects of soot particle number density and diameter on NO_x remediation were investigated. Increasing either the diameter of the soot or its number density results in increased exit densities of NO when using single pulses, as shown in Fig. 5.16a. The increase in NO is a result of the heterogeneous conversion of NO_2 to NO following the larger surface area of the soot. At small soot diameters and soot densities (40 nm, 10^7 cm^{-3}), negligible heterogeneous conversion of NO_2 to NO occurs and so most of the NO_2 produced in the gas phase exits the reactor. At large soot diameters and soot densities (200 nm, 10^9 cm^{-3}) most of the NO_2 is converted to NO by heterogeneous reactions. Heterogeneous reactions occur on a time scale of ~10s of ms at which time most of the radicals which convert NO to NO_2 (for example, βHAPs, HO_2 and O_3) have been consumed. As a result, the exit composition of NO_x is primarily NO. Since the

heterogeneous NO_x reactions result in only the conversion of NO_2 to NO, the total NO_x density remains nearly a constant, as shown in Fig. 5.16b.

The densities of NO and NO_x as a function of soot density and diameter for repetitive pulses are shown in Fig. 5.17. The production of NO consuming radicals during each pulse (see Fig. 5.7) results in the gas phase conversion of NO to NO_2. As a result the NO densities are smaller compared to using a single pulse. At either small soot densities and large diameters, or at large soot densities and small diameters, the homogeneous conversion of NO to NO_2 dominates the heterogeneous conversion of NO_2 to NO and so most of the NO_x is NO_2. However, at large soot densities and large diameters (10^9 cm^{-3}, 200 nm), the rates for the heterogeneous conversion of NO_2 to NO exceed the rates for the homogeneous conversion of NO to NO_2 and so the exit composition of NO_x is dominantly NO. The homogeneous and heterogeneous processes involving NO and NO_2 result mainly in their interconversion and so the total NO_x density almost remains unaffected. The smaller NO_x density with multiple pulses is due to the increased rates of reactions of NO and NO_2 with radicals such as CH_3O (Eqs. 5.62 and 5.63), C_2H_5O (Eq. 5.64), $C_2H_5O_2$ (Eq. 5.65), OH (Eqs. 5.37 and 5.38) and HO_2 (Eq. 5.61), producing CH_3ONO_2, CH_3ONO, C_2H_5ONO, $C_2H_5ONO_2$, HNO_2 and HNO_3. The increased rates are a result of the increased overlap in time of the densities of NO and NO_2 with the radical densities.

5.3 Concluding Remarks

The effects of repetitive pulses and soot chemistry on the plasma remediation of NO_x using dielectric barrier discharges were investigated. In the absence of soot, using

repetitive pulses resulted in higher conversion of NO to NO_2 compared to using a single pulse case. Single pulses with soot result in an initial gas phase oxidation of NO to NO_2, followed by a heterogeneous conversion of NO_2 to NO on the soot. Due to the larger gas phase NO_2 density using repetitive pulses, there is an increased flux of NO_2 to the soot surface, resulting in increased soot oxidation and larger rates of heterogeneous conversion of NO_2 to NO. At 30 J/l, using single pulses with and without soot produced about 30% NO_x removal. The final NO_x was primarily NO_2 (almost 100%) in the absence of soot whereas with soot the NO_x was 88% NO and 12% NO_2. When using multiple pulses, 30 J/l resulted in 35% NO_x removal in the absence of soot and 37% with soot. The *W*-value for soot oxidation at 30 J/l improved from 0.5 J/μg with a single pulse to 0.3 J/μg with multiple pulses. The combined effects of multiple pulses and heterogeneous chemistry on NO_x remediation and soot oxidation are twofold. Improved NO_x removal by the increased production of HNO_2, HNO_3, organic nitrates and nitrites due to the more favorable overlap in time of NO_2 and reactive radical densities; and increased soot oxidation because of larger NO_2 densities.

5.4 Figures

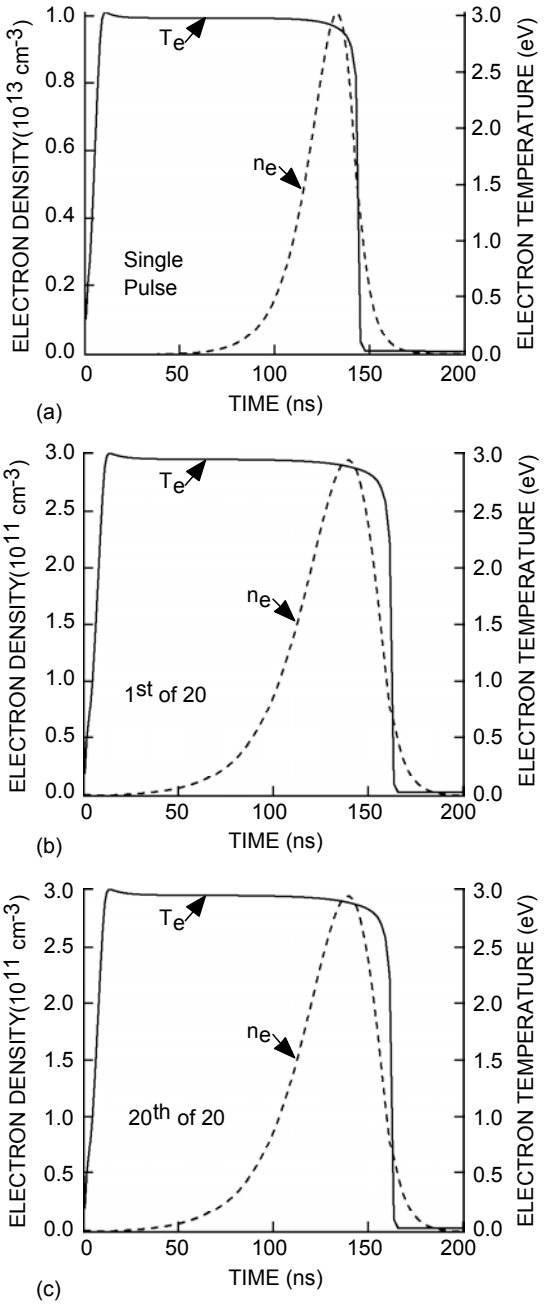

Fig 5.1. Plasma parameters for single and repetitive pulses. a) n_e, T_e for a single pulse. b) n_e, T_e during the 1st pulse of 20 pulses. c) n_e, T_e for the last pulse of 20 pulses. Conditions are 1 atm, 453 K, $N_2/O_2/H_2O/CO_2$ = 79/8/6/7 with 260 ppm NO, 400 ppm CO, 133 ppm H_2, and 500 ppm C_3H_6. Gas residence time is 0.2 s and the gas gap is 2.5 mm. The applied voltage for the single pulse case is 18 kV and that for 20 pulses is 13 kV for total energy deposition of 30 J/l. Following the current pulse (around 150 ns), electrons are lost primarily by attachment to H_2O and O_2.

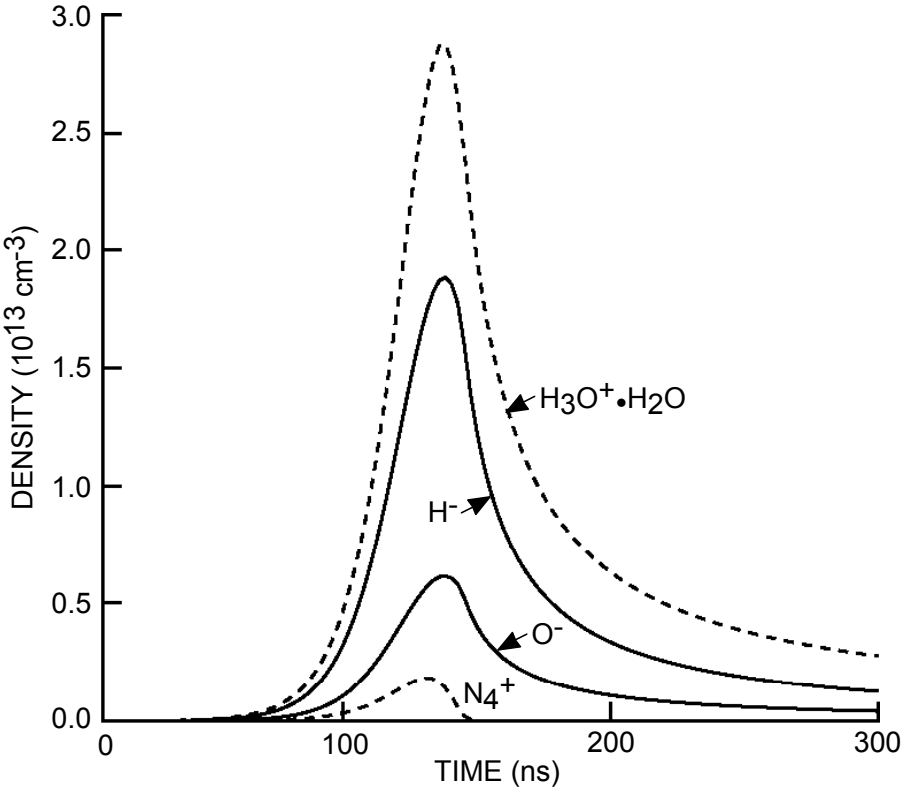

Fig. 5.2. Time dependence of the densities of charged species during the single pulse plasma processing of NO_x. The dominant positive ion is $H_3O^+ \cdot H_2O$ and the dominant negative ions are O^- and H^-, which are primarily lost by charge neutralizations with each other. The conditions are the same as for Fig. 5.1.

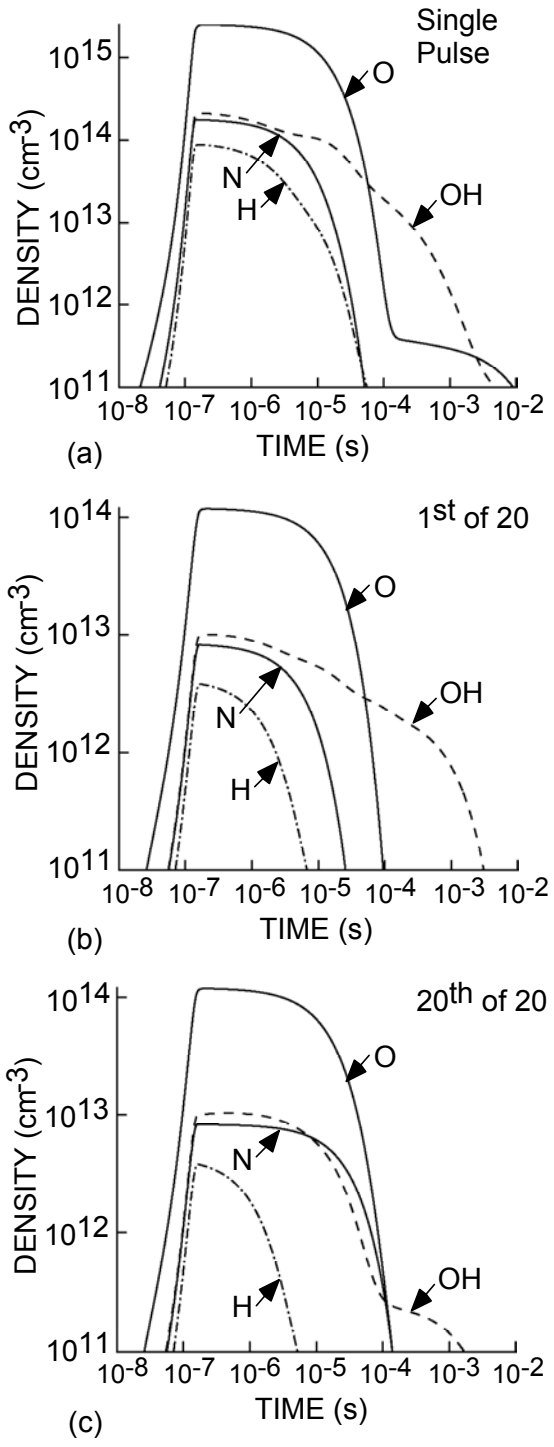

Fig. 5.3. Time dependence of N, O, OH and H densities. (a) Single pulse. (b) 1st of 20 repetitive pulses. (c) 20th of 20 pulses. Conditions are same as for Fig. 5.1. Electron impact reactions with N_2, O_2, H_2O and CO produce N, O, OH and H.

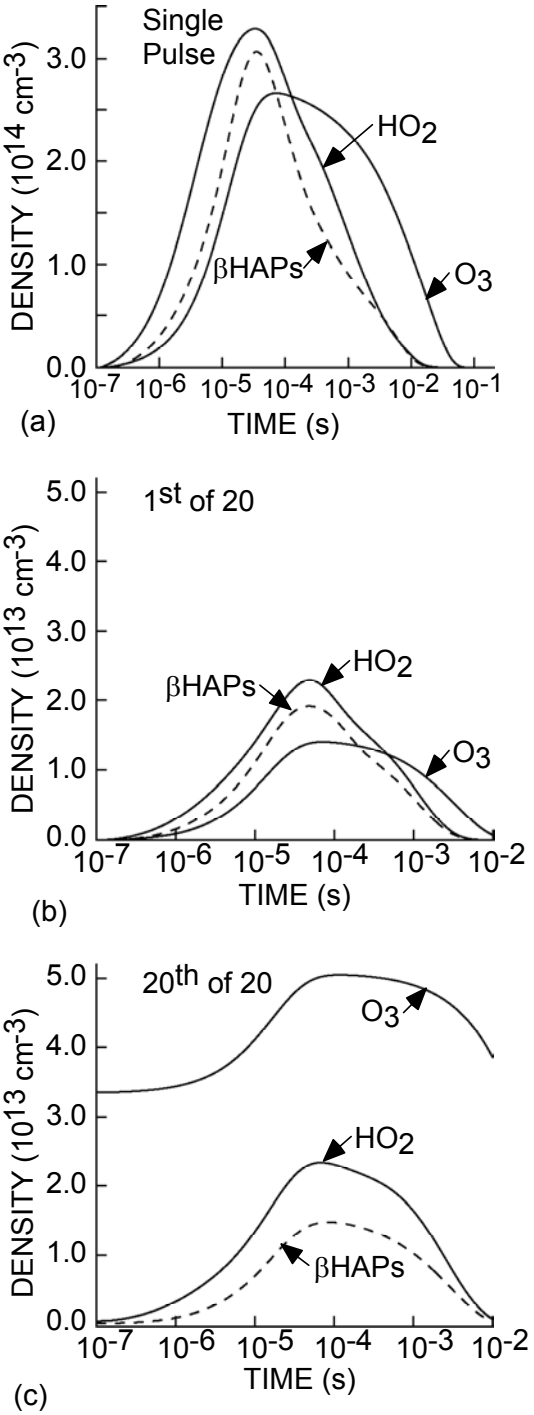

Fig. 5.4. Time dependencies of the NO consuming radicals βHAPs, HO_2 and O_3. (a) Single pulse. (b) 1^{st} of 20 repetitive pulses. (c) 20^{th} of 20 pulses. Due to the depletion of NO with every pulse the residual radical densities increase with multiple pulses. O_3 being the least reactive of the three with NO has a larger residual density.

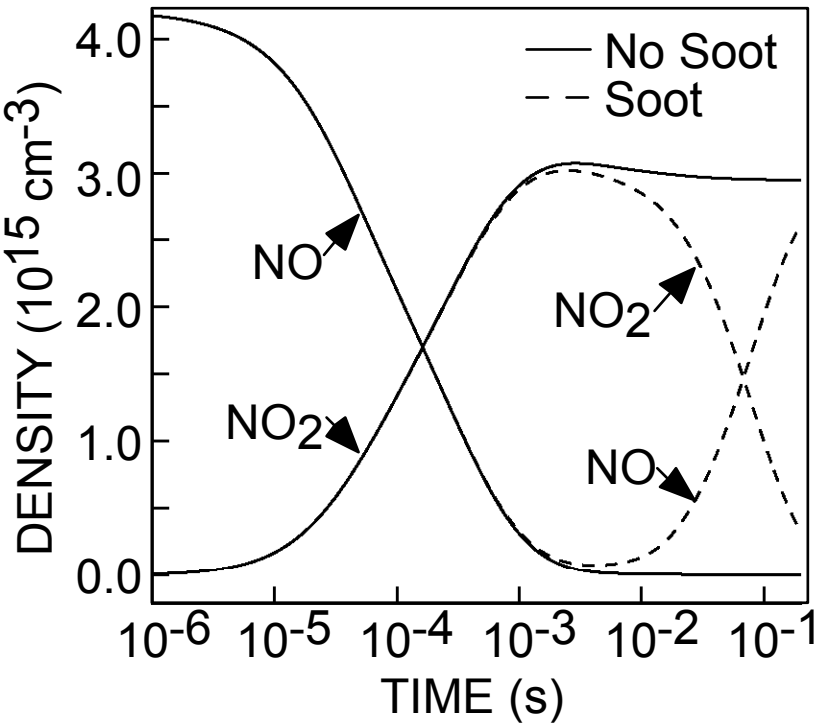

Fig. 5.5. NO and NO_2 densities as a function of time for a single pulse with and without soot. With soot, the heterogeneous reaction of NO_2 regenerates NO in the gas phase. This reaction occurs on a time scale of ~10s ms when most of the NO consuming radicals are depleted. As a result, NO accumulates.

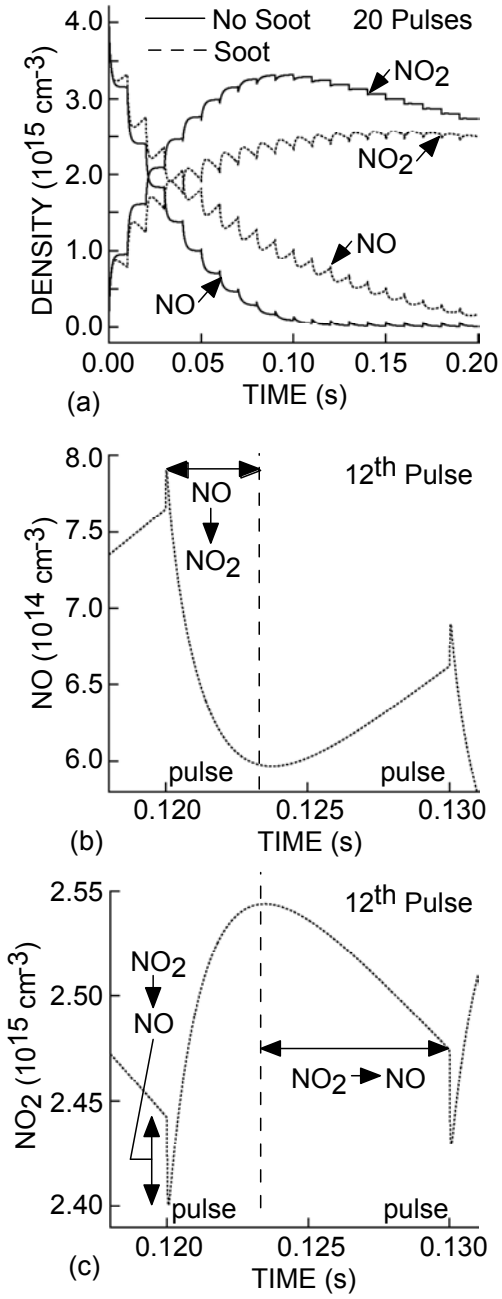

Fig. 5.6. NO and NO_2 densities as a function of time for repetitive pulses with and without soot. (a) NO and NO_2 densities for all pulses. (b) NO density during the 12th pulse. (c) NO_2 density during the 12th pulse. The heterogeneous conversion of NO_2 on soot increases the gas phase density of NO and decreases the NO_2 density. After about 5 pulses, there are three distinct phases for NO evolution. Initial conversion of NO_2 to NO by reaction with O and N atoms, homogeneous conversion of NO to NO_2 by reaction with radicals such as βHAPs, HO_2 and O_3, and heterogeneous generation of NO from NO_2.

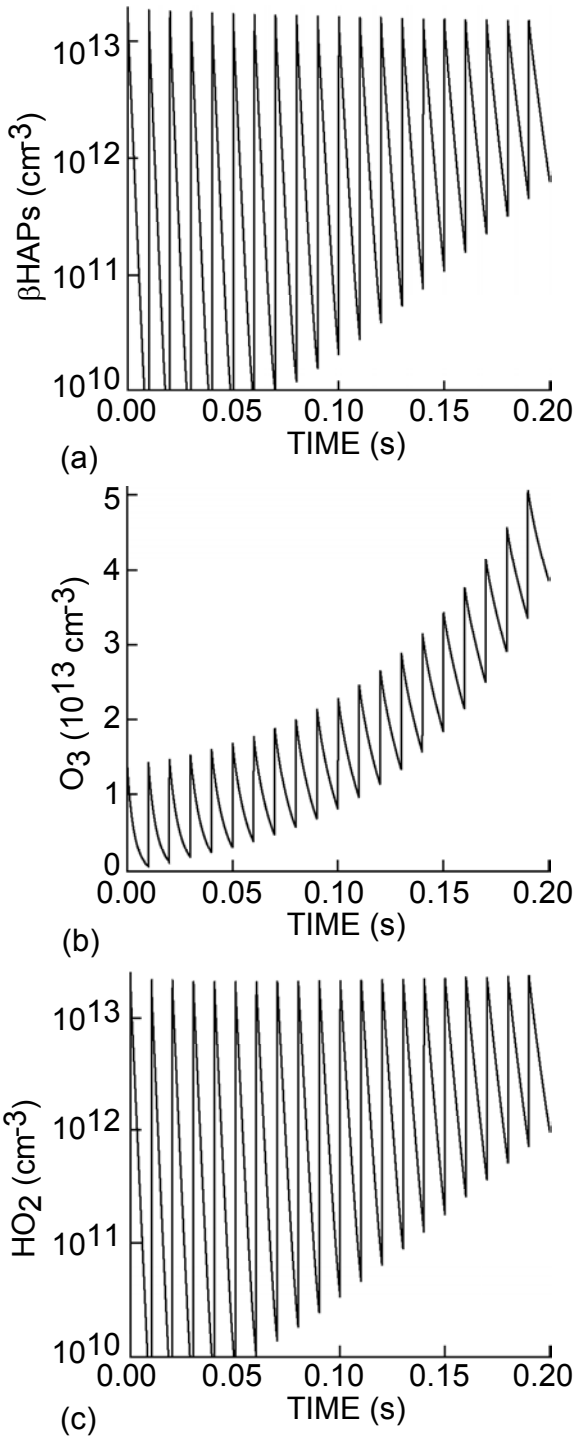

Fig. 5.7. Densities of NO consuming radicals. (a) βHAPs. (b) O_3. (c) HO_2. Since the density of NO decreases with each pulse, the rate of reaction of NO with these radicals decreases. As a result, their residual densities increase with time.

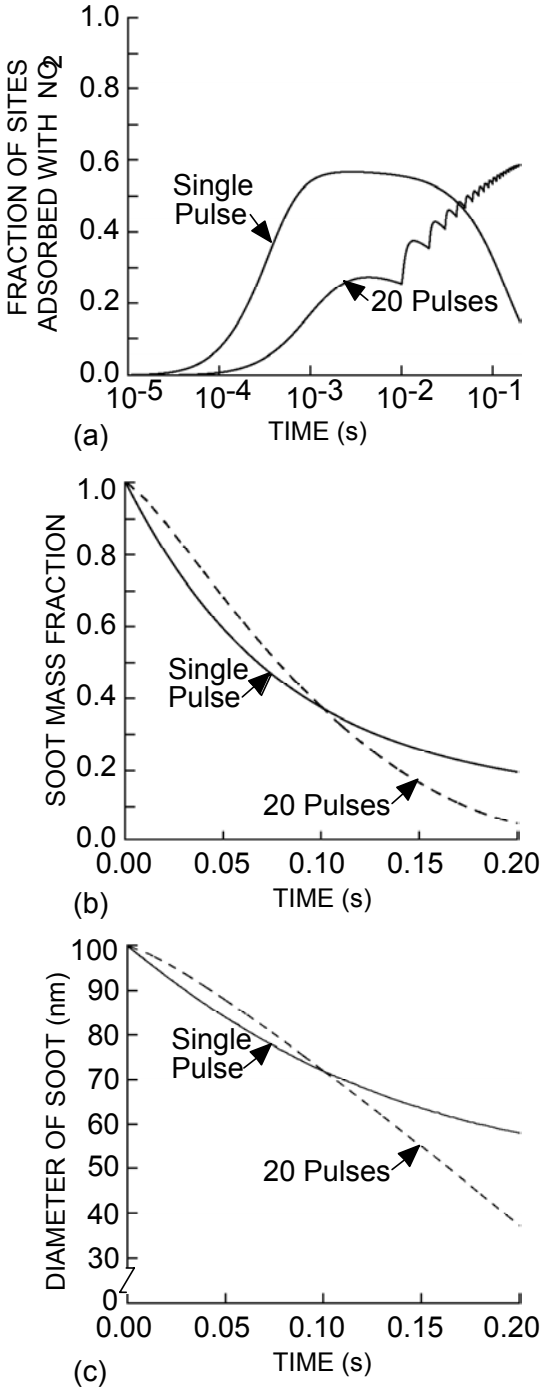

Fig. 5.8. Surface properties of soot with single and multiple pulses as a function of time. (a) Fraction of sites adsorbed with NO_2. (b) Soot mass fraction. (c) Diameter of soot After a few ms, heterogeneous conversion of NO_2 on the soot regenerates NO with a single pulse. There is a constant flux of NO_2 to the soot using multiple pulses resulting in a larger adsorbed fraction. More soot oxidation also occurs.

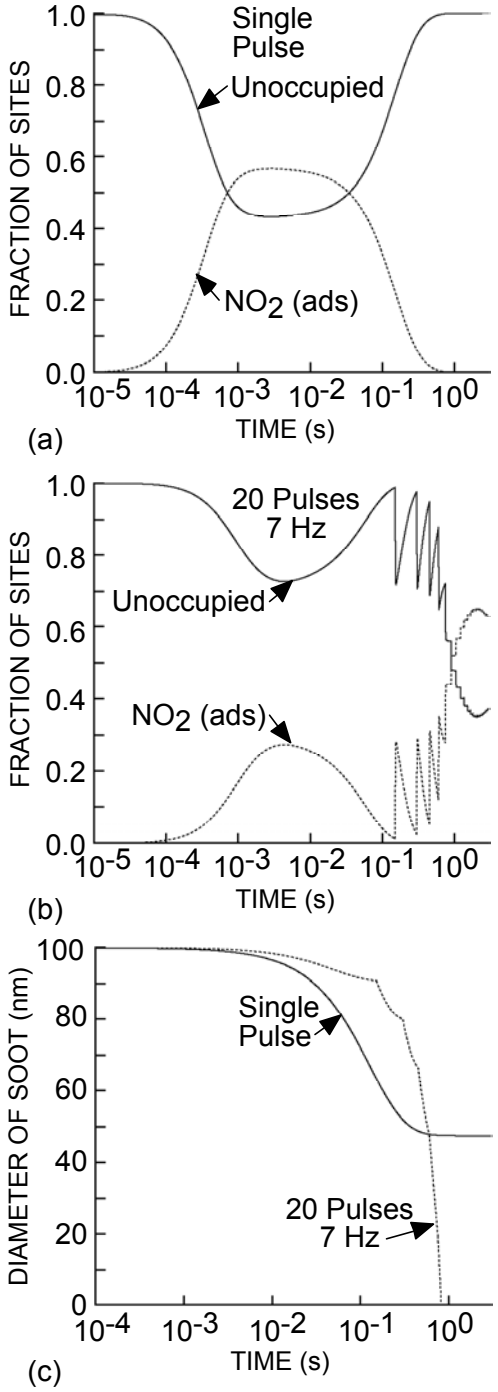

Fig. 5.9. Soot properties for a residence time of 3 s. (a) Site occupancy for a single pulse. (b) Site occupancy for multiple pulses. (c) Diameter of the soot. Almost all of the adsorbed NO_2 desorbs to produce NO with a single pulse. When using multiple pulses, the soot is almost completely oxidized due to the increased time for desorption between pulses.

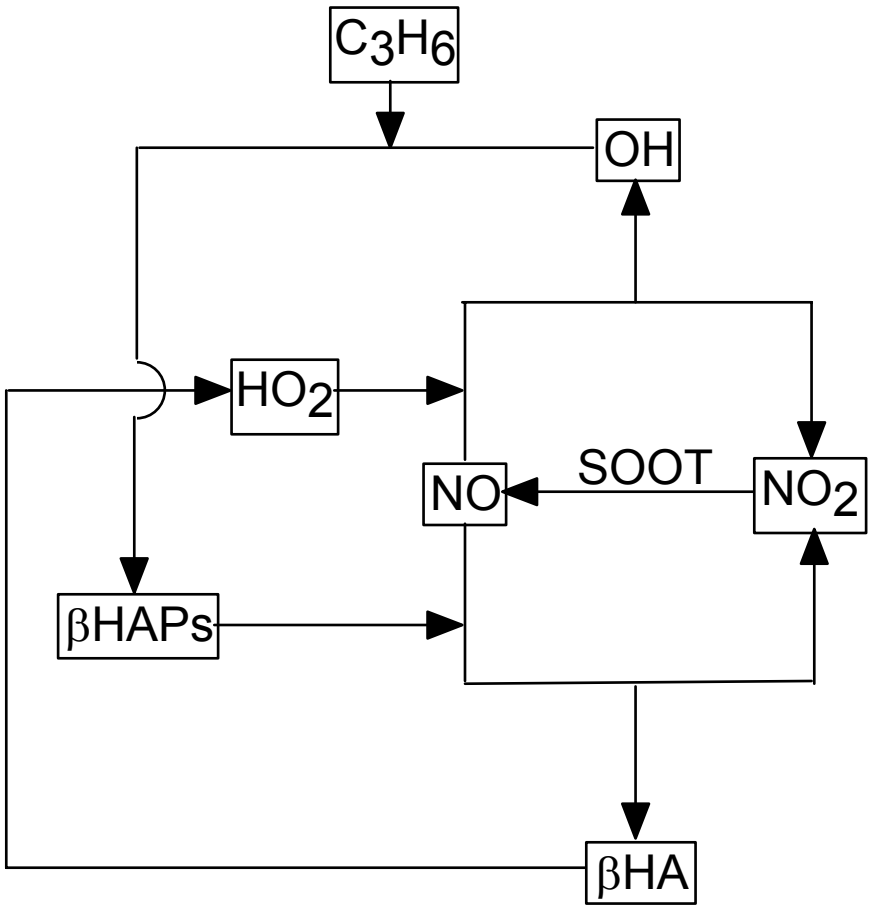

Fig. 5.10. Circular NO and NO_2 chemistry. In the absence of soot particles, NO to NO_2 conversion by reaction with HO_2 produces OH, and by reactions with βHAPs leads to formation of HO_2. The reaction of OH with C_3H_6 starts a chain reaction which results in the formation of βHAPs. The reaction of HO_2 with NO therefore leads to the formation of βHAPs and those of βHAPs with NO lead to HO_2 formation. The products of the conversion of NO to NO_2 are themselves the reactions for further NO to NO_2 conversion. With soot, this cycle is more pronounced due to the heterogeneous conversion of NO_2 back to NO.

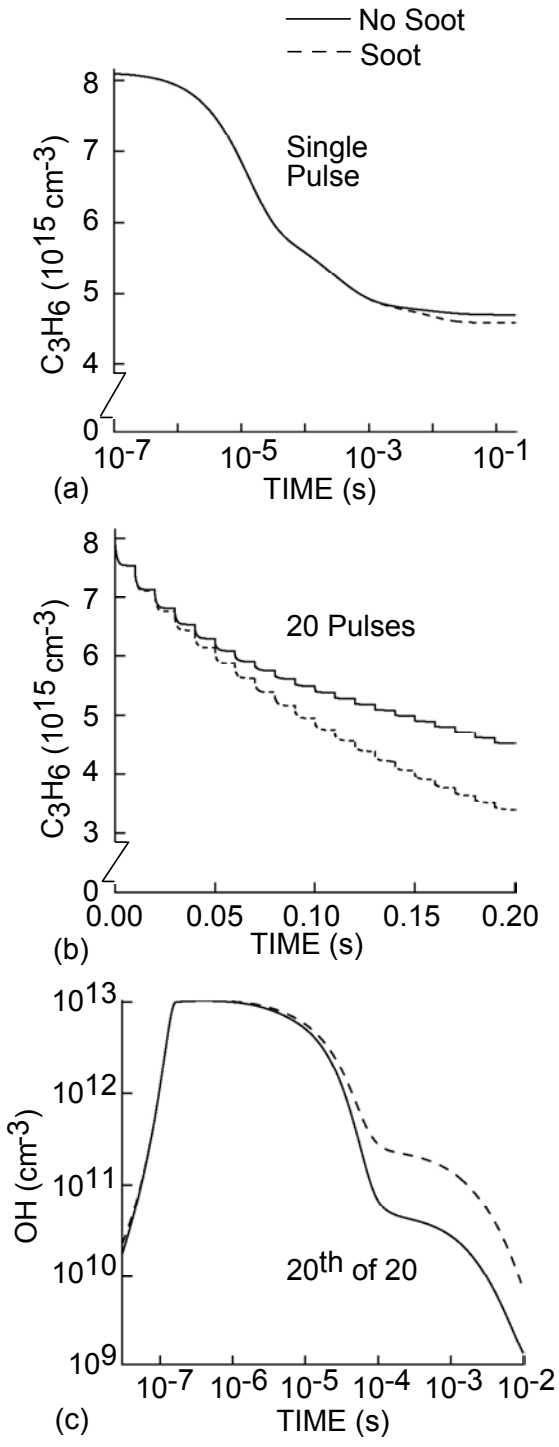

Fig. 5.11. Molecular and radical densities for cases with and without soot as a function of time. (a) C_3H_6 for a single pulse. (b) C_3H_6 for multiple pulses. (c) OH for 20^{th} of 20 pulses. Due to the more pronounced circular chemistry with soot, more OH production results and so more C_3H_6 is consumed. There is increased overlap in time of reacting species densities with multiple pulses and so larger C_3H_6 consumption occurs.

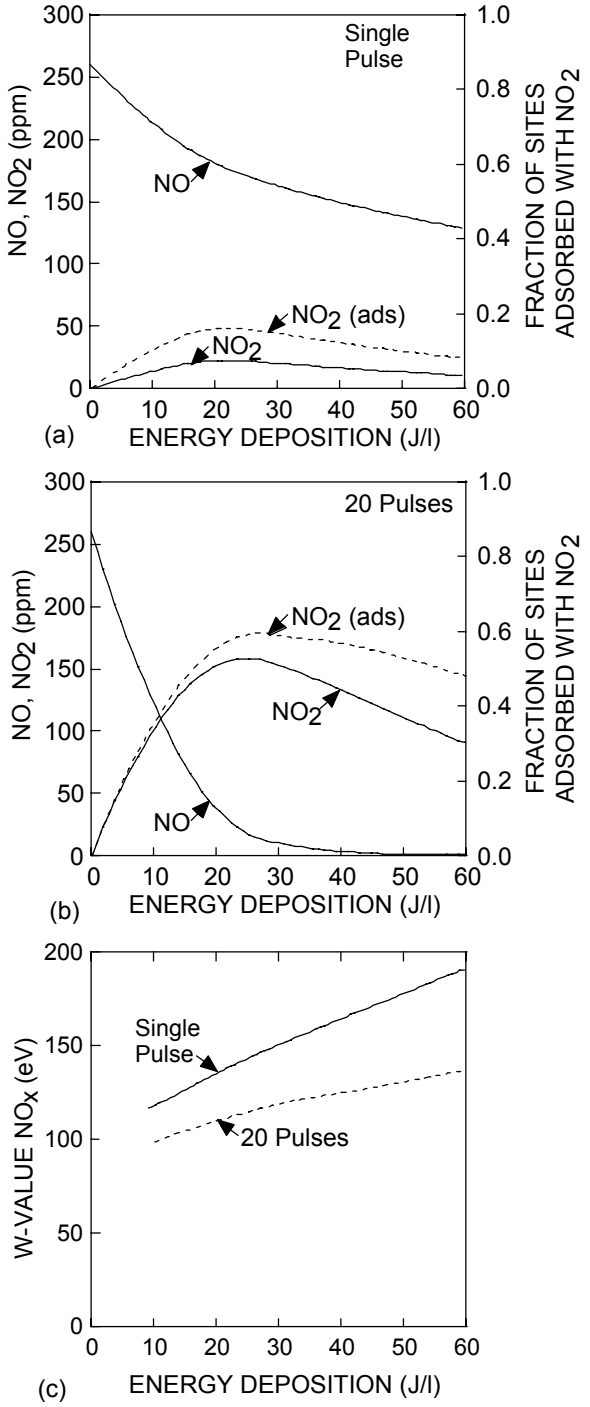

Fig. 5.12. Remediation parameters as a function of energy deposition. (a) Gas phase densities of NO and NO_2, and fraction of surface sites on soot adsorbed with NO_2 for a single pulse. (b) Gas phase densities of NO and NO_2, and fraction of surface sites on soot adsorbed with NO_2 with multiple pulses. (c) *W*-value for NO_x for single and multiple pulses. Multiple pulses are more efficient for NO_x removal due to the increased overlap in time of densities of NO_2 and NO with consuming radical densities.

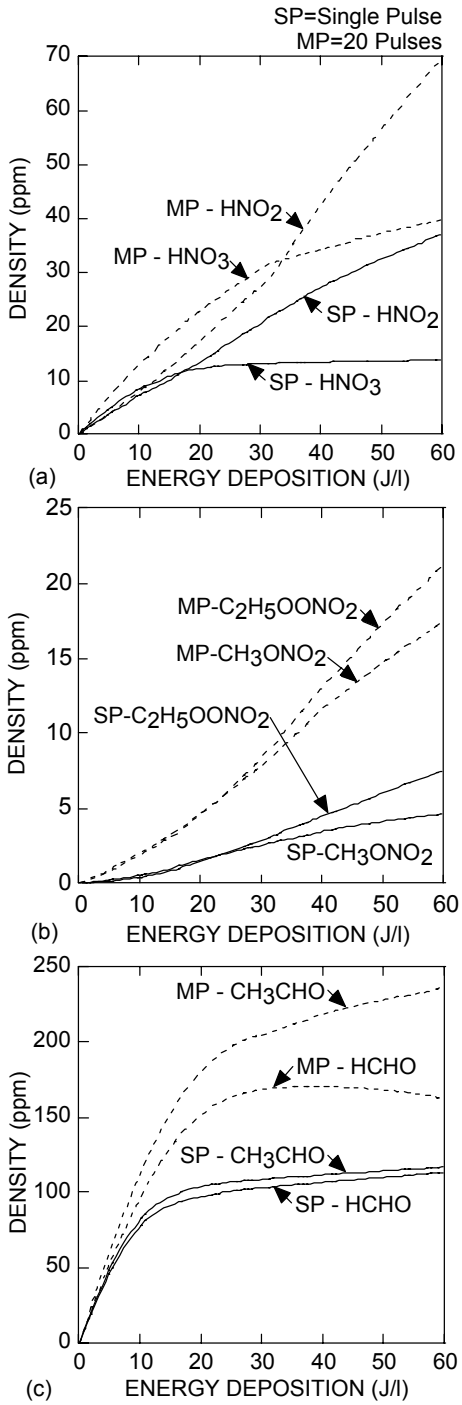

Fig. 5.13. Densities of nitrogen containing products and aldehydes as a function of time when using single and multiple pulses with soot. (a) HNO_3 and HNO_2. (b) CH_3ONO_2 and $C_2H_5OONO_2$. (c) CH_3CHO and HCHO. Due to the increased overlap in time of the densities of NO and NO_2 with the radicals produced during each pulse, multiple pulses in general lead to larger densities of aldehydes and nitrogen containing products.

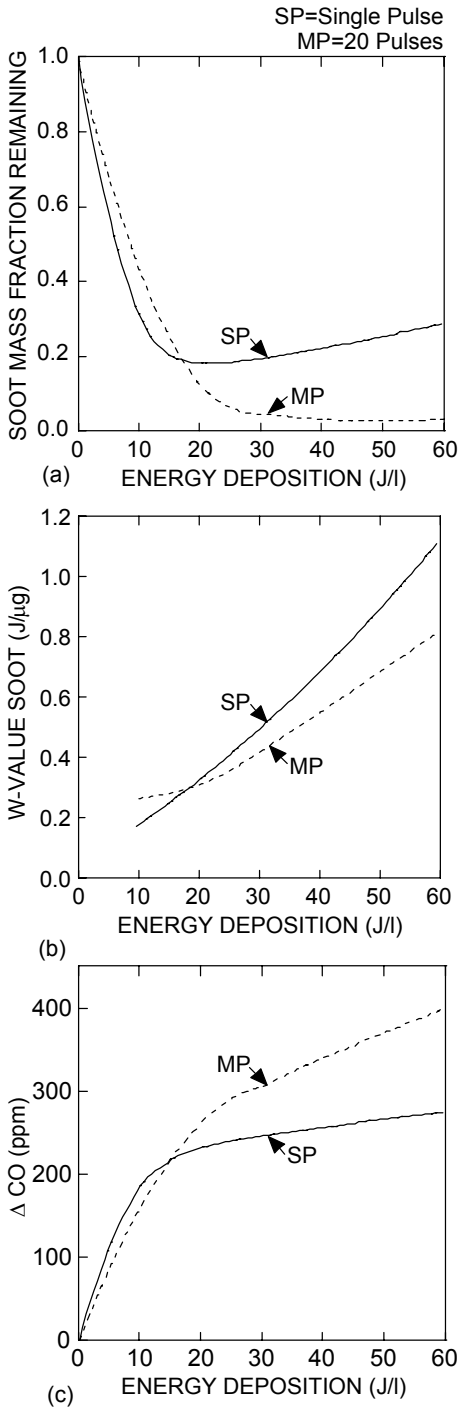

Fig. 5.14. Soot removal parameters as a function of energy deposition when using single and multiple pulses. (a) Mass fraction of soot. (b) *W*-value for soot oxidation. (c) Increase in CO. In general multiple pulses are more efficient for soot oxidation because of the sustained densities of NO_2 compared to the single pulse case.

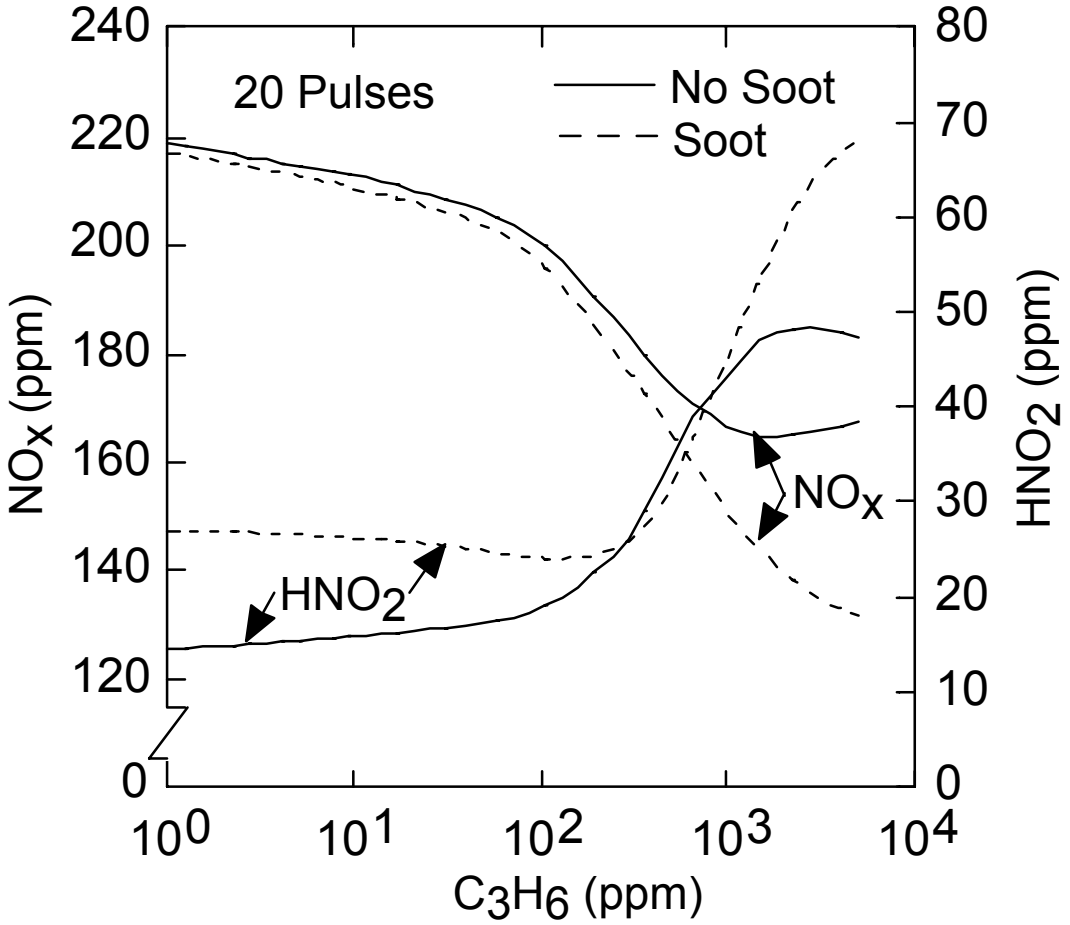

Fig. 5.15. NO_x and HNO_2 densities as a function of C_3H_6 inlet density for multiple pulses. There is increased NO_2 to NO conversion with soot and so larger NO and HNO_3 densities result. The interconversion between NO and NO_2 is a combined result of the heterogeneous reaction of NO_2 and the homogeneous conversion of NO by βHAP radicals. With increasing densities of UHCs, larger densities of βHAPs are generated and the rate of interconversion between NO and NO_2 increases, leading to the increased formation of HNO_2, and larger NO_x removal.

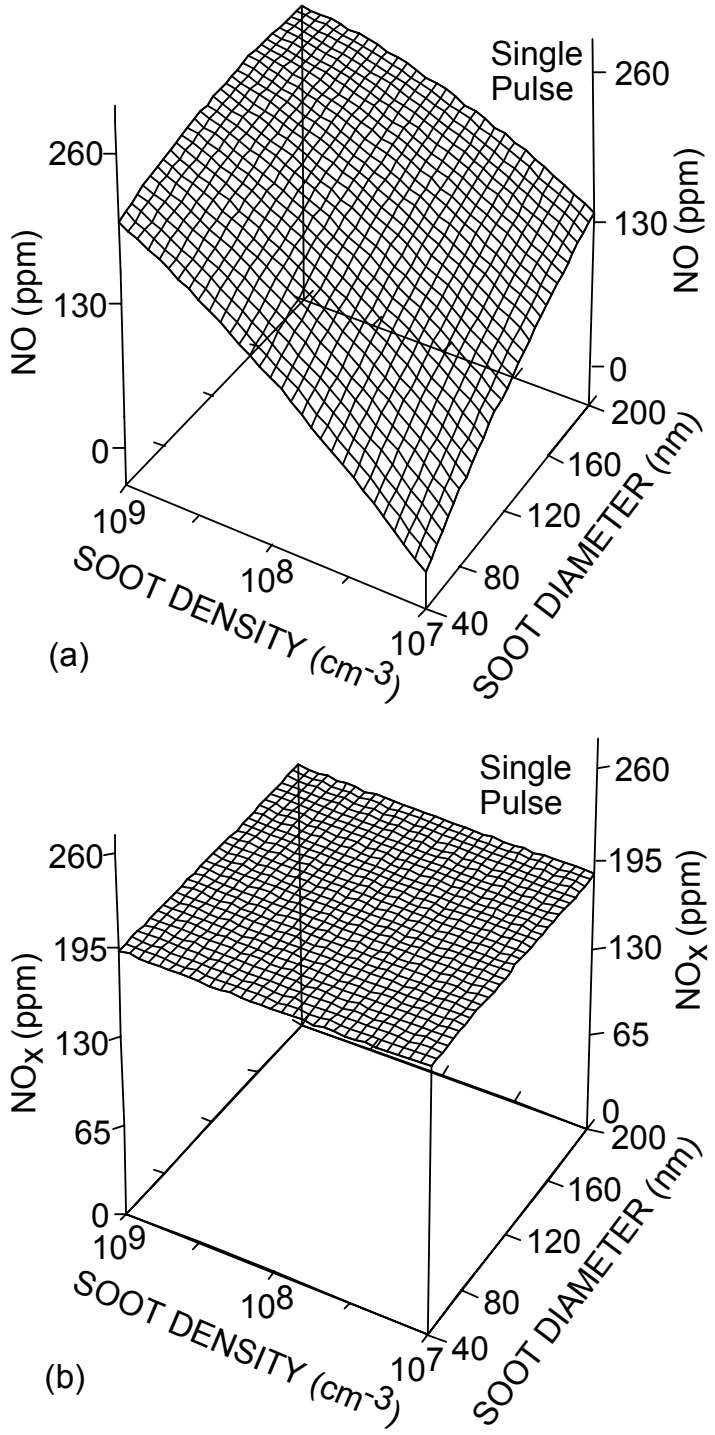

Fig. 5.16. NO and NO_x densities as a function of soot density and diameter when using a single pulse. (a) NO. (b) NO_x. Increasing the soot density and diameter results in a larger surface area for heterogeneous NO_2 to NO conversion leading to larger exit densities of NO. Since this process only converts NO_2 to NO, the overall NO_x density remains nearly a constant.

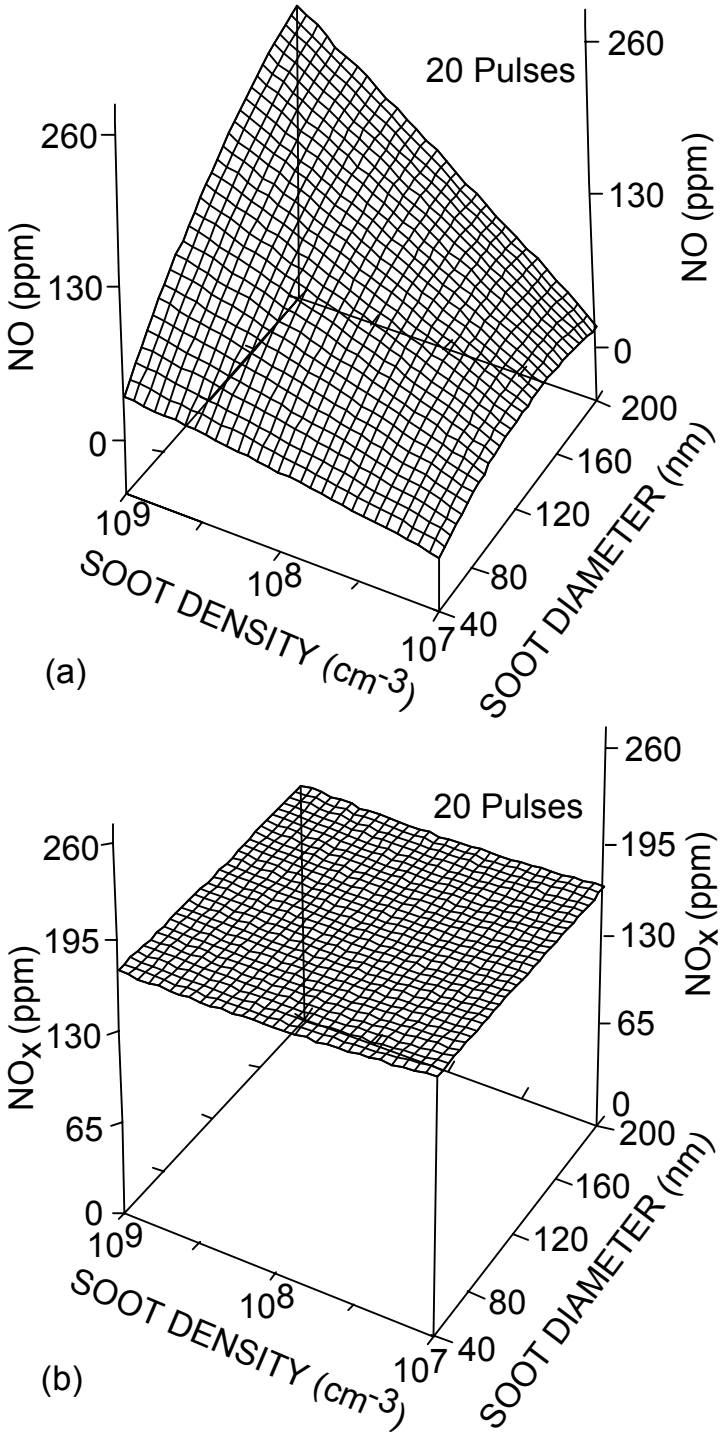

Fig. 5.17. NO and NO_x densities as a function of soot density and diameter when using multiple pulses. (a) NO. (b) NO_x. Due to the increased overlap in time of radical densities and the densities of NO and NO_2, more NO_x removal occurs compared to using single pulses. The interconversion between NO and NO_2 only leads to a change in the composition of NO_x without appreciably altering its density.

5.5 References

1. J. Hoard, P. Laing, M. L. Balmer, and R. Tonkyn, SAE Technical Paper Series **2000-01-2895** (2000).
2. Y. Ikezoe, S. Matsuoka, M. Takebe, and A. Viggiano, *Gas Phase Ion-Molecule Reaction Rate Constants Through 1986* (Ion Reaction Research Group of The Mass Spectroscopy Society of Japan, Tokyo, 1987).
3. J. C. Person and D. O. Ham, Radiat. Phys. Chem. **31,** 1 (1988).
4. Y. Mirokin and G. Mallard, The NIST Chemical Kinetics Database (1998).
5. R. Atkinson, D. L. Baulch, R. A. Cox, R. F. Hampson Jr., J. A. Kerr, and J. Troe, J. Phys. Chem. Ref. Data **18**, 881 (1989).
6. R. Atkinson, J. Phys. Chem. Ref. Data **26**, 215 (1997).
7. D. L. Baulch, C. J. Cobos, R. A. Cox, C. Esser, P. Frank, Th. Just, J. A. Kerr, M. J. Pilling, J. Troe, W. R. Walker, and J. Warnatz, J. Phys. Chem. Ref. Data **21**, 411 (1992).
8. W. Tsang and J. T. Herron, J. Phys. Chem. Ref. Data **20**, 609 (1991).
9. R. Atkinson, D. L. Baulch, R. A. Cox, R. F. Hampson Jr., J. A. Kerr, M. J. Rossi, and J. Troe, J. Phys. Chem. Ref. Data **26**, 521 (1997).
10. W. Tsang, J. Phys. Chem. Ref. Data **16**, 471 (1987).
11. D. L. Baulch, C. J. Cobox, R. A. Cox, P. Frank, G. Hayman, Th. Just, J. A. Kerr, T. Murrells, M. J. Pilling, J. Troe, R. W. Walker, and J. Warnatz, J. Phys. Chem. Ref. Data **23**, 847 (1994).
12. A. F. Wagner, I. R. Slagle, D. Sarzynski, and D. Gutman, J. Phys. Chem. **94**, 1853 (1990).

13. C. A. Rogaski, D. M. Golden, and L. R. Williams, Geophys. Res. Lett. **24,** 381 (1997).

14. K. Tabor, L. Gutzwiller, and M. J. Rossi, J. Phys. Chem. **98,** 6172 (1994).

6. CONSEQUENCES OF UNBURNED HYDROCARBONS ON THE TRANSPORT IN MICROSTREAMERS DURING THE DBD PROCESSING OF NO_X

6.1 Introduction

In this chapter, we extend our study on plasma remediation of NO_x to include diffusive and advective transport in microstreamers in addition to the chemical kinetics. Gentile and Kushner [1] showed that radial transport of species to and from the microstreamer region significantly influences the efficiency of NO_x remediation. Localized energy deposition in these microstreamers results in spatially nonuniform temperature and species densities which initiate advective and diffusive transport leading to the movement of species into and out of the microstreamer. We saw in Chapter 3 that UHCs significantly influence the NO_x chemistry during the plasma processing of NO_x in diesel exhausts. In this investigation we study the combined effects of UHCs and species transport on the overall remediation of NO_x.

A description of the one-dimensional radial model used to study the streamer evolution and the hydrodynamics is given in Section 2.4. Results from this model on the consequences of UHCs-NO_x reactions and advective and diffusive transport on the NO_x remediation are discussed in Section 6.2. Concluding remarks are given in Section 6.3.

6.2 Consequences of UHCs on the Transport in Microstreamers During DBD Processing of NO_x

The base case conditions are $N_2/O_2/H_2O$=86/8/6 with 500 ppm NO (1 atm, 453 K), electrode separation of 3 mm, gas residence time of 10^{-2} s, and a pulse repetition frequency of 300 Hz. A voltage of 10 kV is applied across the gap to produce a streamer-

volume averaged energy deposition of 170 J/L. The computational area is 1 cm × 1 cm and the initial streamer radius is 10 μm. This large disparity in the sizes is deliberately made so as to minimize edge effects (for example, reflection of acoustic waves). Since the reaction mechanisms for NO_x remediation in the absence of UHCs and in the presence of C_3H_6 have been discussed in detail previously,[1,2] only those reactions of direct importance to this study will be addressed.

The electron density (n_e) and the on axis electron temperature (T_e) for the first and the last pulse are shown in Fig. 6.1. During the current pulse which lasts ≈70 ns, electron avalanche in the streamer region occurs through electron impact ionizations of N_2, O_2, and H_2O and results in the production of N, O, and OH radicals. Peak on axis electron temperature is 3.2 eV and the peak electron density is 3.7×10^{13} cm^{-3}. Following the current pulse, electrons are rapidly lost to O_2 and H_2O by attachment and as a result their diffusion to regions far beyond the streamer is limited. Since the densities of the dominant background gases do not significantly change after any given pulse, the electron temperature and electron densities for the first and the last pulse are not significantly different.

The gas temperature, mass flux, and the total gas density during and following the current pulse are shown in Fig. 6.2. With the flow of current through the microstreamer, the gas temperature rises by ≈120 K producing a pressure gradient which initiates advection radially outward. The advection wave can be compared to a weak blast wave which pushes the hot mass out of the streamer region producing significantly increased temperatures at radii noticeably outside of the streamer region. Following the current pulse, temperature begins to decrease by expansion cooling and thermal conduction and

the peak in the mass flux moves radially outward continuing to push hot mass away from the streamer region. Once the temperature in the streamer decreases sufficiently, the pressure gradient reverses resulting in an influx of mass back into the streamer region. With time, the wave is widened and flattened as a result of opposing forces of viscosity, and pressure and thermal gradients. Advection at longer times (>1 μs) is restricted to small acoustic waves which propagate back and forth throughout the gas. Owing to their small amplitude, these waves do not contribute significantly to changes in species densities at these times.

The densities of O atoms for the first and last pulses are shown in Figs. 6.3a and 6.3b. During the current pulse, O atoms are dominantly produced in the streamer region by the electron impact dissociation of O_2. Most of the O is consumed by reactions with O_2 to form O_3,

$$O + O_2 + M \rightarrow O_3 + M, \qquad k = 3.4\times10^{-34}(T/298)^{-1.2}\ cm^6 s^{-1}\ [3]. \qquad (6.1)$$

The production of O atoms in the regions outside of the microstreamer during and slightly after the current pulse (a few hundred ns) is mainly due to the ambipolar diffusion of electrons which produce O by the dissociation of O_2. Due to their high reactivity, O atoms are quickly exhausted (a few hundred μs) and hence do not accumulate pulse to pulse. Since the density of O_2, its primary precursor and consumer does not change from pulse to pulse, O atom densities are not significantly different for the first and the last pulse.

To determine the effects of UHCs, 2000 ppm of C_3H_6 were added to the base case mixture. The densities of O atoms for the first and the last pulse are shown in Figs. 6.3c and 6.3d. The initial production of O atoms, primarily by the electron impact dissociation of O_2 is not significantly influenced by the presence of C_3H_6 and so does not differ from the case without C_3H_6. At longer times (> many μs) and in the presence of C_3H_6, O atoms are also consumed by reactions with C_3H_6 and hence their densities are smaller,

$$O + C_3H_6 \rightarrow \text{Methyl Oxirane}, \quad k = 1.2\times10^{-12}\ cm^3 s^{-1}\ [4], \tag{6.2}$$

$$\rightarrow C_2H_5CHO, \quad k = 1.2\times10^{-12}\ cm^3 s^{-1}\ [4], \tag{6.3}$$

$$\rightarrow CH_2CHO + CH_3, \quad k = 0.8\times10^{-12}\ cm^3 s^{-1}\ [4], \tag{6.4}$$

$$\rightarrow C_2H_5 + HCO, \quad k = 0.8\times10^{-12}\ cm^3 s^{-1}\ [4]. \tag{6.5}$$

Since the rates for consumption of O atoms by reactions with C_3H_6 are larger than that by the reaction with O_2 (Eq. 6.1), O atoms are preferentially and more rapidly consumed by reactions with C_3H_6 and as a result their diffusion to regions outside of the microstreamer is limited. Due to the decreased availability of O for reactions with O_2, the densities of O_3 are smaller compared to the case without C_3H_6, as shown in Fig. 6.4. Subsequently, diffusion of O_3 to regions outside of the microstreamer becomes restricted in the case with C_3H_6. In both cases, most of the O_3 is consumed by reactions with NO to form NO_2,

$$NO + O_3 \rightarrow NO_2 + O_2, \qquad k = 4.3\times10^{-12}\exp(-1598/T)\ cm^3 s^{-1},$$

$$k_{298} = 2.1\times10^{-14}\ cm^3 s^{-1}\ [4]. \qquad (6.6)$$

Since NO is abundant both within and outside the streamer region, most of the O_3 is consumed and so the density of O_3 does not accumulate pulse to pulse.

The densities of OH for the first and the last pulse for the cases with and without C_3H_6 are shown in Fig. 6.5. Initially (t< 100 ns), OH is produced in the streamer region primarily by the electron impact dissociation of H_2O. At times following the current pulse, OH is produced in regions outside of the streamer mainly by the dissociation of H_2O by electrons resulting from ambipolar diffusion from the streamer region. At later times and in the absence of C_3H_6, OH is depleted in the streamer region by reactions with NO to form HNO_2 and by diffusion to regions outside,

$$\mathrm{OH + NO + M \rightarrow HNO_2 + M}, \qquad k = 8.6\times10^{-31}(T/298)^{-2.5}\exp(34/T)\ cm^6 s^{-1},$$

$$k_{298} = 9.7\times10^{-31}\ cm^6 s^{-1}\ [5]. \qquad (6.7)$$

In the presence of C_3H_6, OH is favorably and more rapidly consumed by reactions with C_3H_6 to form C_3H_6OH,

$$\mathrm{OH + C_3H_6 \rightarrow C_3H_6OH}, \qquad k = 4.9\times10^{-12}\exp(504/T)\ cm^3 s^{-1},$$

$$k_{298} = 2.6\times10^{-11}\ cm^3 s^{-1}\ [4], \qquad (6.8)$$

and as a result, diffusion of OH to regions far beyond the streamer region is not as pronounced as in the case without C_3H_6. C_3H_6OH quickly reacts with O_2 to form $C_3H_6(OH)O_2$ (β-hydroxy alkyl peroxy radicals or simply βHAPs),

$$C_3H_6OH + O_2 \rightarrow \beta HAPs, \qquad k = 1.6\times10^{-11}\, cm^3 s^{-1} \text{ [4]}, \tag{6.9}$$

which further react with NO to form NO_2 and $C_3H_6(OH)O$ (β-hydroxy alkoxy radicals or simply βHAs),

$$NO + \beta HAPs \rightarrow NO_2 + \beta HAs, \qquad k = 5.4\times10^{-12}\exp(360/T)\, cm^3 s^{-1},$$
$$k_{298} = 1.8\times10^{-11}\, cm^3 s^{-1} \text{ [4]}. \tag{6.10}$$

Electron impact dissociation of H_2O also produces H in addition to OH. Most of the H reacts with O_2 to form HO_2,

$$H + O_2 + M \rightarrow HO_2 + M, \qquad k = 1.8\times10^{-32}(T/298)^{-0.8}\, cm^6 s^{-1} \text{ [6]}. \tag{6.11}$$

The densities of HO_2 are shown in Fig. 6.6 for the cases with and without C_3H_6. In the presence of C_3H_6, more HO_2 is produced by the reactions of O_2 with the products of βHA radical decomposition,

$$\beta HA \rightarrow \beta\text{-hydroxy alkyl radicals} + HCHO,$$

$$k = 7.9\times10^{13}\exp(-10517/T)\ s^{-1}, \qquad k_{298} = 3.7\times10^{-2}\ s^{-1}\ [3], \quad (6.12)$$

β-hydroxy alkyl radicals + $O_2 \rightarrow CH_3CHO + HO_2$,

$$k = 1.9\times10^{-11}\ cm^3 s^{-1}\ [7]. \quad (6.13)$$

Since these reactions occur on time scales of tens of μs, HO_2 densities are sustained for longer times in the presence of C_3H_6. Depletion of HO_2 occurs by diffusion to outer radii and by reaction with NO to produce NO_2,

$$NO + HO_2 \rightarrow NO_2 + OH, \qquad k = 3.5\times10^{-12}\exp(240/T)\,cm^3 s^{-1},$$

$$k_{298} = 7.8\times10^{-12}\ cm^3 s^{-1}\ [4]. \quad (6.14)$$

The densities of NO for the cases with and without C_3H_6 are shown in Fig. 6.7. The NO density in the streamer region initially decreases due to the rarefaction of the core resulting from advection. Peak in the NO density occurs in the region outside of the streamer corresponding to the peak in the shock wave which results from the current impulse. At later times, reversal of the pressure gradient and back diffusion refills NO in the streamer region. This refilling of core from the large reservoir of NO around the streamer region being larger than the depletion of NO by reactions, NO densities in the streamer region increase. At the end of the afterglow period, the density of NO in the streamer region is almost the same as that of the outer regions and so the densities of NO during subsequent pulses do not significantly differ. In the presence of C_3H_6, more NO is consumed by reactions with βHAPs (Eq. 6.10) and HO_2 (Eq. 6.14) and as a result the

density of NO at a given time and radial location is smaller compared to the case without C_3H_6. Correspondingly, it takes longer time to repopulate NO in the streamer region by diffusion from outside.

The densities of NO on the axis (r = 0) and slightly off the streamer edge (r = 12 μm) as a function of time are shown in Fig. 6.8. For t< 100 ns, rarefaction of the streamer region by radial advection depletes NO on the axis and results in a peak in the NO density slightly outside the streamer region. Reversal of the pressure gradient and back diffusion refill NO in the streamer region at later times. Due to the larger consumption of NO by βHAPs, NO densities in the presence of C_3H_6, both on the axis as well as slightly off the streamer edge are less compared to those without C_3H_6. At t> 10^{-4} s, the density of NO is leveled by diffusion.

The densities of NO_2 with and without C_3H_6 are shown in Fig. 6.9. In general larger amount of NO_2 is produced in the presence of C_3H_6 by the reactions of βHAP radicals with NO (Eq. 6.10). In the absence of C_3H_6, NO_2 is mainly formed by the reactions of NO with O_3 and HO_2 (Eq. 6.6 and 6.14) at time scales on the order of a few to 10s of μs. The rarefaction of the core and the abundance of NO and O_3 outside the streamer region results in an off-axis peak in the density of NO_2 at t≈ 3×10^{-5} s. Due to the smaller reactivity of NO_2 compared to NO, the density of NO_2 accumulates from pulse to pulse, with the accumulation more pronounced in the presence of C_3H_6 due to the larger production of NO_2.

The on-axis densities of NO_2 for the cases with and without C_3H_6 are shown in Fig. 6.10. During the first pulse, the densities of NO_2 at the start of the current pulse are insignificant and hence are not affected by advection. With the accumulation of NO_2

from pulse to pulse, the initial depletion of on axis NO_2 by radial advection becomes increasingly evident, with the effect more pronounced in the presence of C_3H_6. Typically, the density of NO_2 increases until ≈10s of μs due to production from NO and at later times decreases due to the depletion by diffusion to regions outside the streamer.

The densities of C_3H_6 and βHAPs are shown in Fig. 6.11. Initial radial advection depletes C_3H_6 from the streamer region and results in a peak in its density at the crest of the shock wave. Refilling of the core at later times restores the density of C_3H_6. Although significant depletion of C_3H_6 in the streamer region occurs by reactions with O and OH, diffusion from the large volume of C_3H_6 outside the streamer region overshadows the effect. Consumption of C_3H_6 by OH leads to the formation of βHAP radicals (Eqs. 6.8 and 6.9), which further react with NO to produce NO_2. More βHAPs are consumed outside the streamer region due to the abundant NO. With time, βHAPs in the streamer region are exhausted by reactions with NO and by diffusion to outer radii.

Although most of the NO removed is by conversion to NO_2, some amount of NO is also lost by reactions with OH to form HNO_2 (Eq. 6.7). The densities of HNO_2 with and without C_3H_6 are shown in Fig. 6.12. In the presence of C_3H_6, OH is preferentially consumed by reactions with C_3H_6 and so less is available for reactions with NO and so the initial production of HNO_2 is smaller compared to the case without C_3H_6. At later times, larger densities of HNO_2 are sustained in the presence of C_3H_6 by the reaction of HO_2 with NO_2,

$$HO_2 + NO_2 \rightarrow HNO_2 + O_2, \qquad k = 1.2\times10^{-13}\ cm^3 s^{-1}\ [3]. \qquad (6.15)$$

Since the densities of HO_2 and NO_2 are larger and are sustained for longer periods in the presence of C_3H_6 (see Figs. 6.6 and 6.9), more HNO_2 is produced at longer times.

6.3 Concluding Remarks

In the filamentary mode of operation of atmospheric pressure plasmas, energy is dominantly deposited in confined volumes resulting in localized temperature rise in these regions. This initiates advection leading to transport of species to and from the microstreamer. C_3H_6, representative of the UHCs typically found in diesel exhausts, reacts with the O and OH radicals produced in the streamer region and limits their convection to larger radii, and thus decreases the remediation of NO in the regions outside of the streamer. However, NO conversion increases in the streamer region in the presence of C_3H_6 due to the larger production of βHAPs and HO_2 which efficiently convert NO to NO_2. Thus, in the presence of C_3H_6, the removal of NO increases in the streamer region and decreases at outer radii.

6.4 Figures

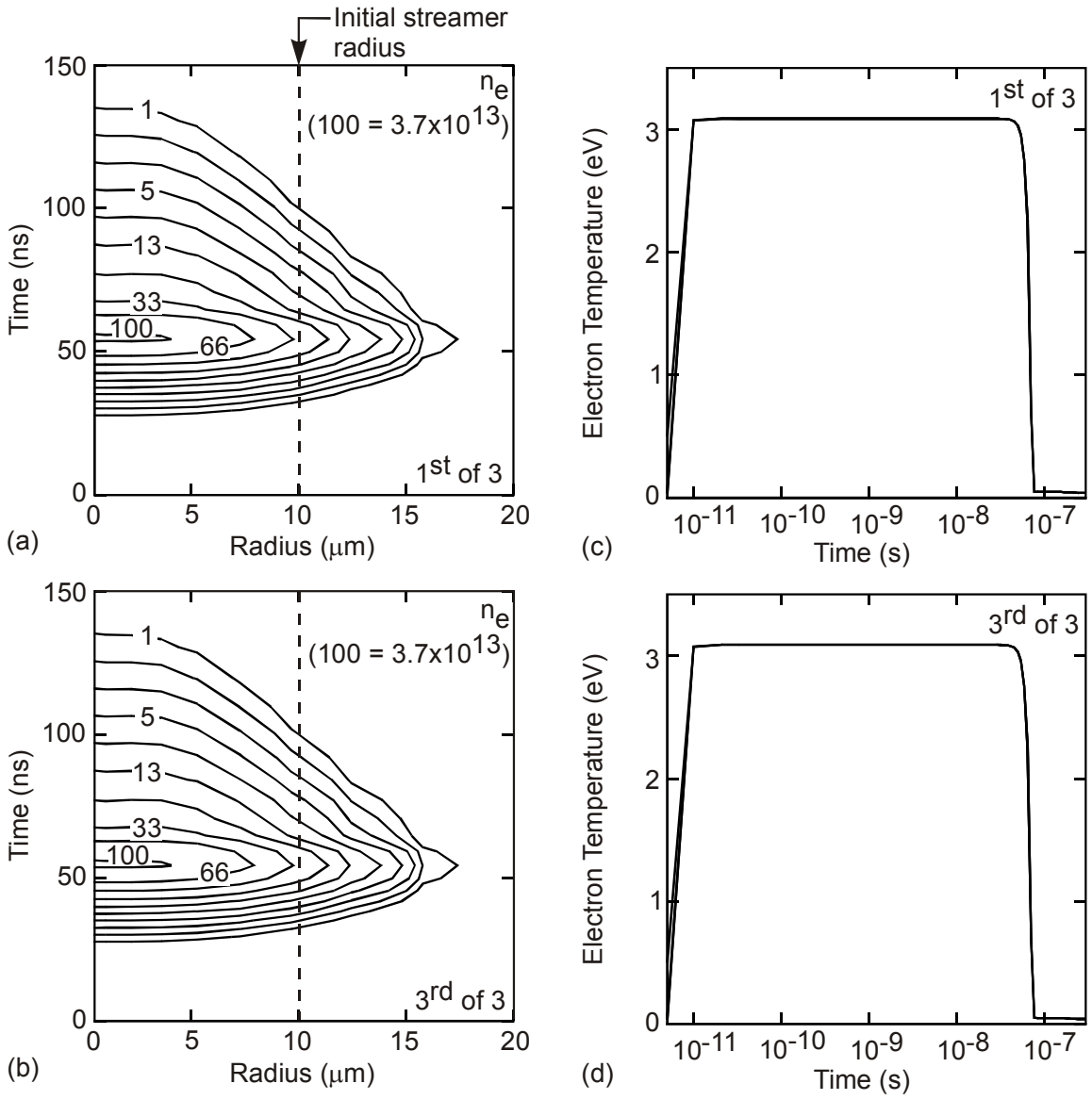

Fig. 6.1. Electron density (n_e) (cm^{-3}) and on-axis electron temperature (T_e) for the 1st and the 3rd pulse. (a) n_e for the 1st pulse. (b) n_e for the 3rd pulse. (c) On-axis T_e for the 1st pulse. (d) On-axis T_e for the 3rd pulse. Conditions are $N_2/O_2/H_2O$=86/8/6 with 500 ppm NO (1 atm, 453 K), gas residence time of 10^{-2} s, 300 Hz, streamer-volume averaged energy deposition = 170 J/L.

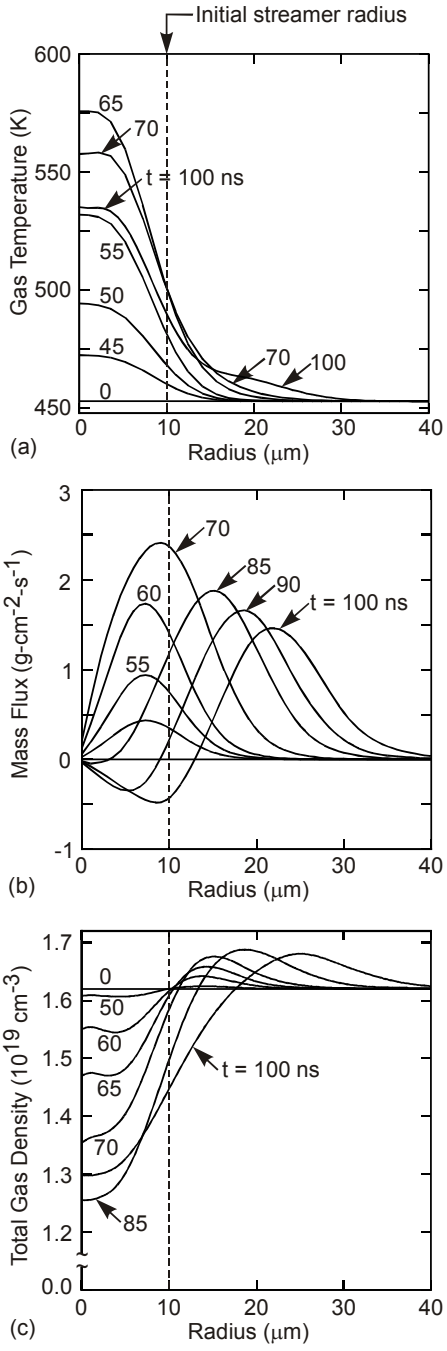

Fig. 6.2. Microstreamer characteristics during the initial 100 ns. The current pulse lasts ≈70 ns. Localized energy deposition in the microstreamer results in a temperature rise which initiates radial advection leading to the movement of hot mass to regions outside the streamer. Following the current pulse, temperature decreases by cooling and thermal conduction.

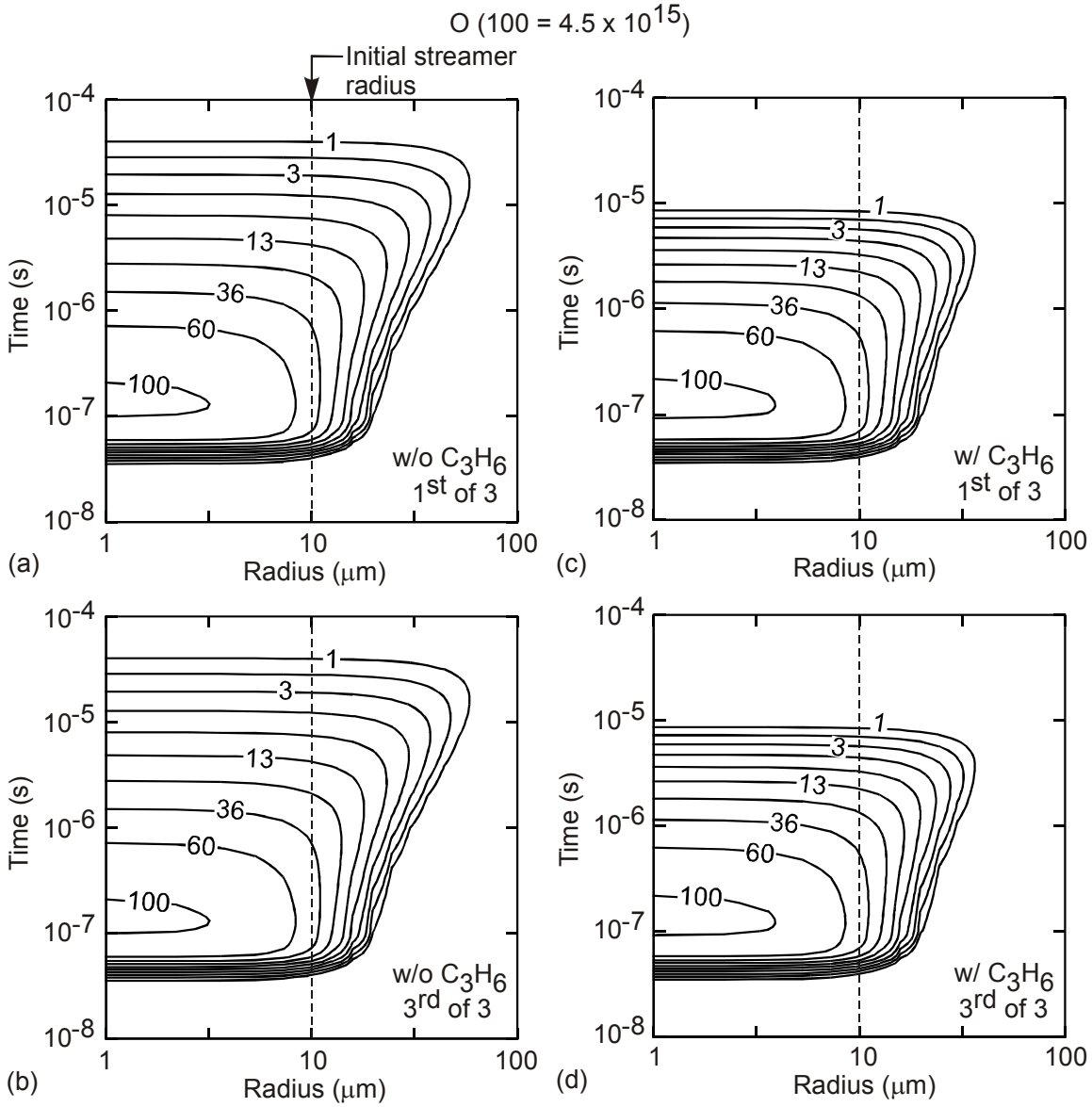

Fig. 6.3. Densities of O (cm^{-3}). (a) Without C_3H_6, 1st pulse. (b) Without C_3H_6, 3rd pulse. (c) With C_3H_6, 1st pulse. (d) With C_3H_6, 3rd pulse. Conditions are as in Fig. 6.1. O atoms are more rapidly consumed in the presence of C_3H_6 and hence their diffusion to larger radii is limited.

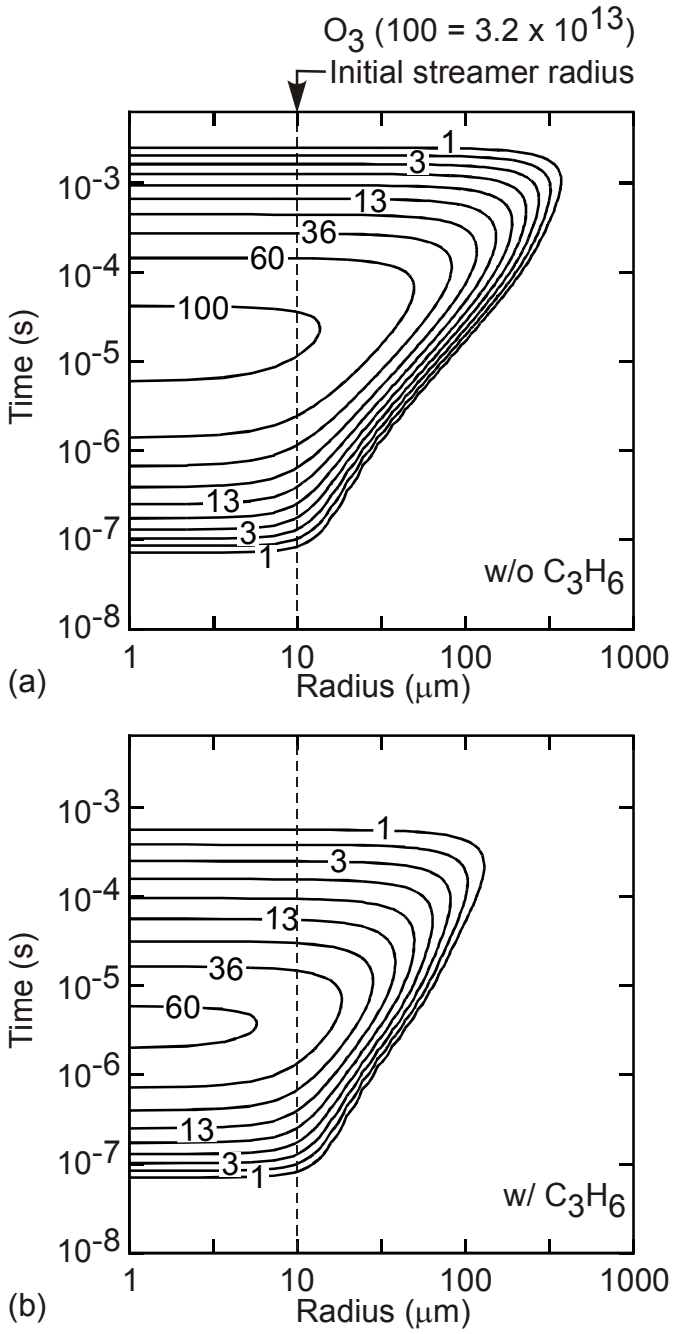

Fig. 6.4. Density of O_3 (cm^{-3}). (a) Without C_3H_6. (b) With C_3H_6. Due to the preferential consumption of O by C_3H_6, O_3 production is limited in the presence of C_3H_6 and as a result, diffusion to larger radii at longer times becomes restricted. Conditions are as in Fig. 6.1

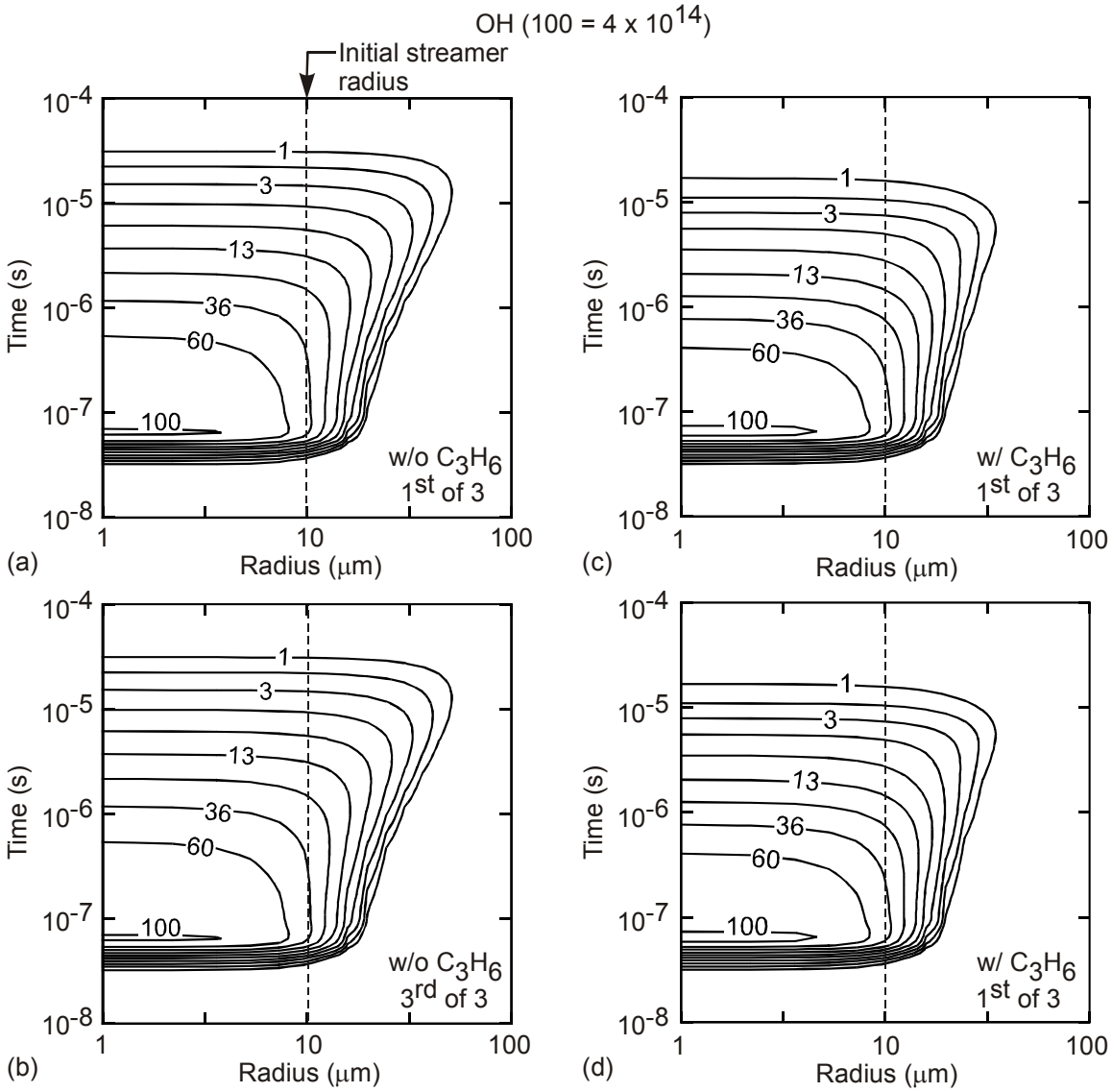

Fig. 6.5. Densities of OH (cm^{-3}). (a) Without C_3H_6, 1st pulse. (b) Without C_3H_6, 3rd pulse. (c) With C_3H_6, 1st pulse. (d) With C_3H_6, 3rd pulse. Conditions are as in Fig. 6.1. OH radicals are more rapidly consumed in the presence of C_3H_6 and hence their diffusion to larger radii is limited.

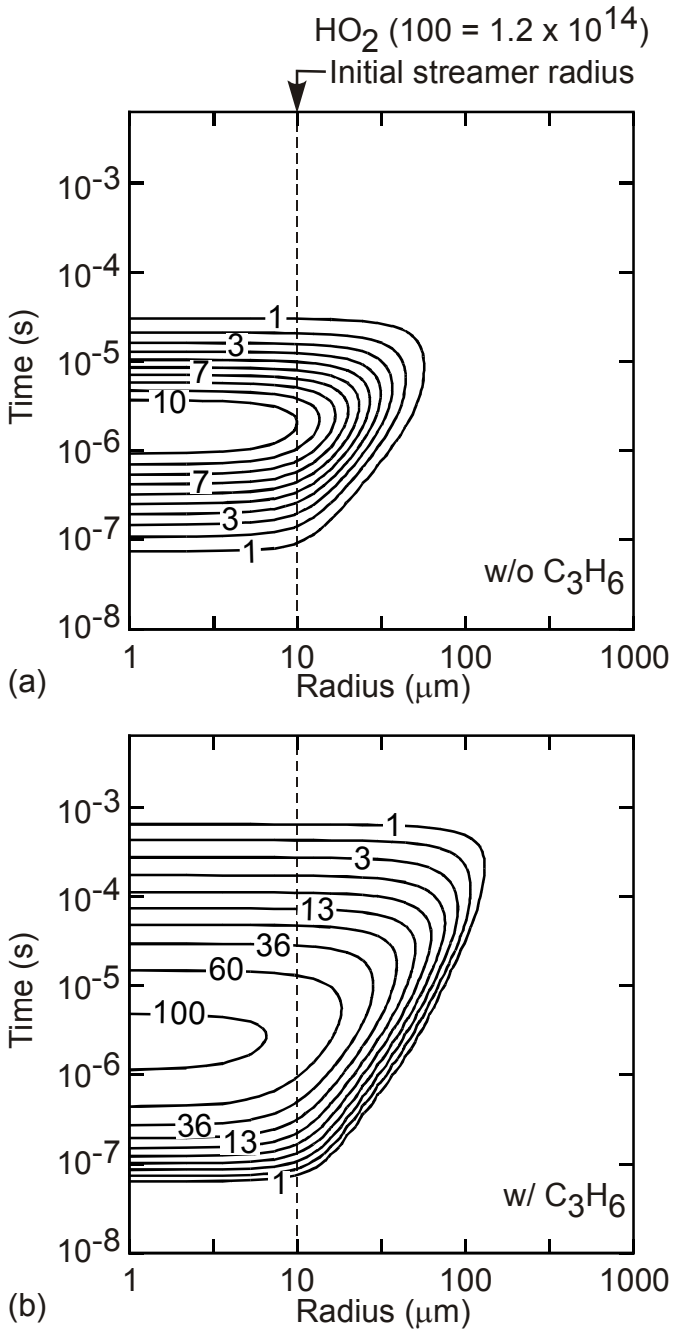

Fig. 6.6. Density of HO_2 (cm^{-3}). (a) Without C_3H_6. (b) With C_3H_6. Due to the additional production of HO_2 by C_3H_6 initiated reactions, the densities of HO_2 are larger for the case with C_3H_6.

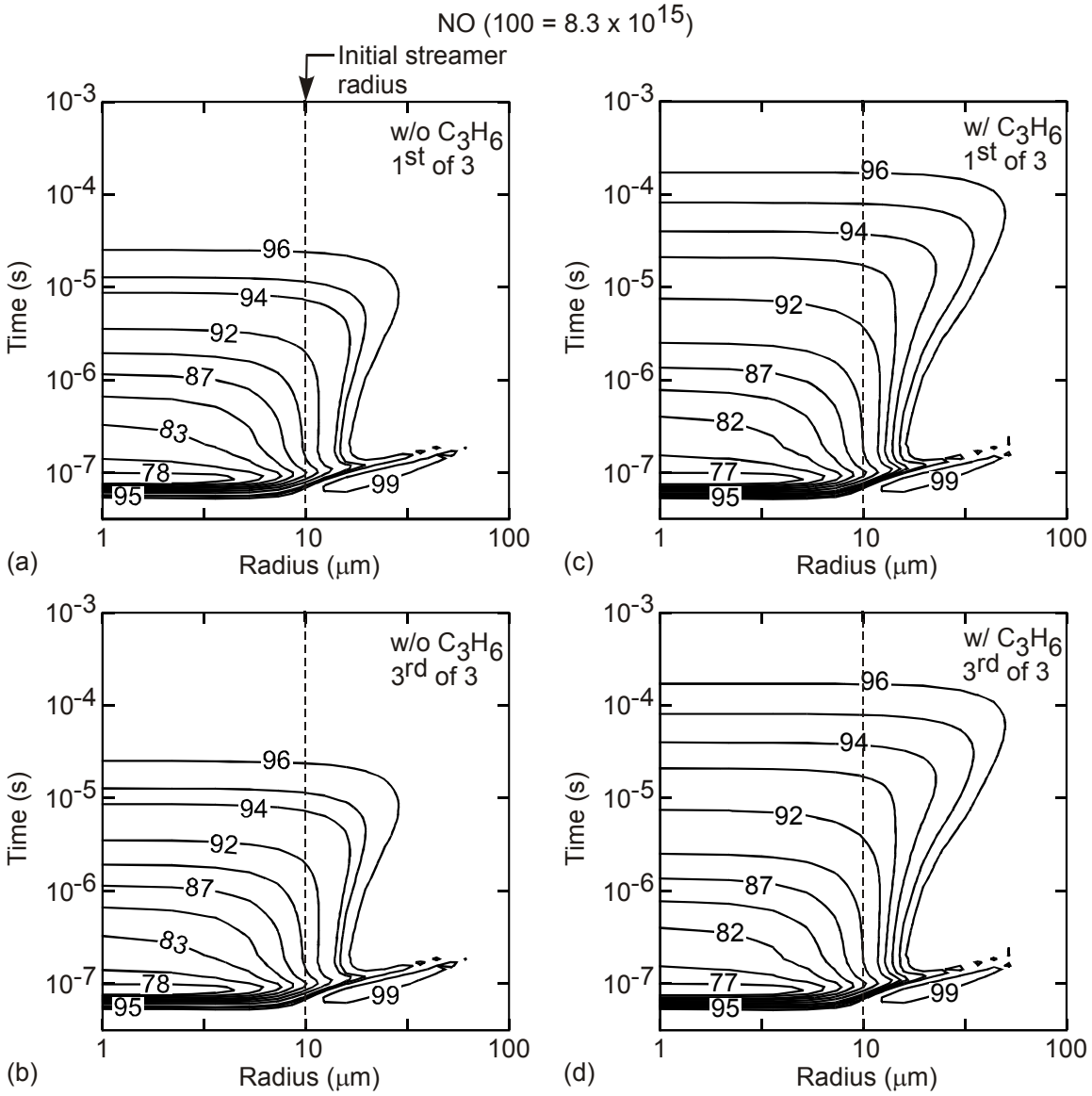

Fig. 6.7. Densities of NO (cm^{-3}). (a) Without C_3H_6, 1st pulse. (b) Without C_3H_6, 3rd pulse. (c) With C_3H_6, 1st pulse. (d) With C_3H_6, 3rd pulse. Conditions are as in Fig. 6.1. In the presence of C_3H_6, larger amount of NO is consumed in the streamer region by reactions with βHAP radicals and as a result NO densities are smaller at any given time compared to the case without C_3H_6.

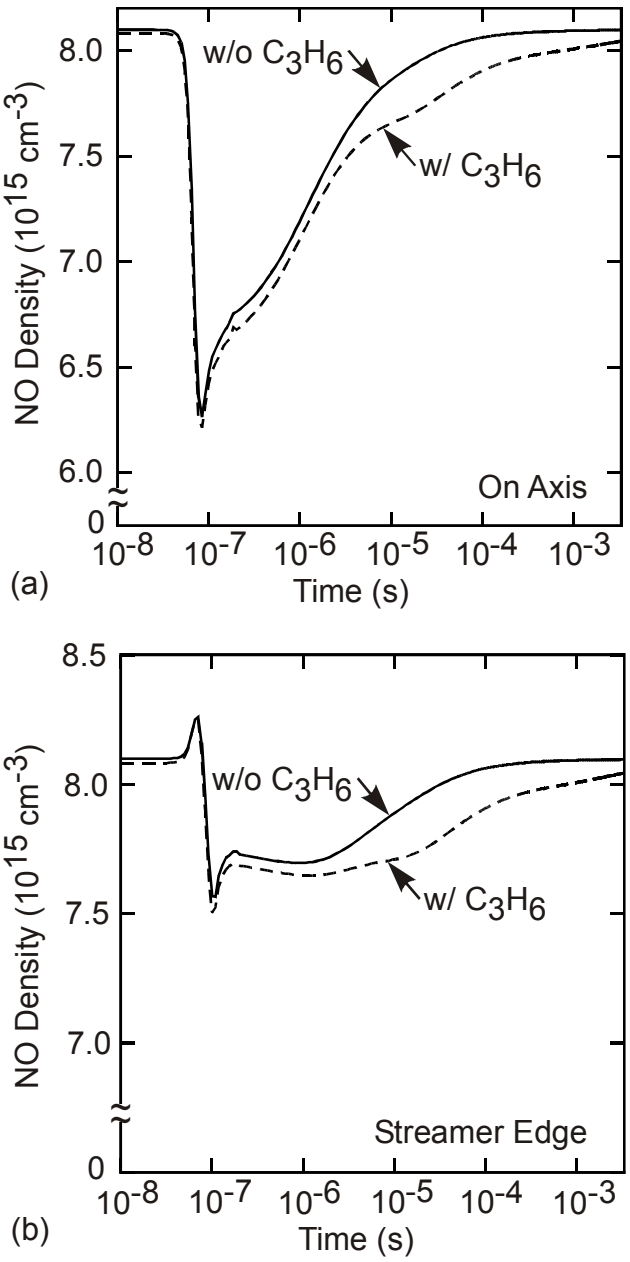

Fig. 6.8. NO density at different locations in the gas. (a) On-axis. (b) Slightly off the streamer edge. Advection at $t \approx$ 70 ns results in depletion of NO along the axis. The radial outward motion of mass results in accumulation of NO near the streamer edge. In the presence of C_3H_6, more NO is consumed by reactions with βHAPs and as a result, NO densities are smaller.

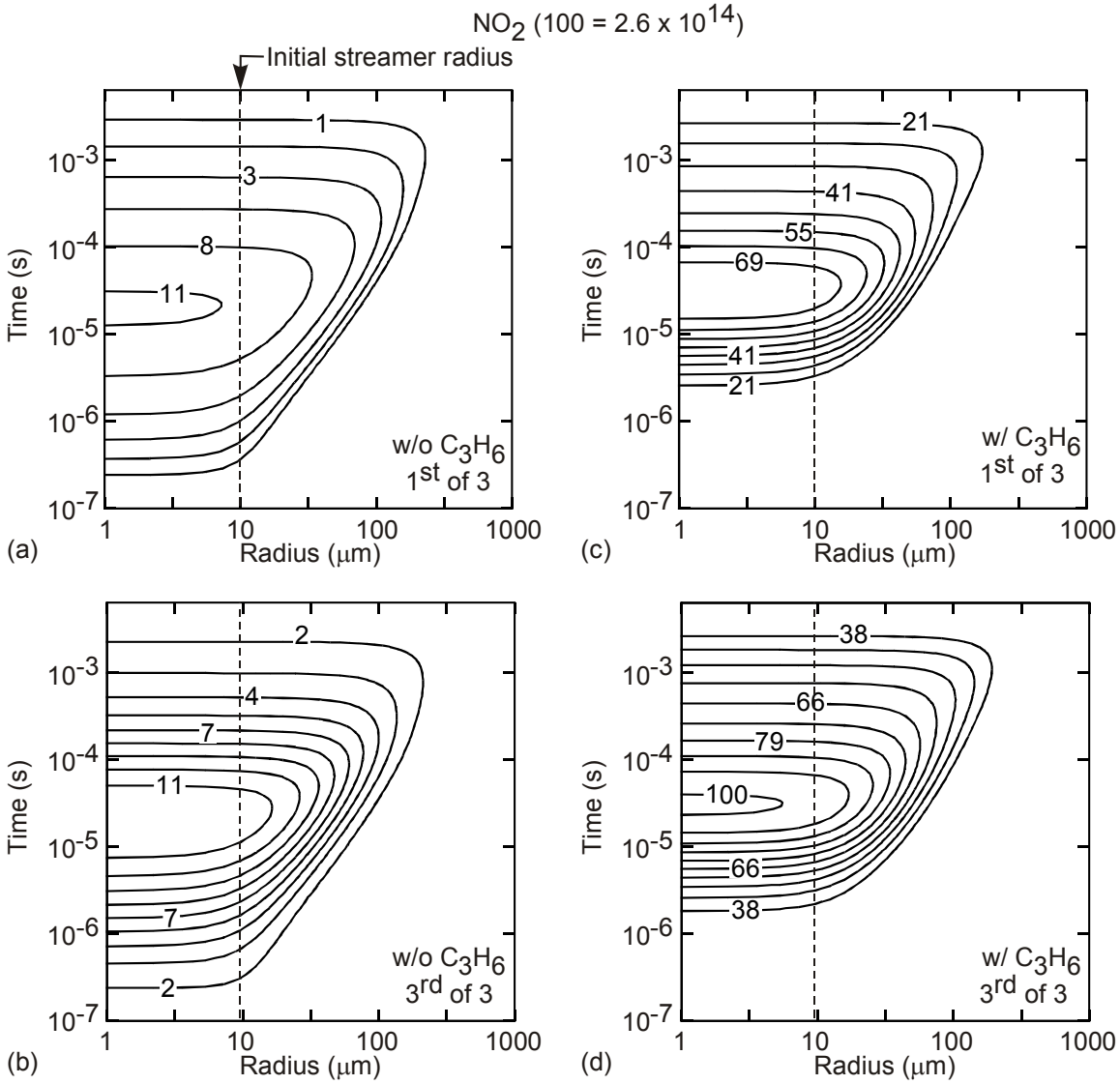

Fig. 6.9. Densities of NO_2 (cm^{-3}). (a) Without C_3H_6, 1st pulse. (b) Without C_3H_6, 3rd pulse. (c) With C_3H_6, 1st pulse. (d) With C_3H_6, 3rd pulse. Conditions are as in Fig. 6.1. Due to the increased conversion of NO to NO_2 in the presence of C_3H_6, NO_2 densities are larger.

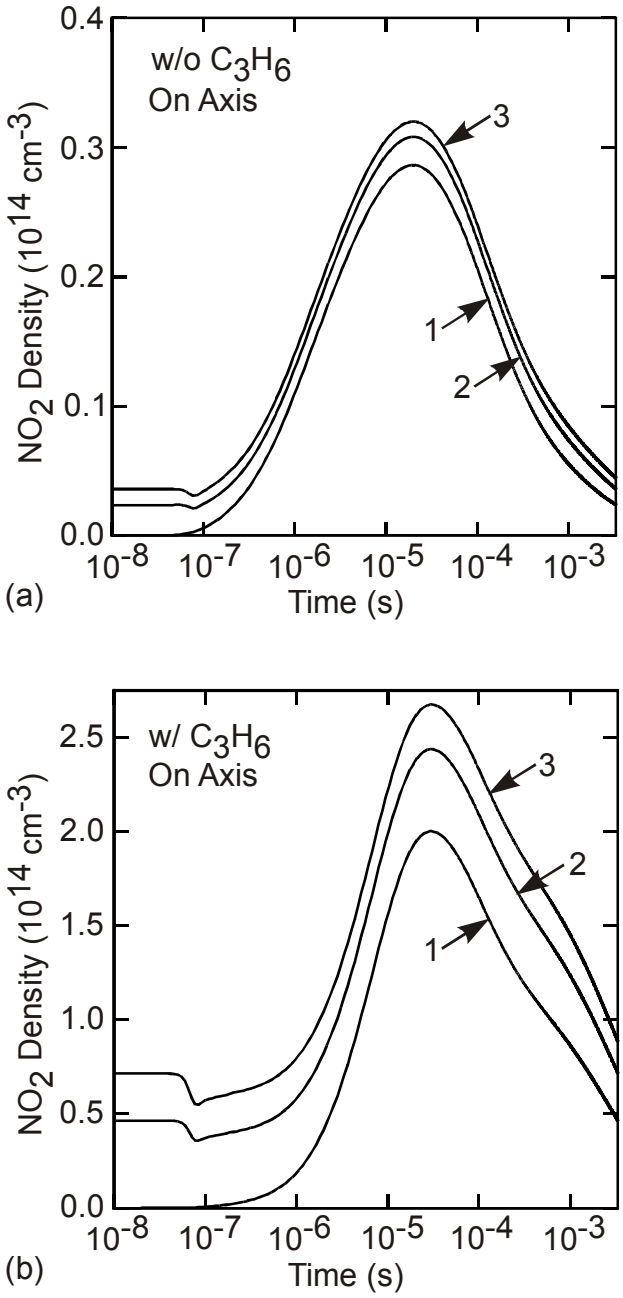

Fig. 6.10. On axis densities of NO. (a) Without C_3H_6. (b) With C_3H_6. Due to the larger production of NO_2 in the presence of C_3H_6, the initial effects of advection are more prominent.

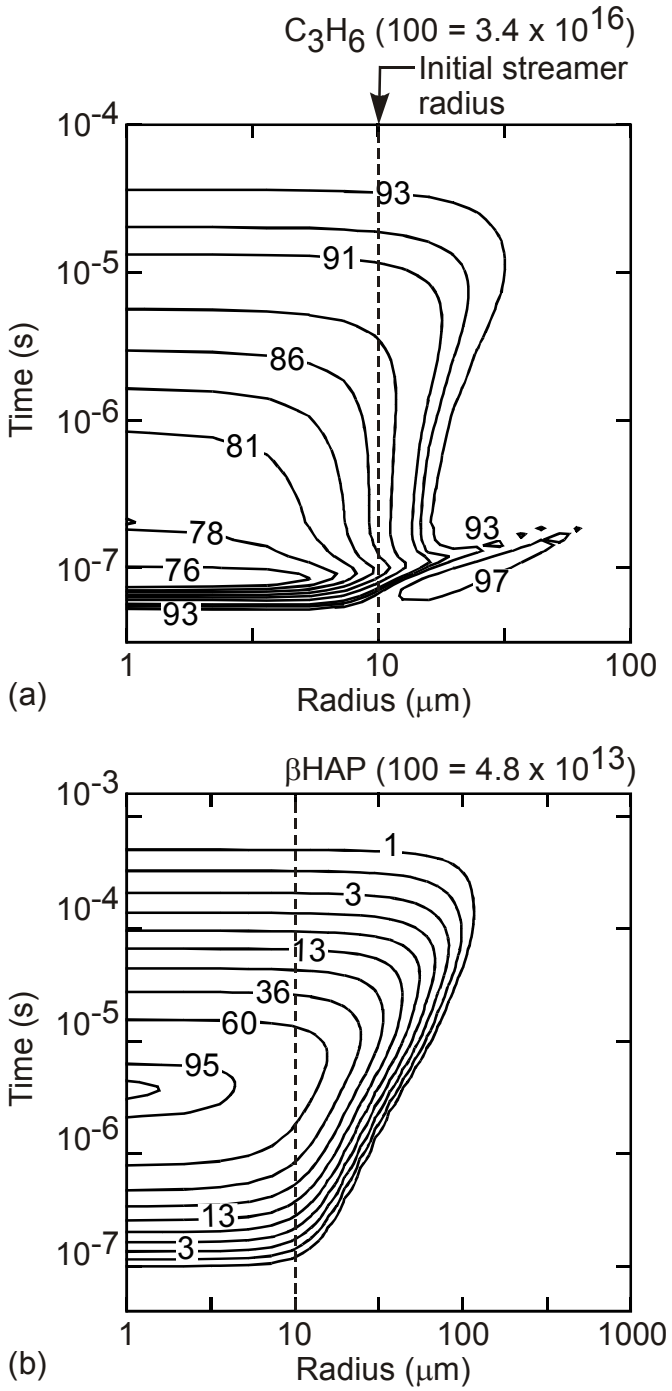

Fig. 6.11. Species density (cm^{-3}). (a) C_3H_6. (b) βHAPs. Radial advection results in movement of C_3H_6 to regions outside of the streamer. C_3H_6 is consumed by reactions with O and OH.

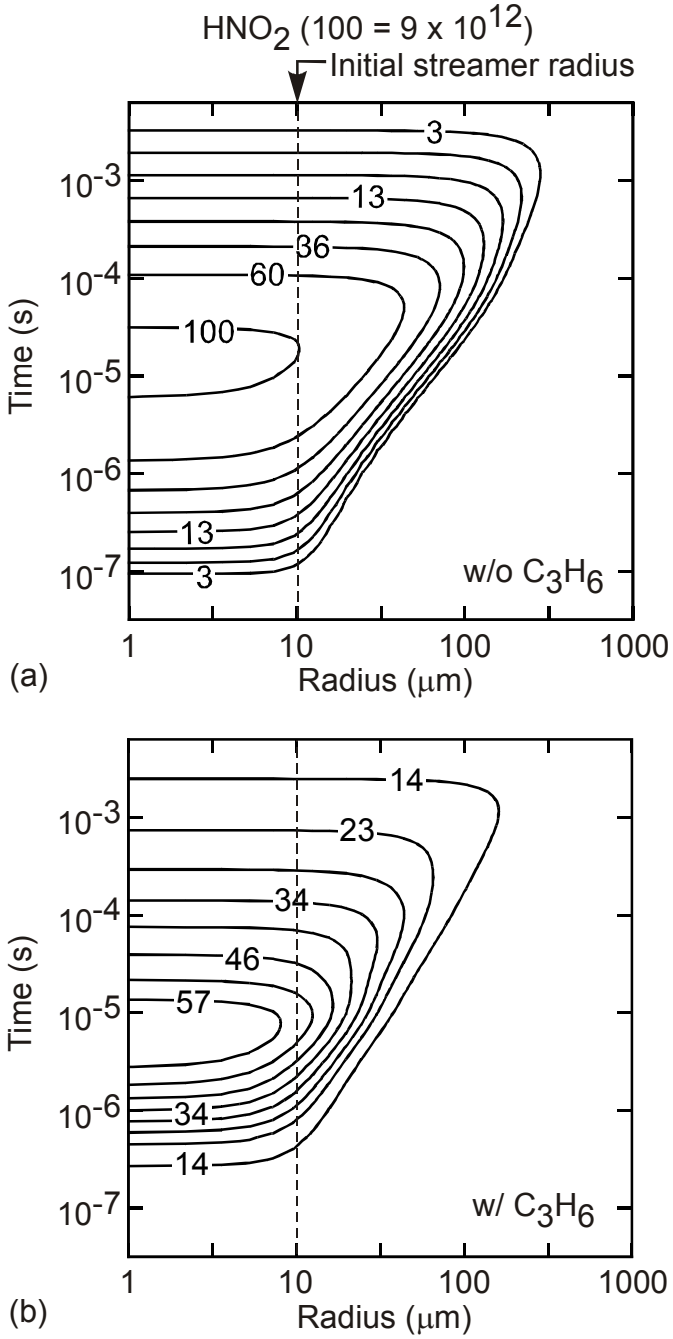

Fig. 6.12. Densities of HNO_2 (cm^{-3}). (a) Without C_3H_6. (b) With C_3H_6. For t< tens of μs, HNO_2 is primarily produced by the reactions of OH with NO. Due to the increased consumption of OH in the presence of C_3H_6, less HNO_2 is produced initially. The larger densities of HNO_2 at longer times in the presence of C_3H_6 are due to the increased densities of HO_2 and NO_2, which also react to produce HNO_2.

6.5 References

1. A. C. Gentile and M. J. Kushner, J. Appl. Phys. **79,** 3877 (1996).
2. R. Dorai, M. S. Thesis, University of Illinois at Urbana-Champaign, 2000.
3. Y. Mirokin and G. Mallard, The NIST Chemical Kinetics Database (1998).
4. R. Atkinson, J. Phys. Chem. Ref. Data **26**, 215 (1997).
5. W. Tsang, and J. T. Herron, J. Phys. Chem. Ref. Data **20**, 609 (1991).
6. D. L. Baulch, C. J. Cobox, R. A. Cox, P. Frank, G. Hayman, Th. Just, J. A. Kerr, T. Murrells, M. J. Pilling, J. Troe, R. W. Walker, and J. Warnatz, J. Phys. Chem. Ref. Data **23**, 847 (1994).
7. R. Atkinson, D. L. Baulch, R. A. Cox, R. F. Hampson Jr., J. A. Kerr, M. J. Rossi, and J. Troe, J. Phys. Chem. Ref. Data **26**, 521 (1997).

7. PLASMA SURFACE MODIFICATION OF POLYPROPYLENE

7.1 Introduction

In this chapter, we present results from our computational investigations on the gas phase and surface kinetics during the modification of polypropylene (PP) in humid-air plasmas. A pseudo-homogeneous global kinetics model interfaced to a surface site balance model was developed and validated against experiments. The consequences of process variables which have experimentally been found to control the resulting surface properties,[1] (energy deposition, relative humidity (RH), gas temperature, and web speed) were investigated. We found that increasing energy deposition not only results in increased densities of peroxy and acid groups on the PP surface, but also increases the production of gas phase byproducts such as N_xO_y and O_3. Increasing the RH resulted in decreased production of O_3 and increased concentrations of peroxy and acid groups on the surface. Increasing the gas temperature increased the surface concentration of peroxy radicals and decreased the concentrations of alcohol, carbonyl, and acid groups. For a given energy deposition, increasing the web speed resulted in decreased densities of peroxy, alcohol, carbonyl, and acid groups on the PP surface.

The modified form of GLOBAL_KIN used for the study is described in Section 2.5. The gas phase reaction mechanism for humid air and the surface reaction mechanism for PP are described in Sections 7.2 and 7.3. Results for plasma surface modification of PP are presented in Section 7.4. Concluding remarks are in Section 7.5.

7.2 Gas Phase Reaction Mechanism for Humid Air

Consider humid air plasma treatment of PP having $N_2/O_2/H_2O$=79/20/1 (1% H_2O corresponds to a RH of approximately 30% at 300 K, 1 atm). The species considered in this model are listed in Appendix A and the gas phase reactions pertaining to them are in Appendix B. The reaction mechanism involves 90 species (65 in the gas phase and 25 on the polymer surface) and nearly 400 reactions.

The fractional energy deposition by electron impact processes as a function of electric field/total gas number density (E/N) is shown in Fig. 7.1 (At 300 K, 1 atm, N ≈ 2.4×10^{19} cm^{-3}). The current pulse typically lasts a few ns during which E/N ≈300-600 Td (1 Td = 1 Townsend = 1.0×10^{-17} V-cm^2). For these E/N, energy is dissipated mainly by electronic excitation and ionization of N_2 and O_2, dissociation of N_2, and vibrational excitation of N_2,

$$e + N_2 \rightarrow N_2^* + e, \tag{7.1}$$

$$e + O_2 \rightarrow O_2^* + e, \tag{7.2}$$

$$e + N_2 \rightarrow N_2^+ + e + e, \tag{7.3}$$

$$e + O_2 \rightarrow O_2^+ + e + e, \tag{7.4}$$

$$e + N_2 \rightarrow N + N + e, \tag{7.5}$$

$$e + N_2 \rightarrow N_2(v) + e. \tag{7.6}$$

In Eqs. 7.1 and 7.2, N_2^* and O_2^* represent the sum of excited states of N_2 and O_2. We used $N_2(A)$ and $O_2(^1\Delta)$ for their characteristics.

Most of the N_2^* relaxes to N_2 by collisions with N_2 while some collide with O_2 to produce O atoms,

$$N_2^* + N_2 \rightarrow N_2 + N_2, \qquad k = 1.9\times10^{-13}\ cm^3 s^{-1}\ [2], \tag{7.7}$$

$$N_2^* + O_2 \rightarrow O + O + N_2, \qquad k = 1.5\times10^{-12}\ cm^3 s^{-1}\ [2], \tag{7.8}$$

where k is the rate coefficient for the reaction.

Most of the O_2^* is consumed by reaction with O_3 (ozone), while a smaller fraction is quenched by collisions with N_2,

$$O_2^* + O_3 \rightarrow O + O_2 + O_2, \qquad k = 5.2\times10^{-11}\exp(-2840/T)\ cm^3 s^{-1},$$

$$k_{298} = 3.8\times10^{-15}\ cm^3 s^{-1}\ [3], \tag{7.9}$$

$$O_2^* + N_2 \rightarrow O_2 + N_2, \qquad k = 3.0\times10^{-18}\exp(-200/T)\ cm^3 s^{-1},$$

$$k_{298} = 1.5\times10^{-18}\ cm^3 s^{-1}\ [4], \tag{7.10}$$

where k_{298} is the reaction rate coefficient at 298 K.

The reaction mechanism for the charged species is given in Fig. 7.2a. The initiation reactions are the ionization of N_2, O_2, and H_2O producing secondary electrons, N_2^+ (Eq. 7.3), O_2^+ (Eq. 7.4) and H_2O^+,

$$e + H_2O \rightarrow H_2O^+ + e + e. \tag{7.11}$$

Most of the N_2^+ reacts with N_2 to form N_4^+ while some N_2^+ undergoes charge exchange with O_2 and H_2O to produce O_2^+ and H_2O^+,

$$N_2^+ + N_2 + M \rightarrow N_4^+ + M, \qquad k = 1.1\times10^{-29}\ cm^6 s^{-1}\ [5]. \tag{7.12}$$

$$N_2^+ + O_2 \rightarrow O_2^+ + N_2, \qquad k = 5.1\times10^{-11}\ cm^3 s^{-1}\ [5], \tag{7.13}$$

$$N_2^+ + H_2O \rightarrow H_2O^+ + N_2, \qquad k = 2.0\times10^{-9}\ cm^3 s^{-1}\ [6]. \tag{7.14}$$

O_2^+ is also formed by the dissociative charge exchange reaction of N_4^+ with O_2,

$$N_4^+ + O_2 \rightarrow O_2^+ + N_2 + N_2, \qquad k = 2.5\times10^{-10}\ cm^3 s^{-1}\ [5]. \tag{7.15}$$

Most of the O_2^+ reacts with H_2O to form the cluster ion $O_2^+\cdot H_2O$ which further reacts with H_2O to form H_3O^+,

$$O_2^+ + H_2O + M \rightarrow O_2^+\cdot H_2O + M, \qquad k = 2.5\times10^{-28}\ cm^6 s^{-1}\ [5], \tag{7.16}$$

$$O_2^+\cdot H_2O + H_2O \rightarrow H_3O^+ + OH + O_2, \qquad k = 1.2\times10^{-9}\ cm^3 s^{-1}\ [5]. \tag{7.17}$$

H_2O^+ also reacts with H_2O to form H_3O^+ and OH,

$$H_2O^+ + H_2O \rightarrow H_3O^+ + OH, \qquad k = 1.7\times10^{-9}\ cm^3 s^{-1}\ [5]. \tag{7.18}$$

Most of the H_3O^+ then forms the cluster ion $H_3O^+ \cdot H_2O$ by reaction with H_2O,

$$H_3O^+ + H_2O + M \rightarrow H_3O^+ \cdot H_2O + M, \qquad k = 5.0 \times 10^{-27}\ cm^6 s^{-1}\ [5]. \tag{7.19}$$

Most of the electrons are lost by three-body attachment to O_2, while some are consumed by recombination with $H_3O^+ \cdot H_2O$ and $O_2^+ \cdot H_2O$,

$$e + O_2 + M \rightarrow O_2^- + M. \tag{7.20}$$

$$e + H_3O^+ \cdot H_2O \rightarrow H + H_2O + H_2O, \tag{7.21}$$

$$e + O_2^+ \cdot H_2O \rightarrow O_2 + H_2O. \tag{7.22}$$

$H_3O^+ \cdot H_2O$ and $O_2^+ \cdot H_2O$ are also neutralized by reactions with O_2^- forming O_2, H, and H_2O,

$$O_2^- + H_3O^+ \cdot H_2O \rightarrow O_2 + H + H_2O + H_2O, \qquad k = 2.0 \times 10^{-6}\ cm^3 s^{-1}\ [5], \tag{7.23}$$

$$O_2^- + O_2^+ \cdot H_2O \rightarrow O_2 + O_2 + H_2O, \qquad k = 2.0 \times 10^{-6}\ cm^3 s^{-1}\ [5]. \tag{7.24}$$

The reaction mechanism for free radical chemistry in the gas phase is shown in Fig. 7.2b. The initiating reactions are the electron impact dissociations of N_2 (Eq. 7.5), O_2, and H_2O producing N, O, OH and H,

$$e + O_2 \rightarrow O + O + e, \tag{7.25}$$

$$e + H_2O \rightarrow OH + H + e. \tag{7.26}$$

N atoms are consumed by reactions with OH, NO, and O_2 forming NO and N_2,

$$N + OH \rightarrow NO + H, \qquad k = 3.8\times10^{-11}\exp(85/T)\ cm^3s^{-1},$$

$$k_{298} = 7.7\times10^{-17}\ cm^3s^{-1}\ [7], \tag{7.27}$$

$$N + NO \rightarrow N_2 + O, \qquad k = 3.4\times10^{-11}\exp(-24/T)\ cm^3s^{-1},$$

$$k_{298} = 3.2\times10^{-11}\ cm^3s^{-1}\ [8], \tag{7.28}$$

$$N + O_2 \rightarrow NO + O, \qquad k = 4.4\times10^{-12}\exp(-3220/T)\ cm^3s^{-1},$$

$$k_{298} = 7.7\times10^{-17}\ cm^3s^{-1}\ [7]. \tag{7.29}$$

Apart from the electron impact dissociation of O_2, other pathways for O production include dissociation of O_2 by N_2^* (Eq. 7.8), and dissociation of O_3 by O_2^* (Eq. 7.9). O atoms are consumed to a large extent by reactions with O_2 to form O_3, and to a smaller extent by reactions with HO_2, OH, and O_3,

$$O + O_2 + M \rightarrow O_3 + M, \qquad k = 3.4\times10^{-34}(T/298)^{-1.2}\ cm^6s^{-1}\ [8]. \tag{7.30}$$

$$O + HO_2 \rightarrow OH + O_2, \qquad k = 2.9\times10^{-11}\exp(-200/T)cm^3s^{-1},$$

$$k_{298} = 1.5\times10^{-11}\ cm^3s^{-1}\ [7], \tag{7.31}$$

$$O + OH \rightarrow H + O_2, \qquad k = 2.3\times10^{-11}\exp(110/T)\,cm^3s^{-1},$$

$$k_{298} = 3.3\times10^{-11}\,cm^3s^{-1}\ [9], \tag{7.32}$$

$$O + O_3 \rightarrow O_2 + O_2, \qquad k = 8.0\times10^{-12}\exp(-2060/T)\,cm^3s^{-1},$$

$$k_{298} = 8.0\times10^{-15}\,cm^3s^{-1}\ [7]. \tag{7.33}$$

OH radicals are produced by the electron impact dissociation of H_2O (Eq. 7.26) and by the reactions of H with O_3, $O_2^+\cdot H_2O$ with H_2O, and O with HO_2,

$$H + O_3 \rightarrow OH + O_2, \qquad k = 1.4\times10^{-10}\exp(-470/T)\,cm^3s^{-1},$$

$$k_{298} = 2.9\times10^{-11}\,cm^3s^{-1}\ [8], \tag{7.34}$$

$$O_2^+\cdot H_2O + H_2O \rightarrow H_3O^+ + OH + O_2, \qquad k = 1.2\times10^{-9}\,cm^3s^{-1}\ [5], \tag{7.35}$$

$$O + HO_2 \rightarrow OH + O_2, \qquad k = 2.9\times10^{-11}\exp(200/T)\,cm^3s^{-1},$$

$$k_{298} = 5.7\times10^{-11}\,cm^3s^{-1}\ [8]. \tag{7.36}$$

OH is primarily consumed by reactions with N (Eq. 7.27) and HO_2 forming NO and H_2O, and secondarily by the reactions with O atoms (Eq. 7.32), O_3, and NO_2,

$$OH + HO_2 \rightarrow H_2O + O_2, \qquad k = 8.0\times10^{-11}\,cm^3s^{-1}\ [8]. \tag{7.37}$$

$$OH + O_3 \rightarrow HO_2 + O_2, \qquad k = 1.9\times10^{-12}\exp(-1000/T)\,cm^3s^{-1},$$

$$k_{298} = 6.6\times10^{-14}\,cm^3s^{-1}\ [10], \tag{7.38}$$

$$OH + NO_2 + M \rightarrow HNO_3 + M, \quad k = 2.2\times10^{-30}(T/298)^{-2.9}\ cm^6 s^{-1}\ [8]. \quad (7.39)$$

H atoms are produced by the electron impact dissociation of H_2O (Eq. 7.26) and by the reactions of N with OH (Eq. 7.27), O with OH (Eq. 7.32), and $H_3O^+ \cdot H_2O$ with O_2^- (Eq. 7.23). H atoms are mainly consumed by reactions with O_3 to form OH (Eq. 7.34), and by reactions with O_2 to form HO_2,

$$H + O_2 + M \rightarrow HO_2 + M, \qquad k = 1.8\times10^{-32}(T/298)^{-0.8}\ cm^6 s^{-1}\ [11]. \qquad (7.40)$$

HO_2 radicals mutually react to produce hydrogen peroxide (H_2O_2), which is also produced by mutual reactions of OH,

$$HO_2 + HO_2 + M \rightarrow H_2O_2 + O_2 + M, \quad k = 1.9\times10^{-33}\exp(980/T)\,cm^6 s^{-1},$$

$$k_{298} = 5.1\times10^{-32}\ cm^6 s^{-1}\ [4]. \qquad (7.41)$$

$$OH + OH + M \rightarrow H_2O_2 + M, \qquad k = 6.9\times10^{-31}(T/298)^{-0.8}\ cm^6 s^{-1}\ [4]. \qquad (7.42)$$

H_2O_2 is consumed by reactions with OH to form H_2O and HO_2,

$$H_2O_2 + OH \rightarrow H_2O + HO_2, \qquad k = 2.9\times10^{-12}\exp(-160/T)\,cm^6 s^{-1},$$

$$k_{298} = 1.7\times10^{-12}\ cm^3 s^{-1}\ [4]. \qquad (7.43)$$

Major N-containing products in the gas phase include NO, NO_2, N_2O, N_2O_5, HNO_2, and HNO_3. NO is produced dominantly by the reactions of N with OH (Eq. 7.27), N with O_2 (Eq. 7.29), and O with NO_2,

$$\text{O} + \text{NO}_2 \rightarrow \text{NO} + \text{O}_2, \qquad k = 6.5\times10^{-12}\exp(120/T)\ cm^3 s^{-1},$$

$$k_{298} = 9.7\times10^{-12}\ cm^3 s^{-1}\ [7]. \qquad (7.44)$$

NO is consumed primarily by reactions with N (Eq. 7.28), O_3, OH, and HO_2, forming N_2, NO_2, HNO_2, and NO_2 respectively,

$$\text{NO} + \text{O}_3 \rightarrow \text{NO}_2 + \text{O}_2, \qquad k = 4.3\times10^{-12}\exp(-1598/T)\,cm^3 s^{-1},$$

$$k_{298} = 2.1\times10^{-14}\ cm^3 s^{-1}\ [12], \qquad (7.45)$$

$$\text{NO} + \text{OH} + \text{M} \rightarrow \text{HNO}_2 + \text{M}, \qquad k = 8.6\times10^{-31}(T/298)^{-2.5}\exp(34/T)\ cm^6 s^{-1},$$

$$k_{298} = 9.7\times10^{-31}\ cm^6 s^{-1}\ [13], \qquad (7.46)$$

$$\text{NO} + \text{HO}_2 \rightarrow \text{NO}_2 + \text{OH}, \qquad k = 3.5\times10^{-12}\exp(240/T)\,cm^3 s^{-1},$$

$$k_{298} = 7.8\times10^{-12}\ cm^3 s^{-1}\ [12]. \qquad (7.47)$$

NO_2 is produced mainly by the reactions of NO with O_3 and HO_2 (Eqs. 7.45 and 7.47), and by the reaction of OH with HNO_2,

$$\text{OH} + \text{HNO}_2 \rightarrow \text{NO}_2 + \text{H}_2\text{O}, \qquad k = 1.8\times10^{-11}\exp(-390/T)\,cm^3 s^{-1},$$

$$k_{298} = 4.9 \times 10^{-12}\ cm^3 s^{-1}\ [8]. \qquad (7.48)$$

Important consumption channels for NO_2 include reactions with OH, O, and N forming HNO_3 (Eq. 7.39), NO (Eq. 44), N_2O (nitrous oxide), and NO_3,

$$NO_2 + N \rightarrow N_2O + O, \qquad k = 2.4 \times 10^{-12}\ cm^3 s^{-1}\ [5], \qquad (7.49)$$

$$NO_2 + O + M \rightarrow NO_3 + M, \qquad k = 9.0 \times 10^{-32} (T/298)^{-2.0}\ cm^6 s^{-1}\ [8]. \qquad (7.50)$$

NO_3 is also produced by the reaction of OH with HNO_3,

$$OH + HNO_3 \rightarrow NO_3 + H_2O, \qquad k = 1.5 \times 10^{-14} \exp(650/T)\ cm^3 s^{-1},$$

$$k_{298} = 1.3 \times 10^{-13}\ cm^3 s^{-1}\ [10]. \qquad (7.51)$$

NO_3 is consumed by reactions with NO_2 forming N_2O_5 (dinitrogen pentoxide),

$$NO_3 + NO_2 + M \rightarrow N_2O_5 + M, \qquad k = 2.7 \times 10^{-30} (T/298)^{-3.4}\ cm^6 s^{-1}\ [7]. \qquad (7.52)$$

N_2O_5 decomposes to regenerate NO_2 and NO_3,

$$N_2O_5 \rightarrow NO_3 + NO_2, \qquad k = 9.7 \times 10^{14} (T/298)^{0.1} \exp(-11080/T)\ s^{-1},$$

$$k_{298} = 0.07\ s^{-1}\ [4]. \qquad (7.53)$$

HNO_2 is primarily produced by the reaction of OH with NO (Eq. 7.46) and dominantly consumed by the reaction with OH to form NO_2 (Eq. 7.48). HNO_3 is produced by the reaction of OH with NO_2 (Eq. 7.39) and is consumed by reaction with OH to form NO_3 (Eq. 7.51).

7.3 Surface Reaction Mechanism For PP

PP is a saturated hydrocarbon polymer with a carbon backbone containing hydrogen and methyl ($-CH_3$) groups arranged in an alternating fashion. We used 10^{15} cm^{-2} for the total density of surface sites, as reported for virgin PP.[14]

The reactivities of the hydrogen groups in PP depend on the nature of the C atom to which they are attached. There are three types of C atoms in any given monomer unit of PP, primary C, to which only one C atom is bonded; secondary C, to which two C atoms are bonded; and tertiary C, to which three C atoms are bonded (see Fig. 7.3a). In general, the reactivities of hydrogen bound to these C atoms scale as: $H_{tert} > H_{sec} > H_{pri}$.

A monomer unit of PP consists of two secondary H atoms, a tertiary H atom, and a methyl ($-CH_3$) group. Assuming equal likelihood for any of these four groups to be pointing out towards the plasma, their initial surface densities are, $N_{H,sec} = 0.5 \times 10^{15}$ cm^{-2}, $N_{H,tert} = 0.25 \times 10^{15}$ cm^{-2}, and $N_{methyl} = 0.25 \times 10^{15}$ cm^{-2}. The total number of surface sites is, however, allowed to vary with treatment time. When a "hole" is made in the PP chain, the diffusing species are allowed to react with the newly formed dangling bonds in the broken chains as well as with the exposed PP chain below, as shown in Fig. 7.3b.

The plasma surface modification of PP is primarily oxidative by reactions with free radicals in the gas phase. The reactions with gas phase ions can be neglected in comparison. The loss frequencies for ions in the gas phase are orders of magnitude larger than their loss frequencies with PP and as a result, ions are preferentially consumed in the gas phase. For example, the loss frequency for $H_3O^+ \cdot H_2O$ in the gas phase is $\approx 10^7$ s^{-1}. For a unit reaction probability for the reaction with the PP surface, the loss frequency for $H_3O^+ \cdot H_2O$ is $\approx 10^4$ s^{-1}. The densities of free radicals are generally both larger and are sustained for longer periods in the gas phase (~ ms) and so their reactions with the PP surface are more important in comparison. The ions arriving at the PP surface are thermal due to the collisional sheath and so do not contribute to energy activated reactions with PP such as sputtering. On that basis we have little justification to differentiate ions from the free radicals with respect to their reactivities.

The surface reaction mechanism for PP is given in Table 7.1. In general, the eactions can be classified as: initiation, propagation, and termination.

7.3.1 Initiation

The initiating reactions are abstractions of hydrogen from the PP chain. Although cleavage of PP at the C-C bond is possible, the resulting radicals, due to their mutual proximity have been found to quickly recombine to yield back the polymer. The dominant reactive species in the gas phase are O_2^*, O_3, H, N, HO_2, O, and OH. Investigations have shown that O_2^* reactions on saturated hydrocarbons are slow at best.[15] The rate constant for O_3 reactivity on PP is 1.3×10^{-22} cm^3 s^{-1},[16] which is at least a few orders of magnitude smaller than both the rate constant for the gas phase

consumption of O_3 and the rate constant for the reaction of O or OH with PP (which is ≈ 10^{-11} cm^3 s^{-1} [8]). The reactivities for H abstraction by H atoms are two to four orders of magnitude smaller than those for O or OH and hence, H atoms are less likely to be a significant source of H abstraction.[17] Similarly, the reactivities of N and HO_2 towards PP are significantly smaller compared to those of O and OH and so can be safely neglected. Oxidation by molecular oxygen is not likely since gas temperatures above 700 K are typically required for such processes to be important.

OH has been observed spectroscopically during the oxidation of hydrocarbon polymers by atomic oxygen as evidence of H-abstraction.[18] H can be abstracted from any of the primary, secondary, and tertiary sites in PP. The probability of abstraction scales as $H_{tert} > H_{sec} > H_{pri}$ and this ranking is generally independent of the nature of the attacking radical.[19] This trend is supported by the observation that oxidative attack in atactic PP (a configuration of PP in which the methyl groups are placed randomly on both sides of the chain) at tertiary sites is approximately 20 times faster than at secondary sites.[20] Another example is the abstraction of H from iso-butane (iso-C_4H_{10}) by O atoms,

$$\text{O + iso-}C_4H_{10} \rightarrow \text{OH + iso-}C_4H_9, \qquad k_{iso,298} = 2.0\times10^{-15}\ cm^3 s^{-1}\ [8], \tag{7.54}$$

$$\text{O + iso-}C_4H_{10} \rightarrow \text{OH + tert-}C_4H_9, \qquad k_{tert,298} = 150.0\times k_{iso,298}\ [8]. \tag{7.55}$$

The rate of tertiary H abstraction is 150 times larger than that of secondary H. Similar trends have been observed in reactions of O with n-heptane where rate constants for

abstraction of secondary hydrogen are approximately two orders of magnitude larger than those for primary hydrogen.[8]

O atoms abstract H from PP to produce a PP alkyl radical and OH,

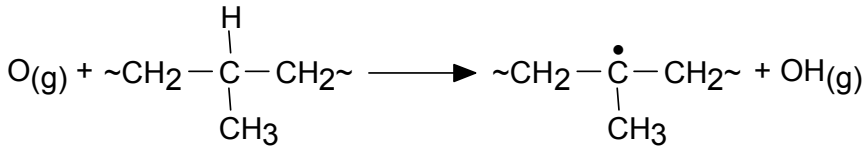

(7.56)

Based on the work by Gomez *et al.* [21], at atmospheric pressure the surface reaction probability for this reaction is < 0.01. For this work, we used $\gamma_{tert} = 10^{-3}$, $\gamma_{sec} = 10^{-4}$, and $\gamma_{pri} = 10^{-5}$.

OH radicals also abstract H from PP to produce a PP alkyl radical and H_2O,

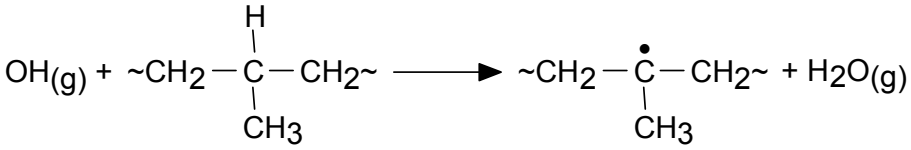

(7.57)

As reaction probabilities for H-abstraction by OH are not well known, estimates were obtained based on analogies with rate constants for gas phase reactions of OH with long chain saturated hydrocarbons. The rate constant for the reaction of OH with large hydrocarbon molecules (for example, $C_{16}H_{34}$) is $\approx 2.5\times10^{-11}$ cm^3 s^{-1}.[8] A gas-kinetic rate constant is $\approx 10^{-10}$ cm^3 s^{-1}. Assuming that a unit surface reaction probability corresponds to a gas-kinetic rate constant, the surface reaction probability for H abstraction from PP by OH can be estimated as $\gamma_{tert} = 0.25$. Also, the branching ratios for H-abstractions from

the tertiary, secondary, and primary sites of long chain saturated hydrocarbons in the gas phase are such that $k_{tert}/k_{sec} \approx 5$ and $k_{sec}/k_{pri} \approx 20$.[8] Therefore we estimated that $\gamma_{sec} = 0.05$ and $\gamma_{pri} = 0.0025$.

This method of estimating surface reaction probabilities typically provides only a lower limit. There are other factors such as orientation of the reactant with respect to the surface, its angle of incidence, and the catalytic activity of the surface which influence the surface reaction probabilities. For a strong interaction with the surface, this approach likely provides a reasonable lower limit to the reactivity because of neglect of the catalytic effect of the surface. For a weak interaction, this method provides a better estimate.

7.3.2 Propagation

The PP alkyl radicals produced by H abstraction by O and OH (Eqs. 66 and 67) react with O_2 to form PP peroxy radicals,

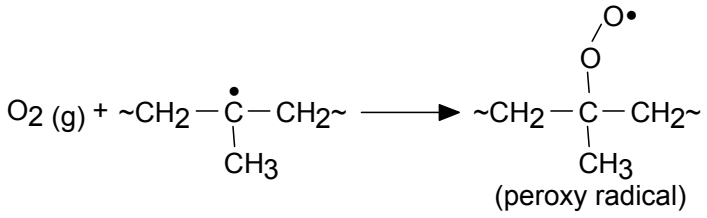

(7.58)

The reactivity of O_2, however, depends on the nature of the alkyl radicals. Studies by Kuzuya *et al.* showed that mid-chain alkyl radicals are much less reactive with O_2 compared to end-chain alkyl radicals.[22] The reactions with end-chain radicals are usually diffusion controlled [19] and can be taken to occur at close to the encounter frequency.[23]

The PP alkyl radicals can also react with O to form alkoxy radicals [18],

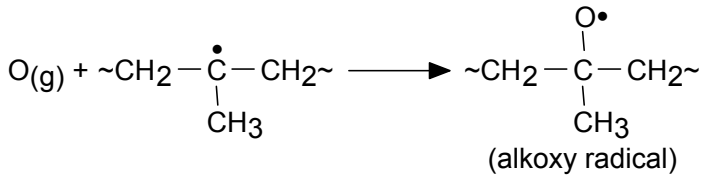

(7.59)

This direct pathway to the formation of alkoxy radicals is not significant. Hydrocarbon alkyl radicals are known to react with O_3 in the gas phase at a rate up to five times faster than O_2.[24] The analogous process for reactions of O_3 with alkyl surface groups could be a possible route to alkoxy radical formation,

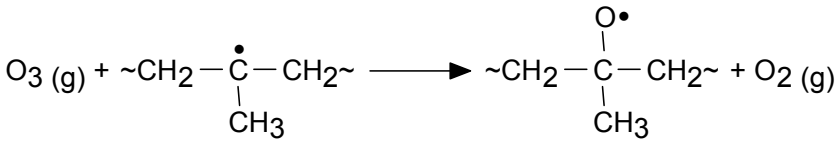

(7.60)

The PP peroxy radicals abstract hydrogen from other polymer chains or from neighboring sites on the same chain to yield PP hydroperoxides.[19] The ratio of intermolecular to intramolecular attack on the H sites by peroxy radicals is ≈1:13.[15] The intramolecular attack, being more favored, leads to sequences of neighboring hydroperoxide groups along a backbone. This series of reactions has been observed during the early stages of oxidation of PP,[15]

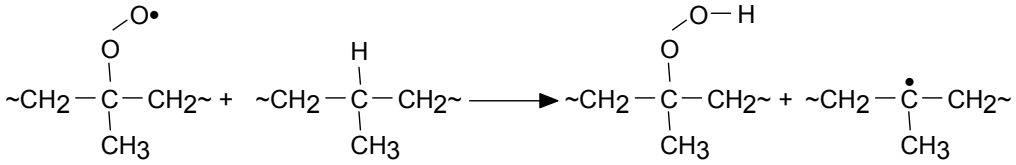

(7.61)

,

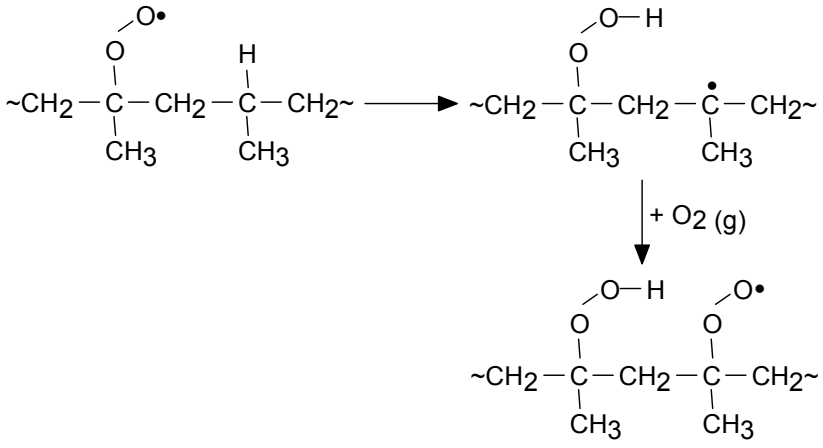

(7.62)

The mean time for the reaction of polymer peroxy radicals between propagation steps, based on their reaction with neighboring tertiary radicals, is ≈5 s.[15] Decomposition of the resulting hydroperoxides leads to a variety of oxidized functional groups.[19] This decomposition, is however slow compared to the formation of alkoxy or peroxy radicals. For example, Poncin-Epaillard *et al.* [25] exposed PP previously treated by a N_2-plasma to O_2. Hydroperoxides were formed, with densities up to 10^{16} cm^{-2}, which then decomposed with a half life of 30 h. This long-term decomposition of the hydroperoxides is excluded from the reaction mechanism as the residence times for the conditions of interest are at best a few seconds. However, note should be made that the hydroperoxides are not necessarily the end products.

Polymer alkoxy radicals ($PO^{\bullet}$) are the main source of the chain backbone scission that typically occurs during the oxidation of PP.[19,26] The rate coefficient for the β-scission of PP alkoxy radicals is $k \approx 10^3$ s^{-1}.[15] Such β-scissions on tertiary carbon atoms lead to the formation of ketones while those on secondary carbon atoms result in aldehydes,

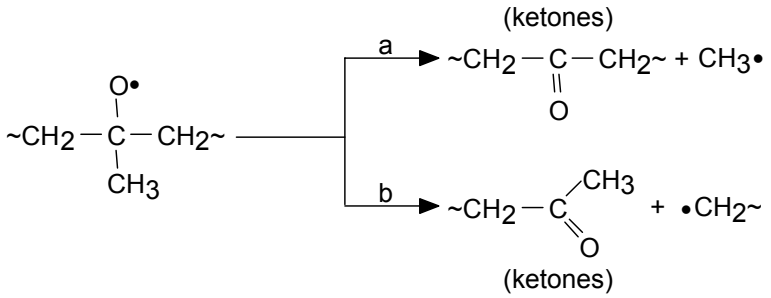

(7.63)

,

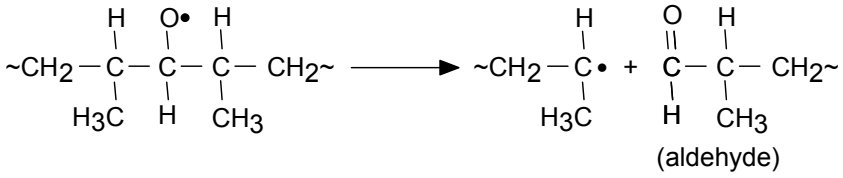

(7.64)

.

In the β-scission of tertiary alkoxy radicals (Eq. 7.63), channel (b) is more favorable because the resulting secondary polymer hydrocarbon radical is more stable than the primary CH_3 radical formed by channel (a). β-scission is known to account for only 65% of the alkoxy degradation. The remaining alkoxies react with the PP matrix to produce alcohol groups.[27]

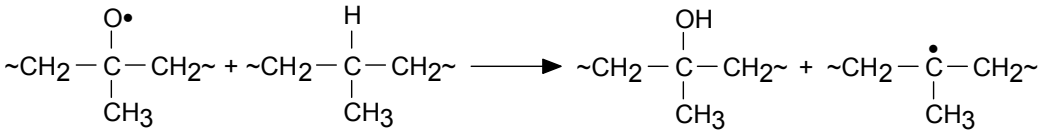

(7.65)

.

Further reactions of the alcohol groups with O and OH radicals regenerate alkoxy radicals,

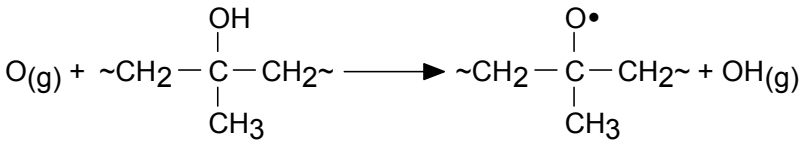

(7.66)

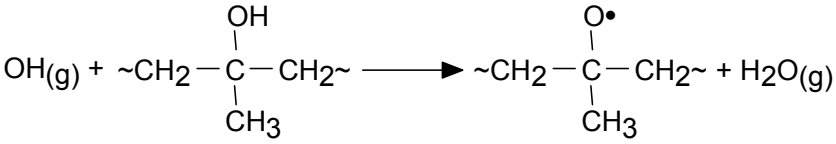

(7.67)

Erosion of PP to produce gas phase products is initiated by the abstraction of H in the aldehydes groups by O or OH to produce carbonyl radicals. These carbonyl radicals further react with O atoms to produce CO_2 and PP alkyl radicals,

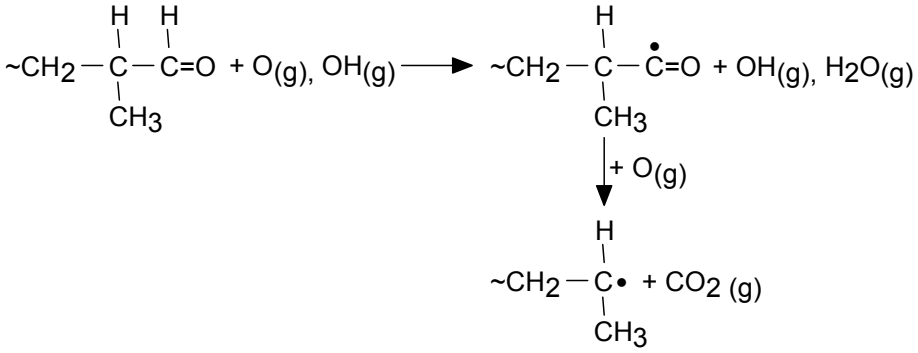

(7.68)

The etched product CO_2 exposes the site beneath for further oxidation.

7.3.3 Termination

While hydrogen atoms are less likely than O or OH to abstract H from PP, they compete with O and OH for the PP alkyl radicals,[28]

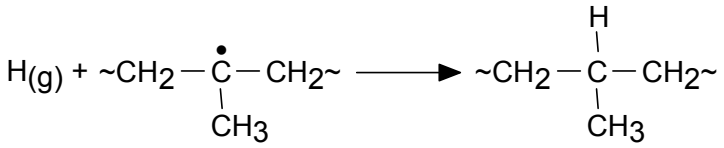

(7.69)

Reactions of OH with alkyl and carbonyl radicals result in the formation of alcohols and acids,

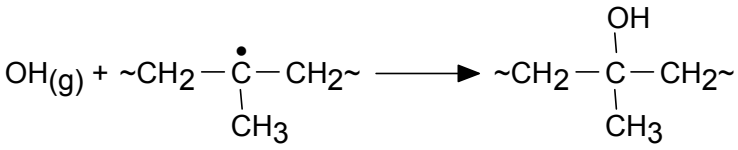

(7.70)

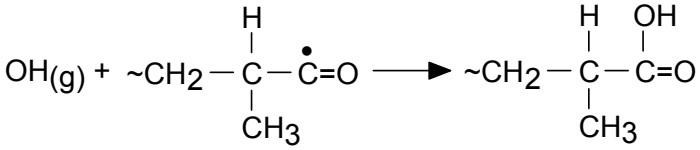

(7.71)

These reactions are considered terminal because of the stability of the end products compared to the free radicals.

7.4 Plasma Surface Modification of Polypropylene

To validate the surface reaction mechanism, comparisons were made to experiments conducted by O'Hare *et al*.[29] for humid-air plasma treatment of PP. The gas composition was $N_2/O_2/H_2O$ = 78.9/20.0/1.1, at 1 atm and initially 300 K (1.1% H_2O corresponds to a RH of ≈30%). The downstream electrode length is 12 cm and the PP web speed is 250 cm/s producing a gas residence time of 0.05 s. The applied voltage is

sinusoidal at 9.6 kHz across a 3 mm gap providing 460 voltage pulses per site. The energy deposition was varied (0 - 1.5 J-cm^{-2}) by changing the applied voltage (0 - 20 kV). The base case uses 0.8 J-cm^{-2}.

The electron density (n_e) and electron temperature (T_e) for the first, last, and select intermediate pulses as a function of time for the base case are shown in Fig. 7.4. The time scale is relative to the beginning of each voltage pulse. During the first voltage pulse, the potential across the gap is mainly a result of the applied voltage. The seed electrons accelerated by the electric field gain energy and ionize the background gases, N_2, O_2, and H_2O, producing secondary electrons, N_2^+, O_2^+, and H_2O^+ (Eqs. 7.3, 7.4, and 7.11). For the first pulse, the peak electron temperature is 3.4 eV and the peak electron density is 7×10^{12} cm^{-3}.

With the flow of current through the discharge, the dielectric on the surface of the electrodes is charged, thereby removing voltage from the gap and terminating the discharge. During subsequent pulses, the voltage across the dielectric adds to the gap voltage, enabling a more rapid avalanche and shorter current pulses producing larger n_e (5×10^{13} cm^{-3}) and T_e (6.0 eV) compared to the first pulse. The differences in n_e after 10^{-7} s for pulses later than the first are due to changes in the composition of the background gases.

The peak E/N during later discharge pulses is ≈400 Td for which nearly 70% of the energy deposition is expended in the electronic excitation of N_2 (Eq. 7.1) and about 10% is expended in the electron excitation of O_2 (Eq. 7.2). The densities of N_2^* and O_2^* during the first, last, and select intermediate pulses as a function of time are shown in Fig. 7.4. Most of the N_2^* (> 90%) and a smaller amount of O_2^* (< 10%) are quenched by

collisions with the background gases (Eqs. 7.7 and 7.10). Other channels for N_2^* consumption (< 10%) include reactions with O_2 to produce O (Eq. 7.8). The dominant channel for O_2^* consumption is the reaction with O_3 to produce O (Eq. 7.9). O_2^* is less reactive compared to N_2^* and hence, its density accumulates over the pulses.

Other channels for electron energy loss include ionization of N_2 and O_2 to produce N_2^+ and O_2^+ (Eqs. 7.4 and 7.5), whose densities are shown in Fig. 7.5. Due to the nearly constant density of N_2 and O_2 and similarity in loss channels, the differences in the densities of N_2^+ and O_2^+ with pulses after the first are small. N_2^+ is lost by association with N_2 to form N_4^+ (Eq. 7.12). N_4^+ charge exchanges with O_2 to form O_2^+ (Eq. 7.15), which further reacts with H_2O to form the cluster ion $O_2^+ \cdot H_2O$ (Eq. 7.16). $O_2^+ \cdot H_2O$ reacts with H_2O to form H_3O^+, which further reacts with H_2O to produce $H_3O^+ \cdot H_2O$ (Eqs. 7.17 and 7.19). The time dependence of the densities of $H_3O^+ \cdot H_2O$ and the dominant negative ion, O_2^-, for the first, last, and select intermediate pulses are also shown in Fig. 7.5. O_2^- is produced by the attachment of electrons to O_2 (Eq. 7.20). $H_3O^+ \cdot H_2O$ and O_2^- recombine to yield O_2, H, and H_2O (Eqs. 7.23 and 7.24).

Electron impact dissociation of the background gases produces N, O, and OH (Eqs. 7.5, 7.25, and 7.26), whose densities are shown in Fig. 7.6. N atoms are consumed by reactions with OH and O_2 (Eqs. 7.27 and 7.29) to produce NO; and with NO to produce N_2 (Eq. 7.28). The contributions of the reactions with OH, NO, and O_2 towards N consumption are 40%, 45%, and 10% respectively. N being less reactive than other radicals accumulates in the discharge from pulse to pulse.

The electron impact dissociation of O_2 (Eq. 7.25) accounts for ≈25% of the O atom production; while dissociation of O_2 by N_2^* (Eq. 7.8) and O_3 by O_2^* (Eq. 7.9) each

contribute ≈30%. O atoms are primarily consumed by reactions with O_2 (≈85%) to form O_3 (Eq. 7.30); and with HO_2 (6%), OH (4%), and O_3 (2%) to produce O_2 (Eqs. 7.31-7.33). After a few hundreds of pulses, the density of O reaches a periodic steady state.

Although the initial inventory of OH in a given pulse is created by electron impact dissociation of H_2O (Eq. 7.26), the contribution of this process to the overall production of OH is only 2%. Dominant channels for OH production include reactions of H with O_3 (Eq. 7.34), $O_2^+ \cdot H_2O$ with H_2O (Eq. 7.35), and O with HO_2 (Eq. 7.36) with their contributions being 35%, 35%, and 20% respectively. OH is primarily consumed by reactions with N (Eq. 7.27) and HO_2 (Eq. 7.37) forming NO (≈30%) and H_2O (≈30%) respectively; and by reactions with O (Eq. 7.32), O_3 (Eq. 7.38), and NO_2 (Eq. 7.39) with their contributions being 11%, 18%, and 7%. The density of OH increases with pulses due to the increase in the density of O_3 (see below), which reacts with H to produce OH (Eq. 7.34). Similar to O, the density of OH reaches a periodic steady state after a few hundreds of pulses.

The densities of H, HO_2, and O_3 as a function of time are shown in Fig. 7.7. H atoms are mainly produced by the reactions of N with OH (Eq. 7.27), O with OH (Eq. 7.32), and $H_3O^+ \cdot H_2O$ with O_2^- (Eq. 7.23), with their contributions being 38%, 15%, and 42%. H atoms primarily react with O_3 to form OH (Eq. 7.34), and with O_2 to form HO_2 (Eq. 7.40). The density of H reaches a periodic steady state within 10s of pulses.

HO_2 (hydroperoxy) radicals are formed by the reactions of H with O_2 (Eq. 7.40). The production of HO_2 dominantly occurs during the first microsecond. Later, consumption of HO_2 by reactions with HO_2 (Eq. 7.41) and NO (Eq. 7.47) to produce

H_2O_2 and NO_2 dominate. As HO_2 is less reactive, its density also accumulates from pulse to pulse.

O_3 is produced by the reaction of O with O_2 (Eq. 7.30) and is primarily consumed by reactions with O_2^* (66%, Eq. 7.9), H (12%, Eq. 7.34), and OH (10%, Eq. 7.38) to form O, OH, and HO_2. The rapid production of O_3 from O and O_2 dominates over losses and so O_3 accumulates from pulse to pulse.

N-containing products in the gas phase include NO and NO_2, whose densities are shown in Fig. 7.8. NO is produced by the reactions of N with OH (Eq. 7.27), N with O_2 (Eq. 7.29), and O with NO_2 (Eq. 7.23), with their contributions being 70%, 15%, and 10%. NO is consumed primarily by reactions with N, O_3, OH, and HO_2 to produce N_2 (Eq. 7.28), NO_2 (Eq. 7.45), HNO_2 (Eq. 7.46), and NO_2 (Eq. 7.47) respectively, with contributions of 60%, 20%, 10%, and 10%. Due to the increase in the density of N and OH with time (see Fig. 7.6), more NO is progressively generated by the reaction of N with OH (Eq. 7.27).

NO_2 is produced mainly by the reactions of NO with O_3 and HO_2 (Eqs. 7.45 and 7.47), and OH with HNO_2 (Eq. 7.48), with their contributions being 50%, 22%, and 21% respectively. NO_2 is primarily consumed by reactions with OH, O, N forming HNO_3 (Eq. 7.39), NO (Eq. 7.44), and N_2O (Eq. 7.49) with their contributions being 50%, 10%, and 21%. Approximately 5% of NO_2 is consumed by reactions with O forming NO_3 (Eq. 7.50). Since the densities of O_3 and N increase with time, the density of NO_2 accumulates over the pulses.

The consequences of varying energy deposition on the exit densities of O_3, N_yO_x, HNO_x, and CO_2 are shown in Fig. 7.9. With increasing energy deposition, larger

densities of O, N, and OH are produced. As O_3 is primarily formed by the reaction of O with O_2 (Eq. 7.30), its density increases with increasing energy deposition. Similarly, NO is dominantly produced by the reaction of N with OH (Eq. 7.27) and so the NO production increases. O_3 and NO react to produce NO_2 (Eq. 7.45) and so the density of NO_2 also increases with energy deposition. This further leads to the increased production of N_2O_5 (Eq. 7.52) and N_2O (Eq. 7.49). OH reacts with NO to produce HNO_2 (Eq. 54) and with NO_2 to form HNO_3 (Eq. 7.39), and so their densities increase. The density of CO_2 increases due to increased erosion of PP initiated by O and OH (Eq. 68).

The relative surface concentrations of alcohol, acid, peroxy, and carbonyl groups on PP as a function of energy deposition are shown in Fig. 7.10. With increasing energy deposition, the surface concentrations of the peroxy and acid groups increase and saturate with a small surface coverage, while those of the alcohol groups initially increase and then decrease. The initial increase in the densities of peroxy and acid groups is due to the increased availability of radicals. Their saturation at higher energy deposition is due to the balance between the consumption and production of alkyl radicals, their precursor. The densities of alcohols and carbonyls decrease at higher energy deposition because of consumption by O and OH to form alkoxy radicals and CO_2 (Eqs. 7.66-7.68). The computed surface densities of alcohol groups agree well with the experiments of O'Hare *et al*.[29] The less good agreement for the densities of peroxy and carbonyl groups at high energy deposition is due to the overestimation of the erosion of PP by the model. With larger erosion, more alkyl radicals and subsequently more peroxy radicals are generated. The agreement for the densities of acid groups is within 25%.

The surface densities of the alkyl, peroxy, and alkoxy radicals on PP as a function of time are shown in Fig. 7.11. Alkyl radicals are formed by the abstraction of H from PP by O and OH (Eqs. 7.56 and 7.57). Due to the production of O and OH in the gas phase with every discharge pulse (see Fig. 7.6), there is a constant flux of O and OH to the PP surface and so the alkyl radicals are produced with each pulse. During a given pulse, the production of alkyl radicals dominantly occurs for $t < 20$ μs. At later times, these radicals are consumed by reactions with O_2 and O_3 to form peroxy and alkoxy radicals (Eqs. 7.58 and 7.60). As the free sites on the PP surface are depleted at later pulses, the densities of the alkyl radicals decrease. There is little intra-pulse structure in the densities of alkoxy and peroxy radicals as their densities receive a small increment each pulse.

The surface densities of the alcohol and carbonyl groups on PP as a function of time are shown in Fig. 7.12. As with the alkoxy and peroxy radicals, the densities of these species have little intrapulse structure. The alkoxy radicals react with the hydrogen in the neighbouring sites to produce alcohols (Eq. 7.65). Alcohol groups are consumed by reactions with O and OH in the gas phase to regenerate alkoxy radicals (Eqs. 7.66 and 7.67). Carbonyl groups, namely aldehydes and ketones, are produced by the β-scission of alkoxy radicals (Eqs. 7.63 and 7.64).

Studies by Foulon-Belkacemi *et al*. [30] have shown that the surface composition of polymers subjected to humid-air coronas is sensitive to the RH. The time-averaged densities of O and OH (denoted as <O> and <OH>) and the exit density of O_3 are shown in Fig. 7.13a as a function of RH. For a given energy deposition, with increasing RH, more energy is channeled into H_2O decomposition and so more OH is produced.

Correspondingly, the production of O is decreased. This decrease results in decreased O_3 densities, ≈30% from RH of 1 to 100%. The relative concentrations of peroxy, alcohol, carbonyl, and acid groups as a function of RH are shown in Fig. 7.13b. Since more OH is produced at larger RH and since OH is more reactive than O, the rate of the initial step of H abstraction from PP is increased and so more alkyl radicals are generated (Eq. 7.57). Since the density of O_3 decreases, PP alkyl radicals are preferentially consumed by O_2 and so larger densities of peroxy radicals are formed. The surface density of the alcohol groups initially increases and then decreases. The increased formation of alkyl radicals and subsequently alkoxy radicals (Eqs. 7.57 and 7.60) result in an initial increase in the surface concentration of alcohols with RH (Eq. 7.65). Due to the decreased flux of O_3 to the PP surface, fewer alkoxy radicals are generated and so production of alcohols and carbonyl radicals decreases (Eqs. 7.60, 7.63-7.65). The densities of alcohols also decrease with RH due to their increased consumption by OH (Eq. 7.67). Similarly, the decrease in carbonyl radicals with RH is in part due to the increased consumption by reaction with OH to form acids (Eq. 7.71).

The densities of NO, NO_2, N_2O_5, N_2O, HNO_2, and HNO_3 in the gas phase as a function of RH are shown in Figs. 7.14c and 7.14d. The densities of NO and NO_2 increase only slightly with RH. Due to their high reactivities, NO and NO_2 are mostly converted into species such as HNO_3 (Eq. 7.39), N_2O (Eq. 7.49), HNO_2 (Eq. 7.46), and N_2O_5 (Eq. 7.52). As NO is dominantly produced by the reaction of N with OH (Eq. 7.27), the increased production of OH with RH increases the density of NO. The density of NO_2 also increases since it is primarily produced from NO (Eqs. 7.45 and 7.47). As a result, the densities of HNO_2 and HNO_3 also increase (Eqs. 7.39 and 7.46). OH further

reacts with HNO_3 to produce NO_3 and H_2O (Eq. 7.51). The increasing densities of NO_3 and NO_2 then produce N_2O_5 (Eq. 7.52). N_2O is dominantly produced by the reaction of N with NO_2 (Eq. 7.49). NO_2 is preferentially consumed by reaction with OH to form HNO_3 (Eq. 7.39). Therefore, less NO_2 is available for reaction with N and so the production of N_2O decreases. CO_2 is produced as a result of the erosion of PP (Eq. 7.68). The initial increase in the density of CO_2 with RH is due to the increased production of carbonyl radicals (Eq. 7.68). However, as the density of OH increases with RH, carbonyl radicals are preferentially consumed by reaction with OH to form acids and so the density of CO_2 decreases.

The surface concentrations of alcohols, acids, carbonyl, and peroxy radicals and the densities of the dominant gas phase products as a function of gas temperature are shown in Fig. 7.14. Although the rate constant for the production of O_3 from O increases with temperature (Eq. 7.30), the rate constants for the consumption of O_3 (for example, with NO (Eq. 7.45)) also increase, resulting in a net decrease of O_3. This decrease in O_3 results in the decreased formation of alkoxy radicals on the PP surface (Eq. 7.60) and therefore a decreased production of alcohols, carbonyl, and acid groups (Eqs. 7.63-7.65, 7.71). The small decrease in the density of carbonyl groups does not significantly affect the erosion process (Eq. 7.68) and so the density of CO_2 remains almost constant. Due to the lower rate of consumption of alkyl radicals by reaction with O_3 with increasing gas temperature, more alkyl radicals are available for reaction with O_2 and so the peroxy radical concentration increases (Eq. 7.58).

The increased rate of reaction of O_3 with NO produces larger densities of NO_2 (Eq. 7.45) and so the density of HNO_3 also increases (Eq. 7.39). Due to the high

reactivities of NO and NO_2, their densities are relatively small compared to products such as HNO_3 and N_2O. Most of the NO is lost by reduction to N_2 (Eq. 7.28) and oxidation to NO_2 (Eqs. 7.45 and 7.47) and to a lesser degree to HNO_2 (Eq. 7.46). Most of the NO_2 is converted to HNO_3 (Eq. 7.39). The end result of the increased production of NO and NO_2 is the increased density of HNO_3 and N_2O. N_2O_5 is mainly produced by the reaction of NO_2 with NO_3 (Eq. 7.52) and so its production increases. This increase is offset by the increase in its unimolecular decomposition and so its density decreases.

The web speed and repetition rate of the discharge pulses determine the energy deposition and the time between generation of radicals. For example, as the web speed increases, the residence time of PP decreases and so the discharge frequency must be increased to keep the energy deposition constant (for a fixed voltage). Time-averaged and exit densities of gas phase species and concentrations of surface species are shown in Fig. 7.15 as a function of web speed for a constant energy deposition. As the pulse repetition frequency increases with web speed, O and OH radicals are refreshed more frequently, their time-averaged densities increase, and so their fluxes to the PP surface increase (Fig. 7.15a). Although the fluxes of O and OH increase with web speed, the surface concentrations of the alcohol, peroxy, carbonyl, and acid groups decrease (Fig. 7.15b). As the web speed increases from 150 cm/s to 350 cm/s, the residence time of the PP decreases from 0.08 s to 0.03 s. Since the reactions on the PP surface that produce these groups occur on time scales on the order of a few tens of ms, a factor of two change in the residence time noticeably affects their surface concentrations.

Although the densities of NO and NO_2 increase with the web speed (Fig. 7.15c), the change is not significant. Most of the NO is consumed to produce N_2 and NO_2 (Eqs.

7.28, 7.45, and 7.47) and most of the NO_2 is consumed by OH to produce HNO_3 (Eq. 7.39). Since these reactions occur on time scales of less than 1 ms, the densities of NO, NO_2 and the products they form (HNO_3, N_2O, N_2O_5) are not significantly affected by the change in the residence time (Figs. 7.15c and 7.15d). The density of O_3 slightly decreases due to the smaller time available for the reaction of O with O_2 to produce O_3 (Eq. 7.30). Due to the decrease in the density of carbonyl groups with web speed, the production of CO_2 also decreases.

7.5 Concluding Remarks

The gas phase and surface kinetics during the atmospheric pressure humid-air plasma processing of PP have been investigated. Using a pseudo-homogeneous global kinetics model, the consequences of process variables such as energy deposition, RH, web speed, and gas temperature on the surface properties of PP were investigated. Increasing energy deposition leads to an increased production of alcohol, carbonyl, acid, and peroxy radicals on the PP surface while increasing the gas phase production of O_3 and N_xO_y. Increasing the RH resulted in decreased production of O_3. The surface concentrations of peroxy radicals increased with RH while those of alcohol, carbonyl, and acid groups decreased. Increasing the gas temperature resulted in decreased surface concentrations of alcohol, carbonyl, and acid groups while the concentration of peroxy radicals increased. While keeping the energy deposition constant, increasing the web speed resulted in decreased concentrations of alcohols, peroxy radicals, carbonyl, and acid groups, indicating that residence time is an important process variable.

7.6 Tables and Figures

Table 7.1. Surface reaction mechanism for PP

Reaction [a)]	Probabilities or reaction rate coefficient [b)]	Comments
Initiation		
$O_g + PP\text{-}H \rightarrow PP^{\bullet} + OH_g$	10^{-3}, 10^{-4}, 10^{-5}	c
$OH_g + PP\text{-}H \rightarrow PP^{\bullet} + H_2O_g$	0.25, 0.05, 0.0025	c
Propagation		
$PP^{\bullet} + O_g \rightarrow PP\text{-}O^{\bullet}$	10^{-1}, 10^{-2}, 10^{-2}	c
$PP^{\bullet} + O_{2,\,g} \rightarrow PP\text{-}O_2^{\bullet}$	1.0×10^{-3}, 2.3×10^{-4}, 5.0×10^{-4}	c
$PP^{\bullet} + O_{3,\,g} \rightarrow PP\text{-}O^{\bullet} + O_{2,\,g}$	1.0, 0.5, 0.5	c
$PP\text{-}O_2^{\bullet} + PP\text{-}H \rightarrow PP\text{-}OOH + PP^{\bullet}$	5.5×10^{-16} cm^2 s^{-1}	
$PP\text{-}O^{\bullet} \rightarrow$ aldehydes $+ PP^{\bullet}$	10 s^{-1}	
$PP\text{-}O^{\bullet} \rightarrow$ ketones $+ PP^{\bullet}$	500 s^{-1}	
$O_g + PP{=}O \rightarrow OH_g + {}^{\bullet}PP{=}O$	0.04	
$OH_g + PP{=}O \rightarrow H_2O_g + {}^{\bullet}PP{=}O$	0.4	
$O_g + {}^{\bullet}PP{=}O \rightarrow CO_{2,\,g} + PP\text{-}H$	0.4	
$OH_g + {}^{\bullet}PP{=}O \rightarrow (OH)PP{=}O$	0.12	
$PP\text{-}O^{\bullet} + PP\text{-}H \rightarrow PP\text{-}OH + PP^{\bullet}$	8.0×10^{-14} cm^2 s^{-1}	
$O_g + PP\text{-}OH \rightarrow PP\text{-}O + OH_g$	7.5×10^{-4}	
$OH_g + PP\text{-}OH \rightarrow PP\text{-}O + H_2O_g$	8.2×10^{-3}	

Termination

$H_g + PP^{\bullet} \rightarrow PP\text{-}H$	0.2, 0.2, 0.2	c
$OH_g + PP^{\bullet} \rightarrow PP\text{-}OH$	0.2, 0.2, 0.2	c

a) Subscript g denotes gas phase species. PP-H denotes polypropylene.
b) Those coefficients without units are reaction probabilities.
c) Reaction probabilities for tertiary, secondary, and primary radicals respectively.

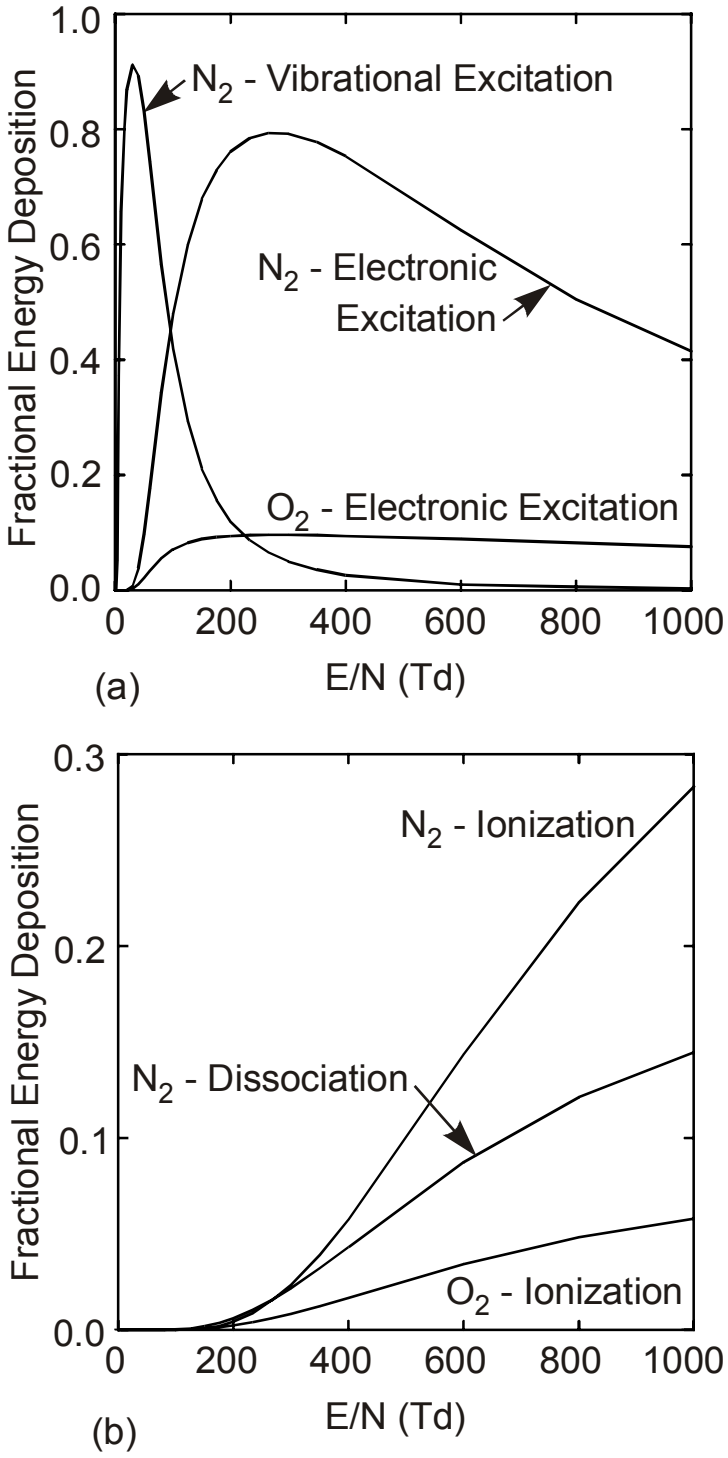

Fig. 7.1. Fractional disposition of energy deposition into electron impact processes as a function of electric field/gas number density (E/N) (1 Td = 1.0×10^{-17} V-cm^2). Conditions are: $N_2/O_2/H_2O$ = 78.9/20.0/1.1, 1 atm, 300 K. The E/Ns of interest are 300-600 Td. (a) Electronic and vibration excitation. (b) Dissociation and ionization.

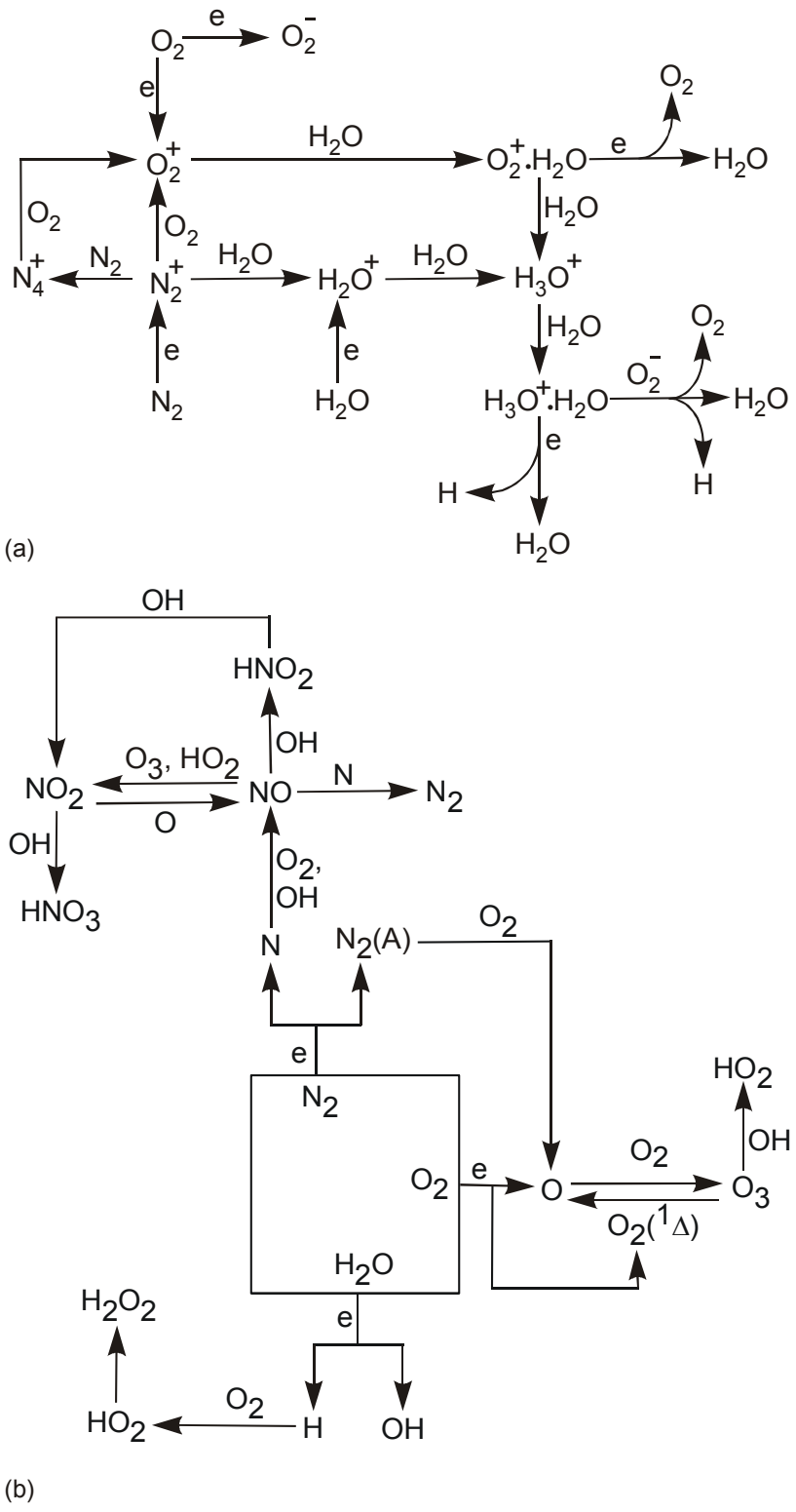

Fig. 7.2. Reaction mechanism for gas phase chemistry in humid-air plasma. (a) Charged species chemistry. (b) Free radical chemistry.

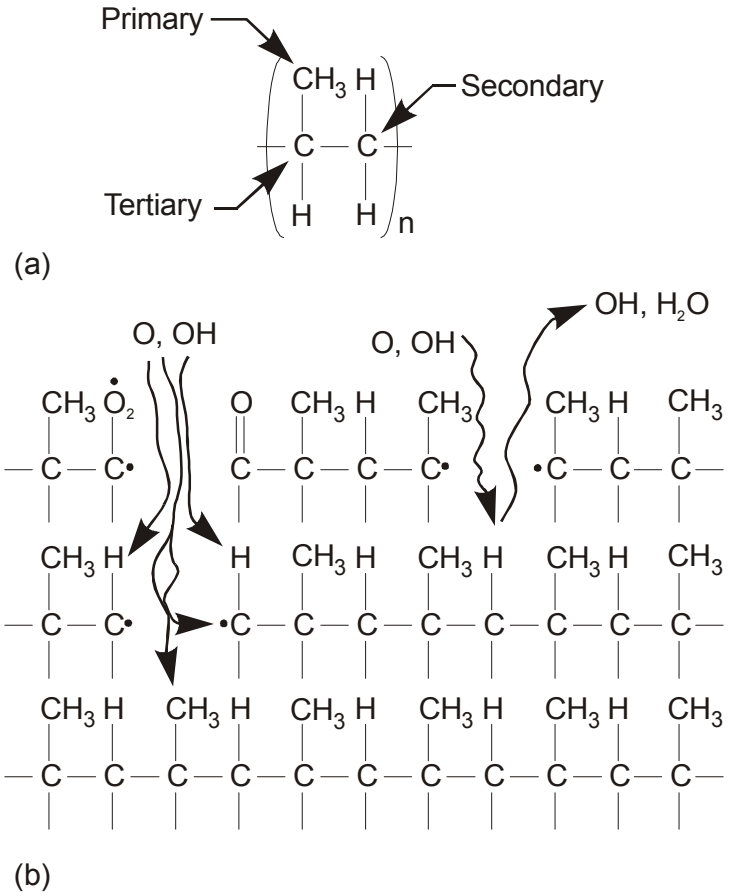

Fig. 7.3. Surface reaction mechanism. (a) A monomer unit in PP. (b) Surface site balance model. PP is a saturated hydrocarbon polymer consisting of two secondary Hs, a tertiary H, and a methyl group attached to a carbon backbone. The total number of surface sites is allowed to vary.

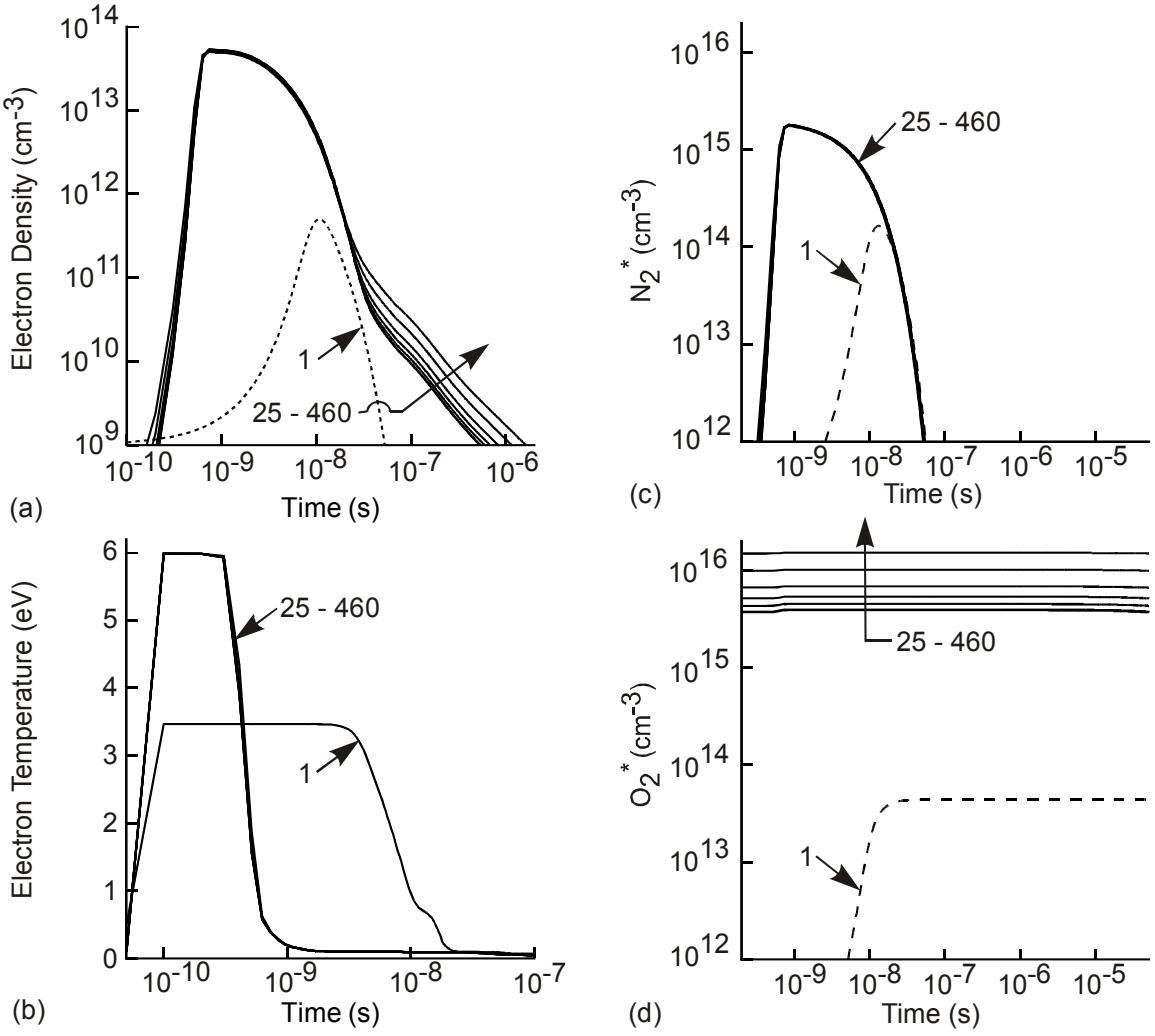

Fig. 7.4. Plasma parameters and densities of excited species for the base case conditions. (a) Electron density (n_e). (b) Electron temperature (T_e). (c) N_2^*. (d) O_2^*. Conditions are $N_2/O_2/H_2O$ = 78.9/20.0/1.1, 1 atm, 300 K (1.1% H_2O corresponds to a relative humidity of approximately 30%). The energy deposition is 0.8 J cm^{-2} and the applied voltage is 15 kV. Due to the charging of the dielectric, the T_e and n_e are larger for later pulses. O_2^* being a relatively stable species, has a longer lifetime and its density accumulates with time.

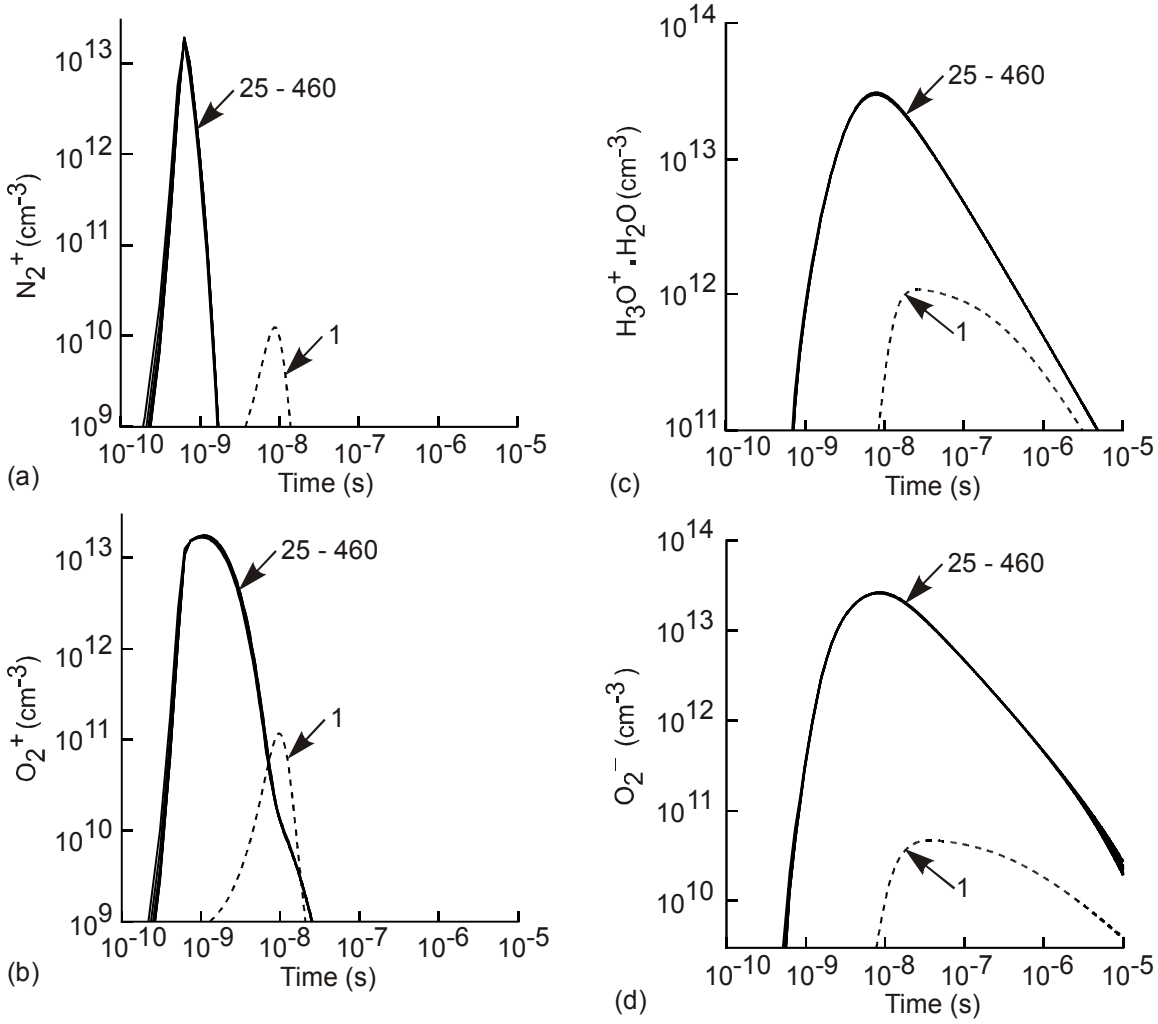

Fig. 7.5. Time dependence of densities of charged species. (a) N_2^+. (b) O_2^+. (c) $H_3O^+ \cdot H_2O$. (d) O_2^-. N_2^+ and O_2^+ are formed mainly by the electron impact ionization of N_2 and O_2. N_2^+ is mainly consumed by reactions with N_2 to form N_4^+ (Eq. 22). O_2^+ is primarily consumed by reactions with H_2O to form the cluster ion $O_2^+ \cdot H_2O$. The end result of the ion chemistry is the production of the $H_3O^+ \cdot H_2O$ and O_2^-.

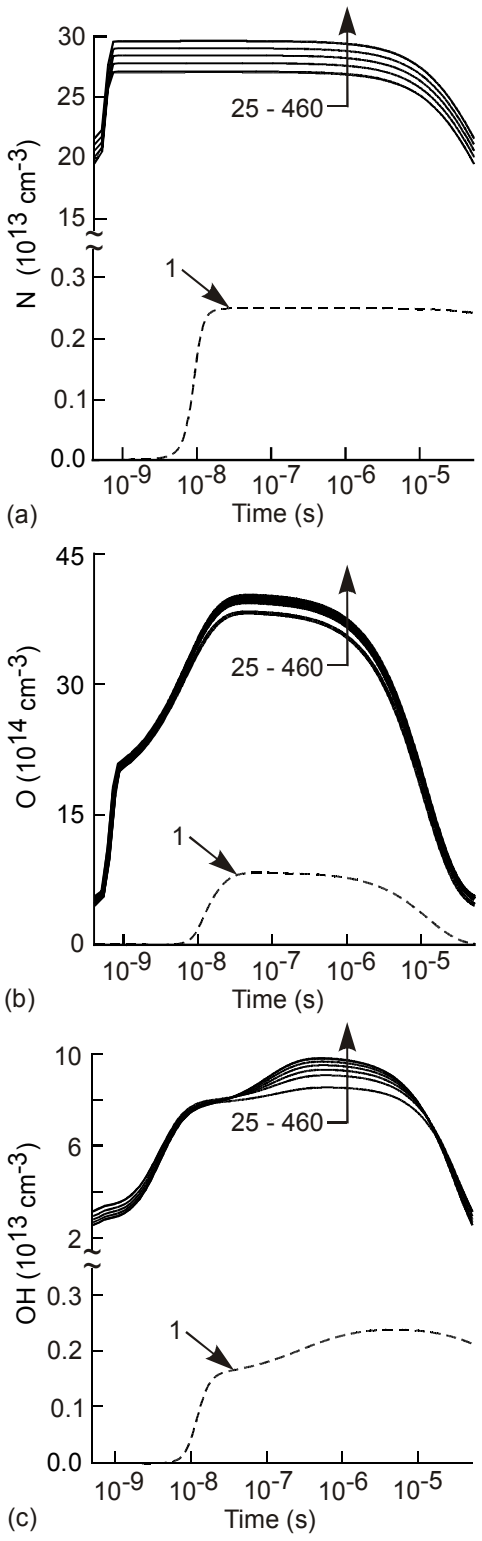

Fig. 7.6. Densities of primary radicals as a function of time. (a) N. (b) O. (c) OH. N being less reactive than O and OH accumulates between pulses. O and OH are largely consumed in the interpulse period.

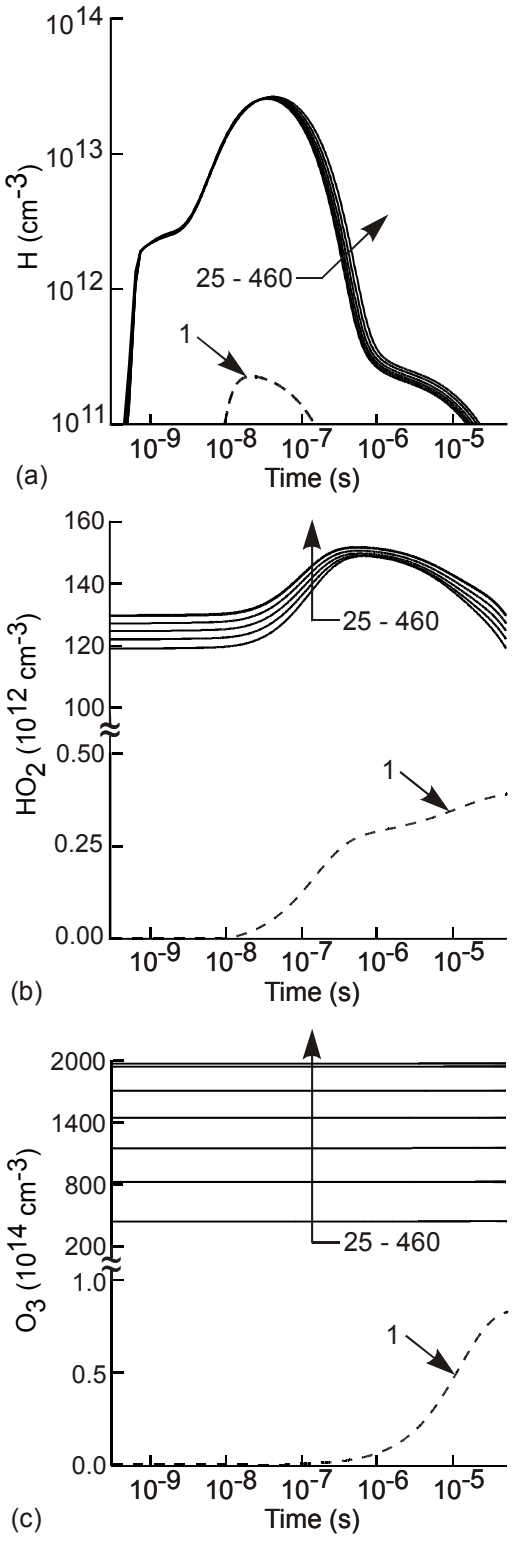

Fig. 7.7. Densities of radicals as a function of time. (a) H. (b) HO_2. (c) O_3. HO_2 and O_3 being less reactive compared to H accumulate over pulses.

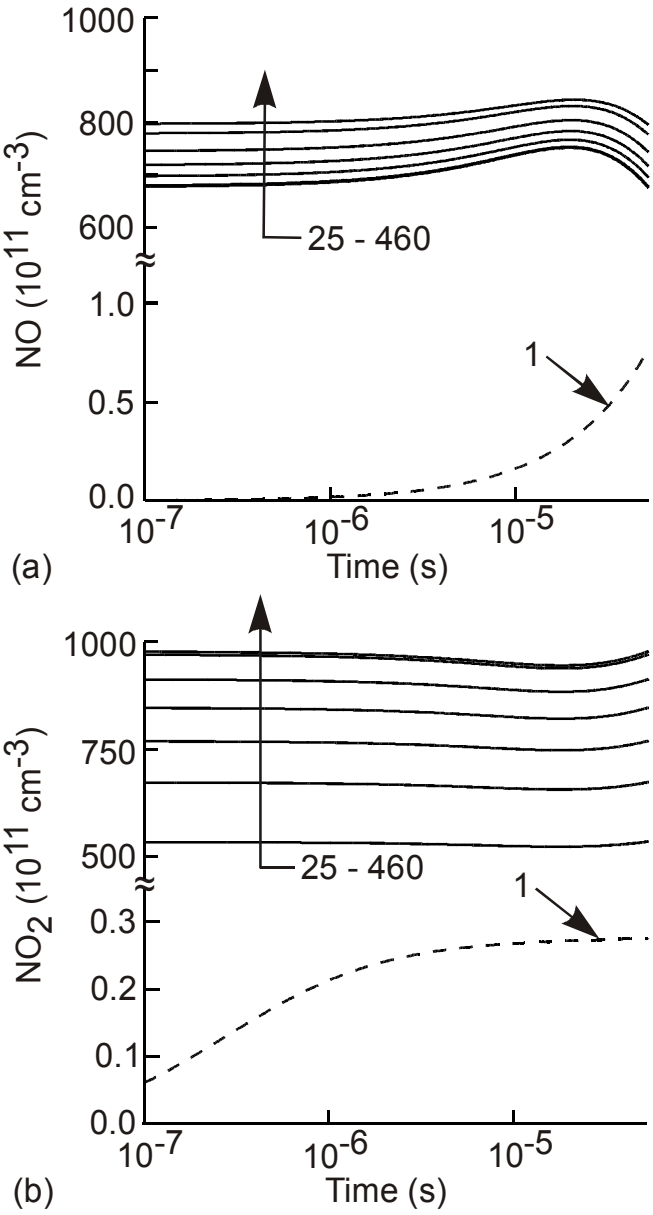

Fig. 7.8. Densities of NO_y as a function of time. (a) NO. (b) NO_2. Most of the NO and NO_2 are primarily converted to HNO_3 (Eq. 7.39) and N_2O (Eq. 7.49).

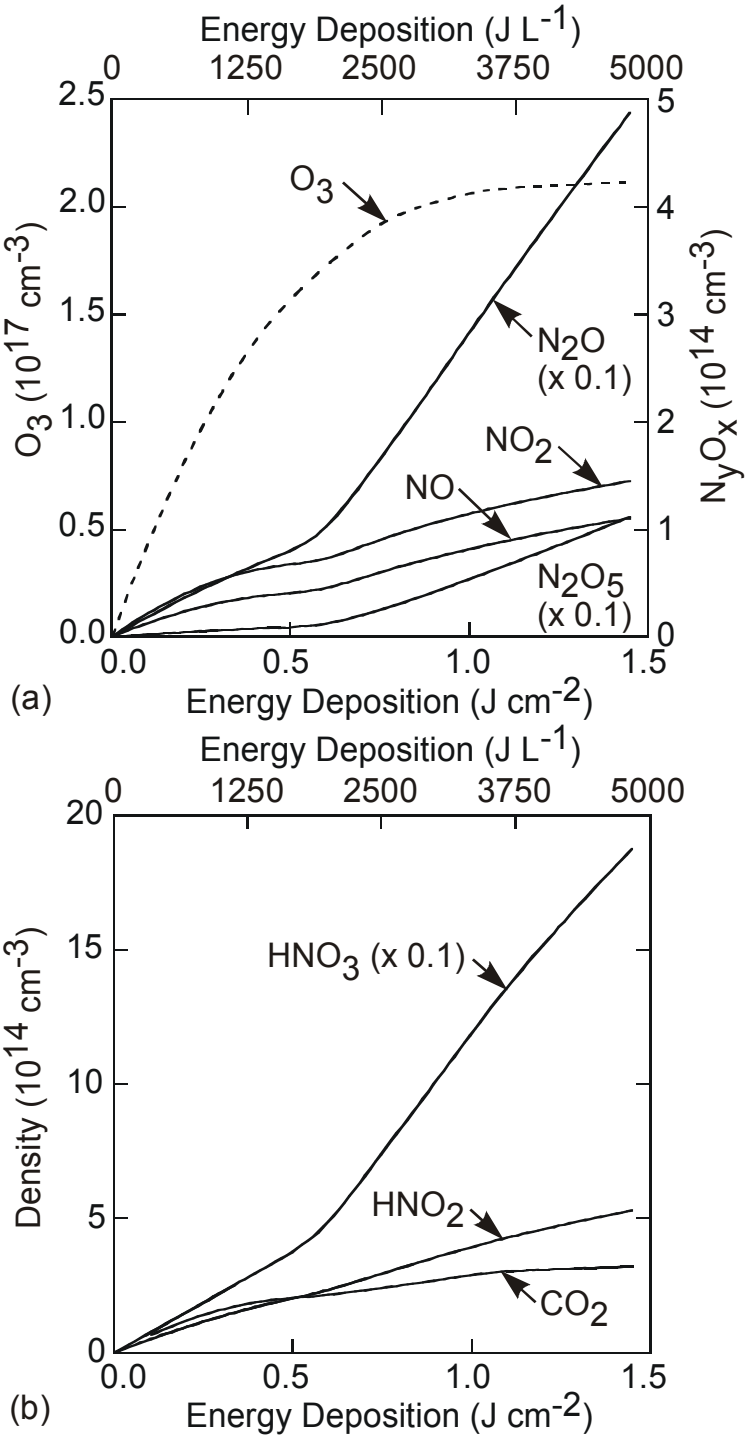

Fig. 7.9. Effect of energy deposition on the exit densities of gas phase species. (a) O_3 and N_yO_x. (b) HNO_x. With increasing energy deposition, larger densities of O, OH, and N are produced thereby increasing the production of O_3, NO, NO_2, N_2O_5, N_2O, HNO_2, and HNO_3.

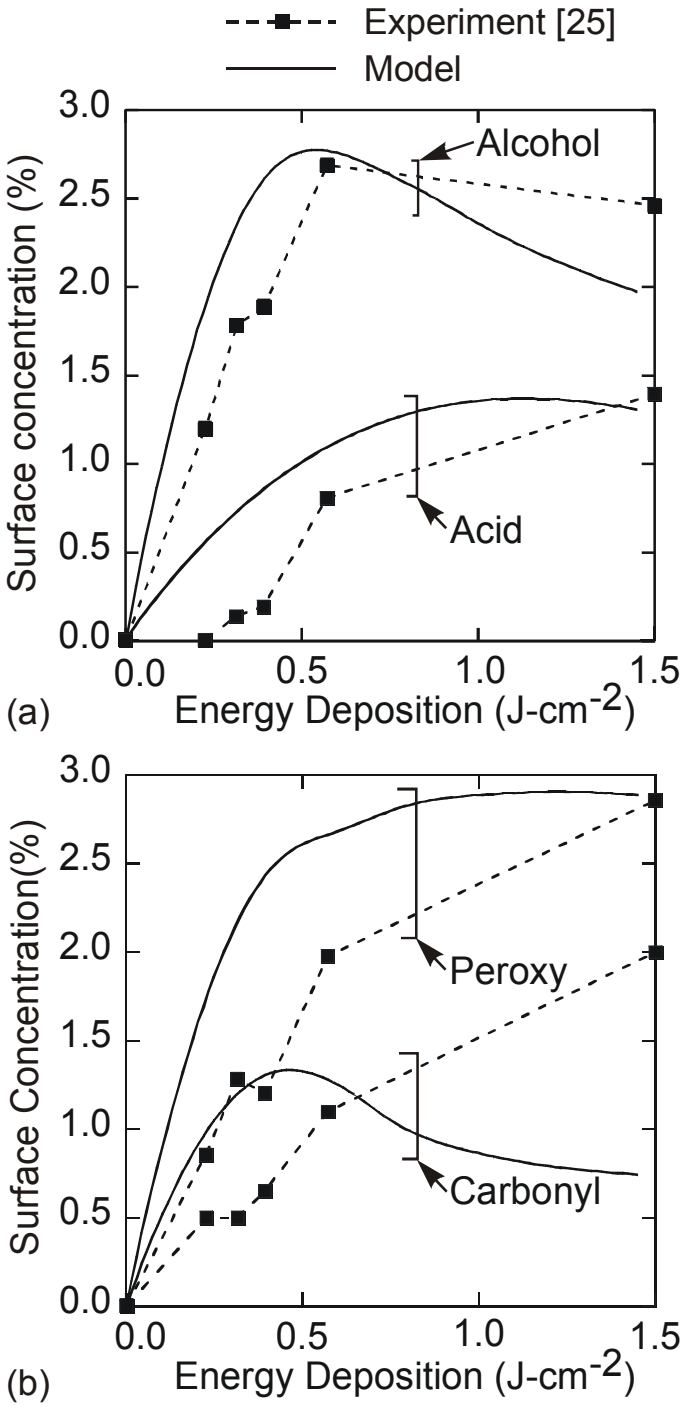

Fig. 7.10. Experimental [29] and modeling results for percentage coverage of PP by functional groups after humid-air corona treatment. (a) Alcohol: C-OH. (b) Peroxy: C-OO. (c) Acid: HO-C=O. (d) Carbonyl: C=O. The energy deposition is varied by changing the applied voltage. With increasing energy deposition, the relative surface concentration of the acid increases, while those of the alcohol and carbonyl groups initially increase and then decrease. Conditions are as in Fig. 7.4.

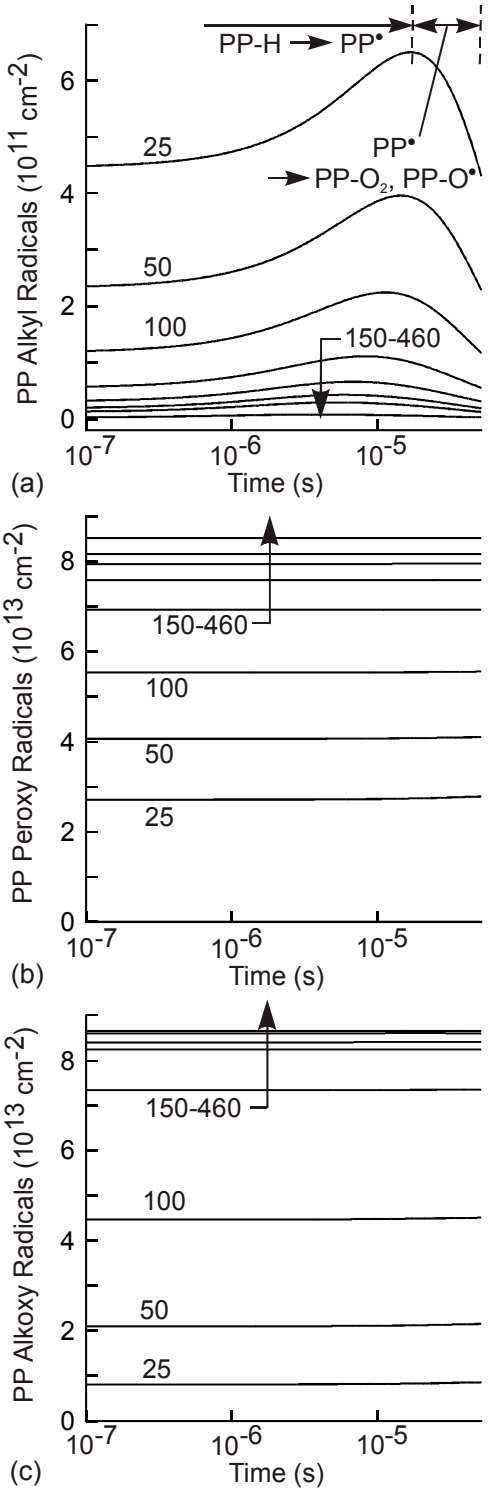

Fig. 7.11. Time dependence of surface densities. (a) Alkyl radicals. (b) Peroxy radicals. (c) Alkoxy radicals. Alkyl radicals are produced by the reaction of O with PP-H (Eqs. 7.57 and 7.58) and are consumed by the reactions with O_2 and O_3 to form peroxy and alkoxy radicals (Eqs. 7.59 and 7.61).

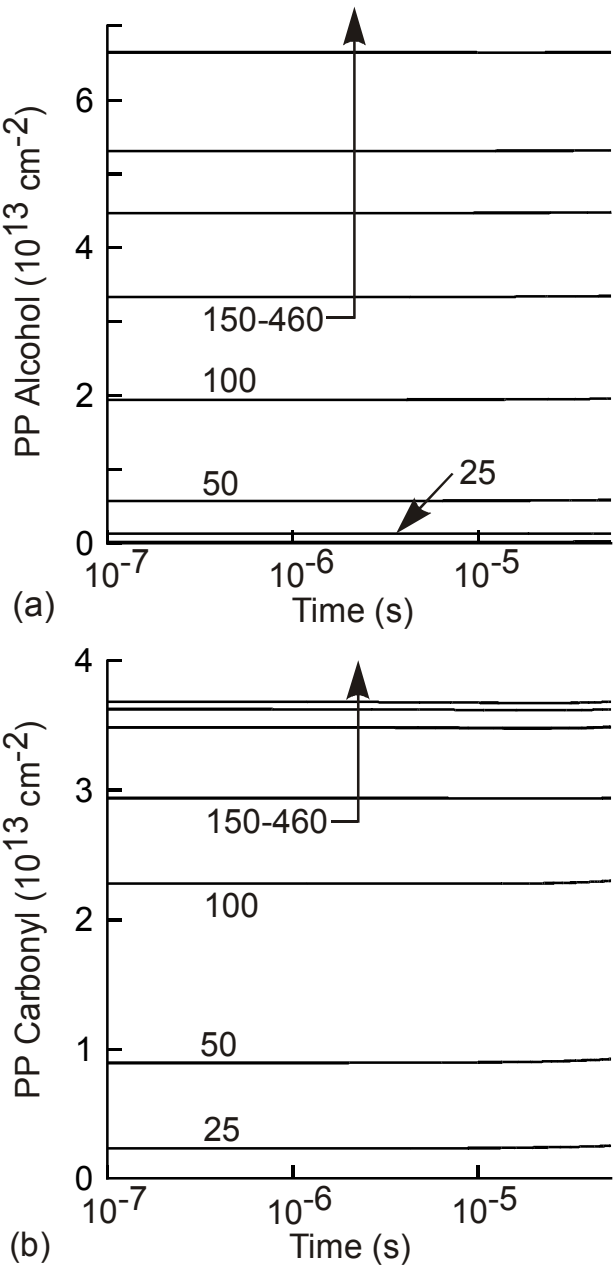

Fig. 7.12. Surface densities as a function of time. (a) Alcohols. (b) Carbonyls. There is little intrapulse structure. Alcohol groups are produced by the abstraction of H from neighbouring sites on PP by alkoxy radicals (Eq. 7.66). Carbonyl groups are produced by the β-scission of alkoxy radicals (Eqs. 7.64 and 7.65).

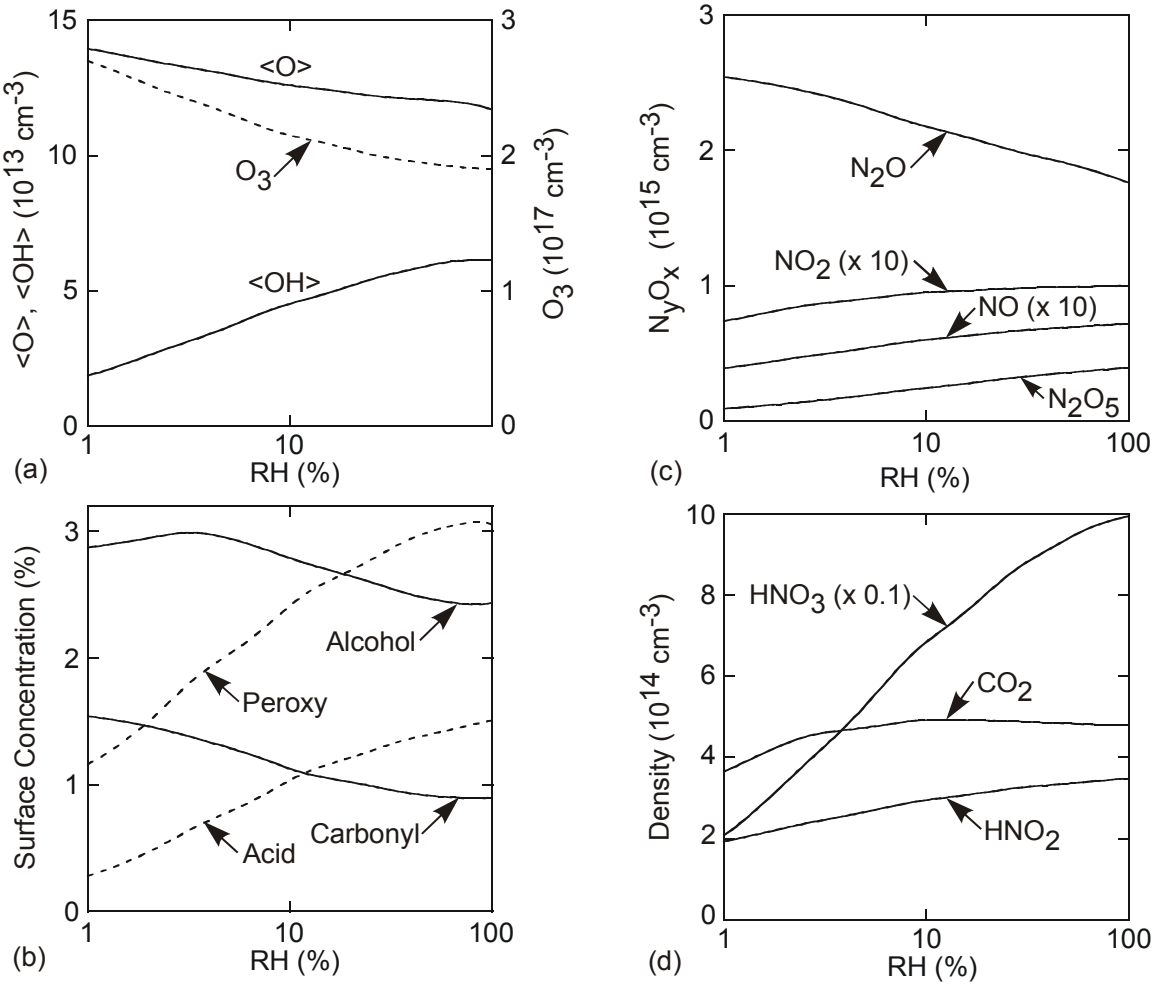

Fig. 7.13. Consequences of varying RH on the exit surface composition of PP and on the time-averaged and exit densities of gas phase species. (a) Time-averaged densities of O and OH (denoted as <O> and <OH>) and exit density of O_3. (b) Surface concentrations of alcohol, peroxy, carbonyl, and acid groups. (c) Exit N_yO_x. (d) Exit CO_2 and HNO_x. Conditions are same as in Fig. 7.4.

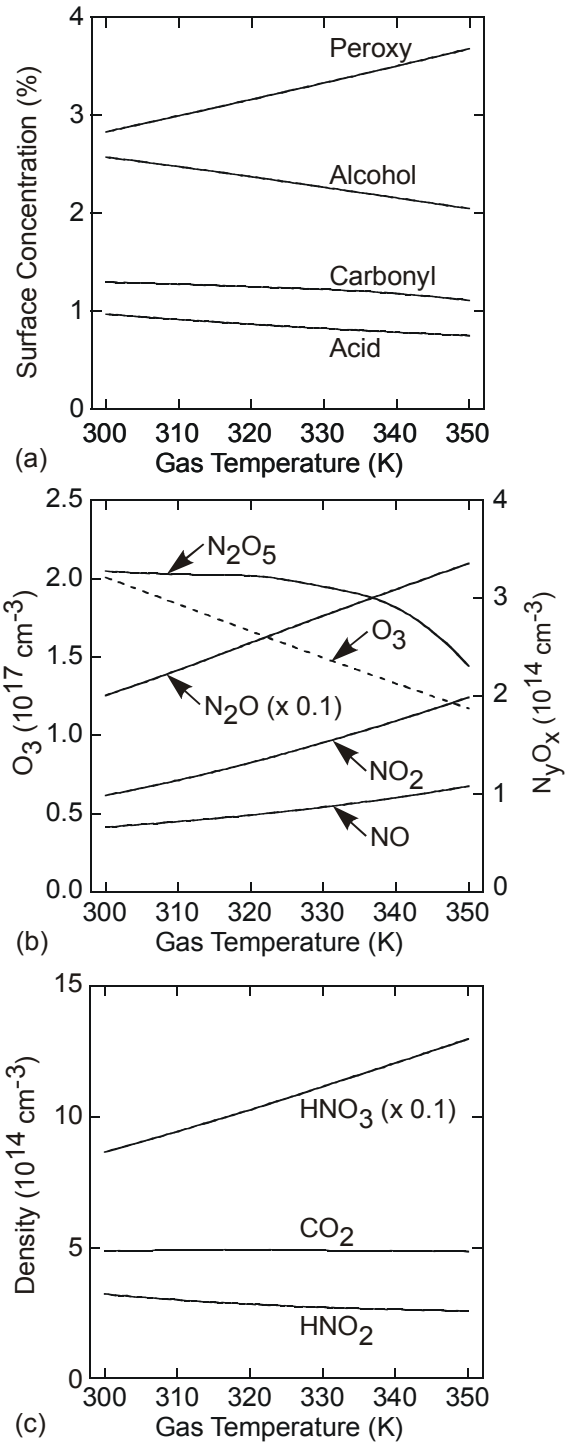

Fig. 7.14. Effects of gas temperature on the exit surface properties of PP and the densities of important gas phase products during the humid-air corona processing of PP. (a) Surface concentrations of alcohol, peroxy, carbonyl, and acid groups. (b) Exit O_3 and N_yO_x. (c) Exit CO_2 and HNO_x. Conditions are same as in Fig. 7.4.

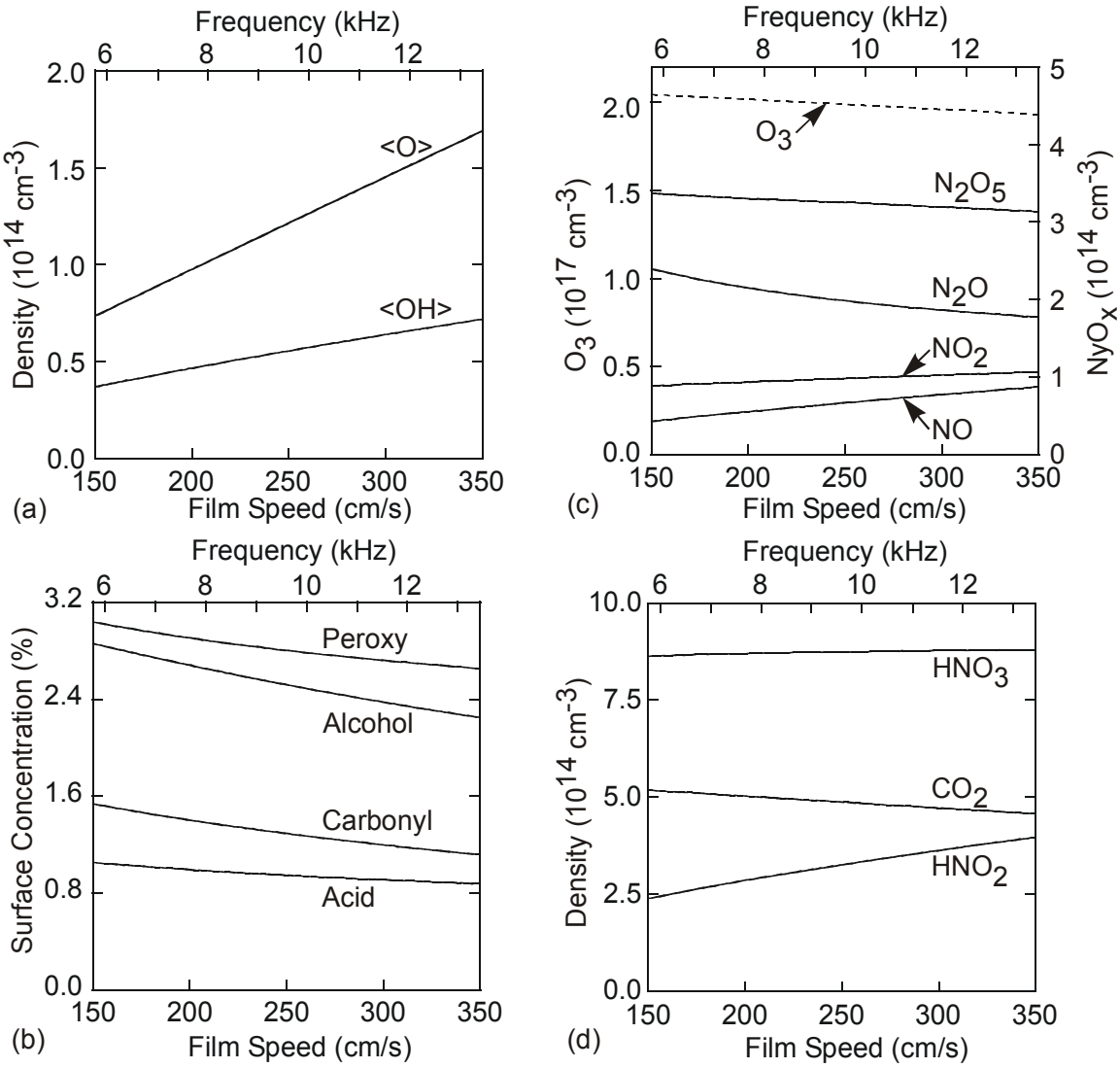

Fig. 7.15. Exit surface properties of PP and time-averaged and exit densities of gas phase species as a function of web speed. (a) Time-averaged densities of O and OH (denoted as <O> and <OH>). (b) Exit surface concentrations of alcohol, peroxy, carbonyl, and acid groups. (c) Exit O_3 and N_yO_x. (d) Exit CO_2 and HNO_x. Conditions are same as in Fig. 7.4. To keep the energy deposition constant, the discharge frequency was adjusted.

7.7 References

1. C.-M. Chan, *Polymer Surface Modification and Characterization*, 1 ed. (Hanser/Gardner Publications, Inc., New York, 1994).
2. L. G. Piper, J. Chem. Phys. **87,** 1625 (1987).
3. R. Atkinson, D. L. Baulch, R. A. Cox, R. F. Hampson Jr., J. A. Kerr, M. J. Rossi, and J. Troe, J. Phys. Chem. Ref. Data **26,** 521 (1997).
4. R. Atkinson, D. L. Baulch, R. A. Cox, R. F. Hampson Jr., J. A. Kerr, M. J. Rossi, and J. Troe, J. Phys. Chem. Ref. Data **26,** 1329 (1997).
5. J. C. Person and D. O. Ham, Radiat. Phys. Chem. **31,** 1 (1988).
6. Y. Ikezoe, S. Matsuoka, M. Takebe, and A. Viggiano, *Gas Phase Ion-Molecule Reaction Rate Constants Through 1986* (Ion Reaction Research Group of The Mass Spectroscopy Society of Japan, Tokyo, 1987).
7. R. Atkinson, D. L. Baulch, R. A. Cox, R. F. Hampson Jr., J. A. Kerr, and J. Troe, J. Phys. Chem. Ref. Data **18,** 881 (1989).
8. Y. Mirokin and G. Mallard, The NIST Chemical Kinetics Database (1998).
9. W. Tsang and R. F. Hampson Jr., J. Phys. Chem. Ref. Data **15,** 1087 (1986).
10. S. Mukkavilli, C. K. Lee, K. Varghese, and L. L. Tavlarides, Trans. Plasma Sci. **16,** 652 (1988).
11. D. L. Baulch, C. J. Cobox, R. A. Cox, P. Frank, G. Hayman, T. Just, J. A. Kerr, T. Murrells, M. J. Pilling, J. Troe, R. W. Walker, and J. Warnatz, J. Phys. Chem. Ref. Data **23,** 847 (1994).
12. R. Atkinson, J. Phys. Chem. Ref. Data **26,** 215 (1997).
13. W. Tsang and J. T. Herron, J. Phys. Chem. Ref. Data **20,** 609 (1991).

14. F. Poncin-Epaillard, B. Chevet, and J.-C. Brosse, J. Adhesion Sci. Technol. **8,** 455 (1994).

15. D. J. Carlsson and D. M. Wiles, J. Macromol. Sci.-Rev. Macromol. Chem. **C14,** 65 (1976).

16. S. D. Razumovskii, A. A. Kefeli, and G. E. Zaikov, Eur. Polym. J. **7,** 275 (1971).

17. M. Strobel, M. C. Branch, M. Ulsh, R. S. Kapaun, S. Kirk, and C. S. Lyons, J. Adhesion Sci. Technol. **10,** 515 (1996).

18. R. H. Hansen, J. V. Pascale, R. De Benedictis, and P. M. Rentzepis, J. Polym. Sci.: Part A: Poly. Chem. **3,** 2205 (1965).

19. J. F. Rabek, *Polymer Photodegradation: Mechanisms and Experimental Methods*, 1 ed. (Chapman & Hall, London, 1995).

20. E. Niki, C. Decker, and F. R. Mayo, J. Polym. Sci.: Polym. Chem. **11,** 2813 (1973).

21. S. Gomez, P. G. Steen, and W. G. Graham, Appl. Phys. Lett. **81,** 19 (2002).

22. M. Kuzuya, S.-i. Kondo, M. Sugito, and T. Yamashiro, Macromolecules **31,** 3230 (1998).

23. D. J. Carlsson and S. Chmela, in *Mechanisms of Polymer Degradation and Stabilization*, 1 ed., edited by G. Scott (Elsevier Applied Science, London, 1990), p. 329.

24. R. Paltenghi, E. A. Ogryzlo, and K. D. Bayes, J. Phys. Chem. **88,** 2595 (1984).

25. F. Poncin-Epaillard, J. C. Brosse, and T. Falher, Macromol. Chem. Phys. **200,** 989 (1999).

26. S. H. Wheale, C. P. Barker, and J. P. S. Badyal, Langmuir **14,** 6699 (1998).

27. C. Decker and F. R. Mayo, J. Polym. Sci.: Polym. Chem. **11,** 2847 (1973).

28. F. Clouet and M. K. Shi, J. Appl. Poly. Sci. **46,** 1955 (1992).

29. L.-A. O'Hare, S. Leadley, and B. Parbhoo, Surf. Interface Anal. **33,** 335 (2002).

30. N. Foulon-Belkacemi, M. Goldman, A. Goldman, and J. Amouroux, IEE Proc.-Sci. Meas. Technol. **142,** 477 (1995).

8. CONCLUDING REMARKS

We have developed 0-D and 1-D (radially dependent) computer models for dielectric barrier discharge (DBD) processing of gases and surfaces at atmospheric pressure. In particular, we applied these models to investigate the plasma remediation of nitrogen oxides (NO_x) from diesel exhausts and to study the plasma surface treatment of polypropylene (PP). The models allow for a detailed analysis of the plasma induced chemical reactions both in the gas phase and on the surface. The goals of the analyses include optimizing the energy efficiencies and minimizing the formation of harmful byproducts.

Unburned hydrocarbons (UHCs) present in diesel exhausts significantly affect the plasma remediation of NO_x by oxidizing NO, the major form of NO_x in the exhaust, into NO_2. The efficiency of NO_x removal improves when a given amount of energy is deposited in a large number of shorter duration pulses than in a single pulse. This increase in efficiency is due to the increased formation of organic nitrates resulting from the larger overlap in the densities of hydrocarbon radicals and NO_2. With each pulse, radicals initiating the plasma chemistry are generated and during the interpulse period, these radicals undergo reactions thereby changing the composition of the plasma. The reaction chemistry for the follow-on pulses is different from that which would be obtained from an equivalent energy deposition in a single or smaller number of pulses due to the accumulation of these inter-pulse products.

Soot influences the chemistry of NO_x plasma remediation dominantly through NO_2-soot interactions and influences the ionization kinetics through electron attachment

to and ion neutralizations with the particles. The resulting changes of electron density and temperature may then affect the rates of electron-impact processes. When using a single pulse, NO_x removal improves by as high as 10% in the presence of soot. With soot, higher energies were required for the removal of a given amount of NO. By regenerating the NO from NO_2 and by indirectly leading to the increase in the density of OH radicals, soot increases the formation of HNO_2, thereby improving NO_x removal. The increase in the density of OH also results in increased UHC consumption. CO is the primary product of soot oxidation.

When using repetitive pulses in the presence of soot, the efficiency of NO_x removal increases further. Single pulses with soot result in an initial gas phase oxidation of NO to NO_2, followed by a heterogeneous conversion of NO_2 to NO on the soot. Due to the larger gas phase density of NO_2 when using repetitive pulses, there is an increased flux of NO_2 to the soot surface, resulting in increased soot oxidation and larger rates of heterogeneous conversion of NO_2 to NO. The combined effects of multiple pulses and heterogeneous chemistry on NO_x remediation and soot oxidation are twofold. Improved NO_x removal by the increased production of HNO_2, HNO_3, organic nitrates and nitrites due to the more favorable overlap in time of NO_2 and reactive radical densities; and increased soot oxidation because of larger NO_2 densities.

Spatially nonuniform energy deposition in DBDs results in spatial gradients in gas temperature and species densities which initiate advection and diffusion leading to transport of species to and from the microstreamer region. UHCs consume the primary radicals, O and OH, produced dominantly in the streamer region, and thereby their diffusion to regions outside of the streamer. As a result, the remediation of NO_x at outer

radii decreases while more NO_x is removed within the streamer region due to the increased production of hydrocarbon radicals.

Plasma surface treatment of polypropylene in humid air results in the formation of alcohol, peroxy, carbonyl, and acid groups on the surface. With increasing energy deposition, the surface concentrations of these groups increase. However, significant amounts of O_3 and N_xO_y are generated in the gas phase. Increasing the relative humidity decreases the production of O_3 and increases the concentrations of peroxy and acid groups on the surface. Increasing the gas temperature increases the surface concentration of peroxy radicals and decreases the concentrations of alcohol, carbonyl, and acid groups. For a given energy deposition, increasing the web speed results in decreased surface densities of peroxy, alcohol, carbonyl, and acid groups.

The major sources of inaccuracies in the models come from the simplifications in the streamer behavior and the inherent uncertainties in the reaction coefficients for heavy particle reactions and cross sections for electron impact reactions. In addition to addressing these sources of accuracies, future work could consider multiple streamers in the discharge, with variable spacing and formation times, as this is likely to change the spatial distribution of species and thereby the chemistry. In the context of plasma surface treatment of polymers, the present model could be used to study the surface treatment of other polymers such as polyethylene and poly-tetraflouroethylene.

APPENDIX A. LIST OF SPECIES FOR $N_2/O_2/H_2O/CO_2/CO/NO_x/H_2/C_3H_6/C_3H_8$ PLASMAS

e	O_2	O_2	N_2O_4
O_2^+	O_2^-	O	H_3O
$O(^1D)$	O^+	O^-	H_2NO
N_2	$N_2(A)$	$N(^2D)$	H_2CN
N_2^+	N	OH	CH_3O_2
H_2O	O_3	NO_2	CN
HCO	HO_2	H	NCCN
NO	HNO_2	NO_3	CH_4
H^-	HNO	C	CH_3O
H_2	N_2O	CO_2	H_2^+
CO	CO^+	HO_2NO_2	HCN
CO_2^+	HNO_3	NH	HOCN
H_2O_2	N_2O_5	N_3^+	CNN
H_2O^+	H_3O^+	NO_2^-	CH
NO^+	NO_2^+	N^+	CH_3
NO_3^-	NO^+*O_2	$H_3O^+·H_2O$	C_2H_6
N_4^+	$O_2^+·H_2O$	NH_2	HCOOH
H_2NO^+	NH_3	$NO^+·H_2O$	NCO
NH_3^+	NH_4^+	CCN	HNCO
$H_3O^+·(H_2O)_2$	$H_3O^+·(H_2O)_3$	$C_2H_5OONO_2$	NC_3H_7
C_2O	i-C_3H_7	CH_3COO	$NC_3H_7O_2$
C_3H_8	NC_3H_7OH	CH_2OHNO	$(CH_3)_2CHO$
C_3H_7CHO	NC_3H_7O	CH_3NCH_3	C_3H_3
$(CH_3)_2CHO_2$	C_3H_5	$CH_3CO_3NO_2$	C_2H_5CHO
C_3H_6	$C_2H_5COCH_3$	$HOCH_2NO_2$	C_2H_5OH
C_2H_5	$C_2H_5O_2$	HCOO	C_2H_4OH
C_2H_5NO	C_2H_4	$NC_3H_7ONO_2$	C_2H_3CO
C_2H_5O	C_2H_3CHO	C_2H_2OH	CH_3CONO
C_2H_3	C_2H_2	C_2H	NC_3H_7OOH
C_2H_3O	CHOCHO	CH_3CHO	$(CH_3)_2CHONO_2$
C_2HO	C_2HCO	$CH_3CHOHCH_2$	$(CH_3)_2CHOOH$
C_2	CH_3CHCH_2OH	$CH_3CH(O)CH_2OH$	C_2H_5ONO
CH_3CHCH	$CH_3CH(OO)CH_2OH$	CH_3COO_2	$ONCH_2CHO$
$CH_3CHOHCH_2(OO)$	CH_3CHCO	CH_3COCH_3	$CONH_2$
$CH_3CHOHCH_2O$	CH_3COCHO	CH_3ONO_2	CH_3CHOH
CH_3CO	CH_3ONO	CH_3OOH	CH_2
CH_3NO_2	CH_3OCH_3	CH_2CHO	Methyl Oxirane
CH_3OH	CH_2CCH_2	CH_2CHCH_2O	HCHO
CH_2CCH_3	CH_2CHCH_2	CH_2OH	CH_2CO
CH_2CHCHO	$C_2H_5ONO_2$	CH_2CHCO	

APPENDIX B. LIST OF REACTIONS FOR $N_2/O_2/H_2O/CO_2/CO/NO_x/H_2/C_3H_6/C_3H_8$ PLASMAS

Electron impact reactions

Reaction	Rate Coefficient [a]	Ref
$e + N_2 \rightarrow N_2^+ + e + e$	b	1
$e + N_2 \rightarrow N_2(v) + e$	b	1
$e + N_2(v) \rightarrow N_2 + e$	b	1
$e + N_2 \rightarrow N_2(A) + e$	b	1
$e + N_2 \rightarrow N + N + e$	b	1
$e + N_2(A) \rightarrow N_2(v) + e$	b	1
$e + N_2(A) \rightarrow N_2 + e$	b	1
$e + N_2(A) \rightarrow N_2^+ + e + e$	b	1
$e + O_2 \rightarrow O^- + O$	b	2
$e + O_2 \rightarrow O_2^+ + e + e$	b	2
$e + O_2 \rightarrow O_2(^1\Delta) + e + e$	b	2
$e + O_2 \rightarrow O + O + e$	b	2
$e + O_2 \rightarrow O(^1D) + O + e$	b	2
$e + O \rightarrow O(^1D) + e$	b	3
$e + O \rightarrow O^+ + e + e$	b	3
$e + O(^1D) \rightarrow O + e$	b	3
$e + O(^1D) \rightarrow O^+ + e + e$	b	3
$e + H_2O \rightarrow H_2O^+ + e + e$	b	4
$e + H_2O \rightarrow H + OH + e$	b	4
$e + H_2O \rightarrow H^- + OH$	b	4
$e + N_2^+ \rightarrow N(^2D) + N$	$2 \times 10^{-7}\ T_e^{-0.5}$	5
$e + N_3^+ \rightarrow N + N_2$	$2 \times 10^{-7}\ T_e^{-0.5}$	5
$e + H_3O^+ \cdot (H_2O)_2 \rightarrow H + (H_2O)_3$	$2 \times 10^{-7}\ T_e^{-0.5}$	5

$e + NO_2^+ \rightarrow NO + O$	$2 \times 10^{-7}\ T_e^{-0.5}$	5
$e + NO_2^+ \rightarrow NO + O(^1D)$	$2 \times 10^{-7}\ T_e^{-0.5}$	5
$e + H_2NO^+ \rightarrow H_2O + N$	$2 \times 10^{-7}\ T_e^{-0.5}$	5
$e + NO^+ \rightarrow N(^2D) + O$	$2 \times 10^{-7}\ T_e^{-0.5}$	6
$e + NO^+ \rightarrow N + O(^1D)$	$2 \times 10^{-7}\ T_e^{-0.5}$	4
$e + O_2 + M \rightarrow O_2^- + M$	$1 \times 10^{-31}\ cm^6\ s^{-1}$	5
$e + NO^+ \cdot O_2 \rightarrow NO + O_2$	$2 \times 10^{-7}\ T_e^{-0.5}$	5
$e + NO_2 \rightarrow NO_2^-$	4×10^{-11}	5
$e + N_4^+ \rightarrow N_2 + N_2$	$2 \times 10^{-7}\ T_e^{-0.5}$	5
$e + NO^+ \cdot (H_2O)_2 \rightarrow NO + H_2O + H_2O$	$2 \times 10^{-7}\ T_e^{-0.5}$	5
$e + H_2O^+ \rightarrow OH + H$	$6.6 \times 10^{-6}\ T_e^{-0.5}$	6
$e + H_2O^+ \rightarrow O + H + H$	$2.88 \times 10^{-6}\ T_e^{-0.5}$	6
$e + H_2O^+ \rightarrow O + H_2$	$2.52 \times 10^{-6}\ T_e^{-0.5}$	6
$e + H_3O^+ \rightarrow H_2O + H$	$2 \times 10^{-7}\ T_e^{-0.5}$	6
$e + O_2^+ \rightarrow O(^1D) + O$	$2 \times 10^{-7}\ T_e^{-0.5}$	5
$e + H_2^+ \rightarrow H_2$	$2 \times 10^{-7}\ T_e^{-0.5}$	c
$e + O_2^+ \cdot H_2O \rightarrow O_2 + H_2O$	$2 \times 10^{-7}\ T_e^{-0.5}$	c
$e + H_3O^+ \cdot H_2O \rightarrow H + H_2O + H_2O$	$2 \times 10^{-7}\ T_e^{-0.5}$	5
$e + NH_3^+ \rightarrow NH_2 + H$	$2 \times 10^{-7}\ T_e^{-0.5}$	c
$e + NH_4^+ \rightarrow NH_3 + H$	$2 \times 10^{-7}\ T_e^{-0.5}$	c
$e + NO^+ \cdot H_2O \rightarrow NO + H_2O$	$2 \times 10^{-7}\ T_e^{-0.5}$	5
$e + NO^+ \cdot (H_2O)_3 \rightarrow NO + H_2O + H_2O + H_2O$	$2 \times 10^{-7}\ T_e^{-0.5}$	5
$e + CO_2^+ \rightarrow CO + O$	$2 \times 10^{-7}\ T_e^{-0.5}$	c
$e + O_3 \rightarrow e + O_2 + O(^1D)$	5×10^{-10}	c
$e + CO_2 \rightarrow O + CO + e$	b	7

$e + CO_2 \rightarrow CO_2^+ + e + e$	b	7
$e + CO_2 \rightarrow O^- + CO$	b	7

Reactions of $N_2/O_2/H_2O/NO$

Reaction	Rate Coefficient[d]	Ref
$O + O_2 + M \rightarrow O_3 + M$	$6.9 \times 10^{-34} (T/300)^{-1.25}$	8
$H + OH + M \rightarrow H_2O + M$	4.3×10^{-31} cm^6 s^{-1}	5
$N_2O_5 \rightarrow NO_2 + NO_3$	$5.49 \times 10^{14} T^{0.1} \exp(-11080/T)$	8
$NO + O_2 + NO \rightarrow NO_2 + NO_2$	1.4×10^{-38} cm^6 s^{-1}	8
$NO + HO_2 \rightarrow NO_2 + OH$	$3.7 \times 10^{-12} \exp(240/T)$	9
$N(^2D) + N_2 \rightarrow N + N_2$	2.4×10^{-14}	5
$NO + O + O_2 \rightarrow NO_2 + O_2$	$2.44 \times 10^{-27} T^{-1.8}$ cm^6 s^{-1}	9
$N(^2D) + O_2 \rightarrow NO + O$	6.8×10^{-12}	5
$NO + OH + M \rightarrow HNO_2 + M$	$7.4 \times 10^{-31} (T/300)^{-2.4}$ cm^6 s^{-1}	9
$N(^2D) + NO \rightarrow N_2 + O$	6.3×10^{-11}	5
$NO + H + M \rightarrow HNO + M$	3.4×10^{-32} cm^6 s^{-1}	5
$N(^2D) + N_2O \rightarrow NO + N_2$	2.6×10^{-12}	5
$NO + NO_3 \rightarrow NO_2 + NO_2$	$1.6 \times 10^{-11} \exp(150/T)$	9
$HO_2 + NO + M \rightarrow HNO_3 + M$	5.6×10^{-33} cm^6 s^{-1}	8
$HO_2 + NO \rightarrow O_2 + HNO$	$9.0 \times 10^{-19} \exp(2819/T)$	8
$N(^2D) + NO_2 \rightarrow N_2O + O$	1.5×10^{-12}	5
$NO + O_3 \rightarrow NO_2 + O_2$	$2.0 \times 10^{-12} \exp(-1400/T)$	8
$N(^2D) + NO_2 \rightarrow NO + NO$	1.5×10^{-12}	5
$NO + N \rightarrow N_2 + O$	3.1×10^{-11}	5
$H + O_2 + M \rightarrow HO_2 + M$	$5.64 \times 10^{-28} T^{-1.6}$ cm^6 s^{-1}	5
$H + H + M \rightarrow H_2 + M$	4.8×10^{-33} cm^6 s^{-1}	5
$H + NO_2 \rightarrow OH + NO$	8×10^{-11}	5

$H + HO_2 \rightarrow OH + OH$	2.8×10^{-10} exp(-440/T)	8
$N_2(A) + N_2 \rightarrow N_2 + N_2$	1.9×10^{-13}	10
$H + O_3 \rightarrow OH + O_2$	1.4×10^{-10}exp(-480/T)	9
$N_2(A) + NO \rightarrow NO + N_2$	3.6×10^{-10}	10
$H + HNO \rightarrow H_2 + NO$	1×10^{-11}	5
$N_2(A) + O_2 \rightarrow O + O + N_2$	1.5×10^{-12}	10
$N + NO_2 \rightarrow N_2O + O$	2.4×10^{-12}	5
$N_2(A) + O_2 \rightarrow O_2 + N_2$	2.8×10^{-11}	10
$N + NO_2 \rightarrow NO + NO$	6×10^{-13}	5
$N_2(A) + N_2O \rightarrow N_2 + N_2 + O$	1.4×10^{-11}	10
$N_2(A) + N_2O \rightarrow N_2 + N_2O$	1.7×10^{-10}	10
$N + N + M \rightarrow N_2 + M$	3.9×10^{-33} cm^6 s^{-1}	5
$N_2(A) + NO_2 \rightarrow NO + O + N_2$	1.0×10^{-12}	10
$N_2(A) + H_2 \rightarrow N_2 + H_2$	2.6×10^{-11}	10
$N + OH \rightarrow NO + H$	3.8×10^{-11} exp(85/T)	9
$O(^1D) + N_2 \rightarrow O + N_2$	1.8×10^{-11} exp(107/T)	9
$N + O + M \rightarrow NO + M$	5.46×10^{-33} exp(155/T) cm^6 s^{-1}	11
$O(^1D) + O_2 \rightarrow O + O_2$	3.8×10^{-11}	5
$N + O_2 \rightarrow NO + O$	4.4×10^{-12} exp(-3220/T)	9
$N + O_3 \rightarrow NO + O_2$	5×10^{-16}	5
$O(^1D) + H_2O \rightarrow O + H_2O$	1.2×10^{-11}	5
$O(^1D) + H_2O \rightarrow OH + OH$	2.2×10^{-10}	5
$O + HO_2 \rightarrow OH + O_2$	2.9×10^{-11} exp(200/T)	9
$O + O_3 \rightarrow O_2 + O_2$	8.0×10^{-12} exp(-2060/T)	9
$O + NO_2 + M \rightarrow NO_3 + M$	9.0×10^{-32} $(T/300)^{-2.0}$ cm^6 s^{-1}	9
$NO_3 + NO_3 \rightarrow NO_2 + NO_2 + O_2$	1.2×10^{-15}	5

$OH + OH \rightarrow O + H_2O$	$3.5 \times 10^{-16}\ T^{1.4} \exp(200/T)$	12
$N_2O_5 + H_2O \rightarrow HNO_3 + HNO_3$	5×10^{-21}	5
$NH + NO \rightarrow N_2O + H$	1.3×10^{-12}	5
$OH + NO_2 + N_2 \rightarrow HNO_3 + N_2$	$2.2 \times 10^{-30}\ (T/300)^{-2.9}\ cm^6\ s^{-1}$	9
$NH + O_2 \rightarrow HNO + O$	2.3×10^{-13}	5
$OH + HNO_3 \rightarrow NO_3 + H_2O$	$1.5 \times 10^{-14} \exp(650/T)$	5
$OH + HNO \rightarrow H_2O + NO$	$2.15 \times 10^{-17}\ T^{1.88} \exp(481/T)$	8
$OH + HO_2 \rightarrow H_2O + O_2$	8×10^{-11}	c
$H_2O^+ + H_2O \rightarrow H_3O^+ + OH$	1.7×10^{-9}	5
$OH + HNO_2 \rightarrow NO_2 + H_2O$	$1.8 \times 10^{-11} \exp(-390/T)$	9
$H_2O^+ + O_2 \rightarrow O_2^+ + H_2O$	4.3×10^{-10}	5
$OH + O_3 \rightarrow HO_2 + O_2$	$1.9 \times 10^{-12} \exp(-1000/T)$	5
$N_3^+ + O_2 \rightarrow NO^+ + N_2O$	3.6×10^{-11}	5
$OH + N_2O \rightarrow HNO + NO$	3.8×10^{-17}	5
$N_3^+ + O_2 \rightarrow NO_2^+ + N_2$	1.5×10^{-11}	5
$HO_2 + NO_2 + N_2 \rightarrow HO_2NO_2 + N_2$	$1.5 \times 10^{-31}\ (T/300)^{-3.2}\ cm^6\ s^{-1}$	9
$N_3^+ + NO \rightarrow NO^+ + N + N_2$	1.4×10^{-10}	5
$HO_2 + O_3 \rightarrow OH + O_2 + O_2$	$1.4 \times 10^{-14} \exp(-600/T)$	5
$N_3^+ + NO_2 \rightarrow NO^+ + NO + N_2$	7×10^{-11}	5
$NO_2 + O_3 \rightarrow NO_3 + O_2$	$1.2 \times 10^{-13} \exp(-2450/T)$	9
$N_3^+ + NO_2 \rightarrow NO_2^+ + N + N_2$	7×10^{-11}	5
$N_3^+ + N_2O \rightarrow NO^+ + N_2 + N_2$	5×10^{-11}	5
$O + NO_2 \rightarrow NO + O_2$	$6.5 \times 10^{-12} \exp(120/T)$	9
$O + NO_3 \rightarrow O_2 + NO_2$	1×10^{-11}	5
$N_3^+ + NO_2^- \rightarrow N + N_2 + NO_2$	$2 \times 10^{-6}\ (T/300)^{-0.5}$	5

$O + OH \rightarrow H + O_2$	$2.3 \times 10^{-11} \exp(110/T)$	12
$O^+ + N_2 \rightarrow NO^+ + N$	1.2×10^{-12}	5
$OH + OH + O_2 \rightarrow H_2O_2 + O_2$	$6.9 \times 10^{-31} (T/300)^{-0.8}$ cm^6 s^{-1}	9
$O^+ + NO \rightarrow NO^+ + O$	1.7×10^{-12}	5
$OH + H_2O_2 \rightarrow H_2O + HO_2$	$2.9 \times 10^{-12} \exp(-160/T)$	5
$O^+ + O_2 \rightarrow O_2^+ + O$	1.9×10^{-11}	5
$H + HO_2 \rightarrow H_2 + O_2$	$1.1 \times 10^{-10} \exp(-1070/T)$	12
$O^+ + NO_2 \rightarrow NO_2^+ + O$	1.6×10^{-9}	5
$HO_2NO_2 + O_2 \rightarrow HO_2 + NO_2 + O_2$	$3.6 \times 10^{-6} \exp(-10000/T)$	5
$O^+ + NO_2^- \rightarrow O + NO_2$	$2 \times 10^{-6} (T/300)^{-0.5}$	5
$O_2^+ + NO \rightarrow NO^+ + O_2$	4.4×10^{-10}	5
$O_2^+ + NO_2 \rightarrow NO_2^+ + O_2$	8.8×10^{-9}	5
$O_2^+ \cdot H2O + H_2O \rightarrow H_3O^+ + OH + O_2$	1.2×10^{-9}	5
$H_3O^+ + H_2O + M \rightarrow H_3O^+ \cdot H_2O + M$	5×10^{-27} cm^6 s^{-1}	5
$O_2^+ + NO_2^- \rightarrow O_2 + NO_2$	$2 \times 10^{-6} (T/300)^{-0.5}$	5
$H_3O^+ \cdot H_2O + H_2O \rightarrow H_3O^+ \cdot (H_2O)_2$	1×10^{-9}	5
$NO_2^+ + NO \rightarrow NO^+ + NO_2$	2.9×10^{-10}	5
$H_3O^+ \cdot (H_2O)_2 + NO_2^- \rightarrow H + (H_2O)_3 + NO_2$	$2 \times 10^{-7} (T/300)^{-0.5}$	5
$H_3O^+ \cdot (H_2O)_2 + NO_3^- \rightarrow H + (H_2O)_3 + NO_3$	$2 \times 10^{-7} (T/300)^{-0.5}$	5
$NO_2^+ + NO_2^- \rightarrow NO_2 + NO_2$	$3 \times 10^{-6} (T/300)^{-0.5}$	5
$NO_2^+ + NO_3^- \rightarrow NO_2 + NO_3$	$3 \times 10^{-6} (T/300)^{-0.5}$	5
$N_2^+ + NO \rightarrow NO^+ + N_2$	3.3×10^{-10}	5
$N_3^+ + H_2O \rightarrow H_2NO^+ + N_2$	3.3×10^{-10}	5

$N_2^+ + NO_2 \rightarrow NO_2^+ + N_2$	3.3×10^{-10}	5
$N_2^+ + NO_2 \rightarrow NO^+ + N_2O$	5.0×10^{-11}	5
$H_2NO^+ + NO_2^- \rightarrow H_2O + N + NO_2$	$2 \times 10^{-6} (T/300)^{-0.5}$	5
$H_2NO^+ + NO_3^- \rightarrow H_2O + N + NO_3$	$2 \times 10^{-6} (T/300)^{-0.5}$	5
$NO_2^- + HNO_3 \rightarrow NO_3^- + HNO_2$	1.6×10^{-9}	5
$N_2^+ + NO_2^- \rightarrow N_2 + NO_2$	$3 \times 10^{-6} (T/300)^{-0.5}$	5
$NO_2^- + NO_2 \rightarrow NO_3^- + NO$	1×10^{-13}	5
$N_2^+ + NO_3^- \rightarrow N_2 + NO_3$	$3 \times 10^{-6} (T/300)^{-0.5}$	5
$NO_2^- + N_2O \rightarrow NO_3^- + N_2$	5×10^{-13}	5
$NO_2^- + N_2O_5 \rightarrow NO_3^- + NO_2 + NO_2$	7×10^{-10}	5
$NO_2^- + O_3 \rightarrow NO_3^- + O_2$	1.2×10^{-10}	5
$NO_3^- + NO \rightarrow NO_2^- + NO_2$	5×10^{-13}	5
$NO^+ + NO2^- \rightarrow NO + NO2$	$3 \times 10^{-6} (T/300)^{-0.5}$	5
$NO^+ + NO_3^- \rightarrow NO + NO_3$	$3 \times 10^{-6} (T/300)^{-0.5}$	5
$O_2^- + NO_2 \rightarrow NO_2^- + O_2$	7×10^{-10}	5
$NO^+ + O_2 + M \rightarrow NO^+ \cdot O_2 + M$	3×10^{-31} cm^6 s^{-1}	13
$O_2^- + N_2^+ \rightarrow N_2 + O_2$	$2 \times 10^{-6} (T/300)^{-0.5}$	5
$NO^+ \cdot O_2 + NO_2^- \rightarrow NO + O_2 + NO_2$	$3 \times 10^{-6} (T/300)^{-0.5}$	5
$N(^2D) + NH_3 \rightarrow NH + NH_2$	5×10^{-11}	5
$NO^+ \cdot O_2 + NO_2^- \rightarrow NO_3 + NO_2$	$2 \times 10^{-7} (T/300)^{-0.5}$	5
$NO^+ \cdot O_2 + NO_3^- \rightarrow NO + O_2 + NO_3$	$3 \times 10^{-6} (T/300)^{-0.5}$	5
$OH + NH_3 \rightarrow NH_2 + H_2O$	$3.5 \times 10^{-12} \exp(-925/T)$	9
$O(^1D) + NH_3 \rightarrow NH_2 + OH$	2.5×10^{-10}	5

$NH_2 + NO \rightarrow N_2 + H_2O$	$1.6 \times 10^{-11}\ (T/300)^{-1.5}$	9
$N^+ + N_2 + M \rightarrow N_3^+ + M$	$5.2 \times 10^{-30}\ cm^6\ s^{-1}$	5
$NH_2 + NO_2 \rightarrow N_2O + H_2O$	$1.9 \times 10^{-11}\ (T/300)^{-2.2}$	9
$N^+ + O_2 \rightarrow NO^+ + O$	2.6×10^{-10}	5
$O_2^+ + NH_3 \rightarrow NH_3^+ + O_2$	1×10^{-9}	13
$N^+ + O_2 \rightarrow O_2^+ + N$	3.1×10^{-10}	5
$NH_3^+ + NH_3 \rightarrow NH_4^+ + NH_2$	2.2×10^{-9}	5
$N^+ + O_2 \rightarrow O^+ + NO$	3.6×10^{-11}	5
$H_3O^+ + NH_3 \rightarrow NH_4^+ + H_2O$	2.5×10^{-9}	5
$N^+ + NO \rightarrow NO^+ + N$	9×10^{-10}	5
$N^+ + NH_3 \rightarrow NH_3^+ + N$	2.4×10^{-9}	5
$N_2^+ + N_2 + M \rightarrow N_4^+ + M$	1.1×10^{-29}	5
$N_3^+ + NH_3 \rightarrow NH_3^+ + N + N_2$	2.1×10^{-9}	5
$N_2^+ + O_2 \rightarrow O_2^+ + N_2$	5.1×10^{-11}	5
$N_2^+ + NH_3 \rightarrow NH_3^+ + N_2$	1.9×10^{-9}	5
$N_4^+ + NO \rightarrow NO^+ + N_2 + N_2$	1.8×10^{-9}	5
$N_4^+ + NO_2 \rightarrow NO_2^+ + N_2 + N_2$	2.5×10^{-10}	5
$NH_3^+ + NO_3^- \rightarrow NH_3 + NO_3$	$5 \times 10^{-6}\ (T/300)^{-0.5}$	c
$N_4^+ + NO_2 \rightarrow NO^+ + N_2O + N_2$	5×10^{-11}	5
$NH_4^+ + NO_3^- \rightarrow NH_3 + H + NO_3$	$3 \times 10^{-6}\ (T/300)^{-0.5}$	5
$N_4^+ + O_2 \rightarrow O_2^+ + N_2 + N_2$	2.5×10^{-10}	5
$NO^+ + H_2O + M \rightarrow NO^+ \cdot H_2O + M$	$1.6 \times 10^{-28}\ cm^6\ s^{-1}$	5
$NO^+ \cdot H_2O + H_2O + M \rightarrow NO^+ \cdot (H_2O)_2 + M$	1×10^{-27}	5
$N_4^+ + NO_2^- \rightarrow NO_2 + N_2 + N_2$	$3 \times 10^{-6}\ (T/300)^{-0.5}$	5
$NO^+ \cdot (H_2O)_2 + M \rightarrow$	1.3×10^{-12}	5

$NO^+ \cdot H_2O + H_2O + M$		
$N_4^+ + NO_3^- \rightarrow NO_3 + N_2 + N_2$	$3 \times 10^{-6} (T/300)^{-0.5}$	5
$NO^+ \cdot (H_2O)_2 + H_2O \rightarrow NO^+ \cdot (H_2O)_3$	1×10^{-9}	5
$O_2^+ + H_2O + M \rightarrow O_2^+ \cdot H_2O + M$	2.5×10^{-28} cm^6 s^{-1}	5
$NO^+ \cdot (H_2O)_3 + H_2O \rightarrow$ $H_3O^+ \cdot (H_2O)_2 + HNO_2$	8×10^{-11}	5
$NH_2 + O \rightarrow NH + OH$	1.2×10^{-11}	13
$NH_2 + O \rightarrow HNO + H$	7.6×10^{-11}	13
$HO_2NO_2 + N_2 \rightarrow$ $HO_2 + NO_2 + N_2$	$5 \times 10^{-6} \exp(-10000/T)$	9
$OH + NO_2 + O_2 \rightarrow HNO_3 + O_2$	$2.6 \times 10^{-30} (T/300)^{-2.9}$ cm^6 s^{-1}	9
$OH + H_2 \rightarrow H_2O + H$	$7.7 \times 10^{-12} \exp(-2100/T)$	12
$O(^1D) + H_2O \rightarrow H_2 + O_2$	2.3×10^{-12}	5
$O(^1D) + H_2 \rightarrow OH + H$	1.1×10^{-10}	5
$O + H_2O_2 \rightarrow OH + HO_2$	$1.4 \times 10^{-12} \exp(-2000/T)$	12
$O + H_2 \rightarrow OH + H$	$1.6 \times 10^{-11} \exp(-4570/T)$	5
$H + HO_2 \rightarrow H_2O + O$	9.4×10^{-13}	5
$HO_2 + HO_2 + M \rightarrow$ $H_2O_2 + O_2 + M$	$1.9 \times 10^{-33} \exp(980/T)$ cm^6 s^{-1}	9
$O + NO + N_2 \rightarrow NO_2 + N_2$	$9.1 \times 10^{-28} T^{-1.6}$ cm^6 s^{-1}	9
$NO_2 + NO_3 + M \rightarrow N_2O_5 + M$	$2.7 \times 10^{-30} (T/300)^{-3.4}$ cm^6 s^{-1}	9
$N^+ + H_2O \rightarrow H_2O^+ + N$	$5.55 \times 10^{-8} T^{-0.52}$	5
$H_2O^+ + NO_2^- \rightarrow H_2O + NO_2$	$2 \times 10^{-6} (T/300)^{-0.5}$	14
$H_2O^+ + NO_3^- \rightarrow H2O + NO_3$	$2 \times 10^{-6} (T/300)^{-0.5}$	14
$H_2O^+ + O_2^- \rightarrow H_2O + O_2$	$2 \times 10^{-6} (T/300)^{-0.5}$	14
$H_3O^+ + NO_2^- \rightarrow H_2O + H + NO_2$	$2 \times 10^{-6} (T/300)^{-0.5}$	14
$H_3O^+ + NO_3^- \rightarrow H_2O + H + NO_3$	$2 \times 10^{-6} (T/300)^{-0.5}$	14
$H_3O^+ + O_2^- \rightarrow H_2O + H + O_2$	$2 \times 10^{-6} (T/300)^{-0.5}$	14

$O_2^+ + NO_3^- \rightarrow O_2 + NO_3$	$2 \times 10^{-6} (T/300)^{-0.5}$	14
$O_2^+ + O_2^- \rightarrow O_2 + O_2$	$2 \times 10^{-6} (T/300)^{-0.5}$	14
$N_3^+ + NO_3^- \rightarrow N_2 + N + NO_3$	$2 \times 10^{-6} (T/300)^{-0.5}$	c
$N_3^+ + O_2^- \rightarrow N_2 + N + O_2$	$2 \times 10^{-6} (T/300)^{-0.5}$	c
$NO^+ + O_2^- \rightarrow NO + O_2$	$2 \times 10^{-6} (T/300)^{-0.5}$	14
$NO_2^+ + O_2^- \rightarrow NO_2 + O_2$	$2 \times 10^{-6} (T/300)^{-0.5}$	14
$O^+ + NO_3^- \rightarrow O + NO_3$	$2 \times 10^{-6} (T/300)^{-0.5}$	14
$O^+ + O_2^- \rightarrow O + O_2$	$2 \times 10^{-6} (T/300)^{-0.5}$	14
$NO^+ \cdot O_2 + O_2^- \rightarrow NO + O_2 + O_2$	$2 \times 10^{-6} (T/300)^{-0.5}$	c
$N^+ + O_2^- \rightarrow N + O_2$	$2 \times 10^{-6} (T/300)^{-0.5}$	14
$N^+ + NO_2^- \rightarrow N + NO_2$	$2 \times 10^{-6} (T/300)^{-0.5}$	14
$N^+ + NO_3^- \rightarrow N + NO_3$	$2 \times 10^{-6} (T/300)^{-0.5}$	14
$N_4^+ + O_2^- \rightarrow N_2 + N_2 + O_2$	$2 \times 10^{-6} (T/300)^{-0.5}$	c
$O_2^+ \cdot H_2O + O_2^- \rightarrow O_2 + O_2 + H_2O$	$2 \times 10^{-6} (T/300)^{-0.5}$	c
$O_2^+ \cdot H_2O + NO_3^- \rightarrow O_2 + NO_3 + H_2O$	$2 \times 10^{-6} (T/300)^{-0.5}$	c
$O_2^+ \cdot H_2O + NO_2^- \rightarrow O_2 + H_2O + NO_2$	$2 \times 10^{-6} (T/300)^{-0.5}$	c
$H_3O^+ \cdot H_2O + NO_2^- \rightarrow H + H_2O + H_2O + NO_2$	$2 \times 10^{-6} (T/300)^{-0.5}$	c
$H_3O^+ \cdot H_2O + NO_3^- \rightarrow H + H_2O + H_2O + NO_3$	$2 \times 10^{-6} (T/300)^{-0.5}$	c
$H_3O^+ \cdot H_2O + O_2^- \rightarrow H + H_2O + H_2O + O_2$	$2 \times 10^{-6} (T/300)^{-0.5}$	c
$H_3O^+ \cdot (H_2O)_2 + O_2^- \rightarrow H + (H_2O)_3 + O_2$	$2 \times 10^{-6} (T/300)^{-0.5}$	c
$H_2NO^+ + O_2^- \rightarrow H_2O + N + O_2$	$2 \times 10^{-6} (T/300)^{-0.5}$	c
$NH_3^+ + NO_2^- \rightarrow NH_3 + NO_2$	$2 \times 10^{-6} (T/300)^{-0.5}$	14

$NH_3^+ + O_2^- \rightarrow NH_3 + O_2$	$2 \times 10^{-6} (T/300)^{-0.5}$	14
$NH_4^+ + NO_2^- \rightarrow NH_3 + H + NO_2$	$2 \times 10^{-6} (T/300)^{-0.5}$	c
$NH_4^+ + NO_3^- \rightarrow NH_3 + H + NO_3$	$2 \times 10^{-6} (T/300)^{-0.5}$	c
$NH_4^+ + O_2^- \rightarrow NH_3 + H + O_2$	$2 \times 10^{-6} (T/300)^{-0.5}$	c
$NO^+ \cdot H_2O + NO_2^- \rightarrow NO + H_2O + NO_2$	$2 \times 10^{-6} (T/300)^{-0.5}$	c
$NO^+ \cdot H_2O + NO3^- \rightarrow NO + H_2O + NO_3$	$2 \times 10^{-6} (T/300)^{-0.5}$	c
$NO^+ \cdot H_2O + O_2^- \rightarrow NO + H_2O + O_2$	$2 \times 10^{-6} (T/300)^{-0.5}$	c
$NO^+ \cdot (H_2O)_2 + NO_3^- \rightarrow NO + H_2O + H_2O + NO_3$	$2 \times 10^{-6} (T/300)^{-0.5}$	c
$NO^+ \cdot (H_2O)_3 + NO3^- \rightarrow NO + H_2O + H_2O + H_2O + NO_3$	$2 \times 10^{-6} (T/300)^{-0.5}$	c
$NO^+ \cdot (H_2O)_2 + NO_2^- \rightarrow NO + H_2O + H_2O + NO_2$	$2 \times 10^{-6} (T/300)^{-0.5}$	c
$NO^+ \cdot (H_2O)_3 + NO_2^- \rightarrow NO + H_2O + H_2O + H_2O + NO_2$	$2 \times 10^{-6} (T/300)^{-0.5}$	c
$NO^+ \cdot (H_2O)_2 + O_2^- \rightarrow NO + H_2O + H_2O + O_2$	$2 \times 10^{-6} (T/300)^{-0.5}$	c
$NO^+ \cdot (H_2O)_3 + O_2^- \rightarrow NO + H_2O + H_2O + H_2O + O_2$	$2 \times 10^{-6} (T/300)^{-0.5}$	c
$O + H + M \rightarrow OH + M$	1.62×10^{-32} cm^6 s^{-1}	15
$H + H_2O_2 \rightarrow H_2O + OH$	$4 \times 10^{-11} \exp(-2000/T)$	12
$NO_2 + NO_2 + N_2 \rightarrow N_2O_4 + N_2$	$1.4 \times 10^{-33} (T/300)^{-3.8}$ cm^6 s^{-1}	16
$N_2O_4 + N_2 \rightarrow NO_2 + NO_2 + N_2$	$1.29 \times 10^{-5} (T/300)^{-3.8} \exp(-6460/T)$	16
$NH_2 + H_2 \rightarrow NH_3 + H$	$5.98 \times 10^{-12} \exp(-2290/T)$	17

$NH_3 + H \rightarrow NH_2 + H_2$	$1.35 \times 10^{-10} \exp(-3660/T)$	17
$OH + NO_3 \rightarrow HO_2 + NO_2$	2.6×10^{-11}	18
$HO_2 + NO_3 \rightarrow OH + NO_2 + O_2$	3.6×10^{-12}	18
$HO_2 + NO_3 \rightarrow HNO_3 + O_2$	9.2×10^{-13}	18
$H + H_2O_2 \rightarrow HO_2 + H_2$	$8 \times 10^{-11} \exp(-4000/T)$	12
$HNO_3 + NO \rightarrow HNO_2 + NO_2$	7.37×10^{-21}	19
$H_2 + O_2 \rightarrow H + HO_2$	$2.4 \times 10^{-10} \exp(-28500/T)$	12
$H + O_2 \rightarrow OH + O$	$2.8 \times 10^{-7} T^{-0.9} \exp(-8750/T)$	12
$OH + M \rightarrow O + H + M$	$4 \times 10^{-9} \exp(-50000/T)$	12
$OH + O_2 \rightarrow O + HO_2$	$3.7 \times 10^{-11} \exp(-26500/T)$	12
$OH + H \rightarrow O + H_2$	$1.14 \times 10^{-12} T^{0.67} \exp(-518/T)$	6
$HO_2 + M \rightarrow H + O_2 + M$	$2 \times 10^{-5} T^{-1.18} \exp(-24363/T)$	12
$HO_2 + H_2 \rightarrow H_2O_2 + H$	$5 \times 10^{-11} \exp(-13100/T)$	12
$H_2O_2 + O_2 \rightarrow HO_2 + HO_2$	$9 \times 10^{-11} \exp(-20000/T)$	12
$H_2O + H \rightarrow H_2 + OH$	$1.03 \times 10^{-16} T^{1.9} \exp(-9265/T)$	12
$H_2O + O \rightarrow OH + OH$	$7.6 \times 10^{-15} T^{1.3} \exp(-8605/T)$	12
$H^- + N_2^+ \rightarrow H + N_2$	$3 \times 10^{-6} (T/300)^{-0.5}$	c
$O^- + N_2^+ \rightarrow O + N_2$	$3 \times 10^{-6} (T/300)^{-0.5}$	c
$O^- + H_2^+ \rightarrow O + H_2$	$3 \times 10^{-6} (T/300)^{-0.5}$	14
$O_2^- + H_2^+ \rightarrow O2 + H_2$	$3 \times 10^{-6} (T/300)^{-0.5}$	14
$H^- + H_2^+ \rightarrow H + H_2$	$3 \times 10^{-6} (T/300)^{-0.5}$	14
$H^- + H_2O^+ \rightarrow H + H_2O$	$3 \times 10^{-6} (T/300)^{-0.5}$	14
$O^- + H_2O^+ \rightarrow O + H_2O$	$3 \times 10^{-6} (T/300)^{-0.5}$	14
$H^- + H_3O^+ \rightarrow H2 + H_2O$	$3 \times 10^{-6} (T/300)^{-0.5}$	c
$O^- + H_3O^+ \rightarrow OH + H_2O$	$3 \times 10^{-6} (T/300)^{-0.5}$	c
$H^- + O_2^+ + M \rightarrow H_2O + M$	1.2×10^{-25}	c
$O^- + O_2^+ \rightarrow O + O_2$	$3 \times 10^{-6} (T/300)^{-0.5}$	14

$H^- + N_3^+ \rightarrow NH + N_2$	$3 \times 10^{-6} (T/300)^{-0.5}$	c
$O^- + N_3^+ \rightarrow NO + N_2$	$3 \times 10^{-6} (T/300)^{-0.5}$	c
$H^- + NO^+ + M \rightarrow HNO + M$	1.2×10^{-25} cm^6 s^{-1}	c
$O^- + NO^+ \rightarrow NO + O$	$3 \times 10^{-6} (T/300)^{-0.5}$	c
$H^- + NO_2^+ + M \rightarrow HNO_2 + M$	1.2×10^{-25} cm^6 s^{-1}	c
$O^- + NO_2^+ \rightarrow NO_2 + O$	$3 \times 10^{-6} (T/300)^{-0.5}$	14
$H^- + O^+ + M \rightarrow OH + M$	1.2×10^{-25} cm^6 s^{-1}	c
$O^- + O^+ + M \rightarrow O_2 + M$	1.2×10^{-25} cm^6 s^{-1}	c
$H^- + NO^+ \cdot O_2 \rightarrow HNO + O_2$	$3 \times 10^{-6} (T/300)^{-0.5}$	c
$O^- + NO^+ \cdot O_2 \rightarrow NO_2 + O_2$	$3 \times 10^{-6} (T/300)^{-0.5}$	c
$H^- + N^+ + M \rightarrow NH + M$	1.2×10^{-25} cm^6 s^{-1}	c
$O^- + N^+ + M \rightarrow NO + M$	1.2×10^{-25} cm^6 s^{-1}	c
$H^- + N_2^+ \rightarrow H + N_2 + N_2$	$3 \times 10^{-6} (T/300)^{-0.5}$	c
$O^- + N_4^+ \rightarrow O + N_2 + N_2$	$3 \times 10^{-6} (T/300)^{-0.5}$	c
$H^- + O_2^+ \cdot H_2O \rightarrow HO_2 + H_2O$	$3 \times 10^{-6} (T/300)^{-0.5}$	c
$O^- + O_2^+ \cdot H_2O \rightarrow O + O_2 + H_2O$	$3 \times 10^{-6} (T/300)^{-0.5}$	c
$H^- + H_3O^+ \cdot H_2O \rightarrow H_2 + H_2O + H_2O$	$3 \times 10^{-6} (T/300)^{-0.5}$	c
$O^- + H_3O^+ \cdot H_2O \rightarrow OH + H_2O + H_2O$	$3 \times 10^{-6} (T/300)^{-0.5}$	c
$H^- + H_3O^+ \cdot (H_2O)_2 \rightarrow H_2 + (H_2O)_3$	$3 \times 10^{-6} (T/300)^{-0.5}$	c
$O^- + H_3O^+ \cdot (H_2O)_2 \rightarrow OH + (H_2O)_3$	$3 \times 10^{-6} (T/300)^{-0.5}$	c
$H^- + H_2NO^+ \rightarrow H_2 + HNO$	$3 \times 10^{-6} (T/300)^{-0.5}$	c
$O^- + H_2NO^+ \rightarrow OH + HNO$	$3 \times 10^{-6} (T/300)^{-0.5}$	c
$H^- + NH_3^+ \rightarrow H + NH_3$	$3 \times 10^{-6} (T/300)^{-0.5}$	c
$O^- + NH_3^+ \rightarrow O + NH_3$	$3 \times 10^{-6} (T/300)^{-0.5}$	c
$H^- + NH_4^+ \rightarrow H_2 + NH_3$	$3 \times 10^{-6} (T/300)^{-0.5}$	c

$O^- + NH_4^+ \rightarrow OH + NH_3$	$3 \times 10^{-6} (T/300)^{-0.5}$	c
$H^- + NO^+ \cdot H_2O \rightarrow$ $H + NO + H_2O$	$3 \times 10^{-6} (T/300)^{-0.5}$	c
$O^- + NO^+ \cdot H_2O \rightarrow O + NO + H_2O$	$3 \times 10^{-6} (T/300)^{-0.5}$	c
$H^- + NO^+ \cdot (H_2O)_2 \rightarrow$ $HNO + H_2O + H_2O$	$3 \times 10^{-6} (T/300)^{-0.5}$	c
$O^- + NO^+ \cdot (H_2O)_2 \rightarrow$ $NO_2 + H_2O + H_2O$	$3 \times 10^{-6} (T/300)^{-0.5}$	c
$H^- + NO^+ \cdot (H_2O)_3 \rightarrow$ $HNO + H_2O + H_2O + H_2O$	$3 \times 10^{-6} (T/300)^{-0.5}$	c
$O^- + NO^+ \cdot (H_2O)_3 \rightarrow$ $NO_2 + H_2O + H_2O + H_2O$	$3 \times 10^{-6} (T/300)^{-0.5}$	c
$OH + NO_2 + H_2O \rightarrow HNO_3 + H_2O$	$2.2 \times 10^{-30} (T/300)^{-2.9}$	8
$N_2^+ + H_2O \rightarrow H_2O^+ + N_2$	2×10^{-9}	c
$O + OH + M \rightarrow HO_2 + M$	2.76×10^{-31} cm^6 s^{-1}	8
$O(^1D) + O_3 \rightarrow O_2 + O + O$	1.2×10^{-10}	8
$O(^1D) + NO \rightarrow O_2 + N$	8.5×10^{-11}	8
$NH + NO \rightarrow N_2 + OH$	4.5×10^{-11}	8
$N_3 + NO \rightarrow N_2O + N_2$	1.19×10^{-12}	8
$NH_2 + O \rightarrow H_2 + NO$	8.3×10^{-12}	8
$OH + NO_2 \rightarrow HO_2 + NO$	3.03×10^{-11} exp(-3360/T)	8
$NO_3 + NO_2 \rightarrow NO + NO_2 + O_2$	8.21×10^{-14} exp(-1480/T)	8
$O(^1D) + NO_2 \rightarrow O_2 + NO$	2.5×10^{-10}	8
$O(^1D) + N_2O \rightarrow NO + NO$	6.7×10^{-11}	8
$NO_2 + O3 \rightarrow O_2 + O_2 + NO$	1.0×10^{-18}	8
$O + N_3 \rightarrow NO + N_2$	1.12×10^{-11}	8
$O + HNO \rightarrow OH + NO$	1.82×10^{-11}	8
$HNO + O_2 \rightarrow NO + HO_2$	5.25×10^{-12} exp(-1510/T)	8
$O + O + M \rightarrow O_2 + M$	5.21×10^{-35} exp(900/T) cm^6 s^{-1}	8

Additional reactions for CO_2

Reaction	Rate Coefficient [d]	Ref
$N_2(A) + CO_2 \rightarrow N_2 + CO_2$	2.5×10^{-11}	10
$N_2(A) + CO \rightarrow N_2 + CO$	1.1×10^{-10}	10
$O(^1D) + CO_2 \rightarrow O + CO_2$	7.4×10^{-11}	c
$OH + CO \rightarrow CO_2 + H$	$1.12 \times 10^{-13} \exp(-91000/T)$	12
$CO_2^+ + NO \rightarrow NO^+ + CO_2$	1.2×10^{-10}	5
$CO_2^+ + O_2 \rightarrow O_2^+ + CO_2$	5.6×10^{-11}	5
$CO_2^+ + NO_2^- \rightarrow CO_2 + NO_2$	$2 \times 10^{-6} (T/300)^{-0.5}$	14
$CO_2^+ + NO_3^- \rightarrow CO_2 + NO_3$	$2 \times 10^{-6} (T/300)^{-0.5}$	14
$CO_2^+ + O_2^- \rightarrow CO_2 + O_2$	$2 \times 10^{-6} (T/300)^{-0.5}$	14
$CO_2 + H \rightarrow CO + OH$	$2.5 \times 10^{-10} \exp(-13300/T)$	12
$CO_2 + O \rightarrow CO + O_2$	$2.8 \times 10^{-11} \exp(-26500/T)$	12
$CO + O_2 \rightarrow CO_2 + O$	$4.2 \times 10^{-12} \exp(-24000/T)$	12
$CO + O + M \rightarrow CO_2 + M$	$1.7 \times 10^{-33} \exp(-1510/T)$ $cm^6 s^{-1}$	12
$CO + HO_2 \rightarrow OH + CO_2$	$2.5 \times 10^{-10} \exp(-11900/T)$	12
$HCO + M \rightarrow H + CO + M$	$8.5 \times 10^{-3} T^{-2.14} \exp(-10278/T)$	12
$HCO + H_2 \rightarrow CH_2O + H$	$3 \times 10^{-18} T^2 \exp(-8972/T)$	12
$HCO + O_2 \rightarrow HO_2 + CO$	$8.5 \times 10^{-11} \exp(-850/T)$	12
$HCO + H \rightarrow H_2 + CO$	2×10^{-10}	12
$HCO + O \rightarrow H + CO_2$	5×10^{-11}	12
$HCO + O \rightarrow OH + CO$	5×10^{-11}	12
$HCO + OH \rightarrow H_2O + CO$	5×10^{-11}	12
$HCO + HO_2 \rightarrow OH + H + CO_2$	5×10^{-11}	12
$HCO + H_2O_2 \rightarrow CH_2O + HO_2$	$1.7 \times 10^{-13} \exp(-3486/T)$	12
$HCO + H_2O \rightarrow CH_2O + OH$	$3.9 \times 10^{-16} T^{1.35} \exp(-13146/T)$	12

$HCO + HCO \rightarrow CH_2O + CO$	3×10^{-11}	12
$HCO + HCO \rightarrow H_2 + CO + CO$	5×10^{-12}	12
$H^- + CO_2^+ \rightarrow H + CO_2$	$3 \times 10^{-6} (T/300)^{-0.5}$	c
$O^- + CO_2^+ \rightarrow O + CO_2$	$3 \times 10^{-6} (T/300)^{-0.5}$	c
$CH_2O + OH \rightarrow H + HCOOH$	2×10^{-13}	8
$HCOOH + OH \rightarrow H_2O + CO_2 + H$	4.8×10^{-13}	8
$CN + O \rightarrow CO + N$	1.7×10^{-11}	8
$CN + N \rightarrow N_2 + C$	3×10^{-10}	c
$CN + N + M \rightarrow CNN + M$	2.76×10^{-32} cm^6 s^{-1}	8
$CN + NO \rightarrow N_2 + CO$	1.2×10^{-13}	8
$CN + N_2O \rightarrow CNN + NO$	$6.40 \times 10^{-21} T^{2.6} \exp(-1860/T)$	8
$CN + HCN \rightarrow NCCN + H$	$6.31 \times 10^{-17} T^{1.57} \exp(-50/T)$	8
$CN + H_2O \rightarrow HCN + OH$	$1.33 \times 10^{-11} \exp(-3752/T)$	8
$CN + H_2 \rightarrow HCN + H$	$1.13 \times 10^{-10} \exp(-2700/T)$	8
$CN + O_2 \rightarrow NCO + O$	$1.1 \times 10^{-11} \exp(205/T)$	8
$CN + CO_2 \rightarrow NCO + CO$	2×10^{-15}	8
$HCN + O \rightarrow OH + CN$	$4.5 \times 10^{-15} T^{1.58} \exp(-13386/T)$	8
$HCN + O \rightarrow H + NCO$	$3.3 \times 10^{-16} T^{1.47} \exp(-3774/T)$	8
$HCN + O \rightarrow CO + NH$	$9.0 \times 10^{-16} T^{1.21} \exp(-3824/T)$	8
$HCN + OH \rightarrow H_2O + CN$	$1.28 \times 10^{-11} \exp(-4161/T)$	8
$HCN + OH \rightarrow HOCN + H$	$2.01 \times 10^{-11} \exp(-8516/T)$	8
$HCN + OH \rightarrow HNCO + H$	$2.84 \times 10^{-13} \exp(-4397/T)$	8
$HCN + OH \rightarrow NH_2 + CO$	$1.07 \times 10^{-13} \exp(-5892/T)$	8
$HCN + H \rightarrow CN + H_2$	$6.31 \times 10^{-10} \exp(-12400/T)$	8
$NCO + H_2 \rightarrow H + HNCO$	$1.26 \times 10^{-21} T^3 \exp(-2012/T)$	8
$NCO + O \rightarrow NO + CO$	1.48×10^{-11}	8

$NCO + O_2 \rightarrow NO + CO_2$	1.32×10^{-12}	8
$NCO + NO \rightarrow CO + N_2 + O$	7.61×10^{-12}	8
$NCO + NO \rightarrow CO_2 + N_2$	1.45×10^{-11}	8
$NCO + NO \rightarrow N_2O + CO$	1.09×10^{-11}	8
$NCCN + O \rightarrow CN + NCO$	$4.15 \times 10^{-11} \exp(-5500/T)$	8
$NCCN + H \rightarrow NCN + CN$	8.59×10^{-16}	8
$CO + H + M \rightarrow HCO + M$	$1.99 \times 10^{-33} \exp(-842/T)$ cm^6 s^{-1}	8
$CO + NO_2 \rightarrow CO_2 + NO$	$1.48 \times 10^{-10} \exp(-17009/T)$	8
$CO + O3 \rightarrow O_2 + CO_2$	4×10^{-25}	8
$C + CO + M \rightarrow C_2O + M$	6.3×10^{-32} cm^6 s^{-1}	8
$C_2O + O \rightarrow CO + CO$	9.51×10^{-11}	8
$C_2O + O_2 \rightarrow C_2O + CO$	3.3×10^{-13}	8
$C_2O + N \rightarrow CO + CN$	5.5×10^{-10}	8
$C + N + M \rightarrow CN + M$	9.41×10^{-33} cm^6 s^{-1}	8
$C + NCCN \rightarrow CN + CCN$	3×10^{-11}	8
$C + NO \rightarrow CN + O$	4.8×10^{-11}	8
$C + N_2 + M \rightarrow CNN + M$	3.1×10^{-33} cm^6 s^{-1}	8
$C + N_3 \rightarrow CN + N_2$	1.10×10^{-10}	8
$C + O_2 \rightarrow CO + O$	2.6×10^{-11}	8
$CCN+ O \rightarrow CO + CN$	6×10^{-12}	8
$CCN+ N \rightarrow CN + CN$	1×10^{-10}	8
$CO_2 + N \rightarrow CO + NO$	$3.2 \times 10^{-13} \exp(-1710/T)$	8
$C^+ + H^- \rightarrow C + H$	$5 \times 10^{-8} (T/300)^{-0.5}$	14
$C^+ + O^- \rightarrow C + O$	$5 \times 10^{-8} (T/300)^{-0.5}$	14
$C^+ + O_2^- \rightarrow C + O_2$	$5 \times 10^{-8} (T/300)^{-0.5}$	14

Additional reactions for C_3H_6 and C_3H_8

Reaction	Rate Coefficient [d]	Ref
$C_3H_8 + H \rightarrow n\text{-}C_3H_7 + H_2$	$4.31 \times 10^{-12} (T/300)^{2.54} \exp(-3400/T)$	20
$C_3H_8 + H \rightarrow i\text{-}C_3H_7 + H_2$	$1.90 \times 10^{-12} (T/300)^{2.4} \exp(-2250/T)$	20
$C_3H_8 + O \rightarrow n\text{-}C_3H_7 + OH$	$1.39 \times 10^{-12} (T/300)^{2.68} \exp(-1870/T)$	20
$C_3H_8 + O \rightarrow i\text{-}C_3H_7 + OH$	$4.08 \times 10^{-13} (T/300)^{2.71} \exp(-1060/T)$	20
$C_3H_8 + C_2H_5 \rightarrow n\text{-}C_3H_7 + C_2H_6$	$1.65 \times 10^{-15} (T/300)^{3.65} \exp(-4600/T)$	20
$C_3H_8 + C_2H_5 \rightarrow I\text{-}C_3H_7 + C_2H_6$	$9.31 \times 10^{-16} (T/300)^{3.46} \exp(-3760/T)$	20
$C_3H_8 + CH_3 \rightarrow n\text{-}C_3H_7 + CH_4$	$1.65 \times 10^{-15} (T/300)^{3.65} \exp(-3600/T)$	20
$C_3H_8 + CH_3 \rightarrow i\text{-}C_3H_7 + CH_4$	$9.31 \times 10^{-16} (T/300)^{3.46} \exp(-2760/T)$	20
$C_3H_8 + OH \rightarrow n\text{-}C_3H_7 + H_2O$	$7.95 \times 10^{-13} (T/300)^{2} \exp(-2270/T)$	20
$C_3H_8 + OH \rightarrow i\text{-}C_3H_7 + H_2O$	$1.44 \times 10^{-12} (T/300)^{1} \exp(-130/T)$	20
$n\text{-}C_3H_7 + O_2 \rightarrow n\text{-}C_3H_7O_2$	$5.64 \times 10^{-12} (T/300)^{-2.7}$	20
$i\text{-}C_3H_7 + O_2 \rightarrow (CH_3)_2CHO_2$	1.50×10^{-11}	20
$n\text{-}C_3H_7O_2 + NO \rightarrow n\text{-}C_3H_7O + NO_2$	8.69×10^{-12}	21
$n\text{-}C_3H_7O_2 + NO \rightarrow n\text{-}C_3H_7ONO_2$	1.80×10^{-13}	21
$(CH_3)_2CHO_2 + NO \rightarrow (CH_3)_2CHO + NO_2$	$2.70 \times 10^{-12} \exp(-360/T)$	21
$(CH_3)_2CHO_2 + NO \rightarrow (CH_3)_2CHONO_2$	3.80×10^{-13}	21
$n\text{-}C_3H_7O_2 + HO_2 \rightarrow n\text{-}C_3H_7OOH + O_2$	$1.90 \times 10^{-13} \exp(-130/T)$	21
$(CH_3)_2CHO_2 + HO_2 \rightarrow (CH_3)_2CHOOH + O_2$	$1.90 \times 10^{-13} \exp(-130/T)$	23
$n\text{-}C_3H_7O + O_2 \rightarrow C_2H_5CHO + HO_2$	$6.00 \times 10^{-14} \exp(-550/T)$	21
$(CH_3)_2CHO + O_2 \rightarrow CH_3COCH_3 + HO_2$	$1.50 \times 10^{-14} \exp(-200/T)$	21
$n\text{-}C_3H_7 \rightarrow C_2H_4 + CH_3$	$1.20 \times 10^{13} \exp(-15300/T)\ s^{-1}$	20
$n\text{-}C_3H_7 \rightarrow C_3H_6 + H$	$1.09 \times 10^{13} \exp(-17800/T)\ s^{-1}$	20
$n\text{-}C_3H_7 + H_2 \rightarrow C_3H_8 + H$	$3.25 \times 10^{-14} (T/300)^{2.84} \exp(-4600/T)$	20

$n\text{-}C_3H_7 + H \rightarrow C_3H_6 + H_2$	3.00×10^{-12}	20
$n\text{-}C_3H_7 + OH \rightarrow C_3H_6 + H_2O$	4.00×10^{-11}	20
$n\text{-}C_3H_7 + OH \rightarrow n\text{-}C_3H_7OH$	4.00×10^{-11}	20
$n\text{-}C_3H_7 + HO_2 \rightarrow C_2H_5 + OH + HCHO$	4.00×10^{-11}	20
$n\text{-}C_3H_7 + H_2O_2 \rightarrow HO_2 + C_3H_8$	$5.23 \times 10^{-15} (T/300)^{2.11} \exp(-1290/T)$	20
$n\text{-}C_3H_7 + CH_4 \rightarrow C_3H_8 + CH_3$	$3.63 \times 10^{-16} (T/300)^{4.2} \exp(-5470/T)$	20
$n\text{-}C_3H_7 + C_2H_6 \rightarrow C_3H_8 + C_2H_5$	$1.22 \times 10^{-15} (T/300)^{3.82} \exp(-4550/T)$	20
$n\text{-}C_3H_7 + HCHO \rightarrow C_3H_8 + HCO$	$7.63 \times 10^{-14} (T/300)^{2.9} \exp(-2950/T)$	20
$n\text{-}C_3H_7 + HCO \rightarrow C_3H_8 + CO$	1.00×10^{-10}	20
$n\text{-}C_3H_7 + HCO \rightarrow C_3H_7CHO$	2.00×10^{-11}	20
$n\text{-}C_3H_7 + CH_3 \rightarrow CH_4 + C_3H_6$	$3.06 \times 10^{-12} (T/300)^{-0.32}$	20
$n\text{-}C_3H_7 + C_2H_5 \rightarrow C_3H_6 + C_2H_6$	2.40×10^{-12}	20
$n\text{-}C_3H_7 + C_2H_5 \rightarrow C_3H_8 + C_2H_4$	1.90×10^{-12}	20
$n\text{-}C_3H_7 + C_3H_8 \rightarrow C_3H_8 + i\text{-}C_3H_7$	$1.13 \times 10^{-17} (T/300)^{4} \exp(-2380/T)$	20
$n\text{-}C_3H_7 + n\text{-}C_3H_7 \rightarrow C_3H_6 + C_3H_8$	2.80×10^{-12}	20
$n\text{-}C_3H_7O \rightarrow C_2H_5 + HCHO$	$5.01 \times 10^{13} \exp(-785/T)\ s^{-1}$	20
$i\text{-}C_3H_7 \rightarrow C_3H_6 + H$	$1.60 \times 10^{13} \exp(-18000/T)\ s^{-1}$	20
$i\text{-}C_3H_7 + H_2 \rightarrow C_3H_8 + H$	$7.73 \times 10^{-14} (T/300)^{3.28} \exp(-4360/T)$	20
$i\text{-}C_3H_7 + H \rightarrow C_3H_6 + H_2$	6.00×10^{-12}	20
$i\text{-}C_3H_7 + OH \rightarrow C_3H_6 + H_2O$	4.00×10^{-11}	20
$i\text{-}C_3H_7 + HO_2 \rightarrow CH_3CHO + CH_3 + OH$	4.00×10^{-11}	20
$i\text{-}C_3H_7 + H_2O_2 \rightarrow C_3H_8 + HO_2$	$4.92 \times 10^{-15} (T/300)^{2.83} \exp(-2040/T)$	20
$i\text{-}C_3H_7 + C_2H_6 \rightarrow C_3H_8 + C_2H_5$	$3.55 \times 10^{-16} (T/300)^{4.2} \exp(-4390/T)$	20
$i\text{-}C_3H_7 + HCHO \rightarrow C_3H_8 + HCO$	$1.80 \times 10^{-13} \exp(-3500/T)$	20
$i\text{-}C_3H_7 + HCO \rightarrow C_3H_8 + CO$	2.00×10^{-10}	20
$i\text{-}C_3H_7 + HCO \rightarrow C_3H_7CHO$	3.00×10^{-11}	20
$i\text{-}C_3H_7 + CH_3 \rightarrow CH_4 + C_3H_6$	$7.52 \times 10^{-12} (T/300)^{-0.68}$	20

$i\text{-}C_3H_7 + C_2H_5 \rightarrow C_3H_8 + C_2H_4$	$4.16 \times 10^{-12}\ (T/300)^{-0.35}$	20
$i\text{-}C_3H_7 + C_2H_5 \rightarrow C_3H_6 + C_2H_6$	$5.20 \times 10^{-12}\ (T/300)^{-0.35}$	20
$i\text{-}C_3H_7 + C_2H_4 \rightarrow C_3H_6 + C_2H_5$	$4.40 \times 10^{-14} \exp(-3320/T)$	20
$i\text{-}C_3H_7 + C_3H_8 \rightarrow C_3H_8 + n\text{-}C_3H_7$	$3.55 \times 10^{-16}\ (T/300)^{4.2}\ \exp(-4390/T)$	20
$i\text{-}C_3H_7 + n\text{-}C_3H_7 \rightarrow C_3H_6 + C_3H_8$	$1.16 \times 10^{-11}\ (T/300)^{-0.35}$	20
$i\text{-}C_3H_7 + i\text{-}C_3H_7 \rightarrow C_3H_6 + C_3H_8$	$6.50 \times 10^{-12}\ (T/300)^{-0.7}$	20
$CH_4 + H \rightarrow CH_3 + H_2$	$1.01 \times 10^{-12}\ (T/300)^{3}\ \exp(-4410/T)$	12
$CH_4 + HO_2 \rightarrow CH_3 + H_2O_2$	$3.00 \times 10^{-13} \exp(-9350/T)$	12
$C_2H_6 + H \rightarrow C_2H_5 + H_2$	$4.03 \times 10^{-12}\ (T/300)^{2.1}\ \exp(-3510/T)$	12
$C_2H_6 + O \rightarrow C_2H_5 + OH$	$2.91 \times 10^{-12}\ (T/300)^{2.25} \exp(-2520/T)$	12
$C_2H_6 + OH \rightarrow C_2H_5 + H_2O$	$1.62 \times 10^{-12}\ (T/300)^{1.81} \exp(-533/T)$	12
$C_2H_6 + HO_2 \rightarrow H_2O_2 + C_2H_5$	$4.90 \times 10^{-13} \exp(-7520/T)$	12
$HCHO + HO_2 \rightarrow H_2O_2 + HCO$	$3.30 \times 10^{-12} \exp(-5870/T)$	12
$HCHO + NO_2 \rightarrow HCO + HNO_2$	$8.29 \times 10^{-16}\ (T/300)^{3.67} \exp(-6010/T)$	21
$HCHO + NO_3 \rightarrow HCO + HNO_3$	5.80×10^{-16}	21
$CO_2 + N \rightarrow CO + NO$	$3.20 \times 10^{-13} \exp(-1710/T)$	21
$CH_3 + H_2 \rightarrow CH_4 + H$	$2.61 \times 10^{-14}\ (T/300)^{2.77} \exp(-3990/T)$	12
$CH_3 + O_2 \rightarrow HCHO + OH$	$1.60 \times 10^{-15}\ (T/300)^{2.5}\ \exp(-1110/T)$	12
$CH_3 + OH \rightarrow CH_3OH$	$1.15 \times 10^{-08}\ (T/300)^{-4.4} \exp(-1260/T)$	12
$CH_3 + OH \rightarrow CH_2OH + H$	$1.25 \times 10^{-5}\ (T/300)^{-5.0} \exp(-8260/T)$	12
$CH_3 + H_2O_2 \rightarrow CH_4 + HO_2$	$2.00 \times 10^{-14} \exp(-300/T)$	12
$CH_3 + C_2H_6 \rightarrow CH_4 + C_2H_5$	$9.79 \times 10^{-17}\ (T/300)^{5.64} \exp(-2830/T)$	12
$CH_3 + HCHO \rightarrow CH_4 + HCO$	$1.87 \times 10^{-15}\ (T/300)^{4.85} \exp(-1750/T)$	12
$CH_3 + CO \rightarrow CH_3CO$	$1.98 \times 10^{-10}\ (T/300)^{-8.3} \exp(-5270/T)$	12
$CH_3 + HCO \rightarrow CH_4 + CO$	2.00×10^{-10}	12
$CH_3 + HCO \rightarrow CH_3CHO$	3.00×10^{-11}	12
$CH_3 + N \rightarrow H + H + HCN$	3.32×10^{-13}	21

$CH_3 + N \rightarrow HCN + H_2$	8.59×10^{-12}	21
$CH_3 + NO_2 \rightarrow CH_3NO_2$	$3.44 \times 10^{-11} (T/300)^{-0.6}$	21
$CH_3 + NO_2 \rightarrow HCHO + HNO$	5.39×10^{-12}	21
$CH_3 + NO_2 \rightarrow CH_3ONO$	1.16×10^{-13}	21
$CH_3 + NO_2 \rightarrow CH_3O + NO$	2.50×10^{-11}	21
$C_2H_5 \rightarrow C_2H_4 + H$	$4.44 \times 10^{12} (T/300)^{1.2} \exp(-18700/T)\ s^{-1}$	12
$C_2H_5 + H_2 \rightarrow C_2H_6 + H$	$4.22 \times 10^{-15} (T/300)^{3.6} \exp(-4250/T)$	12
$C_2H_5 + O_2 \rightarrow C_2H_4 + HO_2$	$1.40 \times 10^{-12} \exp(-1950/T)$	12
$C_2H_5 + O_2 \rightarrow C_2H_5O_2$	$7.66 \times 10^{-10} (T/300)^{-5.12} \exp(-1490/T)$	12
$C_2H_5 + O_2 \rightarrow CH_3CHO + OH$	$1.14 \times 10^{-13} (T/300)^{-0.12} \exp(-4280/T)$	12
$C_2H_5 + H \rightarrow C_2H_6$	1.66×10^{-10}	12
$C_2H_5 + H \rightarrow CH_3 + CH_3$	$6.05 \times 10^{-10} (T/300)^{-1.4} \exp(-659/T)$	12
$C_2H_5 + H \rightarrow C_2H_4 + H_2$	3.00×10^{-12}	12
$C_2H_5 + O \rightarrow CH_3CHO + H$	1.33×10^{-10}	12
$C_2H_5 + O \rightarrow HCHO + CH_3$	2.67×10^{-11}	12
$C_2H_5 + OH \rightarrow C_2H_4 + H_2O$	4.00×10^{-11}	12
$C_2H_5 + OH \rightarrow CH_3 + H + HCHO$	4.00×10^{-11}	12
$C_2H_5 + HO_2 \rightarrow CH_3 + HCHO + OH$	4.00×10^{-11}	12
$C_2H_5 + HO_2 \rightarrow C_2H_6 + O_2$	5.00×10^{-13}	12
$C_2H_5 + HO_2 \rightarrow C_2H_4 + H_2O_2$	5.00×10^{-13}	12
$C_2H_5 + H_2O_2 \rightarrow C_2H_6 + HO_2$	$1.45 \times 10^{-14} \exp(-490/T)$	12
$C_2H_5 + HCHO \rightarrow C_2H_6 + HCO$	$8.33 \times 10^{-14} (T/300)^{2.81} \exp(-2950/T)$	12
$C_2H_5 + HCO \rightarrow C_2H_6 + CO$	2.00×10^{-10}	12
$C_2H_5 + HCO \rightarrow C_2H_5CHO$	3.00×10^{-11}	12
$C_2H_5 + CH_3 \rightarrow C_3H_8$	$4.70 \times 10^{-11} (T/300)^{-0.5}$	12
$C_2H_5 + CH_3 \rightarrow CH_4 + C_2H_4$	$1.88 \times 10^{-12} (T/300)^{-0.5}$	12
$C_2H_5 + C_2H_5 \rightarrow C_2H_4 + C_2H_6$	2.30×10^{-12}	12

$C_2H_4 + H \rightarrow C_2H_5$	$6.87 \times 10^{-12} (T/300)^{1.49} \exp(-499/T)$	12
$C_2H_4 + H \rightarrow C_2H_3 + H_2$	$4.07 \times 10^{-12} (T/300)^{2.53} \exp(-6160/T)$	12
$C_2H_4 + O \rightarrow CH_3 + HCO$	$1.52 \times 10^{-12} (T/300)^{1.55} \exp(-215/T)$	12
$C_2H_4 + O \rightarrow CH_2CHO + H$	6.24×10^{-13}	12
$C_2H_4 + O \rightarrow CH_2CO + H_2$	3.81×10^{-14}	12
$C_2H_4 + O \rightarrow C_2H_3 + OH$	$1.33 \times 10^{-12} (T/300)^{1.91} \exp(-1880/T)$	12
$C_2H_4 + OH \rightarrow C_2H_3 + H_2O$	$1.69 \times 10^{-13} (T/300)^{2.75} \exp(-2100/T)$	12
$C_2H_4 + OH \rightarrow C_2H_4OH$	9.00×10^{-12}	12
$C_2H_4 + HO_2 \rightarrow CH_3CHO + OH$	$1.00 \times 10^{-14} \exp(-4000/T)$	12
$C_2H_3 + H_2 \rightarrow C_2H_4 + H$	$1.64 \times 10^{-13} (T/300)^{2.63} \exp(-4300/T)$	12
$C_2H_3 + O_2 \rightarrow C_2H_2 + HO_2$	2.00×10^{-13}	12
$C_2H_3 + H \rightarrow C_2H_2 + H_2$	1.60×10^{-10}	12
$C_2H_3 + O \rightarrow CH_2CO + H$	1.60×10^{-10}	12
$C_2H_3 + OH \rightarrow H_2O + C_2H_2$	5.00×10^{-11}	12
$C_2H_3 + OH \rightarrow CH_3CHO$	5.00×10^{-11}	12
$C_2H_3 + HO_2 \rightarrow OH + CH_3 + CO$	5.00×10^{-11}	12
$C_2H_3 + H_2O_2 \rightarrow C_2H_4 + HO_2$	$2.00 \times 10^{-14} \exp(-300/T)$	12
$C_2H_3 + CH4 \rightarrow C_2H_4 + CH_3$	$2.18 \times 10^{-14} (T/300)^{4.02} \exp(-2750/T)$	12
$C_2H_3 + C_2H_6 \rightarrow C_2H_4 + C_2H_5$	$1.50 \times 10^{-13} (T/300)^{3.3} \exp(-5290/T)$	12
$C_2H_3 + HCHO \rightarrow C_2H_4 + HCO$	$8.22 \times 10^{-14} (T/300)^{2.81} \exp(-2950/T)$	12
$C_2H_3 + CO \rightarrow C_2H_3CO$	$2.50 \times 10^{-13} \exp(-2420/T)$	12
$C_2H_3 + HCO \rightarrow C_2H_4 + CO$	1.50×10^{-10}	12
$C_2H_3 + HCO \rightarrow C_2H_3CHO$	3.00×10^{-11}	12
$C_2H_3 + CH_3 \rightarrow C_2H_2 + CH_4$	3.40×10^{-11}	12
$C_2H_3 + CH_3 \rightarrow C_3H_6$	1.20×10^{-10}	12
$C_2H_3 + C_2H_5 \rightarrow C_2H4 + C_2H_4$	8.00×10^{-13}	12
$C_2H_3 + C_2H_5 \rightarrow C_2H_2 + C_2H_6$	8.00×10^{-13}	12

$C_2H_3 + C_2H_3 \rightarrow C_2H_4 + C_2H_2$	1.60×10^{-12}	12
$C_2H_2 + O \rightarrow CH_2 + CO$	$5.15 \times 10^{-12} (T/300)^{1.17} \exp(-1070/T)$	12
$C_2H_2 + O \rightarrow C_2HO + H$	$1.50 \times 10^{-11} \exp(-2290/T)$	12
$C_2H_2 + OH \rightarrow C_2H + H_2O$	$1.04 \times 10^{-13} (T/300)^{2.68} \exp(-6060/T)$	12
$C_2H_2 + HO_2 \rightarrow CH_2CO + OH$	$1.00 \times 10^{-14} \exp(-4000/T)$	12
$C_2H_2 + CH_3 \rightarrow C_3H_5$	$1.00 \times 10^{-12} \exp(-3880/T)$	12
$C_2H_2 + OH \rightarrow C_2H_2OH$	$8.50 \times 10^{-12} \exp(-705/T)$	12
$C_2H + H_2 \rightarrow C_2H_2 + H$	$1.90 \times 10^{-11} \exp(-1450/T)$	12
$C_2H + O_2 \rightarrow CO + HCO$	4.00×10^{-12}	12
$C_2H + O_2 \rightarrow C_2HO + O$	1.00×10^{-12}	12
$C_2H + H \rightarrow C_2H_2$	3.00×10^{-10}	12
$C_2H + O \rightarrow CH + CO$	3.00×10^{-11}	12
$C_2H + OH \rightarrow C_2H_2 + O$	3.00×10^{-11}	12
$C_2H + OH \rightarrow CH_2 + CO$	3.00×10^{-11}	12
$C_2H + HO_2 \rightarrow C_2H_2 + O_2$	3.00×10^{-11}	12
$C_2H + HO_2 \rightarrow C_2HO + OH$	3.00×10^{-11}	12
$C_2H + CH_4 \rightarrow C_2H_2 + CH_3$	$3.00 \times 10^{-12} \exp(-250/T)$	12
$C_2H + C_2H_6 \rightarrow C_2H_2 + C_2H_5$	6.00×10^{-12}	12
$C_2H + CO \rightarrow C_2HCO$	$2.50 \times 10^{-13} \exp(-2420/T)$	12
$C_2H + HCO \rightarrow C_2H_2 + CO$	1.00×10^{-10}	12
$C_2H + CH_3 \rightarrow C_3H_3 + H$	4.00×10^{-11}	12
$C_2H + C_2H_5 \rightarrow C_2H_2 + C_2H_4$	3.00×10^{-12}	12
$C_2H + C_2H_5 \rightarrow C_3H_3 + CH_3$	3.00×10^{-11}	12
$C_2H + C_2H_3 \rightarrow C_2H_2 + C_2H_2$	1.60×10^{-12}	12
$C_2H + C_2H \rightarrow C_2H_2 + C_2$	3.00×10^{-12}	12
$CH_3CO + M \rightarrow CH_3 + CO + M$	$6.44 \times 10^{-3} (T/300)^{-8.62} \exp(-11300/T)$	12
$CH_3CO + O_2 \rightarrow CH_3COO_2$	3.00×10^{-12}	12

$CH_3CO + H \rightarrow CH_3 + HCO$	1.60×10^{-10}	12
$CH_3CO + O \rightarrow CH_3 + CO_2$	1.60×10^{-11}	12
$CH_3CO + OH \rightarrow CH_2CO + H_2O$	2.00×10^{-11}	12
$CH_3CO + OH \rightarrow CH_3 + CO + OH$	5.00×10^{-11}	12
$CH_3CO + HO_2 \rightarrow CH_3 + CO_2 + OH$	5.00×10^{-11}	12
$CH_3CO + H_2O_2 \rightarrow CH_3CHO + HO_2$	3.00×10^{-13} exp(-4140/T)	12
$CH_3CO + HCO \rightarrow CH_3CHO + CO$	1.50×10^{-11}	12
$CH_3CO + HCO \rightarrow CH_3COCHO$	3.00×10^{-11}	12
$CH_3CO + CH_3 \rightarrow CH_3COCH_3$	6.70×10^{-9} $(T/300)^{-0.8}$	12
$CH_3CO + C_2H_5 \rightarrow C_2H_5COCH_3$	5.19×10^{-10}	12
$CH_3CO + C_2H_3 \rightarrow CH_3 + CH_2CHCO$	3.00×10^{-11}	12
$CH_3CO + C_2H \rightarrow C_2HCO + CH_3$	3.00×10^{-11}	12
$CH_3O_2 + H \rightarrow CH_3O + OH$	1.60×10^{-10}	12
$CH_3O_2 + O \rightarrow CH_3O + O_2$	6.00×10^{-11}	12
$CH_3O_2 + OH \rightarrow CH_3OH + O_2$	1.00×10^{-10}	12
$CH_3O_2 + HO_2 \rightarrow CH_3OOH + OH$	7.70×10^{-14} exp(-1300/T)	12
$CH_3O_2 + H_2O_2 \rightarrow CH_3OOH + HO_2$	4.00×10^{-12} exp(-5000/T)	12
$CH_3O_2 + HCO \rightarrow CH_3O + H + CO_2$	5.00×10^{-11}	12
$CH_3O_2 + CH_3 \rightarrow CH_3O + CH_3O$	4.00×10^{-11}	12
$CH_3O_2 + C_2H_5 \rightarrow CH_3O + C_2H_5O$	4.00×10^{-11}	12
$CH_3O_2 + C_2H_3 \rightarrow CH_3O + C_2H_3O$	4.00×10^{-11}	12
$CH_3O_2 + C_2H \rightarrow CH_3O + C_2HO$	4.00×10^{-11}	12
$CH_3O_2 + CH_3CO \rightarrow CH_3 + CO_2 + CH_3O$	4.00×10^{-11}	12
$CH_3O_2 + CH_3O_2 \rightarrow CH_3O + CH_3O + O_2$	1.30×10^{-13}	12
$CH_3O_2 + CH_3O_2 \rightarrow CH_3OH + HCHO + O_2$	2.10×10^{-13}	12
$CH_3O_2 + NO \rightarrow CH_3O + NO_2$	4.20×10^{-12} exp(-180/T)	12
$CH_3O + O_2 \rightarrow HCHO + HO_2$	1.10×10^{-13} exp(-1310/T)	12

$CH_3O + H \rightarrow HCHO + H_2$	3.30×10^{-11}	12
$CH_3O + O \rightarrow HCHO + OH$	1.00×10^{-11}	12
$CH_3O + OH \rightarrow HCHO + OH$	3.00×10^{-11}	12
$CH_3O + HO_2 \rightarrow HCHO + H_2O_2$	5.00×10^{-13}	12
$CH_3O + CH_4 \rightarrow CH_3OH + CH_3$	$2.60 \times 10^{-13} \exp(-4450/T)$	12
$CH_3O + C_2H_6 \rightarrow CH_3OH + C_2H_5$	$4.00 \times 10^{-13} \exp(-3570/T)$	12
$CH_3O + HCHO \rightarrow CH_3OH + HCO$	$1.70 \times 10^{-13} \exp(-1500/T)$	12
$CH_3O + CO \rightarrow CH_3 + CO_2$	$2.60 \times 10^{-11} \exp(-5940/T)$	12
$CH_3O + HCO \rightarrow CH_3OH + CO$	1.50×10^{-10}	12
$CH_3O + CH_3 \rightarrow HCHO + CH_4$	4.00×10^{-11}	12
$CH_3O + CH_3 \rightarrow CH_3OCH_3$	2.00×10^{-11}	12
$CH_3O + C_2H_5 \rightarrow HCHO + C_2H_6$	4.00×10^{-11}	12
$CH_3O + C_2H_3 \rightarrow HCHO + C_2H_4$	4.00×10^{-11}	12
$CH_3O + C_2H \rightarrow HCHO + C_2H_2$	4.00×10^{-11}	12
$CH_3O + CH_3CO \rightarrow CH_3OH + CH_2CO$	1.00×10^{-11}	12
$CH_3O + CH_3CO \rightarrow HCHO + CH_3CHO$	1.00×10^{-11}	12
$CH_3O + CH_3O_2 \rightarrow HCHO + CH_3OOH$	5.00×10^{-13}	12
$CH_3O + CH_3O \rightarrow CH_3OH + HCHO$	1.00×10^{-10}	12
$CH_3O + NO_2 \rightarrow CH_3ONO_2$	1.50×10^{-11}	21
$CH_3O + NO_2 \rightarrow HCHO + HNO_2$	3.00×10^{-13}	21
$CH_3O + NO \rightarrow CH_3ONO$	2.00×10^{-11}	21
$CH_3O + NO \rightarrow HCHO + HNO$	$4.00 \times 10^{-12} (T/300)^{-0.7}$	21
$CH_3OH + O \rightarrow CH_2OH + OH$	$4.63 \times 10^{-14} (T/300)^{3.77} \exp(-340/T)$	22
$CH_3OH + O \rightarrow CH_3O + OH$	$7.08 \times 10^{-13} (T/300)^{1.54} \exp(-1000/T)$	22
$CH_3OH + OH \rightarrow H_2O + CH_2OH$	8.79×10^{-13}	22
$CH_3OH + OH \rightarrow H_2O + CH_3O$	$1.66 \times 10^{-11} \exp(-854/T)$	22
$CH_3OH + H \rightarrow CH_2OH + H_2$	1.39×10^{-11}	22

$CH_3OH + H \rightarrow CH_3O + H_2$	$6.64 \times 10^{-11} \exp(-3070/T)$	22
$C_2H_5 + NO \rightarrow C_2H_5NO$	$6.49 \times 10^{-11} (T/300)^{-3.37} \exp(-1740/T)$	21
$C_3H_6 + O \rightarrow$ Methyl Oxirane	$9.05 \times 10^{-12} \exp(-610/T)$	23
$C_3H_6 + O \rightarrow C_2H_5CHO$	$9.05 \times 10^{-12} \exp(-610/T)$	23
$C_3H_6 + O \rightarrow CH_2CHO + CH_3$	$6.03 \times 10^{-12} \exp(-610/T)$	23
$C_3H_6 + O \rightarrow C_2H_5 + HCO$	$6.03 \times 10^{-12} \exp(-610/T)$	23
$C_3H_6 + OH \rightarrow CH_3CHCH_2OH$	$6.56 \times 10^{-11} (T/300)^{-1.48} \exp(-361/T)$	23
$C_3H_6 + OH \rightarrow CH_3CHOHCH_2$	$3.53 \times 10^{-11} (T/300)^{-1.48} \exp(-361/T)$	23
$C_3H_6 + H \rightarrow CH_3 + C_2H_4$	$1.20 \times 10^{-11} \exp(-655/T)$	8
$C_3H_6 + H \rightarrow i\text{-}C_3H_7$	$1.00 \times 10^{-11} (T/300)^{0.25} \exp(-593/T)$	8
$CH_3CH(OH)CH_2 + O_2 \rightarrow CH_3CH(OH)CH_2OO$	3.90×10^{-12}	23
$CH_3CHCH_2OH + O_2 \rightarrow CH_3CH(OO)CH_2OH$	1.16×10^{-11}	23
$CH_3CH(OH)CH_2OO + NO \rightarrow NO_2 + CH_3CH(OH)CH_2O$	1.00×10^{-14}	23
$CH_3CH(OO)CH_2OH + NO \rightarrow NO_2 + CH_3CH(O)CH_2OH$	1.00×10^{-14}	23
$CH_3CH(OH)CH_2O \rightarrow HCHO + CH_3CHOH$	$7.94 \times 10^{13} \exp(-10500/T)\ s^{-1}$	23
$CH_3CH(O)CH_2OH + M \rightarrow CH_3CHO + CH_2OH + M$	1.00×10^{-11}	23
$CH_3CHOH + O_2 \rightarrow CH_3CHO + HO_2$	1.00×10^{-11}	23
$CH_2OH + O_2 \rightarrow HCHO + HO_2$	$1.06 \times 10^{-10} (T/300)^{-1.58} \exp(-801/T)$	23
$CH_2CHO + NO \rightarrow ONCH_2CHO$	2.51×10^{-11}	24
$CH_2CHO + O_2 \rightarrow CHOCHO + OH$	2.20×10^{-13}	24
$CH_2CHO + O_2 \rightarrow HCHO + CO + OH$	3.00×10^{-14}	24
$CH_2CHCHO + OH \rightarrow H_2O + CH_2CHCO$	2.66×10^{-11}	24

Methyl Oxirane + OH $\rightarrow$ H_2O + Products	4.95×10^{-13}	21
C_2H_6 + N $\rightarrow$ CH_3NCH_3	4.00×10^{-16}	21
$C_2H_5O_2$ + NO $\rightarrow$ C_2H_5O + NO_2	8.90×10^{-12}	21
$C_2H_5O_2$ + NO $\rightarrow$ $C_2H_5ONO_2$	1.30×10^{-13}	21
$C_2H_5O_2$ + NO_2 $\rightarrow$ $C_2H_5OONO_2$	2.59×10^{-10} $(T/300)^{-3.74}$ exp(-1030/T)	21
$C_2H_5O_2$ $\rightarrow$ C_2H_4 + HO_2	1.87×10^{-13} $(T/300)^{-0.6}$ exp(15890/T) s^{-1}	21
C_2H_5O + NO $\rightarrow$ C_2H_5ONO	2.63×10^{-11}	21
C_2H_5O + NO $\rightarrow$ CH_3CHO + HNO	1.30×10^{-11}	21
C_2H_5O + NO_2 $\rightarrow$ $C_2H_5ONO_2$	2.80×10^{-11}	21
C_2H_5O + NO_2 $\rightarrow$ CH_3CHO + HNO_2	6.61×10^{-12}	21
C_2H4 + N $\rightarrow$ HCN + CH_3	2.46×10^{-12} $(T/300)^{-3.28}$ exp(-1360/T)	21
CH4 + N $\rightarrow$ HCN + H_2 + H	2.50×10^{-14}	21
CH_3CHO + N $\rightarrow$ HCN + H_2 + HCO	1.99×10^{-14}	21
CH_3CHO + NO_3 $\rightarrow$ HNO_3 + CH_3CO	2.73×10^{-15}	21
CH_3COO_2 + NO $\rightarrow$ CH_3 + CO_2 + NO_2	2.00×10^{-11}	21
CH_3COO_2 + NO $\rightarrow$ CH_3COO + NO_2	1.40×10^{-11}	21
CH_3COO_2 + NO_2 $\rightarrow$ $CH_3CO_3NO_2$	1.75×10^{-12} exp(-393/T)	21
CH_3CO + NO $\rightarrow$ CH_3CONO	3.32×10^{-13}	21
CH_3CO + NO_2 $\rightarrow$ CH_3 + CO_2 + NO	1.66×10^{-12}	21
CH_3CO + NO_2 $\rightarrow$ CH_3COO + NO	2.50×10^{-11}	21
CH_2OH + NO $\rightarrow$ CH_2OHNO	2.50×10^{-11}	21
CH_2OH + NO_2 $\rightarrow$ $HOCH_2NO_2$	2.30×10^{-11}	21
CH_2OH + O $\rightarrow$ HCHO + OH	1.50×10^{-10}	21
CH_2OH + CH_3 $\rightarrow$ CH_4 + HCHO	4.00×10^{-12}	22
CH_2OH + CH_3 $\rightarrow$ C_2H_5OH	2.00×10^{-11}	22
CH_2CHO + NO_2 $\rightarrow$ CH_2CO + HNO_2	1.48×10^{-11} exp(-80/T)	21
CH_2 + NO $\rightarrow$ $CONH_2$	5.76×10^{-12} exp(-190/T)	21

$CH_2CO + OH \rightarrow CH_2OH + CO$	1.08×10^{-11}	21
$CH_2CO + OH \rightarrow HCO + HCHO$	4.65×10^{-11}	21
$CH_2CO + H \rightarrow CH_3 + CO$	$1.88 \times 10^{-11} \exp(-1730/T)$	21
$CH + NO \rightarrow CO + NH$	2.50×10^{-10}	21
$HCO + NO \rightarrow CO + HNO$	1.20×10^{-11}	21
$HCO + NO_2 \rightarrow H + CO_2 + NO$	$1.95 \times 10^{-10} (T/300)^{-0.75} \exp(-970/T)$	21
$HCO + NO_2 \rightarrow HCOO + NO$	2.71×10^{-11}	21
$HCO + NO_2 \rightarrow CO + HNO_2$	$8.73 \times 10^{-11} \exp(-319/T)$	21
$CH_3ONO \rightarrow HCHO + HNO$	$3.98 \times 10^{13} \exp(-19400/T)$	21
$HO_2 + NO_2 \rightarrow HNO_2 + O_2$	1.20×10^{-13}	21
$O + HNO_2 \rightarrow NO_2 + OH$	$2.00 \times 10^{-11} \exp(-3000/T)$	21

[a] Rate coefficients have units of $cm^3\ s^{-1}$ unless stated otherwise. T_e is the electron temperature in eV.

[b] Computed using the electron energy distribution and electron impact cross section from cited reference.

[c] Estimated.

[d] Rate coefficients have units of $cm^3\ s^{-1}$ unless stated otherwise. T is the gas temperature in K and activation energies have equivalent units of K.

B.1 References

1. Y. Itikawa, M. Hayashi, A. Ichimura, K. Onda, K. Sakimoto, K. Takayanagi, M. Nakamura, H. Nishimura, and T. Takayanagi, J. Phys. Chem. Ref. Data, **15** (3), 985 (1986).
2. A. V. Phelps, JILA Information Center Report Number 28, University of Colorado (1985).
3. R. R. Laher and F. R. Gilmore, J. Phys. Chem. Ref. Data **19**, 277 (1990).
4. M. Hayashi, in Proceedings of the Meeting of the 4th International Swarm Seminar and the Inelastic Electron-Molecular Collision Symposium, July 19-23, (1985), pp.345.
5. J. C. Person and D. O. Ham, Radiat. Phys. Chem., **31**, 1 (1988).
6. B. R. Rowe, F. Vallée, J. L. Queffelec, J. C. Gomet, and M. Morlais, J. Phys. Chem. **88**, 845 (1988).
7. J. J. Lowke, A. V. Phelps, and B. W. Irwin, J. Appl. Phys. **44**, 4664 (1973).
8. Y. Mirokin and W. G. Mallard, The NIST Chemical Kinetics Database-Version 2Q98 (1998).
9. R. Atkinson, D. L. Baulch, R. A. Cox, R. F. Hampson, Jr., J. A. Kerr, and J. Troe, J. Phys. Chem. Ref. Data, **18**, 881 (1989).
10. L. G. Piper, J. Chem. Phys. **87**, 1625 (1987).
11. R. Atkinson, D. L. Baulch, R. A. Cox, R. F. Hampson, Jr., J. A. Kerr, and J. Troe, J. Phys. Chem. Ref. Data **21**, 1125 (1992).
12. W. Tsang and R. F. Hampson, J. Phys. Chem. Ref. Data **15**(3), 1087 (1986).
13. S. Mukkavilli, C. K. Lee, K.Varghese, and L. L. Tavlarides, Trans. Plasma Sci. **16**, 652 (1988).
14. R. E. Olson, J. R. Peterson, and J. Moseley, J. Chem. Phys. **53**, 3391 (1970).
15. R. K. Bera and R. J. Hanrahan, J. Appl. Phys. **62**, 2523 (1987).
16. P. Borrell, C. J. Cobos, and K. Luther, J. Phys. Chem. **92**, 4377 (1988).

17. W. Hack, P. Rouveirolles, and H. G. Wagner, J. Phys. Chem. **90**, 2505 (1986).

18. A. Mellouki, G. Le Bras, and G. Poulet, J. Phys. Chem. **92**, 2229 (1988).

19. R. Svensson and E. Ljungström, Int. J. Chem. Kin. **20**, 857 (1988).

20. W. Tsang, J. Phys. Chem. Ref. Data **17**(2), 887 (1988).

21. W. G. Mallard, F. Westley, J. T. Herron, and R. F. Hampson, NIST Chemical Kinetics Database-Version 6.0, NIST Standard Reference Data, Giathesburg, MD (1994).

22. W. Tsang, J. Phys. Chem. Ref. Data **16**(3), 471 (1987).

23. R. Atkinson, J. Phys. Chem. Ref. Data **26**, 215 (1997).

24. R. Atkinson, J. Phys. Chem. Ref. Data. **2**, 1 (1994).

VITA

Rajesh Dorai was born in Madras, India. He received his B. Tech. degree in Chemical Engineering from the Indian Institute of Technology, Madras, India, and his M.S. degree in Chemical Engineering from the University of Illinois at Urbana-Champaign. Under the direction of Professor Mark J. Kushner, he has studied atmospheric pressure plasma processing of gases and surfaces since January 1999. His work has resulted in 5 refereed journal publications and 10 conference presentations.